*Author:*
**McGarry, Bryony**

*Title:*
**A preclinical and clinical investigation into quantitative magnetic resonance imaging as a tool for estimating onset time in hyperacute ischaemic stroke**

# A preclinical and clinical investigation into quantitative magnetic resonance imaging as a tool for estimating onset time in hyperacute ischaemic stroke

by

**Bryony Louise McGarry**


A dissertation submitted to the University of Bristol in accordance with the requirements for award of the degree of Doctor of Philosophy in the

**Faculty of Life Sciences**

**March 2020**

*Word count: Fifty-four thousand one hundred and thirty-nine*

# Abstract

Ischaemic stroke is a major cause of adult death and disability and is one of the most expensive neurological conditions. Currently, thrombolysis by rtPA is the only pharmacotherapy for hyperacute ischaemic stroke, and in routine practice it must be administered within 4.5 hours of symptom onset. Consequently, most patients with unknown onset time are precluded from thrombolytic therapy, despite the possibility of still being within the 4.5 hour treatment window. Unknown onset time, therefore, poses a substantial challenge in the management of hyperacute stroke patients.

Multiparametric quantitative magnetic resonance imaging (qMRI) is a potential tool for estimating stroke onset time due to its sensitivity to hydrodynamic and haemodynamic changes in the ischaemic brain. This thesis explores the potential abilities of MRI based stroke timing methods in a preclinical rat model of ischaemia and hyperacute ischaemic stroke patients. Both the preclinical and clinical results suggest that quantifying the change in the $T_2$ relaxation time is a more accurate and reliable method for onset time estimation than measuring the intensities of signals represented in the $T_2$-based weighted images typically acquired in clinics. Results also suggest that $T_2$ distributional information within grey matter lesions may provide a reference-independent stroke timing method.

The translation of preclinical methods and MRI findings to stroke patients demonstrated in the thesis highlights the importance of preclinical research in identifying MRI biomarkers that could aid treatment decisions. Clinical MRI scanners can transform conventional weighted magnetic resonance images that are usually acquired and assessed visually (e.g., $T_2$ weighted), into their 'absolute' parametric counterparts (e.g., $T_2$ relaxometry maps). Exploiting this ability will enable ischaemia to be identified and onset time estimated more accurately and reliably. Ultimately, the encouraging results from this thesis warrant further investigation into the quantification of $T_2$ for informing treatment decisions regarding hyperacute ischaemic stroke patients, in a more extensive clinical study.

# Acknowledgments

I want to thank the following people:

- First and foremost, my principal supervisor, Professor Risto Kauppinen, for his unconditional and unwavering support throughout both the research and writing stages of this PhD. Thank you, Risto, for everything you have taught me over the years; for introducing me to the fascinating world of MRI and turning this former social psychologist into a clinical neuroimaging researcher!
- My second supervisor, Professor Iain Gilchrist, for his kind support and for his suggestions regarding clinical stroke during the course of the PhD projects.
- Three wonderful post-docs, Dr Michael Knight, Dr Terence Norton and Dr Robin Damion, who all, with admirable amounts of skill and patience, contributed to my development as an MRI researcher and data scientist.
- Professor Olli Gröhn and Dr Kimmo Jokivarsi for letting me analyse their rat stroke MRI data, teaching me how to perform my own rat stroke MRI studies, and for their hospitality during my visits to the University of Eastern Finland.
- Professor Peter Flach and Dr Meelis Kull from the University of Bristol, for their advice on precision-recall-gain analysis.
- To the stroke neurologists, radiographers, researchers and nurses at Southmead Hospital (Bristol), AVIC Radcliffe Department of Medicine (Oxford), and Queen Elizabeth University Hospital (Glasgow) for all their efforts in recruiting hyperacute stroke patients for MRI scans.
- Every stroke patient who had an MRI scan, especially for the studies in this thesis, in what must have been an extremely frightening time.
- The EPSRC for funding my PhD, the University of Bristol School of Psychological sciences for funding the rat stroke MRI studies, and the Dunhill Medical Trust for funding the scans of hyperacute stroke patients.
- Mum, Dad, my partner Chris, and my close friends, for their constant encouragement, unconditional support, and for volunteering their brains for MRI studies at CRIC.
- Last but not least, Dr Grant Mair and Professor Jonathon Rossiter, thank you for taking the time to read my work. I hope that it is an enjoyable and informative experience for you both!

# Publications

The work of this thesis has been published, in part, in the following papers.

**Chapter 5**:

- McGarry, B. L., Rogers, H. J., Knight, M. J., Jokivarsi, K. T., Gröhn, O. H. J., & Kauppinen, R. A. (2016). Determining stroke onset time using quantitative MRI: High accuracy, sensitivity and specificity obtained from magnetic resonance relaxation times. *Cerebrovascular Diseases Extra*, *6*(2), 60–65.

- McGarry, B. L., Rogers, H. J., Knight, M. J., Jokivarsi, K. T., Sierra, A., Gröhn, O. H., & Kauppinen, R. A. (2016). Stroke onset time estimation from multispectral quantitative magnetic resonance imaging in a rat model of focal permanent cerebral ischemia. *International Journal of Stroke*, *11*(6), 677–682.

- McGarry, B. L., Jokivarsi, K. T., Knight, M. J., Grohn, O. H. & Kauppinen, R. A. (2017). Magnetic resonance imaging protocol for stroke onset time estimation in permanent cerebral ischemia. *Journal of Visualized Experiments,* (127), e55277.

**Chapter 7**:

- McGarry, B. L., Damion, R. A., Chew, I., Knight. M. J., Harston, G. J., Carone, D. Jezzard, P., Sitaram, A, Muir, W. K. Clatworthy, P. L., & Kauppinen, R. A. (2019). $T_2$ relaxation times identify acute ischaemic stroke patients within the thrombolysis treatment window with higher accuracy than $T_2$-weighted signal intensities. *Conference abstracts of ISMRM*, 27 (0737), Montreal, Canada.

- McGarry, B. L., Damion, R. A., Chew, I., Knight. M. J., Harston, G. J., Carone, D. Jezzard, P., Sitaram, A, Muir, W. K. Clatworthy, P. L., & Kauppinen, R. A. (2020). A comparison of $T_2$ relaxation-based MRI stroke timing methods in hyperacute ischaemic stroke patients: A pilot study. *Journal of Central Nervous System and Disease,* recommended for publication subject to minor revisions, 26th May 2020.

**Chapter 8:**

- McGarry, B. L., Damion, R. A., Norton, T. J., Knight. M. J., Harston, G. J., Clatworthy, P. L., Muir, W. K., & Risto A. Kauppinen. Kauppinen, R. A. (2020). Determining stroke onset time using $T_2$ relaxation times: A comparison of reference and reference-independent methods in ischaemic stroke patients. *Conference abstracts of ISMRM*, virtual conference.

# Contributions

The author was directly responsible for all aspects of this thesis and the data analysis and writing of manuscripts for the published papers, with the exception of the following:

- Operations to induce focal ischaemia in rats in were performed by Ms. Maarit Pulkkinen (University of Eastern Finland, Kuopio, Finland).
- Dr Kimmo Jokivarsi (University of Eastern Finland, Kuopio, Finland) acquired the 4.7T rat MRI data (Jokivarsi et al., 2010).
- The initiation and ethics for scanning hyperacute ischaemic stroke patients at Southmead hospital (North Bristol NHS Trust), Queen Elizabeth University Hospital (University of Glasgow) and Radcliffe Department of Medicine (University of Oxford) was carried out by Professor Risto Kauppinen (University of Bristol), Dr Philip Clatworthy, Dr Rose Bosnell (North Bristol NHS trust), Professor Keith Muir (University of Glasgow), Professor Peter Jezzard, Dr George Harston and Dr Davide Carone (University of Oxford).
- The MRI protocol for hyperacute ischaemic stroke patients was designed by Professor Risto Kauppinen and Dr Michael Knight (University of Bristol) and patients were recruited by clinicians and research nurses at each of the hospitals.
- Dr Michael Knight and Dr Robin Damion (University of Bristol) created the ADC defined ischaemic volumes of interest and computed the echo summed weighted images and the relaxometry maps from the rat and patient MRI data (Damion, Knight, McGarry et al., 2019; Knight, McGarry, et al., 2016; Knight, Damion, McGarry et al., 2019).
- Dr Robin Damion (University of Bristol) performed segmentation of ADC volumes of interest in to grey and white matter volumes of interest for Chapter 8 (Damion, Knight, McGarry et al., 2019).

Signed: (Professor Risto Kauppinen) Date: 4th March 2020

Signed: (Bryony McGarry) Date: 4th March 2020

# Declaration

I declare that the work in this dissertation was carried out in accordance with the requirements of the *University's Regulations and Code of Practice for Research Degree Programmes* and that it has not been submitted for any other academic award. Except where indicated by specific reference in the text, the work is the candidate's own work. Work done in collaboration with, or with the assistance of, others, is indicated as such. Any views expressed in the dissertation are those of the author.

Signed: ..... Date: 4$^{th}$ March 2020

# Table of Contents

# List of Figures

# List of Tables

# Abbreviations

ADC: Apparent diffusion coefficient

AI: Artificial intelligence

AIC: Akaike information criteria

AICc: Akaike information criteria controlled for sample size

AMPA: α-amino-3-hydroxy-5-methyl-4-isoxazolepropionic acid

ATP: Adenosine triphosphate

AUC: area under the curve

AUPRG: area under the precision-recall-gain curve

$B_0$: main magnetic field

$B_1$: applied magnetic field (RF pulse)

BET: brain extraction tool

BOLD effect: blood oxygen level dependent effect

$Ca^{2+}$: calcium

CBF: cerebral blood flow

CBV: cerebral blood volume

CED: cytotoxic oedema dissociation model

CI: confidence interval

$CMRO_2$: cerebral metabolic rate of oxygen

CNR: contrast to noise ratio

CPMG: Carr-Purcell-Meiboom-Gill (multi-echo pulse sequence)

CSF: cerebral spinal fluid

CT: computerised tomography

Dav: Trace of diffusion tensor

DTI: diffusion tensor imaging

$f_1$: volume of elevated $T_1$ relaxation times in the ADC defined ischaemic region

$f_2$: volume of elevated $T_2$ relaxation times in the ADC defined ischaemic region

FA: flip angle

FAST: FMRIB's automated segmentation tool

FFE: fast field echo

FLAIR: fluid attenuated inversion recovery (pulse sequence)

FLASH $T_1$: fast low angle shot $T_1$ (pulse sequence)

FMRIB: Functional magnetic resonance imaging of the brain

FN: false negative

FNIRT: FMRIB's nonlinear registration tool

FOV: field of view

FP: false positive

FSL: the FMRIB software library

GEV: generalised extreme value

GM: grey matter

GRASE: gradient and spin-echo pulse sequence

HWHM: half width at half maximum

IA: intra arterial

ISMRM: International Society for Magnetic Resonance in Medicine

IV: intravenous

$K^+$: potassium

KCl: potassium chloride

LAC: lacunar stroke

LOOCV: leave one out cross validation

MCAo: middle cerebral artery occlusion

MNI: Montreal Neurological Institute

MPRAGE: magnetisation-prepared rapid gradient-echo (pulse sequence)

MR: magnetic resonance

MRI: magnetic resonance imaging

MRS: magnetic resonance spectroscopy

$Na^+$: sodium

NCCA: non-selective cation channel

NCCT: non contrast enhanced computerised tomography

NHS: National Health Service

NIHSS: National Institute of Health Stroke Scale

NMDA: N-methyl-D-aspartate

NMR: nuclear magnetic resonance imaging

NPV: negative predictive value

OEF: oxygen extraction fraction

PAC: partial anterior circulation stroke

POC: posterior circulation stroke

Ppm: parts per million

PPV: positive predictive value

PRG: precision-recall-gain

PWI: perfusion-weighted imaging

qMRI: quantitative magnetic resonance imaging

RF: radio frequency

RMSE: root mean square error

ROC: receiver operating characteristic curve

ROI: region of interest

rtPA: recombinant tissue plasminogen activator

SE-EPI: spin-echo echo planar imaging

SI: signal intensity

SNR: signal to noise ratio

T: Tesla

$T_1$: longitudinal relaxation

$T_1$w: $T_1$ weighted

$T_2$: transverse relaxation

$T_2$w: $T_2$ weighted

TAC: total anterior circulation stroke

TE: echo time

TI: inversion time

TN: true negative

TP: true positive

TR: repetition time

TSE: turbo spin-echo

TTC: triphenyultetrazolium chloride

$V_{overlap}$: volume of overlapping elevated $T_1$ and $T_2$ relaxation times

VOI: volume of interest

WM: white matter

WMH: white matter hyperintensity

# Chapter 1
# Introduction

## 1.1 An introduction to the problem of unknown onset time in hyperacute ischaemic stroke treatment

Stroke is defined as the neurological deficit that results from a focal injury of the central nervous system by a vascular cause (Sacco et al., 2013). Worldwide, stroke is the second leading cause of death and a major cause of adult disability (Johnson et al., 2019). Stroke is one of the most expensive neurological conditions for healthcare in Western countries due to treatment and post-stroke care related costs (Rajsic et al., 2019). A recent projection (Norrving et al., 2018) showed that due to an ageing population the number of strokes and therefore the associated health care and non-healthcare costs are expected to rise considerably and thus the need to minimise the impact of stroke is now more urgent than ever.

Ischaemic strokes are the most prevalent, accounting for 84% of strokes globally (Johnson et al., 2019). The occlusion of a cerebral artery with thrombotic or embolic material results in the abrupt and sustained reduction of blood flow to the surrounding area, causing rapid cell death and permanent brain damage and consequently, a variety of neurological deficits (Meschia & Brott, 2018; Saver, 2006). The narrowing of an artery due to atherosclerosis can also result in severely reduced blood flow, but the disruption is not abrupt. The main therapeutic aim for ischaemic stroke is to restore blood flow as quickly as possible, to prevent further

brain damage. The primary reperfusion-based intervention for hyperacute ischaemic stroke is intravenous (IV) administration of the thrombolytic agent, recombinant tissue plasminogen activator (rtPA) (referred to as alteplase or thrombolysis) (Powers et al., 2018) which is hoped to restore blood flow by actively dissolving the occluding clot. The safety, efficacy and benefit of rtPA when administered intravenously within 4.5 hours of symptom onset, is well established (Hacke et al., 2008; Lees et al., 2016; Sandercock et al., 2012). rtPA has also been shown to be safe and effective when administered intraarterially (IA) to patients with anterior circulation stroke, presenting within six hours of symptom onset (Berkhemer et al., 2015). Patients with a large vessel occlusion, presenting within 24 hours of symptom onset can also be considered for mechanical thrombectomy where reperfusion is achieved by physically removing the clot with an intravascular catheter (Nogueira et al., 2018; Powers et al., 2018). However, both IA rtPA and mechanical thrombectomy are not yet practised routinely (Fiehler et al., 2016; Powers et al., 2018).

Currently, rtPA is the only licensed pharmacotherapy for acute ischaemic stroke (Powers et al., 2018) but only 7.3% of acute ischaemic patients receive it (Aguiar de Sousa et al., 2019). One of the main reasons for such a low treatment rate is that time is the dictating factor as to whether a patient can be considered for IV rtPA (Powers et al., 2018). In most countries, to be eligible, the first neurological symptoms must have happened within 4.5 hours of the patient arriving at the emergency department (Fiehler et al., 2016; Powers et al., 2018). IV rtPA after this time point is associated with a severely increased risk of symptomatic intracranial haemorrhage and other clinically adverse events because the tissue is already dead (Hacke et al., 2008). This time limitation poses a significant barrier to the treatment of acute ischaemic stroke. A multitude of neuroprotective agents targeting different pathophysiological mechanisms and alternative reperfusion strategies have shown potency in preclinical models but have failed in clinical trials (O'Collins et al., 2006). Alternative therapies without a time-window restriction such as those that modulate the adaptive immune response by administration of

stem-cells are an active and promising area of investigation, but at present are far from a clinical application (Hess et al., 2017; Malone et al., 2019).

A fundamental consequence of the 4.5 hour treatment window is that almost one-third of ischaemic stroke patients are automatically precluded from thrombolytic therapy because the time of symptom onset is not known (Dekker et al., 2017). Reasons for unknown onset time include; the patient was unable to communicate time of onset, symptoms were not noticed by the patient or not witnessed by others, or the time could not be pinpointed by a witness (Dekker et al., 2017). 'Wake-up stroke', where the ischaemic event occurred during sleep, and the patient woke with neurological symptoms, is one of the most common reasons for unknown onset time (Thomalla et al., 2017). However, there is accumulating evidence from studies on circadian-rhythms (e.g., Elliott, 1998) and imaging (e.g., Thomalla et al., 2017) that suggest many wake-up stroke patients may still be within the 4.5 hour rtPA treatment window upon awakening. If clinicians had a method or tool that identified patients that may benefit for reperfusion therapies, patients with unknown onset time could be considered for rtPA, which would ultimately minimise the impact of stroke to the individual and society.

Neuroimaging methods, such as computerised tomography (CT) or magnetic resonance imaging (MRI) have been proposed as potential tools for reducing the problem of unknown onset time in the treatment of hyperacute ischaemic stroke patients (e.g., Jokivarsi et al., 2010; Mair et al., 2017; Minnerup et al., 2016; Thomalla et al., 2011). This is because, as a standard of care, all suspected stroke patients must receive some form of imaging on arrival to the emergency department (Fiehler et al., 2016; Powers et al., 2018) and these imaging modalities are sensitive to the hydrodynamic and haemodynamic changes in the ischaemic brain (Dzialowski et al., 2004; Kauppinen, 2014; Mair et al., 2017; Siemund et al., 2009). Typically, non-contrast CT (NCCT) is the preferred imaging modality for stroke in the United Kingdom (UK), as it is widely available, inexpensive and fast and is

used to rule out haemorrhage as a cause of neurological symptoms (Birenbaum et al., 2011; Mair & Wardlaw, 2014). Unlike MRI, NCCT is also better tolerated by unstable and claustrophobic patients (Mair & Wardlaw, 2014) and is safe for patients that have metallic implants (e.g., pacemaker, joint replacement).

MRI, however, is more sensitive to early ischaemia than NCCT and so, unlike NCCT, can be used to diagnose ischaemic stroke (Chalela et al., 2007; Fiebach et al., 2002). MRI also offers the advantage of being multiparametric, in that different sequences are sensitive to different pathophysiological changes in the ischaemic brain (Kauppinen, 2014). This diversity would provide clinicians with much more information for which to base treatment decisions. It is therefore not surprising that MRI is becoming more commonplace as the first-line imaging modality for suspected stroke in specialised stroke centres, most European (Li et al., 2019) and United States hospitals (Burke et al., 2012) and some UK National Health Service (NHS) hospitals (Wardlaw et al., 2014). Multiparametric MRI data can also be acquired within a matter of minutes, with the application of magnetic resonance fingerprinting (MRF) (Ma et al., 2013), which has recently been applied successfully in a clinical study of hyperacute ischaemic stroke patients (Duchaussoy et al., 2019).

There are two potential imaging approaches to overcoming the problem of unknown onset time in hyperacute ischaemic stroke treatment (Biggs et al., 2019; Etherton et al., 2018). One of these is to use imaging as a *tissue clock*, where the decision to treat with thrombolysis would depend on the extent of potentially salvageable tissue evident on the patient's scans (Biggs et al., 2019; Etherton et al., 2018). This approach is referred to as *the infarct core-perfusion mismatch approach* which involves quantifying the extent of irreversibly damaged tissue (infarct core) relative to the amount of hypoxic, potentially salvageable tissue (Etherton et al., 2018), usually identified via contrast agent enhanced CT perfusion or MRI perfusion imaging techniques (Demeestere et al., 2020). If there is a mismatch, where there

is more hypoxic tissue (tissue at risk) than infarct core (irreversibly damaged), the patient could be considered for reperfusion-based therapy regardless of onset time (Etherton et al., 2018).

The benefit of the *tissue clock* approach is that treatment decisions would be made on a patient-specific basis and so accounts for the fact that each patient will tolerate ischaemia differently due to individual differences such as age, collateral status, cerebral reserve and the presence of pre-existing systemic diseases (Wang and Wang, 2019). However, for both perfusion-based CT and MRI *infarct core-perfusion-mismatch* approaches, there is no consensus on the specific thresholds that should be used to differentiate between irreparably damaged and potentially salvageable brain tissue, due to high inter-vendor variability in MRI scanner hardware and software (Dani et al., 2011; González et al., 2013) and incomplete standardisation of image interpretation (Demeestere et al., 2020). Additionally, at the time the studies in this thesis were conducted, the efficacy of treating based on the *infarct core perfusion mismatch* with perfusion CT or perfusion MRI had not been demonstrated, and a positive phase three clinical trial that would warrant incorporation of the *tissue clock* approach into clinical guidelines did not exist (Etherton et al., 2018; Powers et al., 2018). Chronological time remained a barrier to treatment with rtPA (Biggs et al., 2019), and was, therefore, the main motivation for the studies in this thesis. However, as will be discussed in the General Discussion (Chapter 9), since this thesis was written, the field has moved on, with more clinical evidence supporting the adoption of the *tissue clock* approach to treatment decisions of acute ischaemic stroke patients.

The other imaging-based approach to overcoming the problem of unknown onset time in the treatment of acute ischaemic stroke is to use imaging as a *chronological clock* and estimate how long ago the stroke started (Biggs et al., 2019; Etherton et al., 2018). According to this time-based approach, if the estimated time from onset is less than 4.5 hours, the patient with unknown onset could be considered for IV

thrombolysis as per clinical routine (Thomalla et al., 2011). The appeal of this time-based approach is that it is in accordance with current treatment guidelines and compliments the *tissue clock* approach because time is a proxy for tissue viability (Hacke et al., 2008). Patients presenting after 4.5 hours from symptom onset are unlikely to have enough salvageable tissue to benefit from rtPA safely and the risk for iatrogenic haemorrhage increases (Hacke et al., 2008). Unlike the *tissue clock* approach outlined above, the size of the ischaemic region is not considered in the decision to consider a patient for thrombolysis, as the time from symptom onset is considered to be the most important factor. As will be expanded upon in Chapter 4 (Section 4.4) according to this time-based approach, unknown onset can be treated as a binary classification problem, where imaging is used to classify a patient as within or beyond 4.5 hours of symptom onset. For example, the visual MRI based method, *the DWI/FLAIR mismatch*, classifies a patient as within the treatment window if ischaemic tissue is identifiable on DWI but not FLAIR scans, and beyond the treatment window if ischaemic tissue is identifiable on both (Thomalla et al., 2011). Alternatively, the amount of time passed since the first ischaemic event could be estimated by quantifying the difference in image intensities of ischaemic and non-ischaemic regions on NCCT (e.g., Mair et al. 2017) or MRI scans (e.g., Siemonsen et al., 2009; Song et al., 2012).

## 1.2 Aims of this thesis

At the start of this PhD (September 2015), the WAKE-UP trial, which aimed to investigate the safety and efficacy of treating patients with unknown onset time according to the visual-based DWI/FLAIR mismatch criteria was underway (Thomalla et al., 2014). Other studies had investigated various quantitative MRI (qMRI) based approaches, some just in preclinical animal models of ischaemia (e.g., Jokivarsi et al., 2010; Rogers et al., 2014) and some in both preclinical (e.g., Rogers et al., 2014; Xu et al., 2014) and clinical patient studies (e.g., Madai et al., 2016; Siemonsen et al., 2009; Song et al., 2012). Reported accuracies of these approaches were variable across studies, and imaging approaches had not been compared

directly. It was therefore unclear which, if any, imaging methods would serve as the most reliable chronological clock for stroke onset time estimation.

This thesis, therefore, explores the ability of potential MRI based methods at estimating stroke onset time, with the overall goal of identifying which parameter(/s) should be studied further in larger-scale clinical studies. MRI was chosen as the imaging method to study because of its multiparametric abilities (Kauppinen, 2014) and its availability in most clinical settings worldwide (OECD, 2018). It is recognised that a variety of other MRI based techniques have been recommended for onset time estimation, such as magnetic resonance spectroscopy (e.g., Wang et al., 2000), perfusion-weighted imaging (PWI) (e.g., Roldan-Valadez et al., 2012) and diffusion tensor imaging (DTI) (e.g., Puig et al., 2013). However, the MRI parameters researched in this thesis were chosen because they are already part of recommended stroke protocols (e.g., Mair & Wardlaw, 2014) and are easy to acquire and analyse quantitatively in clinical settings. This is important because radiographers and clinicians involved in scanning stroke patients would be familiar with the pulse sequences used, and there would be no extra effort involved in setting up the MRI scanner. Additionally whilst the focus was on onset time estimation, to fit in with the clinical guidelines at the time, as will become evident throughout the course of the thesis and discussed in Chapter 9, the results of the research studies are also relevant to the patient-specific *tissue clock* approach, which throughout the course of 2015 to early 2020, gained more attention in clinical stroke literature.

The purpose of Chapters 2, 3 and 4 is to provide the reader with a background understanding of acute ischaemic stroke and MRI. Chapter 2 provides an essential overview of the pathophysiological changes that occur in the hyperacute ischaemic brain in order to contextualise the changes seen in the MRI parameters studied in this thesis.

Chapter 3 introduces the reader to MRI as a medical imaging technique, including the setup of the MR equipment, how MRI works, how images are acquired, and the different types of contrast MR images can have. The Chapter ends with an introduction to the main quantitative approaches to MR image analysis (qMRI), which differs from the standard qualitative approach used in hospitals and are the main methods of analysis used in the studies of this thesis.

Chapter 4 draws Chapters 2 and 3 together by providing an overview of what the different MRI contrasts studied in this thesis reveal about ischaemia and why they are potentially informative of stroke onset time. This is followed by a description of time-based MRI approaches that have been proposed for overcoming the problem of unknown onset time. Results from previous studies that have adopted these methods are described and explained in this Section as well as the introductions and discussions of the relevant research Chapters in this thesis.

Chapters 5, 7 and 8 are the main research studies. These Chapters were written for publication and so are structured as they would appear in a journal with separate abstracts, introductions, methods, results and discussions.

Chapter 5 is a preclinical study involving rat models of ischaemia that compared the accuracy, sensitivity and specificity of qMRI parameters for stroke timing. Using rats enabled qMRI parameters to be studied under controlled conditions that would not be possible to emulate in patient studies. The purpose of the study was to inform which qMRI parameters should be studied in hyperacute stroke patients.

Chapter 6 introduces the reader to some of the advantages and limitations of preclinical research to study cerebral ischaemia and outlines how the results from

the preclinical study in Chapter 5 and previous clinical studies informed the design of the studies of hyperacute ischaemic stroke patients in Chapters 7 and 8.

Chapters 7 and 8 are pilot studies that explored the potential ability of qMRI parameters to estimate stroke onset time in a cohort of hyperacute ischaemic stroke patients. The overall purpose of these studies was to identify MRI based parameters that would be suited to more rigorous investigation in more extensive clinical studies. The aim of Chapter 7 was specifically to compare the ability of visual and quantitative MRI based methods for stroke timing. The aim of Chapter 8 was to study the potential heterogeneity of the ischaemic lesion by means of $T_2$ relaxation time histograms and the ability of $T_2$ distribution characteristics to time from ischaemia onset.

The final Chapter summarises the results and conclusions of the three research Chapters and the questions that emerged from them. The conclusions are drawn together to form the main conclusion, followed by discussions outlining the original contributions of this thesis and how the conclusions fit in with up-to-date stroke timing literature (up to February 2020). Limitations of the research studies are also addressed, and the Chapter ends with recommendations for further work.

# Chapter 2
# Acute Ischaemic Stroke

## 2.1 Introduction

An ischaemic stroke is defined as an episode of neurological dysfunction caused by focal cerebral infarction (Sacco et al., 2013). The occlusion of a cerebral artery with thrombotic or embolic material results in the abrupt cessation of focal blood supply, and severe reduction in blood flow to surrounding brain parenchyma (Toole, 1999). The narrowing of an artery due to atherosclerosis can also result in severely reduced blood flow, but disruption is not abrupt. In the hypoxic state, the brain can initially engage in compensatory mechanisms, by increasing cerebral blood volume (CBV) to increase oxygen extraction (Muir et al., 2006) and converting to anaerobic glycolysis if glucose is available (Hossmann, 1989). However, once cerebral blood flow (CBF) below the critical threshold for energy metabolism (from the normal average of ~ 50 mL/100g/min to ~ 20 mL/100g/min) oxygen supply is hindered, causing normal physiological processes to cease, which prompts a cascade of pathophysiological events that ultimately contribute to cell death and irreversible brain damage (Heiss & Rossner, 1983; Huang et al., 2019).

The pathophysiological changes that take place in the ischaemic brain and the mechanisms for which they contribute to cell death are highly complex, and it is beyond the scope of this thesis to provide a detailed account of all potential events.

Therefore, the purpose of this Chapter is to provide an essential overview of the ischaemic changes that are directly relevant to the MRI studies in this thesis. As MRI probes changes in tissue water, the focus of this Chapter is mainly on components of the ischaemic cascade related to hydrodynamic changes in the acute ischaemic brain. For more detailed accounts of the pathobiology of ischaemic stroke, the reader is referred to excellent reviews by Dirnagl et al. (1999) and Simard et al. (2007). This Chapter and many previous reviews on the pathophysiology of ischaemia are mainly informed by preclinical animal studies (Muir et al., 2006), which contributes to the theme throughout this thesis of the importance of animal studies in informing clinical research of disease states such as ischaemic stroke.

## 2.2 The three-zone core-penumbra-oligaemia model

The ischaemic brain parenchyma can be broadly summarised into three main zones that reflect the spatial gradient of hypoxia, including the *ischaemic core*, *the penumbra*, and *the oligaemia* (Hossmann, 1994; Simard et al., 2007). The ischaemic core corresponds to the tissue within the immediate vicinity of the occluded artery, where CBF has already dropped below the critical threshold for energy metabolism, and brain tissue is irreversibly damaged (Hossman, 1994). Surrounding the core is the ischaemic penumbra, which is the hypoperfused, potentially viable tissue (Hossmasn, 1994). Outside of the penumbra is the oligaemia which is characterised by small reductions in CBF but in principle, should survive (Muir et al., 2006). These zones and their development over time after ischaemia onset are schematically illustrated in Figure 2.1, and the relevant pathophysiological mechanisms that take place within them are summarised in the Sections that follow.

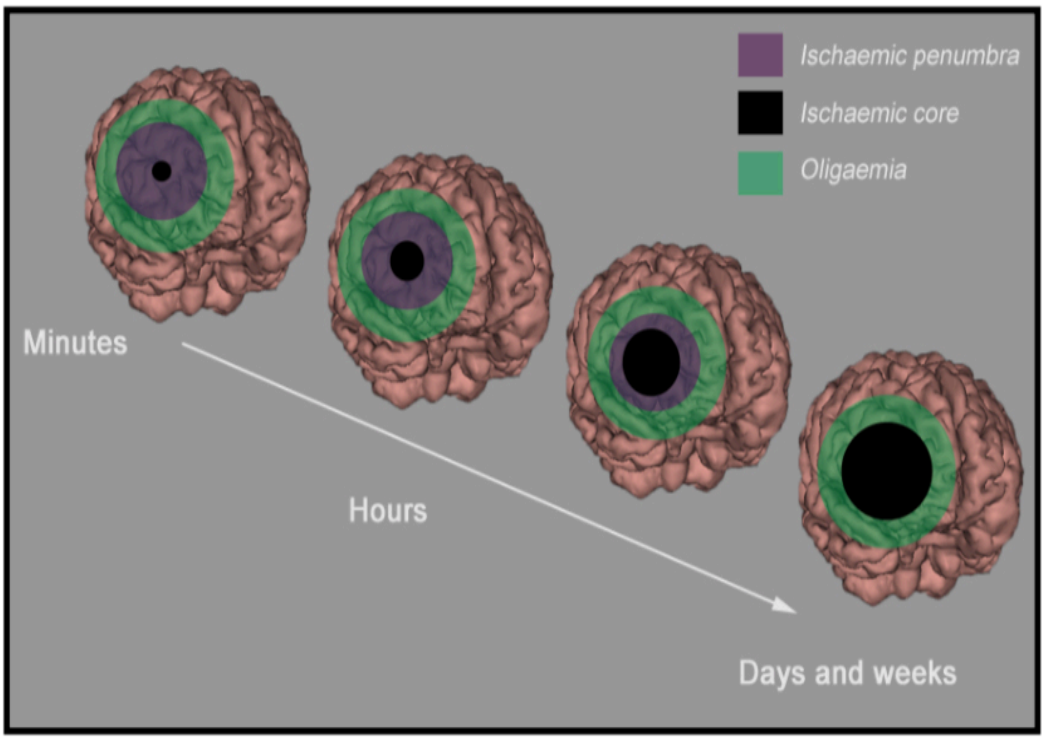


Figure 2.1 Schematic illustration of the three-zone core-penumbra-oligaemia model representing the progression of tissue damage due to ischaemia. Unless reperfusion takes place, the ischaemic penumbra becomes incorporated into the irreversibly damaged ischaemic core. The figure is a recreation of a figure by Dirnagl et al. (1999) which is reproduced from McGarry (2015).

### 2.2.1 The ischaemic core

In the ischaemic core, CBF is below 6 mL/100 g/ min, which results in functional and structural impairment within minutes of onset, due to a number of pathophysiological mechanisms that result from membrane pump failure (Astrup, 1977; Heiss & Rosner, 1983; Jones et al., 1981). The severe energy deprivation that results from lack of oxygen causes a failure of the energy dependent sodium/potassium pumps ($Na^+/K^+$ ATPase pump, ATP: adenosine triphosphate) and thus collapse in membrane function. This anoxic depolarisation causes the death of neural cells as the oxygen and glucose deprivation means they cannot survive the energy demands of repolarisation and has been described as a "wave of

electrical silence propagating across the neocortex" (Anderson et al. 2005, p. 963). Cerebral oedema is one of the main consequences of membrane pump failure, for which there are three main types, *cytotoxic*, *ionic* and *vasogenic*, which are schematically illustrated in Figure 2.2 and described in further detail in this Section.

### Cytotoxic oedema

Normally, $Na^+$ concentrations within serum and extracellular space are the same and higher than in the neural cells (Figure 2.2-part A) (Simard, 2007). However, failure of membrane function causes opening of the non-selective cation channel (NCCA-ATP channel), which results in the efflux of potassium ($K^+$) from the cell into extracellular space and an influx of sodium ($Na^+$), chloride ($Cl^-$) and calcium ($Ca^{2+}$) from extracellular space, into the cell (Figure 2.2-part B) (Astrup et al. 1977; Hansen & Zeuthen, 1981; Simard 2007). This change in intra and extracellular concentrations results in cytotoxic oedema, where osmotically obliged water from extracellular space, follows $Na^+$ into ischaemic neural cells (Astrup et al., 1981; Klatzo, 1967; Simard et al., 2007). This redistribution of water causes the cells to swell and lose structure (Astrup et al., 1981; Klatzo, 1967; Simard et al., 2007). At this stage, the total tissue water content does not change; only the distribution of water. The ischaemic tissue is therefore still potentially salvageable as the blood-brain barrier remains intact. However, the swollen cells eventually lose structure, resulting in oncotic death of the neuronal cells (Figure 2.2-part C) (Astrup et al., 1981; Klatzo, 1967; Simard et al., 2007).

### Ionic oedema

Ionic oedema results from the cytotoxic oedema of endothelial cells (Simard, 2007). The influx of $Na^+$ and water into cells results in less $Na^+$ and water in extracellular space, which in turn causes a $Na^+$ gradient that draws the fluid from capillaries into extracellular space (Figure 2.2-part D) (Simard et al., 2007). This fluid shift is

the first time in the ischaemic process which leads to a net increase in water and transition to irreversible tissue damage (Simard et al., 2007).

### Vasogenic oedema

Over subsequent hours, the endothelial junctions of the blood-brain barrier start to break down marking the start of vasogenic oedema where water and macromolecules such as albumin and plasma proteins leak into extracellular space followed by even more water uptake, causing further cell damage (Figure 2.2-part E) (Huang et al., 2019; Klatzo, 1967; Simard et al., 2007). As a result of the blood-brain barrier break down, inflammatory leukocytes in the blood transfer to brain tissue which also contributes to cell death as they can block microvasculature, causing further reduction in CBF, and production of toxic mediators (Durukan & Tatlisumak, 2007). The increase in extracellular water can also cause an increase in brain volume, which increases intracranial pressure and can result in further ischaemia due to compression of other cerebral arteries (Rosenberg, 1999).

### Further causes of cell death in the core

The $Na^+/K^+$ ATPase pump failure results in other pathophysiological events that contribute to cell death in addition to the progression of oedema. For example, the increase in intracellular $Ca^{2+}$ facilitates the production of free radicals that damage membrane, mitochondria and DNA (Dirnagl et al. 1999). Additionally, excitotoxicity, which is the action by excitatory neurotransmitters (i.e., glutamate on N-methyl-D-aspartate (NMDA) receptors) followed by a cascade of destructive ionic and enzymatic events, is an additional contributor to cell death (Dirnagl et al., 1999). The depolarisation of neurons and glia causes an extracellular accumulation of excitatory amino acids such as glutamate and aspartate, resulting in prolonged stimulation of NMDA and AMPA (α-amino-3-hydroxy-5-methyl-4-isoxazole propionic acid) receptors (Dirnagl et al., 1999). The over prolonged stimulation of AMPA receptors promotes further depolarisation and release of the

NMDA magnesium block ($Mg^{2+}$) causing a further influx of $Ca^{2+}$ (Dirnagl et al., 1999; Doyle et al., 2008). The prolonged stimulation of NMDA receptors exacerbates cytotoxic oedema as it causes a further influx of $Na^{+}$, $Ca^{2+}$ and water into the cells (Dirnagl et al., 1999).

Figure 2.2 Displayed on the right-hand side. Schematic diagram illustrating the types of oedema during ischaemia.

**A. Normal capillary and neuron:** $Na^{+}$ concentrations are higher in extracellular space and $K^{+}$ is higher intracellularly.

**B. Cytotoxic oedema:** when the $Na^{+}$/ $K^{+}$ pumps fail due to severe energy deprivation, $Na^{+}$ enters into the ischaemic neuron / neural cell, which depletes extracellular $Na^{+}$, which sets up an ionic gradient between intravascular and extracellular compartments, causing osmotically obliged water from extracellular space to follow $Na^{+}$ into cells causing them to swell**.**

**C. Oncotic death:** eventually the swollen cells lose structure, resulting in oncotic death of the neural cell.

**D. Ionic oedema:** the cytotoxic oedema of endothelial cells and $Na^{+}$ gradient that draws the fluid from capillaries into extracellular space.

**E. Vasogenic oedema:** the blood brain barrier breaks down and water and macromolecules leak into extracellular space.

Reproduced from The Lancet Neurology, Vol 6, Simard et al., Brain oedema in focal ischaemia: molecular pathophysiology and theoretical implications. P 258-68., Copyright (2007), with permission from Elsevier (Appendix D).

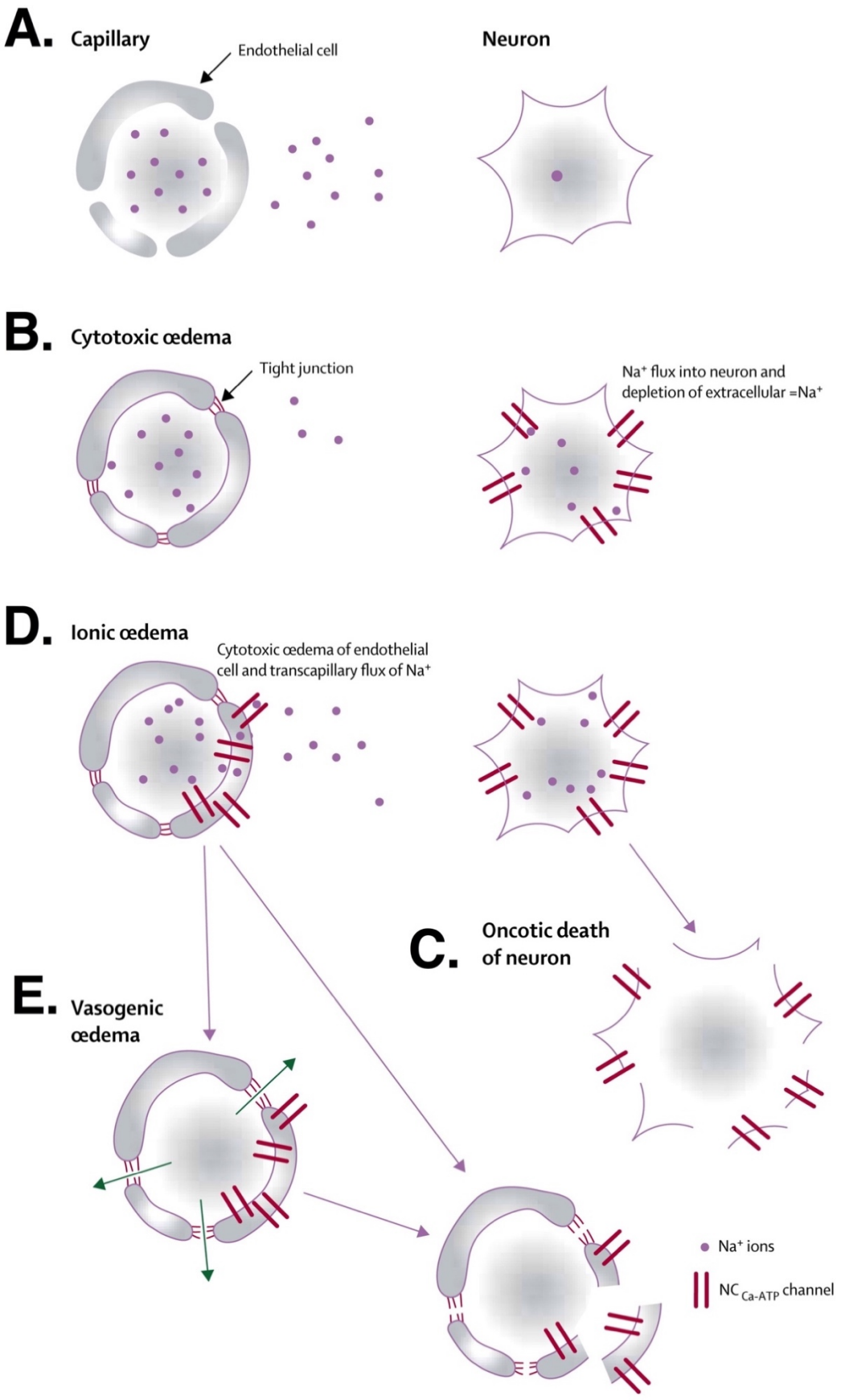
A.
Capillary
Endothelial cell
Neuron
B.
Cytotoxic œdema
Tight junction
Na+ flux into neuron and
depletion of extracellular =Na+
D.
Ionic œdema
Cytotoxic œdema of endothelial
cell and transcapillary flux of Na+
C.
Oncotic death
of neuron
E.
Vasogenic
œdema
Na+ ions
NC Ca-ATP channel

### 2.2.2 The ischaemic penumbra

The ischaemic penumbra is the hypoperfused tissue immediately surrounding the ischaemic core. In this region, CBF is between an upper threshold of 15 mL /100 g/ min between and the critical threshold for energy metabolism of 6 mL/100 g / min (Astrup, 1977; Heiss & Rosner, 1983; Jones et al., 1981). The CBF is less reduced than in the core because other surrounding arterial channels supply the affected region with blood (Hossmann, 1994; Huang et al., 2019). Due to the reduction in blood supply, neural cells in the penumbra are functionally impaired, which contributes to neurological symptoms, but their structural integrity is maintained (Hossmann, 1989). The penumbra is electrically silent, but unlike the core, the cells are still polarised, so there is no anoxic depolarisation (Hossmann, 1989). Thus, in the first minutes and hours of ischaemia, the penumbral tissue is potentially salvageable and thus is the target in treating ischaemic stroke (Muir et al., 2006). If reperfusion happens quickly enough, either spontaneously (i.e., a transient ischaemic attack) or therapeutically (e.g., IV or IA thrombolysis, mechanical thrombectomy) there is potential for penumbral tissue to recover (Huang et al., 2019).

If CBF is not restored, over subsequent hours of ischaemia, the ischaemic core expands into penumbral tissue (Hossman, 1994). This expansion is thought to be partly due to repetitive peri-infarct depolarisations, referred to as, *spreading depression*, where cells are in a constant state of depolarisation and repolarisation, as the elevated $K^+$ concentrations and glutamate release causes cells to depolarise, but the remaining energy supplies enable repolarisation (Hossmann, 1996). The constant depolarisations and repolarisations completely deplete energy supplies over time, and so the cell death that happens in the core also happens in penumbral tissue (Hossmann, 1996). Additional factors that are responsible for the growth of the ischaemic core into penumbral regions include ongoing excitotoxicity, free radical formation and tissue acidosis caused by anaerobic glycolysis (Dirnagl et al., 1999; Rehncrona et al., 1985). Within days and weeks of the first ischaemic event,

cells eventually break down, and all that is left is a fluid-filled cavity (Hossmann, 1989).

### 2.2.3 The oligaemia

The oligaemia represents tissue with very small reductions in CBF, between the normal average of 50 mL/100 g/min and the critical threshold for energy metabolism of 20 mL/100g/min (Muir, 2006). In this region, functional integrity is maintained for a long time, and tissue is unlikely to proceed to infarction. However, secondary events that reduce cerebral perfusion pressure may push the oligaemia into a penumbral state, and therefore, potentially the core (Muir, 2006). Examples of such secondary events include vasogenic oedema, systemic hypotension, hypoglycaemia and pyrexia (Baron, 2001; Muir, 2006).

## 2.3 Concluding comment

It is important to note, that although the progression of ischaemia can be simplified into this three-zone, *core-perfusion-oligaemia model*, the pathogenesis of ischaemia is a highly dynamic and heterogeneous process (Meschia & Brott, 2018). Compensatory and pathophysiological mechanisms described in this Chapter occur in both the core and the penumbra but at different rates, due to differences in collateral blood supply (Muir et al., 2006). Ultimately, the survival of the penumbral tissue overall depends on the collateral circulation. For example, patients with better collaterals have been shown to have better outcomes (Maas et al., 2009) and smaller infarcts (Iwasawa et al., 2016). Other patient-specific factors such as the location of the infarct, age and pre-existing disease states (e.g., diabetes, hypertension) will also contribute to how well ischaemia is tolerated and how fast it progresses (Macrae, 1992; Wang & Wang, 2019).

# Chapter 3
# Magnetic Resonance Imaging

## 3.1 Introduction

Magnetic resonance imaging (MRI) is a non-invasive medical imaging technique that uses strong magnetic fields and radio waves to generate signals that are transformed into detailed images of the body's physiology and anatomy. $^{1}$H Magnetic Resonance (MR) was the chosen imaging modality for studies in this thesis, because compared to non-contrast CT (NCCT), its multiparametric capabilities and sensitivity to different pathophysiological changes in the brain, means it has the potential to provide more information about ischaemic tissue, without exposing the patient to ionising radiation, or injecting a contrast agent (as with perfusion CT). The purpose of this Chapter is to contextualise the MRI signals studied in this thesis for stroke onset time estimation. To this end, the MR equipment and nuclear magnetic resonance (NMR) phenomenon are described, followed by an outline of how the NMR signals are acquired and the different types of image contrasts that can be generated. The Chapter ends with an introduction to the main method of analysis used in this thesis, quantitative MRI (qMRI), and an explanation of how it differs from the conventional qualitative approach traditionally used in hospitals.

## 3.2 The MR equipment

An example of a typical clinical MR system and patient set up is shown in Figure 3.1 and further described in the caption. The MR scanner (without the console) is situated in an isolated room protected by a Faraday cage, which is a copper-lined barrier that ensures potential sources of electromagnetic noise are kept out, and its own electromagnetic fields are kept in (Currie et al., 2013). After correctly positioning the patient within the scanner, the radiographer (Figure 3.1-part A) operates the MR scanner from a separate control room via a computer interface. In the control room the radiographer can select an appropriate MR protocol (pre-set or user-determined) and view the images which are reconstructed by the computer from the signals produced by the MR system.

The MR system contains 360° concentrically arranged coils around the magnet bore (Figure 3.1-part C), including the main superconducting energised coils (Figure 3.1-part B), three gradient coils (Figure 3.1-part D), radiofrequency (RF) coils (Figure 3.1-part E) and shim coils (Figure 3.1-part G) (Currie et al., 2013). The arrangement of these coils is schematically illustrated over a picture of a clinical MRI scanner in Figure 3.1. Chapter 5 of this thesis is a preclinical MRI study. MRI scanners for preclinical animal research have similar hardware arrangement to that of a clinical scanner; however, the magnet bore is much smaller. A photograph of one of the preclinical MRI systems used in Chapter 5 is shown in Figure 3.2.

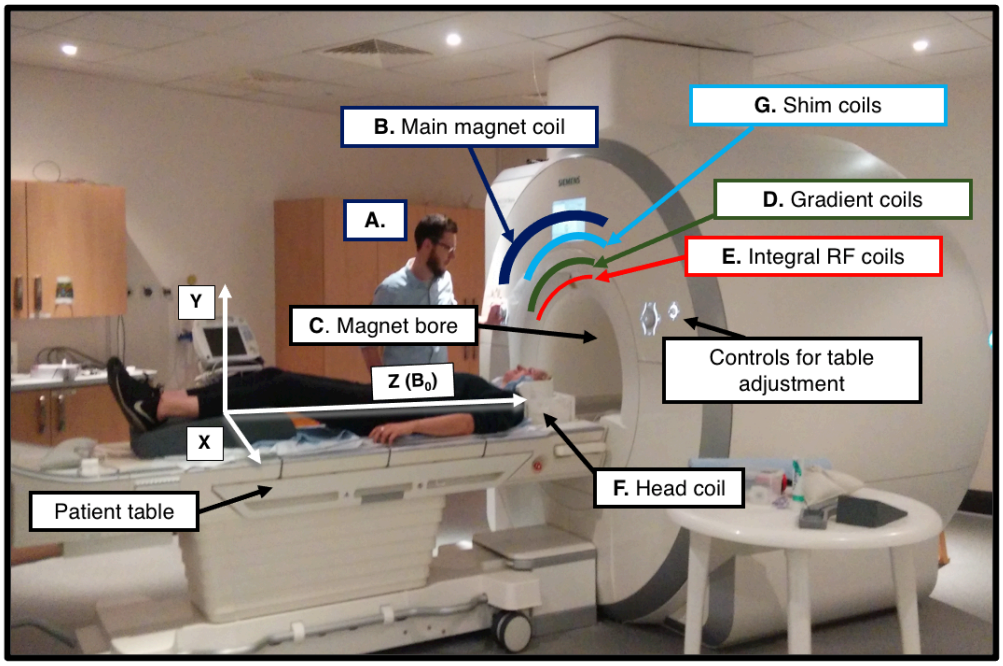


Figure 3.1 An example of a clinical 3T Siemens Magnetom Skyra MRI scanner. The radiographer (**A.**) ensures the subject is comfortable on the patient table with elevated legs and a blanket if needed. The subject is given earplugs to protect hearing. The patient's head is positioned comfortably within the head coil (**F.**) with foam padding. For brain imaging, a separate radio frequency receiver coil (not shown) is placed in front of the subject's face to improve the signal to noise ratio. The subject is asked to lie as still as possible during the scan to reduce movement artefacts. The subject is also given an alarm button (not shown) to hold during the scan to alert the radiographer if needed. Once in place, the radiographer slides the patient table into the magnet bore (**C.**) using control buttons on the side of the scanner and will return to the separate operating room to set up the MR experiment. The concentric arrangement of the 360° degree RF (**E.**), gradient (**D.**) and shim (**G.**) coils are schematically illustrated by the blue, green and red arcs. The X, Y and Z axis is also shown to illustrate the direction of the main magnetic field ($B_0$) and the X, Y planes.

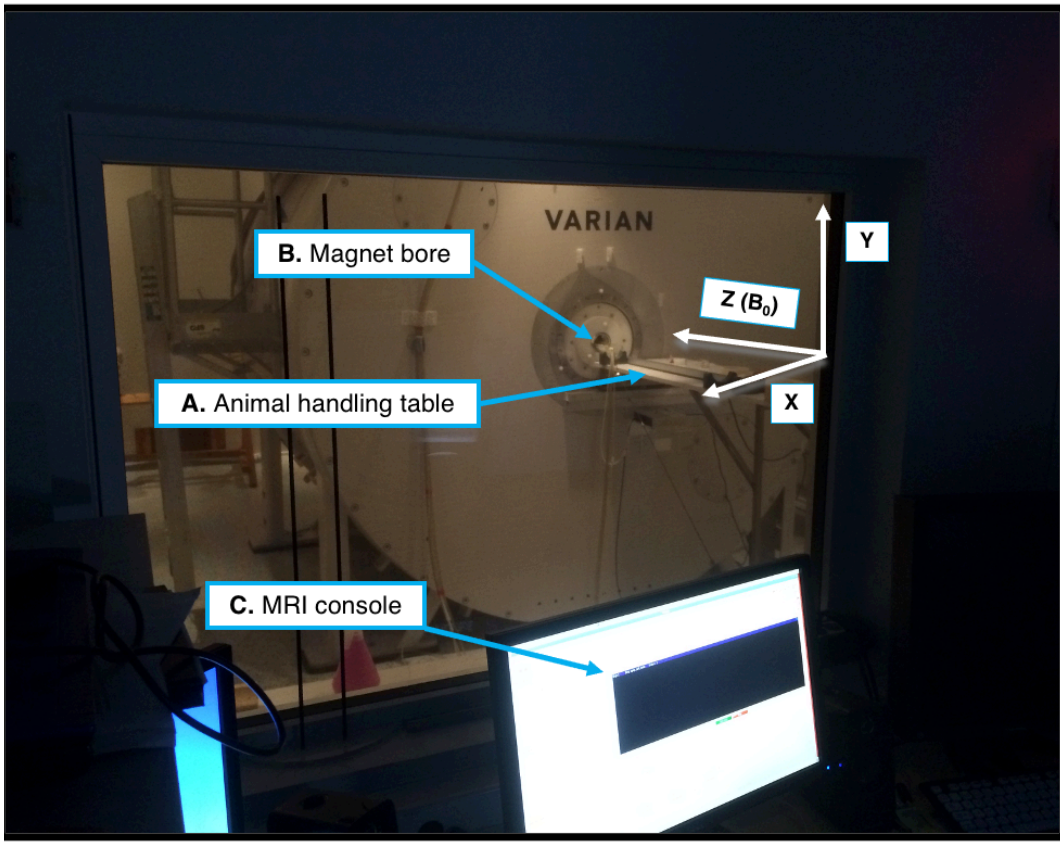


Figure 3.2 The 9.4T animal MRI scanner used in the preclinical study in Chapter 5. The animal is positioned securely on the animal handling table (**A.**) before being slid into the magnet bore (**B.**). As with the clinical setting, the MR equipment is operated in a separate control room using the MRI console (**C.**). The magnetic coils are organised around the bore in the same way as the clinical MRI scanner in Figure 3.1. X, Y and Z axis are also shown to illustrate the direction of the main magnetic field ($B_0$) and the X, Y planes.

## 3.3 Main magnetic coils

The main magnetic coils (Figure 3.1-part B) are superconducting energised coils which are hyper-cooled close to absolute zero (~ 4 K / ~ -269 °C) using cryogenic liquid helium. A strong electric current in these coils generates a strong homogenous external magnetic field ($B_0$) in the bore of the machine (Figure 3.1-part C) along the Z-axis, which is in the head-foot direction (Currie et al., 2013). The strength of the external magnetic field is measured in units of Tesla (T), which is approximately 20,000 times larger than the earth's magnetic field (Currie et al., 2013; Plewes & Kucharczyk, 2012). Most MRI scanners in a hospital setting are 1.5T or 3T (used in Chapter 7 and Chapter 8). MR systems with higher field strengths (e.g., 4.7T, 7T, and 9.4T) offer higher signal to noise ratio (SNR) but are mainly used in preclinical (e.g., Chapter 5) and human imaging research (mainly 7T).

### 3.3.1 Shim coils

In order to correctly localise the MR signal, the main $B_0$ field needs to be as uniform as possible (Currie et al., 2013). However, simply placing an object within the main magnetic field will reduce the homogeneity of $B_0$ due to magnetic susceptibility effects (Currie et al., 2013). Magnetic susceptibility is the extent a substance is magnetised in the presence of an external magnetic field (Currie et al., 2013). Some substances will increase the local external magnetic field by a few parts per million (ppm), and others will decrease it (Plewes & Kucharczyk, 2012; Schneck, 1996). For example, human tissue and bone are diamagnetic, so will reduce the $B_0$ field, whereas iron is paramagnetic and will increase the $B_0$ field (Juchem & de Graaf, 2017). Therefore, when a patient is positioned in the scanner, they will generate small field variations in $B_0$. Shim coils situated close to the magnet bore (Figure 3.1-part G) are necessary to optimise $B_0$ homogeneity (Sprawls, 2000). This can be achieved by adjusting the electrical currents induced by the shim coils on a patient-specific basis via the computer, or when the magnet is serviced (Sprawls, 2000). It

is important to note here, that despite shimming, $B_0$ will never be perfectly homogenous, and so will always influence the MR signal to some extent. This $B_0$ inhomogeneity is an important factor to remember when reading this thesis, as the main quantitative MR imaging parameter ($T_2$ relaxation time introduced in Section 3.4.3 of this Chapter) and proposed for the study of stroke pathophysiology and stroke timing (Chapter 4) is not impacted by $B_0$ inhomogeneities.

### 3.3.2 Gradient coils

During the imaging process, the external magnetic field is distorted with gradients, which is achieved with gradient coils (Figure 3.1-part D) (Sprawls, 2000). Gradients are magnetic fields where the strength of the magnetic field varies depending on the spatial position (Currie et al., 2013). In the MR system, an X-Y-Z coordinate system is used to define the direction of the main magnetic field (as shown in Figures 3.1, 3.2 and 3.3.). A gradient applied in the X direction, for example, will modify the magnetic field strength in that direction. Gradients are important for producing an echo event and signal (introduced later in this Chapter, Section 3.4) and are necessary for localising the MR signal (Plewes & Kucharczyk, 2012; Sprawls, 2000). In the MR system, there are three gradient coils (position shown in Figure 3.1-part D), which represent the three orthogonal directions (X, Y and Z) and lie concentric to each other within the main magnet (Currie et al., 2013). These coils alter the strength of $B_0$ along the direction of the applied gradient field (X, Y or Z direction) (Currie et al., 2013). In addition to the X, Y and Z directions, gradients can be produced in any desired direction by using two or more of the gradient coils together (Sprawls, 2000).

### 3.3.3 Radiofrequency coils

The RF coils are positioned within the gradient coils (Figure 3.1-part D) and generate electromagnetic fields (known as the RF field, RF pulse or $B_1$ field), but

at much lower power (in the MHz range) than the main magnetic field (Tesla). RF coils are similar to an antenna, whereby they transmit RF energy to the tissue of interest, as well as receive the induced RF signal from that same tissue (Currie et al., 2013). Some MR scanners are fitted with RF coils that perform both transmit and receive functions, whereas others have separate coils for transmitting and receiving (Currie et al., 2013). In neuroimaging, a separate receive coil is commonly used, which is positioned around the patient's head (Figure 3.1-part F) to maximise the signal to noise ratio (Currie et al., 2013). When switched on, the RF pulse combines with the main external magnetic field to produce the MR signals that are spatially localised and encoded by the gradient magnetic fields (Currie et al., 2013).

## 3.4 Nuclear magnetic resonance phenomenon

The vast majority of MRI used in clinics today is based on imaging the hydrogen ($^1$H) nucleus because of the high abundance of water in the body. $^1$H nuclei, hence, Nuclear Magnetic Resonance (NMR), behave like tiny bar magnets with a north and a south pole (Plewes & Kucharczyk, 2012). $^1$H nuclei have a single, positively charged proton and possess the quantum property, *angular momentum*, or *spin,* and are referred to as *spin*s (Plewes & Kucharczyk, 2012). The interactions between applied magnetic fields and spins enable spatial encoding of hydrogen atoms within different water-based tissues, to produce the images that are used in the clinic (Brown & Semelka, 2011).

### 3.4.1 Net magnetisation

In MRI, the magnetic field that is generated by the main magnet coils gives rise to *net magnetisation* along the longitudinal axis ($M_Z$) which in the direction of $B_0$ (Z direction, shown in Figure 3.1, Figure 3.2 and Figure 3.3). As there are billions of $^1$H spins in a typical voxel, *net magnetisation,* refers to the sum of magnetisation of these spins (Wolbarst et al., 2013) and is illustrated by the large red arrow in

part A of Figure 3.3 (Brown & Semelka, 2011). $M_{Z\,is}$ also referred to as *longitudinal magnetisation* (Brown & Semelka, 2011). In the presence of the magnetic field, the spins precess around their axes at a constant frequency known as the *Larmor* or *resonant* frequency, which is linearly proportional to the gyromagnetic ratio of the nuclei being observed (42.58 MHz/ T) for hydrogen) and the strength of $B_0$ (e.g., 3T) (Currie et al., 2013). At this stage, the NMR signal is not detected simply by placing the object into the magnet bore. Instead, more elaborate hardware and software are required (Plewes & Kucharczyk, 2012).

In the absence of a magnetic field, spins are aligned nearly randomly with respect to each other (Brown & Semelka, 2011). As illustrated in Figure 3.3 (part A), where black arrows represent individual spins, in the presence of an external magnetic field, the majority of spins align parallel to the direction of the magnetic field (low energy state) and slightly less align anti-parallel to the external magnetic field (high energy state) (Brown & Semelka, 2011). This population difference in the energy state of spins is predicted by the Boltzmann distribution function (Brown & Semelka, 2011).

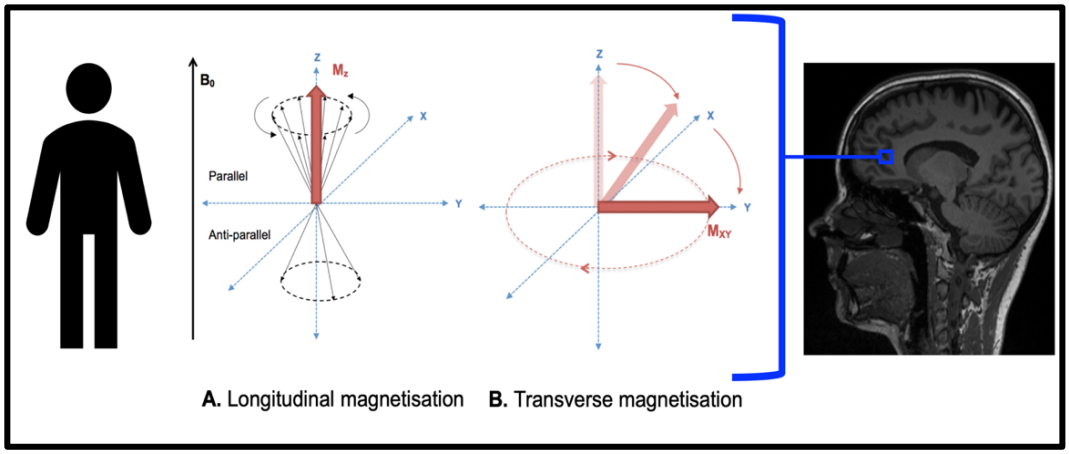


Figure 3.3 Longitudinal and transverse magnetisation. **A.** When the subject is placed in the magnet bore the majority of spins align parallel to the magnetic field, in the Z / head-foot direction, termed longitudinal magnetisation (Mz). **B.** The signal is produced by tipping net magnetisation into the transverse plane (X-Y axis), termed transverse magnetisation (MXY). There are billions of spins within each voxel, and so net magnetisation is the sum of the magnetisation of these spins.

### 3.4.2 Disturbance of net magnetisation

In order to produce the signal that is used to form an image, net magnetisation must be tipped from the longitudinal axis into the transverse plane, which is orthogonal to the direction of the $B_0$ field (Figure 3.3-part B.) (Plewes & Kucharczyk, 2012). Therefore, a second magnetic field, at the Larmor frequency referred to as the radio frequency pulse (RF pulse) and $B_1$ field, is introduced by the transmit RF coils (Plewes & Kucharczyk, 2012). The spins that were aligned parallel to $B_0$ absorb energy from the RF pulse and tilt away from the Z-axis, into the transverse plane (Plewes & Kucharczyk, 2012). The spins that were aligned anti-parallel to $B_0$ release energy and start to align parallel to $B_0$ (Plewes & Kucharczyk, 2012). As a result, the spins precess in synchrony, or *in-phase* with each other, causing the net magnetisation to rotate 90° away from the longitudinal Z-axis, into the transverse X-Y plane (Figure 3.3-part B). The net magnetisation in this plane is referred to as *transverse magnetisation* and $M_{XY}$ (Plewes & Kucharczyk, 2012). In accordance with Faraday's law of induction, where a changing magnetic field induces a voltage in a nearby conductor, it is the precession of net magnetisation during resonance that induces a small electrical current in the receiver coil, which forms the MR signal that is collected and reconstructed by the MR system's computer to form the MR image (Hahn 1953; Sprawls, 2000).

### 3.4.3 Relaxation processes

The NMR signal resulting from the application of the RF pulse decays due to two simultaneously occurring, but independent relaxation processes, *transverse relaxation* ($T_2$) and *longitudinal relaxation* ($T_1$) (Currie et al., 2013). These processes are caused both by dipolar and non-dipolar effects by fluctuating magnetic fields, spin-spin interaction, and energy exchange between the spin and the molecular lattice (Bloembergen et al., 1948). Both $T_1$ and $T_2$ relaxations are central to forming contrast in images and are the key MR parameters studied for stroke timing in this thesis.

### $T_1$ relaxation

*Longitudinal relaxation* or *$T_1$ relaxation* is how rapidly the net magnetisation regrows along the longitudinal axis in the direction of $B_0$ and is described by the time constant $T_1$, which is the time (in milliseconds) for the net magnetisation to return to 63% of its original magnitude in a single exponential system (Plewes & Kucharczyk, 2012). Longitudinal relaxation occurs due to spins emitting the energy that was absorbed by the RF pulse to the surrounding molecular lattice (spin-lattice interaction) (Deoni, 2010). Longitudinal relaxation is modelled as an exponential growth curve with the time constant $T_1$, shown in Figure 3.4 and given by:

$$M = M_0\,(1 - e^{-t/T_1})$$

Where M = magnetisation, $M_0$ = longitudinal magnetisation, t = time and $T_1$ is $T_1$ relaxation time (ms).

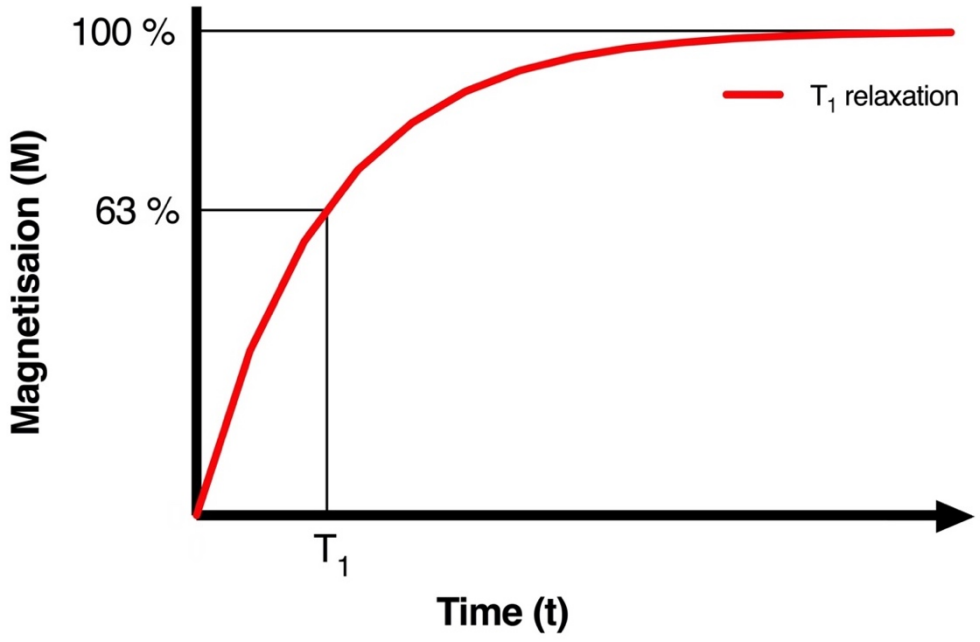


Figure 3.4 $T_1$ recovery curve.

### $T_2$ relaxation

*Transverse relaxation* or *$T_2$ relaxation* is the loss of net magnetisation in the transverse plane due to dephasing of spins and is described by the time constant, $T_2$, which is in milliseconds, the time in which transverse magnetisation drops to 37% of its original size in a single exponential system (Plewes & Kucharczyk, 2012). Transverse relaxation is a random process and occurs due to the exchange of energy between neighbouring spins (spin-spin interaction, a dipolar effect) as well as non-dipolar effects, such as exchange and diffusion. Individual spins move about and so experience small variations in their magnetic fields due to the presence of other spins, which causes slight differences in precessional frequencies, causing spins to fall out of phase (Deoni, 2010). Transverse relaxation is modelled by a simple exponential decay with a time constant $T_2$, shown in Figure 3.5 and is given by:

$$M_{XY} = M_0 e^{-t/T_2}$$

Where M = magnetisation, $M_0$ = longitudinal magnetisation, t = time and $T_2$ is $T_2$ relaxation time (ms).

As discussed earlier in this Chapter (Section 3.3.1 on shim coils), the $B_0$ field will never be perfectly homogenous due to susceptibility effects, and so the magnetic field strength will vary very slightly from one point of the body to another (Currie et al., 2013). These macroscopic magnetic field inhomogeneities cause further dephasing of spins, as the spins experience slightly different precessional frequencies with respect to each other. This dephasing of spins due to magnetic field inhomogeneities is sometimes referred to as *$T_2$ prime* ($T_2$') but is usually acknowledged as $T_2^*$ which is the combined dephasing due to $T_2$ and $T_2$'. $T_2^*$ is always shorter or equal to $T_2$ because it is the combined effects of natural effects (spin-spin interaction) and magnetic field variations (Figure 3.5) (Boulby & Gunn, 2003; Deoni, 2010). Unlike $T_2$, $T_2$' decay is not random and is potentially reversible

(Currie et al., 2013). $T_2$ is measured by the *spin-echo* method (Hahn, 1950), whereas $T_2^*$ is measured by the *gradient-echo* method (Currie et al., 2013; Hahn 1960), which are outlined in Section 3.5 of this Chapter.

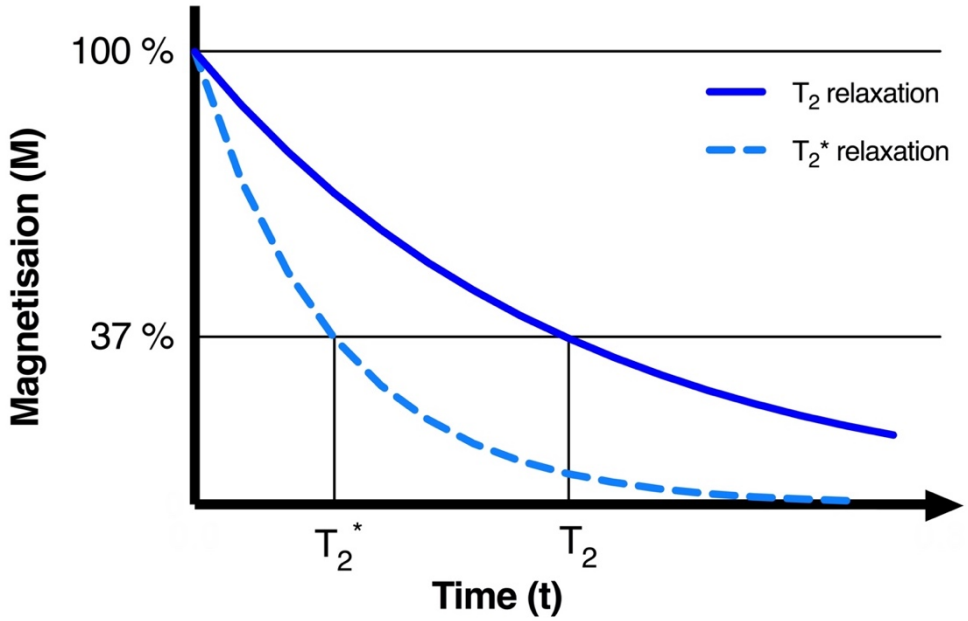


Figure 3.5 $T_2$ decay curve.

As $T_1$ and $T_2$ relaxations result from molecular motion and interactions between spins, the rates of $T_1$ and $T_2$ are different for tissues with different densities (e.g., water content and mobility) (Deoni, 2010). For example, $T_1$ is longer in tissues containing more free fluid because the spins move too rapidly for energy to be transferred back into the surroundings (McRobbie et al., 2006). The $T_2$ relaxation rate depends on how much time an individual spin spends near neighbouring spins (Currie et al., 2013). For example, $T_2$ is also longer in free fluids because spins continually move and interact with each other (Currie et al., 2013). It is these differences in $T_1$ and $T_2$ relaxation times between different tissue types that provide the contrast of the final image (see Section 3.6 of this Chapter) (McRobbie et al., 2006). $T_1$ is approximately five times longer than $T_2$ in biological tissues, with the respective relaxation times ranging between 300-2000 ms and 30-150 ms at the typical clinical $B_0$ (Currie et al., 2013).

### 3.4.4 Free induction decay

A radiofrequency signal (the NMR signal) is produced whenever there is transverse magnetisation (Sprawls, 2000). Immediately after the RF pulse, the free induction decay (FID) signal is produced, and its intensity is proportional to the extent of transverse magnetisation, which is greatest immediately after the RF pulse (Sprawls, 2000). As a result of dephasing, the detectable signal diminishes (Sprawls, 2000). The FID has a constant frequency, and so takes the form of a sinewave which rapidly decays as both $T_1$, and $T_2$ relaxation processes occur (Figure 3.6) (Currie et al., 2013). The FID is generated in the time-domain but is Fourier transformed to give a spectrum in the frequency-domain (Tofts & Waldman, 2003). The FID is not usually measured in MRI as it is disrupted by the magnetic field gradients used to localise and encode the MR signal (Currie et al., 2013). Therefore, the MR signal is usually generated and measured as a *spin-echo* (Hahn, 1950) or a *gradient-echo* (Hahn, 1960) and either spin-echo and gradient-echo pulse sequences, which are described in Section 3.5 of this Chapter, are the basis for most MRI pulse sequences (Elster, 1993).

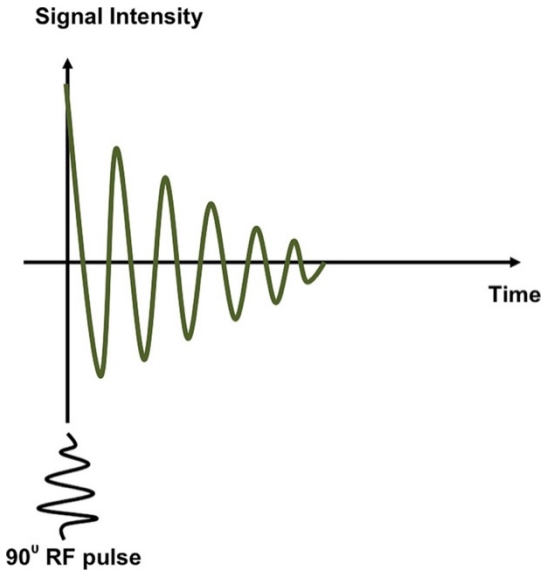


Figure 3.6 Free induction decay (FID). The transverse magnetisation is at its greatest following the 90° RF pulse. As spins begin to lose phase coherence, its amplitude, along with the signal intensity decreases. The decay in the signal is the FID. The Figure is reproduced from 'Understanding MRI: basic MR physics for physicians', Currie et al., volume 89, page 214, 2013, with permission from BMJ Publishing Group Ltd. (see Appendix D for permissions).

## 3.5 Pulse sequences

Pulse sequences involve repeated cycles of a long list of RF pulses (for spin-echo) or gradient pulses (for gradient-echo), activation of gradients, and the collection of spin-echo and/or gradient-echo signals (Sprawls, 2000; Tofts, 2005). Different pulse sequences can be used to generate different strengths of signals and therefore, different types of MR image contrast (introduced in Section 3.6) depending on the purpose of the examination and tissue of interest. The resulting image depends on which RF pulses and gradients are applied, and when they are applied (Sprawls, 2000). The main parameters that can be altered in a pulse sequence, include:

- The excitation *flip-angle* (FA) which is the amount of rotation experienced by the net magnetic field in relation to the direction of $B_0$ after application of the RF pulse (not to be confused with fractional anisotropy, which is also abbreviated as FA in MR research, but is a different concept). The size of the FA is determined by the strength and duration of the RF pulse (Sprawls, 2000). Most imaging methods use both 90° and 180° FAs, however, any size FA can be set (Sprawls, 2000).

- The r*epetition time* (TR), which is the amount of time in milliseconds between the application of two consecutive RF pulses and therefore the amount of time allowed for $T_1$ relaxation to occur (Hendrick, 2005).

- The *echo time* (TE) which is the amount of time in milliseconds between the middle of the RF pulse and the middle of the spin-echo and so is the amount of time that is allowed for $T_2$ relaxation to occur (Hendrick, 2005).

The pulse sequences used in the research Chapters are mainly based on spin-echo, but a combined gradient and spin-echo pulse sequence (GRASE) is also used in Chapters 7 and 8. Therefore, the spin-echo and gradient-echo pulse sequences are briefly outlined next.

### 3.5.1 The spin-echo pulse sequence

The spin-echo pulse sequence, which is illustrated in Figure 3.7, involves applying an additional 180° RF pulse after the initial 90° RF pulse, to refocus the spins and flip the net magnetisation back into the transverse plane (Plewes & Kucharczyk, 2012). In the spin-echo pulse sequence, the magnetisation at the transverse plane is refocused by the 180° pulse to generate the *spin-echo* (Hahn, 1950). The signal is maximum when the spins are aligned, and signal loss occurs when the spins are dephased (Brown & Semelka, 2011).

The refocusing pulses can be repeated several times after a single 90° RF pulse, in a *multi-echo sequence*, which involves repeated 180° RF pulses after a single 90° RF pulse (Figure 3.7) (Brown & Semelka, 2011). Each time the spins in the transverse plane are refocused, the signal from the spin-echo is always less than the previous spin-echo because the RF pulse only refocuses the dephasing due to magnetic field inhomogeneities ($T_2$') (Currie et al., 2013). The dephasing of spins due to spin-spin interaction is not refocused because it is an intrinsically irreversible process (Currie et al., 2013).

There are different variations of the spin-echo sequences, depending on the scanner vendor, the imaging purposes, and the time allocated for scanning patients (Deoni, 2010). The multi-echo $T_2$ sequence is one of the main pulse sequences used in the research studies of the thesis. Generally, multi-echo sequences involve acquiring several weighted images from echoes produced at different user defined TE values with a static TR to give each image a different $T_2$ weighting (Hendrick, 2005).

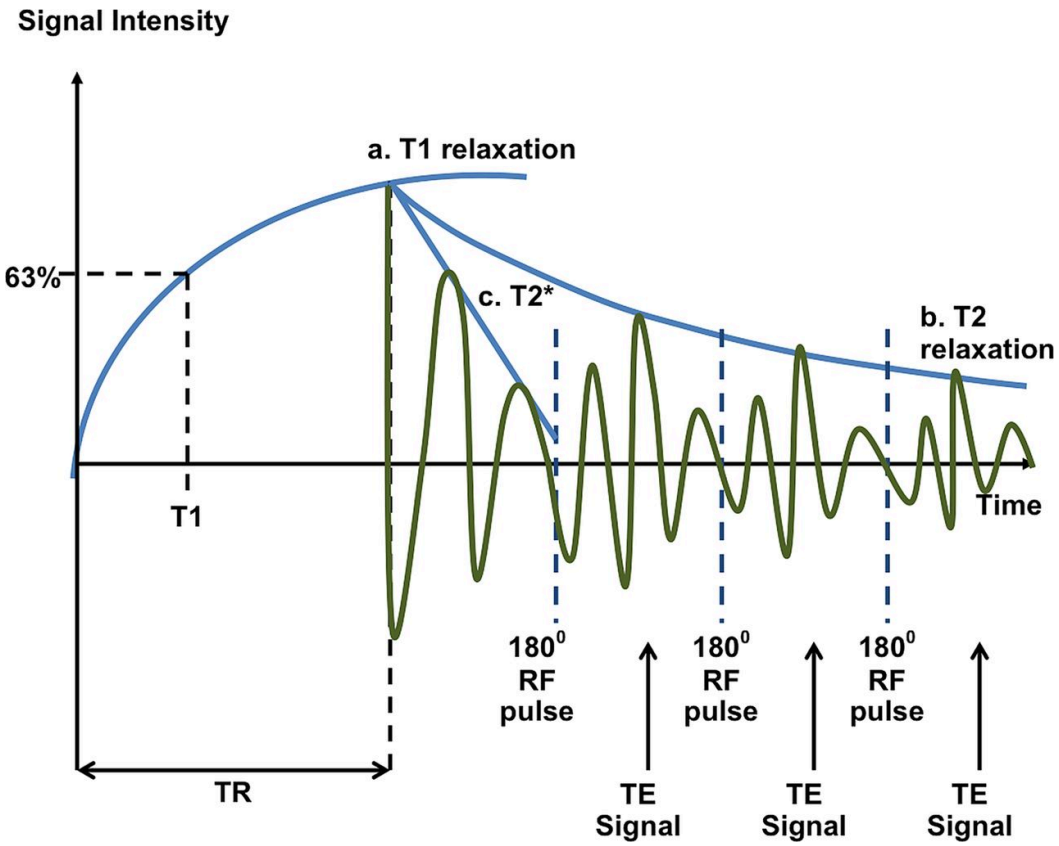


Figure 3.7 $T_1$, $T_2$ and $T_2^*$ relaxation. **a.** $T_1$ recovery curve: plot of the recovery of longitudinal magnetisation overtime after the RF pulse is switched off. **b.** $T_2$ recovery curve: a 180° RF pulse rephases spins, resulting in a temporary gain in signal intensity at time echo time (TE) termed spin-echo. A sequence of 180° RF pulses results in a chain of spin-echoes. Each subsequent echo will be of lower intensity due to spin-spin interactions. The curve connecting the spin-echo intensities is the $T_2$ decay curve. **c**. The $T_2^*$ curve results when 180° RF pulses are not used, and the signal decays due to magnetic field inhomogeneities. The Figure is reproduced from 'Understanding MRI: basic MR physics for physicians', Currie et al., volume 89, page 213, 2013, with permission from BMJ Publishing Group Ltd. (see Appendix D for permissions).

### 3.5.2 The gradient-echo pulse sequence

Like the spin-echo pulse sequence, the gradient-echo pulse sequence also involves refocusing spins (Elster, 1993). However, instead of RF pulses, magnetic field gradients are applied to generate the echoes (Elster, 1993). In a spin-echo sequence the RF pulse is applied to rephase spins after being dephased by magnetic field inhomogeneities ($T_2$') and spin-spin interactions ($T_2$) (described by $T_2^*$), whereas in a gradient-echo sequence, the spins are purposefully dephased by turning on the gradient, and then rephased by reversing the direction of the gradient (Sprawls, 2000). When applied, the magnetic field gradient only refocuses spins that have been rephased by the gradient and not spins that are dephased by magnetic field inhomogeneity (Elster, 1993). Therefore, the signal in gradient-echo images is also influenced by $T_2^*$ (Elster, 1993).

In the patient studies in Chapter 7 and Chapter 8, one of the sequences used for the acquisition of $T_2$ weighted images is the *multi-echo GRASE* sequence. The GRASE method (Gradient and Spin-Echo) is a combination of the gradient and spin-echo methods, which involves a train of 180° RF pulses to generate spin-echoes, and for each spin-echo, there are additional gradient-echoes which are generated by rapidly switching the readout gradient polarity (Caruthers et al., 1998).

### 3.5.3 Localising the signal

In order to map the signal to a spatial position, the origin of the signal must be isolated in three dimensions (X, Y, Z), using three separate magnetic field gradients for slice-selection, phase-encoding and frequency-encoding (Currie et al., 2013). Applying magnetic field gradients in the X, Y and Z directions in the same pulse sequence will mean that each voxel contains spins with different combinations of frequency, amplitude and phase, resulting in the spatial encoding of NMR signals

(Westbrook & Roth, 2011). Ultimately, the signal echoes that are generated are digitised and stored in *k-space,* which is a 2D or 3D raw data matrix. A Fourier transform is applied to k-space to convert the signal information into an image (Currie, 2013; Plewes & Kucharczyk, 2012)

.

## 3.6 MR image contrasts

The NMR signals and the contrast of the resulting MR images are directly related. The MR image is a display of the NMR signal emitted from the tissue, where the brightness of the image indicates the strength of the signal (i.e., level of magnetisation) (Sprawls, 2000). The strength of the MR signal and therefore, the contrast in the resulting image, depends on the physical characteristics of the tissue being imaged, which influences the extent of magnetisation experienced (Sprawls, 2000). The soft tissue contrast on conventional MR images arises from differences in the $T_1$ and $T_2$ relaxation properties and the number of detectable spins in the voxel, referred to as *proton-density* (PD) (Deoni, 2010). The contrast can be manipulated by altering the pulse sequence acquisition parameters outlined in Section 3.5 of this Chapter (Hendrick, 2005). The relationships between tissue properties (PD, $T_1$ relaxation rate, $T_2$ relaxation rate), MR signal intensity (i.e., extent of magnetisation experienced by the tissue) and resulting image contrast is summarised in Figure 3.8 (Sprawls, 2000).

By selecting the appropriate pulse sequences and parameters, images can be weighted toward $T_1$ or $T_2$ relaxation times or PD (Elster, 1988), which means the primary contributor to the signal for PD weighted (Section 3.6.1), $T_1$ weighted (Section 3.6.2) and $T_2$ weighted (Section 3.6.3) will either be PD, $T_1$ relaxation, or $T_2$ relaxation respectively. However, it is important to note that although the contrast of images can be selectively weighted, $T_1$, $T_2$ and PD contribute to the signal of all weighted images to some extent (Deoni, 2010; Elster, 1988). For example, the signal obtained in a $T_2$ sequence will predominantly be determined by

the $T_2$ relaxation time, and therefore contrast on $T_2$ weighted images will reflect the relative $T_2$ relaxation of tissue types; however, the signal that is produced is also partly influenced by $T_1$ relaxation, and PD (Deoni, 2010; Elster, 1988). As will become evident throughout the course of this thesis, the combined influence of these intrinsic properties to the signals is one of the main (and often underappreciated) factors that contribute to variability in results across quantitative MRI based stroke timing studies (Rogers, McGarry et al., 2014; McGarry et al., 2016a).

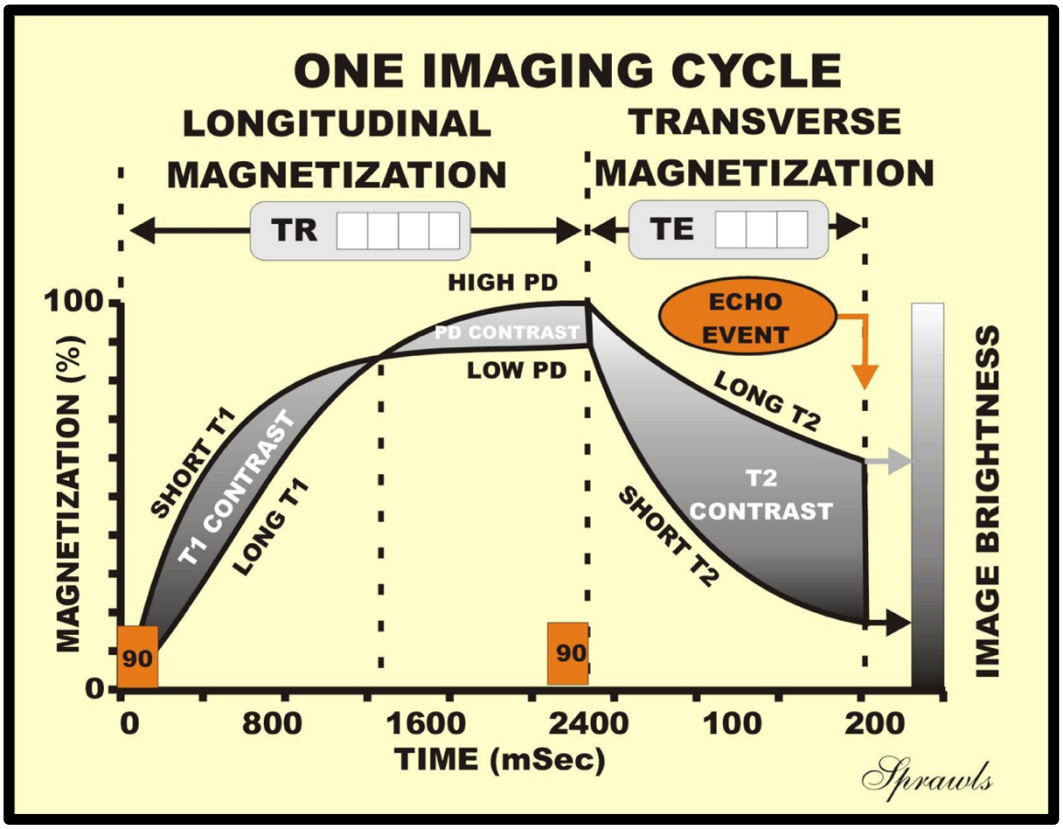


Figure 3.8 Summary of the relationships between signal intensities and the brightness of image contrast. Image is reproduced from Sprawls (2000).

### 3.6.1 Proton-density weighted images

In proton-density (PD) weighted images (Figure 3.9), the tissue contrast is dominated by the number of detectable spins/protons in the voxel. The tissues with the highest density of spins/protons produce the strongest signal and therefore appear brighter on the resulting image. Images that are PD weighted are collected with a short TE to minimise $T_2$ contribution and a long TR to minimise $T_1$ contribution (McRobbie et al., 2006). PD images are not typically used in stroke research but are the first image in the multi-echo $T_2$ sequence.

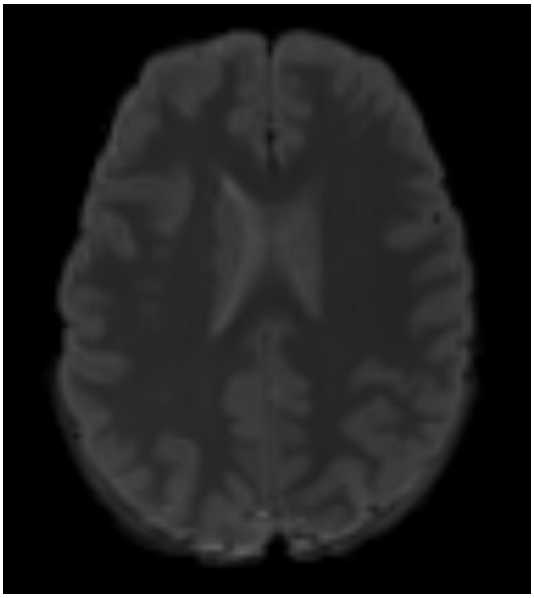

Figure 3.9 Example of a proton-density weighted image.

### 3.6.2 $T_1$ weighted images

In $T_1$ weighted ($T_1$w) images (Figure 3.10), the $T_1$ relaxation rate is the predominant contributor to the signal and therefore, the predominant source of tissue contrast. Tissues with a short $T_1$ have the highest level of magnetisation, which produces a higher signal, and translates to brighter contrast in the resulting image (Sprawls, 2000). For example, grey and white matter have a shorter $T_1$ compared to CSF and appear bright on $T_1$ weighted images. As CSF is a fluid, it has a long $T_1$ and so the signal recovery slowly, resulting in fast signal loss and therefore dark appearance in $T_1$ weighted images (Plewes & Kucharczyk, 2012).

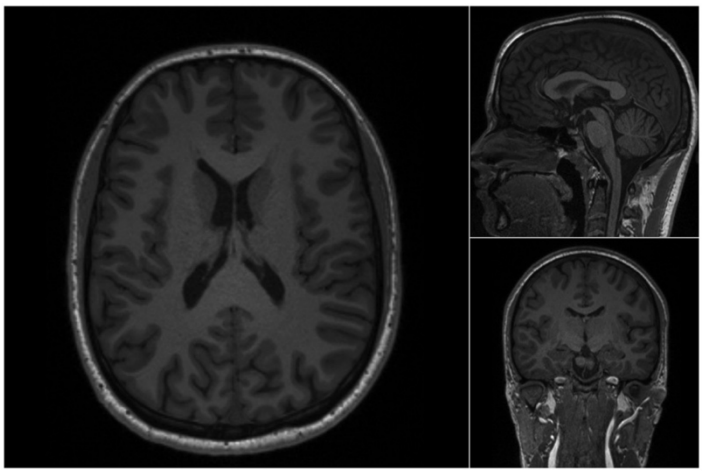

Figure 3.10 Example of $T_1$ weighted images, in the axial, sagittal and coronal planes.

$T_1$w images are usually obtained with a spin-echo inversion recovery pulse sequence or a saturation recovery pulse sequence. The spin-echo inversion recovery sequence begins with a 180° inversion pulse to invert steady-state longitudinal magnetisation in the direction of the minus Z-axis, followed by the typical spin-echo sequence starting with a 90° pulse (Brown & Semelka, 2011). Saturation recovery sequences such as FLASH $T_1$ (used in Chapter 5), involve multiple RF pulses so that magnetisation does not fully recover before the next pulse, hence *saturation* (Haase, 1990). $T_1$ weighting is achieved by setting a short TE to minimise the contribution of $T_2$ to the signal. Also, by setting a TR that is short enough to capture the signal difference due to $T_1$ relaxation before longitudinal magnetisation recovers fully (Plewes & Kucharczyk, 2012). The short TR ensures there is a low signal from regions with a long $T_1$ relative to those with a short $T_1$ (Plewes & Kucharczyk, 2012). As will be explained in Chapter 4, Section 4.2.3, $T_1$w images are not typically acquired for the assessment of acute ischaemic stroke patient, but they were acquired in Chapter 7 and Chapter 8 to aid with image processing.

### 3.6.3 $T_2$ weighted images

$T_2$ weighted ($T_2$w) images (e.g., Figure 3.11) can be acquired with spin-echo or gradient-echo pulse sequences. A long TE is used to ensure $T_2$ is the predominant contributor to the signal. In the GRASE sequence, the weighting is mainly $T_2$, but $T_2^*$ also has some contribution (discussed in Section 3.5.2), which is an important factor in the interpretation of the results of Chapter 8. $T_2$w images, where the signal and therefore, image contrast, is predominantly influenced by the $T_2$ relaxation time, are obtained by setting a long TE and long TR (McRobbie et al., 2006). The contribution of $T_1$ is minimised by setting a long TR to ensure magnetisation recovers fully (McRobbie et al., 2006). Additionally, the longer transverse magnetisation persists, the stronger the signal will be, resulting in brighter contrast (McRobbie et al., 2006). Thus, setting a long TE ensures the $T_2$ decay of different tissue types is captured (McRobbie et al., 2006). Fluids, such as cerebrospinal fluid (CSF) have a long $T_2$, and so have a stronger signal, which appears bright on $T_2$ w images (McRobbie et al., 2006). Grey and white matter, which have a shorter $T_2$ appear darker on $T_2$w images due to signal loss (McRobbie et al., 2006). $T_2$* weighted images can be produced by using a gradient-echo sequence with relatively long TE (Plewes & Kucharczyk, 2012).

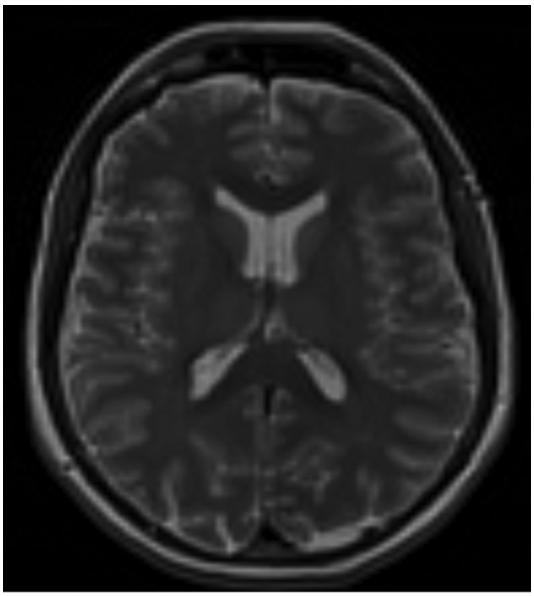

Figure 3.11 Example of a $T_2$ weighted image.

### 3.6.4 $T_2$ weighted FLAIR images

$T_2$w images can also be acquired where the signal from CSF is suppressed, in order to improve the contrast of other fluids. CSF suppression is achieved with a $T_2$w fluid attenuated inversion recovery ($T_2$w FLAIR) sequence (Hajnal et al., 1992), which has a long inversion time to null the signal from CSF (which has a long $T_1$) as well as a long TE to give the image a $T_2$ weighting. The $T_2$ weighting and no signal from CSF result in images greater anatomical detail and lesion signal intensity than standard $T_2$w images (Hajnal et al., 1992) and is, therefore, the preferred $T_2$w sequence for imaging stroke patients. An example of a $T_2$w FLAIR image is shown in Figure 3.12.

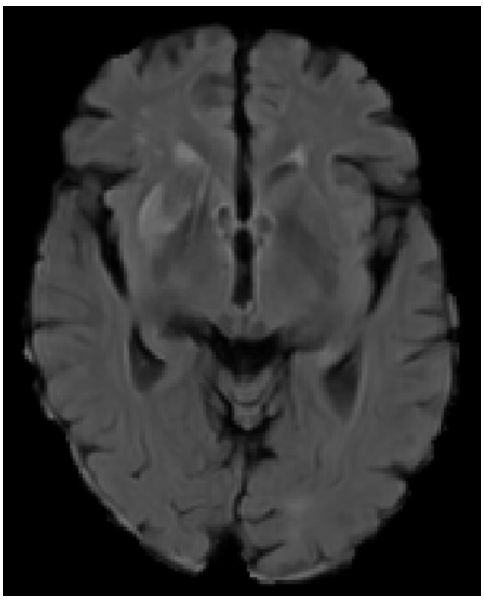

Figure 3.12 Example of a $T_2$ weighted FLAIR image.

### 3.6.5 Diffusion weighted images

Diffusion weighted images (DWI) are arguably one of the most important MR images for studying acute ischaemic stroke as they reveal regions of the brain affected by ischaemia within minutes of stroke onset (Moseley, 1990). The reasons for which will be explained in Chapter 4 Section 4.2.1. An example of a diffusion-weighted image from an acute ischaemic stroke patient is shown in Figure 3.13.

The contrast of diffusion-weighted images predominantly reflects the relative amount of diffusion (random thermal motion) of water molecules within the voxels (Hendrick, 2005). The diffusion-weighted pulse sequence (Stejskal & Tanner, 1965) first involves obtaining a $T_2$w image with a spin-echo sequence with no diffusion weighting ($b_0$, not to be confused with $B_0$). This is followed by applying the *pulsed gradient method* which is a spin-echo sequence where two magnetic field gradients of the same magnitude but in opposing directions, are applied either side of the 180° RF pulse (Baird & Warach, 1998). The first gradient causes spins to lose phase-coherence, and the second gradient causes spins to re-gain phase-coherence, provided that they are stationary during the time between the gradients (Baird & Warach, 1998).

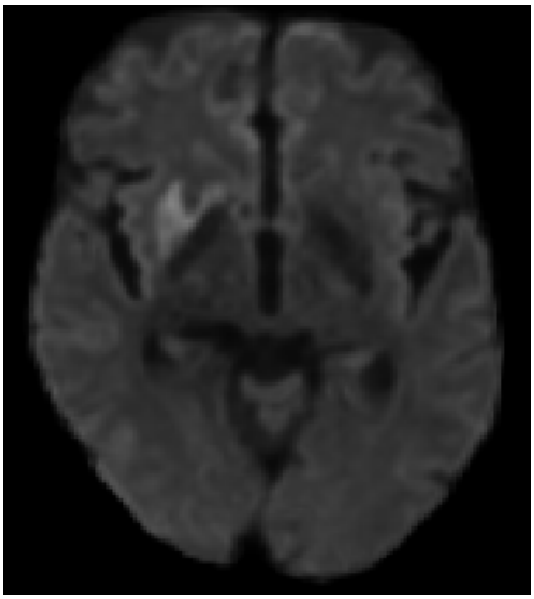

Figure 3.13 Example of a diffusion weighted image from an acute ischaemic stroke patient.

If water molecules are mobile, for example, in CSF, spins do not rephase due to fast translational motion, resulting in large signal loss, and therefore dark appearance on the resulting image (Baird & Warach, 1998). When water molecules are less mobile, such as in white matter, the signal is only slightly reduced, and contrast, therefore, appears bright on the image (Baird & Warach, 1998). The

diffusion-sensitising gradients are applied in one or more directions (e.g., X/Y/Z) to produce source images, which are averaged to produce the diffusion-weighted images used for clinical diagnosis (Baird & Warach, 1998). The strength and timing of the gradients in the pulse sequence are given by the b-value (secs/mm$^2$). The b-values can be set to produce optimal diffusion weighting for the tissue of interest, where higher b-values give more diffusion weighting, but also low signal to noise ratio (SNR) (Kingsley & Monahan, 2004). However, due to a relatively long TE needed to include diffusion gradients into the pulse sequence, diffusion-weighted images also have some $T_2$ weighting, termed *$T_2$ shine through* (Burdette et al., 1999). Therefore bright contrast on the image could also reflect the presence of fluid, rather than decreased diffusion.

## 3.7 Quantitative MRI

In a clinical setting, the assessment of the MR signal in weighted images (i.e., DWI, $T_1$, $T_2$, in Section 3.6) is almost always qualitative, and images are produced according to the scanner settings. Routinely, the radiographer or clinician will visually assess the images and can measure the volume of lesions or anatomical regions that are defined by the image contrast but will not extract information about the tissue properties from standard weighted images (Tofts, 2005). However, the MRI scanner is capable of providing much more information (Tofts, 2005). The concept of quantitative MRI (qMRI) merges the traditional visual assessment of MRI with the scientific process of measurement, where MRI is not only a 'picture-taking tool' but also a scientific instrument (Tofts, 2005). qMRI is the main method of analysis used in the research Chapters of this thesis.

The purpose of the quantitative approach to MRI, especially when informing clinical decisions, is to reduce problems of bias and low-interrater reliability which is often encountered when images are assessed visually (e.g., Galinovic et al., 2014). The goal of qMRI is, therefore, to transform MRI into a reliable, reproducible form

of measurement that requires minimum human training or intervention (Tofts, 2005). In any image acquired with MRI, each voxel is represented by a number, and as with any other area of scientific enquiry, qMRI, therefore, involves recording and measuring these numbers in the region of interest, to identify changes from the normal ranges (Tofts, 2005).

The strength of the MR signal is influenced by PD, and $T_1$ and $T_2$ relaxation times of the imaged tissue. Due to differences in water content and paramagnetic properties, different tissues have distinct relaxation characteristics, which are altered differently by pathology (Deoni, 2010). Thus, by measuring the changes in the MR signal caused by changes in relaxation properties, pathologies such as ischaemic stroke can be identified, investigated, diagnosed and monitored (Deoni, 2010). In stroke timing literature, many have adopted the quantitative approach to analysing MRI data (e.g., Cheng et al., 2013; Jokivarsi et al., 2010; Madai et al., 2016; Siemonsen et al., 2009; Song et al., 2012) but these have taken two different forms.

The first form is the *quantitative analysis of the signal intensities represented in weighted images* (Section 3.7.1) and the second, is *the parametric approach to qMRI* (Section 3.7.2), which involves mathematically parameterising MR signal intensities before measuring them and transforming them into parametric images/maps. In MRI stroke timing research, both quantitative approaches involve measuring changes in values obtained from MR images of ischaemic stroke patients, but, as will become apparent in the following Sections and remainder of the thesis, these approaches differ fundamentally in terms of what is being measured, and how informative and reliable they are.

### 3.7.1 Quantitative analysis of signal intensities represented in weighted images

In standard weighted imaging, each voxel has a signal value, which is an arbitrary number that represents the strength of the MR signal and determines the contrast of the final weighted image (Tofts, 2005). Voxels with strong signal have higher numbers than voxels with comparatively lower signal (Tofts, 2005). For example, in a $T_2$w sequence, the signal of CSF is stronger than the signal of white matter (WM); therefore, voxels containing CSF will have comparatively higher numbers than voxels containing WM. CSF voxels will therefore appear hyperintense on the resulting weighted image. In weighted imaging, the values that are measured are referred to as the *signal intensities* as they are proportional to the signal voltage induced in the RF coil. By extension, signal intensities are also referred to as *image intensities*, as it is the intensity of the MR signal that determines the contrast of the image that is constructed from the signal data (Sprawls, 2000).

The quantitative analysis of signal intensities, therefore, involves measuring the strength of the signal in a given voxel of weighted images (such as those shown in Section 3.6), where the measured signal is influenced by a combination of intrinsic tissue properties (PD, $T_1$, $T_2$) and factors related to MR hardware (e.g., $B_1$, $B_0$). As will be introduced in Chapter 4, these MR signal values increase in weighted images of ischaemic stroke patients due to hydrodynamic changes caused by ischaemia. Thus, a popular approach in clinical stroke research literature is to measure the changes in the MR signals displayed in the weighted images that would usually be used in the visual assessment of strokes, such as DWI, $T_2$w, and $T_2$w FLAIR images (e.g., Madai et al., 2016; Cheng et al., 2013; Song et al., 2012).

A limitation of quantifying the signal intensities represented in weighted images is that the voxels of weighted images do not have a fixed tissue-specific numerical value (Rizzo et al., 2018). Even if the same patient is scanned in the same position, with the same pulse sequence in different sessions, the resulting image will appear

identical, but the voxel intensity values will be different (Madabhushi & Udupa, 2005; Rizzo et al., 2018). Having different voxel intensity values is not problematic when assessing the MR image visually. For example, when identifying the location of ischaemic tissue, the number assigned to each voxel is not important, so long as the affected region is visible to the viewer. However, arbitrary voxel values are problematic if the purpose of the MR scan is to objectively measure and quantify the physical changes caused by disease. If the voxel intensity values are different in the same patient on different occasions, then it would not be clear whether the measured difference was biological in origin, or due to hardware issues of the MR system.

Arbitrary voxel values also have implications for clinical research. If different studies used MR systems with different hardware and software, the performance of the different qMRI parameters cannot be cross-compared, which makes it difficult to draw meaningful conclusions across studies. As will be pointed out in Chapter 4 and the introduction of Chapter 5, one of the main problems in stroke timing research at present, is that there are many studies that have quantified MR signal intensities, but because they were performed at different sites with different MR hardware and software, results are not directly comparable. Therefore, identifying which approach is most appropriate for clinical use becomes extremely difficult.

Furthermore, when developing a quantitative method for studying cerebral ischaemia, whether the purpose is onset time estimation (i.e., the *chronological clock* approach outlined in Chapter 1) or evaluation of tissue status (i.e., the *tissue clock* approach outlined in Chapter 1), the thresholds used to identify ischaemia, and the diagnostic software that is developed, would need to be tailored for the specific MR system if signal intensities are used for onset time estimation. This is the current issue with the core-perfusion-mismatch methods for the *tissue clock* approach (highlighted in Chapter 1 and raised in further detail by Dani et al., 2011 and Demeestere et al. 2020). From a clinical and research perspective, it would be

more practical for methods and software to be universally applicable. For reasons that will be highlighted in the following Section, this may be more achievable if the parametric approach to quantitative MRI is adopted instead.

### 3.7.2 The parametric approach to quantitative MRI

The second qMRI based approach, also involves measuring voxel values of MR data, but first involves mathematically removing factors that contribute to the signal that are not of interest. For example, removing the influence of PD and $T_1$ relaxation from the signal of a $T_2$w sequence, or removing the influence of $T_2$ relaxation from diffusion-weighted signals to eliminate the $T_2$ shine through effect. The parametric approach to qMRI involves transforming signals that are obtained in weighted imaging sequences (e.g., DWI, $T_1$, $T_2$) into data that is parametric (Tofts, 2005). Thus, instead of measuring the arbitrary values associated with NMR signals (as explained in Section 3.7.1), tissue-specific properties can be measured (Deoni, 2010; Tofts, 2005).

Converting MR signal data into parametric data involves fitting the signal intensities acquired during a weighted imaging sequence to equations that describe the parameter of interest (described later in this Section). The main parameters that are computed and measured in stroke research include the average $T_1$ relaxation time (measured in ms) and the average $T_2$ relaxation time (ms). As well as the average diffusion rate of spins in the voxel, referred to as *the apparent diffusion coefficient* (ADC) which is typically measured in $\mu m^2/ms$ (Le Bihan et al., 1992). The computed parameters can also be used to construct parametric images or *maps*, which have the same anatomical distinctions as weighted images but are conceptually different (Tofts, 2005). As with weighted images, each voxel has a number, but for $T_1$ maps, these numbers are in ms, representing the estimated average $T_1$ of spins within the voxel, for $T_2$ maps, the numbers obtained are the

estimated average $T_2$ of spins within the voxel, and for ADC maps, the numbers represent the average diffusion rate of spins within the voxel.

The parametric approach to quantitative MRI overcomes the problems associated with the *quantitative analysis of the signal intensities represented in weighted images* (Section 3.7.1) but has received comparatively less attention in clinical stroke imaging, perhaps due to clinicians and researchers being unaware of good practice in the quantification of MRI images (Tofts, 2005). By computing parametric maps, the contributions of PD, $T_1$, $T_2$ and extraneous sources of signal such as magnetic field inhomogeneities, and variability in the scanner manufacturer's RF hardware and pulse sequences, are separated out (Deoni, 2010). The parametric data and the maps that are produced are, therefore, essentially a purer form of their weighted counterparts (Deoni, 2019).

This purer form of data has a number of advantages. The ability to separate all extraneous factors from the parameter of interest enables a more explicit interpretation of changes in the image intensities of the MRI data in relation to all physiology including normal and pathological factors (Deoni, 2010). As the MR relaxometric properties are sensitive to the local tissue and biochemical environments, measuring changes in these individual parameters, provides richer and more detailed information than the measurements of signal intensities from weighted images (Deoni, 2010). A further advantage is the consistency of parametric data (Deoni, 2010). Unlike the quantitative analysis of weighted images, parameterising MR signal data enables unbiased comparison of MRI data from different patients and imaging centres when identical acquisition methods are used (Deoni et al., 2008). This consistency between sites would be better for longitudinal studies as well as large scale clinical studies, where data from multiple sites are combined, as it would remove the need for complex, sophisticated normalisation techniques (Deoni, 2019). Consistency is also especially important for the clinical research Chapters in this thesis (Chapter 7 and Chapter 8) as the patient data was acquired from three different hospitals with different MR systems.

### Computation of $T_1$ maps

The computation of $T_1$ relaxation times from MR signal data involves fitting signal intensity values obtained in a $T_1$w sequence using different flip-angles (e.g., Deoni et al., 2004) or inversion times (e.g., Nekolla et al., 1992) on a voxel-wise basis to the respective $T_1$ equations. For example, the traditional computation of $T_1$ maps using $T_1$w images with different inversion times involves fitting the signal data to the expression below:

$$S(TI) = S_0\,(1 - 2\,e^{-\frac{TI}{T_1}})$$

Where S(TI) is the signal measured at time TI (inversion time) which is proportional to the Z magnetisation at the time, $S_0$ is the signal that would be acquired from the equilibrium longitudinal magnetisation ($M_0$) (Gowland and Stevenson, 2003).

By converting voxel values into $T_1$ relaxation times, $T_1$ maps or images can be constructed. These parametric maps are not the same as $T_1$w images. Voxels in a $T_1$ map represent the average estimated $T_1$ relaxation time of spins within that voxel, independent of PD and $T_2$ relaxation (Deoni, 2010). In $T_1$w images, regions with long $T_1$ have a dark contrast because of the signal loss and regions with a short $T_1$ have bright contrast because of the stronger signal. Whereas in $T_1$ maps, the contrast is opposite because it is determined by the measured values in ms. Thus fluids, which have a long $T_1$ relaxation time, appear bright on $T_1$ maps. Voxels with a short $T_1$ appear dark. Examples of a $T_1$ map and a $T_1$w image are shown alongside each other in Figures 3.14 and 3.15 (respectively) to demonstrate the difference in contrast.

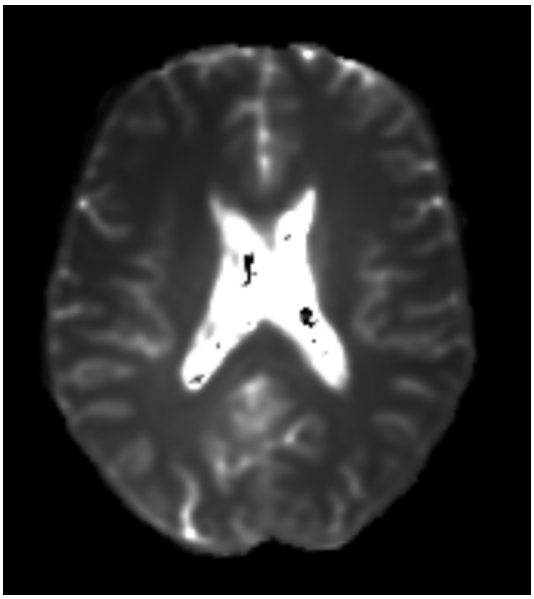

Figure 3.14 Example of a $T_1$ relaxation time map.

Figure 3.15 Example of a $T_1$ weighted image.

### Computation of $T_2$ maps

In order to quantify the $T_2$ relaxation time, and compute a $T_2$ map, the signal values acquired with different TEs (from the multi-echo $T_2$ sequence, see Section 3.5) and static TR are fitted on a voxel-wise basis typically to a single exponential function (Deoni, 2010; Tofts, 2005):

$$S(TE) = S_0\, e^{-TE/T_2}$$

Where $S_0$ is the proton-density, and TE is the echo time (Milford et al., 2015).

By converting voxel values into $T_2$ relaxation times, $T_2$ maps or images can be constructed (Figure 3.16). As with $T_2$ weighted images, fluids, such as CSF have a long $T_2$ relaxation time and so appear bright on $T_2$ maps. Although the tissue contrast is similar, $T_2$ maps are parametric and are not the same as $T_2$w images. Voxels in a $T_2$ map represent the average estimated $T_2$ relaxation time of spins within that voxel, independent of PD, $T_1$ relaxation and magnetic field inhomogeneities (Deoni, 2010).

Figure 3.16 Example of a $T_2$ relaxation time map.

### Computation of apparent diffusion coefficient maps

The parametric approach can also be applied to diffusion data. Apparent diffusion coefficient (ADC) maps are the parametric images that are computed from the signal values obtained from a diffusion-weighted sequence which is achieved by performing a voxel-wise fit of at least two diffusion-weighted images with different b-values ($b$, high and low). The ADC map can be computed by dividing the signal from the diffusion-weighted image ($S_{DWI}$) by the signal ($S_0$) from the corresponding points on the $b_0$ image and taking the logarithms (Schaefer et al., 2000), where:

$$S_{DWI} = S_0\, e^{-bADC} \quad \rightarrow \quad ADC = -\frac{1}{b} \ln\left(\frac{S_{DWI}}{S_0}\right)$$

ADC maps, or images, are not the same as diffusion-weighted images. In DWI, restricted diffusion is represented by higher signal values, and so regions with decreased diffusion, such as ischaemic tissue appears bright (Figure 3.17). Whereas voxels in an ADC map correspond to the mean estimated diffusion rate, commonly given in $\mu m^2/ms$. Thus, in contrast to DWI, as regions with restricted diffusion have low ADC values, they appear dark on ADC maps (Figure 3.18). Fluids have high diffusion and therefore high ADC values, which appear bright on ADC maps (Le Bihan et al., 1992). By computing the ADC maps, $T_2$ shine through is effectively eliminated as the contribution of $T_2$ to the signal is removed (Le Bihan et al., 1992). Therefore, ADC images reflect only the diffusivity of different tissue types (Le Bihan et al., 1992).

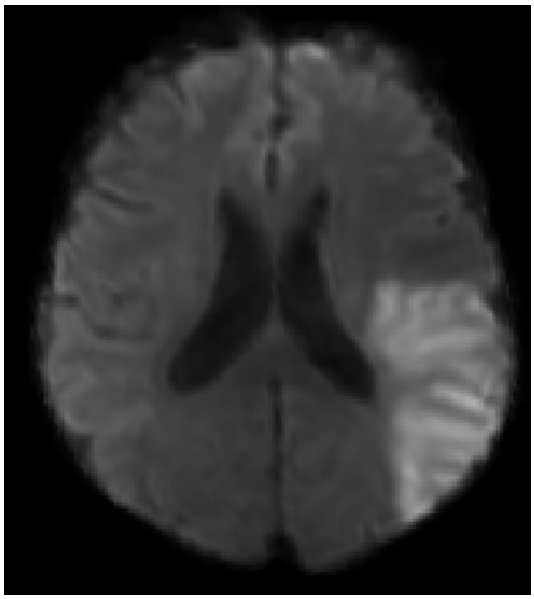

Figure 3.17 Example of a diffusion weighted image from an acute ischaemic stroke patient.

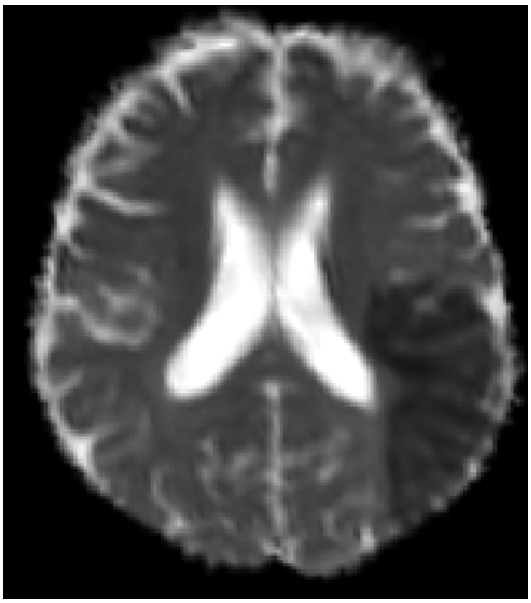

Figure 3.18 Example of an ADC map from the same acute ischaemic stroke patient in Figure 3.17.

### 3.7.3 Magnetic resonance fingerprinting (MRF)

Throughout this thesis, an MR acquisition technique, termed *magnetic resonance fingerprinting* (MRF) (Ma et al., 2013, Siemens Healthcare Limited, 2020) is often referred to. Most clinical MRI scanners can compute parametric maps automatically, but MRF enables these parametric maps to be obtained simultaneously, which reduces the total scan time to a few minutes (Ma et al., 2013). MRF involves under sampled acquisition with varying FAs, TRs and TEs, to extract multiple quantitative tissue parameters from a single scan (Siemens Healthcare Limited, 2020). This acquisition approach causes tissues to make unique signal patterns of data that are recorded as *fingerprints*, whicch reflect the tissue composition (Siemens Healthcare Limited, 2020). These fingerprints are matched to an existing library or database of possible fingerprints using pattern recognition and when there is a match, the matching tissue properties are identified and given in a parametric map (Siemens Healthcare Limited, 2020). Using MRF there is no need to fit an exponential curve (as described in Section 3.7.2 of this Chapter) and multiple types of quantitative data (e.g., $T_1$ relaxation, $T_2$ relaxation, ADC) can be acquired at the same time. This fast acquisition makes MRF as quick as NCCT and therefore tolerable for unstable acute ischaemic stroke patients. Currently MRF is for research use only (Siemens Healthcare Limited, 2020), but if eventually incorporated into hospital MRI scanners, MRF would enable clinicians to utilise the benefits of qMRI parameters (such as those that are studied in this thesis) to aid their diagnoses and treatment decisions.

## 3.8 Summary and clarification of qMRI terminology

In the stroke timing literature that is reviewed over the course of the remaining Chapters, there is a lack of consensus over terminology in the context of qMRI. The purpose of this Section is to provide some clarification over the terminology used throughout this thesis.

As outlined in Section 3.7. of this Chapter, generally, the term *quantitative MRI* is used as an overarching term for two different quantitative approaches to MR data analysis. One popular approach is to measure the signal intensities of voxels that are represented in weighted images that would typically be used in the visual assessment of stroke (Section 3.7.1). The other approach, which has received comparatively less attention in stroke timing literature, involves parametrising the MR signal data so that parameters of interest such as diffusion, $T_1$ relaxation and $T_2$ relaxation can be measured separately (Section 3.7.2). Both approaches involve measuring voxel values, which are either arbitrary numbers that represent the intensity of the MR signal, or separate properties of the MR signal (i.e., relaxation or diffusion).

The terminology associated with the of the type of data that is quantified in stroke timing literature can also be confusing and misleading. Both quantitative approaches do not require an image for the analysis, because it is the numbers associated with each voxel that are being studied (i.e., signal intensity value or relaxation time in ms). However, the signal data is loosely represented by the contrast of the reconstructed images (i.e., weighted image or parametric map). As clinical MRI traditionally involves looking at images, the quantitative values that are measured in both approaches are often referred to in the context of the images that represent them. For example, the image intensity values of weighted images or the image intensity values of $T_2$ relaxation time images/maps.

For consistency, the term *image intensity value* is used in this thesis to refer to signal intensity values that are represented in weighted images, as well as the relaxation times and ADC values obtained from relaxometry and ADC maps respectively. The term *qMRI parameters* is also used to refer to the different types of image intensity values, for example, $T_2$w image intensities, or $T_2$ relaxation time intensities. The reference to images in the context of qMRI also highlights the importance of MR images in studying stroke. qMRI is beneficial because it allows us to delve deeper into the changes in the brain caused by ischaemia and to measure

the changes that are not visible by eye (Deoni, 2010; Tofts, 2005), however, the images are still important for contextualising and anatomically locating these changes (Deoni, 2019).

# Chapter 4
# MRI for the Imaging of Acute Ischaemic Stroke

## 4.1 Introduction

The purpose of this Chapter is to show how MRI can be used to study the pathophysiology of cerebral ischaemia and to contextualise the research studies in this thesis. The Chapter is split into two Sections. The first Section relates the different MR images and qMRI parameters to different aspects of stroke pathophysiology. The second Section explains the main approaches to timing the ischaemic stroke using MRI, with a brief overview of the relevant research and the rationale for the approaches studied in this thesis. The summary of previous research is kept brief because the stroke timing research is also considered in the introductions and discussions of the research Chapters (5, 7 and 8). The Chapter ends with an explanation of the rationale for the methods studied in this thesis, and recognition of potential alternative methods for applying qMRI to the problem of unknown onset time.

## 4.2 MRI and stroke pathophysiology

Different MRI pulse sequences can be used to capture different aspects of stroke pathophysiology (Kauppinen, 2014). There is a consensus that in the clinical stroke centres where MRI is used, at the very least, diffusion-weighted (DWI), $T_2$ weighted ($T_2$w), $T_2$w fluid-attenuated inversion recovery ($T_2$w FLAIR) images and $T_2$* weighted images (for identification of haemorrhage) should be obtained (Mair & Wardlaw, 2014). Therefore, except for $T_2^*$, these images were acquired for the studies of this thesis, with the addition of $T_1$ weighted images ($T_1$w), and the parametric counterparts of the weighted images, including the apparent diffusion coefficient (ADC) maps, $T_2$ relaxometry maps (Chapters 5, 7 and 8) and $T_1$ relaxometry maps (Chapter 5). Throughout this Section, the reader is referred to Figure 4.9, which illustrates how the stages of ischaemia and the different forms of oedema relate to different MR images.

### 4.2.1 Diffusion images

As outlined in Chapter 3 (Section 3.6.5), diffusion is the random thermal motion of free water molecules within tissue (Le Bihan et al., 1992) and images acquired using diffusion sequences portray the diffusivity of water in the parenchyma in the imaged voxel (Le Bihan et al., 1992). Two types of diffusion images are used in the assessment of acute ischaemic stroke and studied in this thesis, diffusion-weighted images (Section 3.6.5) and the parametric counterpart, the *apparent diffusion coefficient* (ADC) maps (Section 3.7.2). Diffusion based images are essential in the MRI protocol for ischaemic stroke patients because they reveal the affected regions, that would not otherwise be identifiable on non-diffusion images, within minutes of ischaemia onset (Moseley et al., 1990). Diffusion images are, therefore, sensitive diagnostic tools for acute ischaemic stroke (Moseley et al., 1990).

### Diffusion weighted images (DWI)

Figure 4.1 is an example of a diffusion weighted image of a hyperacute ischaemic stroke patient. Within minutes of ischaemia onset, the DWI signal increases, due to the decreased diffusion that is attributed to cytotoxic oedema (i.e. shift of extracellular water into the intracellular space, Figure 4.9-partA) (Moseley et al., 1990). As fluid shifts from extracellular to intracellular space, the extracellular space becomes smaller, which reduces the mobility of total tissue water (Moseley et al., 1990) (Figure 4.1-part A). However, unless considered alongside $T_2$ w images or ADC maps, the pathological underpinnings of hyperintensities on DWI images are difficult to separate from each other due to $T_2$ shine through (i.e. whether hyperintensities reflect cytotoxic oedema or vasogenic oedema) (Warach et al., 1995; 1997).

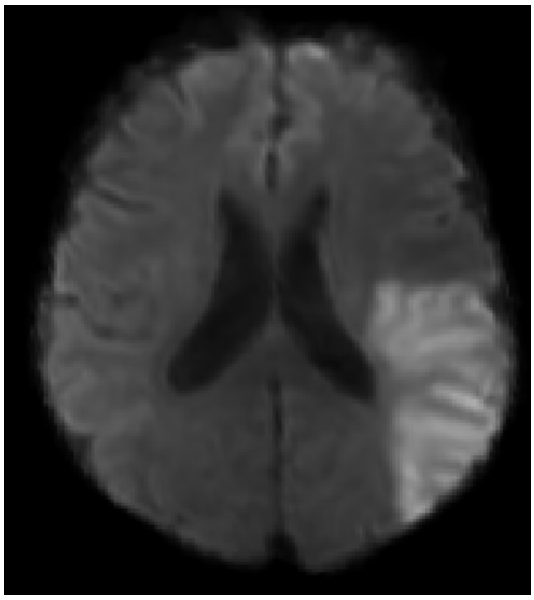

Figure 4.1 Example of a diffusion weighted image from an acute ischaemic stroke patient.

### The apparent diffusion coefficient maps (ADC)

Figure 4.2 shows the ADC map of the same ischaemic stroke patient in Figure 4.1 The ADC map is the parametric counterpart of the diffusion weighted image and as outlined in Chapter 3 (Section 3.7.2), is computed from the values obtained from the diffusion weighted sequence. As with DWI images, ADC maps are useful for

the diagnosis of ischaemic stroke as the ADC value decreases within minutes of ischaemia onset (Hoehn-berlarge et al., 1995). The contrast of ADC maps is determined by the ADC values of the tissue. Therefore, ischaemic regions are visible as hypointensities on ADC maps, where voxels have low ADC values due to decreased diffusion caused by cytotoxic oedema (Figure 4.2 and Figure 4.9-part A).

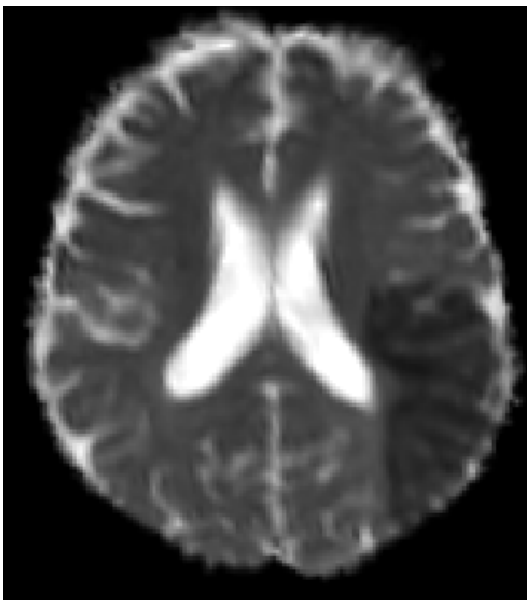

Figure 4.2 Example of an ADC map from an acute ischaemic stroke patient.

As discussed in Chapter 3 (Section 3.7.2), ADC is a purer measure of diffusion than diffusion weighted sequences as by computing ADC maps, the contribution of $T_2$ shine through is eliminated. Therefore, regions with low ADC values mainly reflect cytotoxic oedema and therefore, potentially salvageable tissue (Fiehler et al., 2002; McGarry et al., 2016a, Rogers, McGarry et al., 2014). The main benefit of computing ADC maps is that ischaemia can be consistently and automatically identified. The ADC values of hyperacute ischaemic tissue typically fall within the range of 0.14 – 0.50 $\mu m^2$/ms compared to 0.74 – 0.84 $\mu m^2$/ms in healthy tissue. These values are independent of field strength and scanner characteristics (Sener, 2001) and so can be used detect ischaemia automatically using thresholding techniques (e.g., Knight, Damion, McGarry et al., 2019; Straka et al., 2010).

### 4.2.2 Images based on $T_2$ relaxation contrast

There are three different types of $T_2$ images that can be acquired for assessment of ischaemic stroke; including $T_2$w images (Section 3.6.3), $T_2$w FLAIR images (Section 3.6.4) and $T_2$ relaxation time maps (Section 3.7.2). The $T_2$ relaxation time is the main contributor to the contrast of $T_2$w images and $T_2$w FLAIR images and the only contributor to the contrast of $T_2$ relaxation time maps. $T_2$ is particularly sensitive to ischaemic stroke, as it changes concomitantly with changes in water content, and therefore changes in $T_2$ reflect both ionic and vasogenic oedema.

Preclinical animal research has shown that the $T_2$ relaxation time changes almost instantaneously after the onset of ischaemia, showing an initial shortening due to the negative *blood oxygen level-dependent* (BOLD) effect, whereby the compensatory increase of oxygen extraction from the blood due to graded CBF reduction, causes higher concentrations of deoxyhaemoglobin (Gröhn et al., 1998). The paramagnetic properties of iron in deoxyhaemoglobin cause faster $T_2$ decay (Gröhn et al., 1998; Thulborn et al., 1982). The $T_2$ shortening is followed by a pseudo-normalisation of $T_2$ as oedema advances, and a subsequent linear increase over time due to the accumulation of water from vasogenic oedema (Gröhn et al., 1998) accompanied by the breakdown of cytoplasmic macromolecules, explained by the *cytotoxic oedema – dissociation model* (CED model)(Knight, McGarry, et al., 2016). Regions with an increase in $T_2$, therefore, reflects either tissue that is at risk (cytotoxic oedema) or that is irreversibly damaged (vasogenic oedema) (Gröhn et al., 1998; Kato et al., 1985). As will be explained in Section 4.4 of this Chapter, the linear increase of $T_2$ relaxation times with time from ischaemia onset, also makes it a suitable parameter for estimating stroke onset time (Jokivarsi et al., 2010; Siemonsen et al., 2009).

### $T_2$ weighted images ($T_2$w)

As described in Chapter 3, Section 3.6.3, $T_2$w images are acquired using a spin-echo pulse sequence, with a relatively long TE and the $T_2$ relaxation time is the predominant contributor to the signal. Visually, $T_2$w images are insensitive to early ischaemic changes, and changes caused by stroke may not be visible for many hours after onset. For example, the $T_2$w scan in Figure 4.3 is of a patient who was scanned seven hours after symptom onset. This patient had a confirmed ischaemic stroke (visible in the DWI and ADC images of the same patient in Figures 4.1 and 4.2 respectively and Figure 4.9-part C), but there are no visible changes in the corresponding region on the $T_2$w image (Figure 4.3).

Figure 4.3 Example of a $T_2$ weighted image from an acute ischaemic stroke patient.

As will be seen in Chapter 8, the insensitivity of $T_2$w images to early ischaemia is useful for segmenting ADC defined ischaemic regions so that ischaemic grey and white matter can be studied separately. Additionally, Knight, Damion, McGarry et al. (2019) have recently shown that the intensity of $T_2$w images is useful for estimating pre-ischaemic $T_2$ relaxation time values, which, as will become apparent throughout the course of this thesis, is an important component of MRI based methods for stroke timing. Eventually, in much later hours or days after onset,

hyperintensities on $T_2$w images reveal regions with long $T_2$ due to increased water content and therefore show regions affected by vasogenic oedema (Figure 4.9-part C). Typically, the clinical purpose of $T_2$w images is to identify and determine the extent of irreversibly damaged tissue in the days following stroke onset (Burgess & Kidwell, 2011).

### $T_2$ weighted FLAIR ($T_2$w FLAIR)

An example of a $T_2$w FLAIR image, from the same patient as Figures 4.1, 4.2 and 4.3 is shown in Figure 4.4. The $T_2$w FLAIR sequence nulls the signal from CSF in order to produce greater anatomical detail and lesion signal intensity than standard $T_2$w images (Hajnal et al., 1992). This is evident by comparing the FLAIR and $T_2$w images in Figure 4.9-part C. $T_2$w FLAIR is, therefore, the preferred $T_2$w sequence for imaging stroke patients. $T_2$w FLAIR image hyperintensities are commonly considered to reveal irreversibly damaged tissue due to increased water content caused by ionic oedema (subtle hyperintensities) and vasogenic oedema (clear hyperintensities) (Thomalla et al., 2011). As will be introduced in Section 4.4.2 of this Chapter, $T_2$w FLAIR images can be assessed visually alongside DWI images to identify patients that may be within the 4.5 hour thrombolysis treatment window (Thomalla et al., 2011).

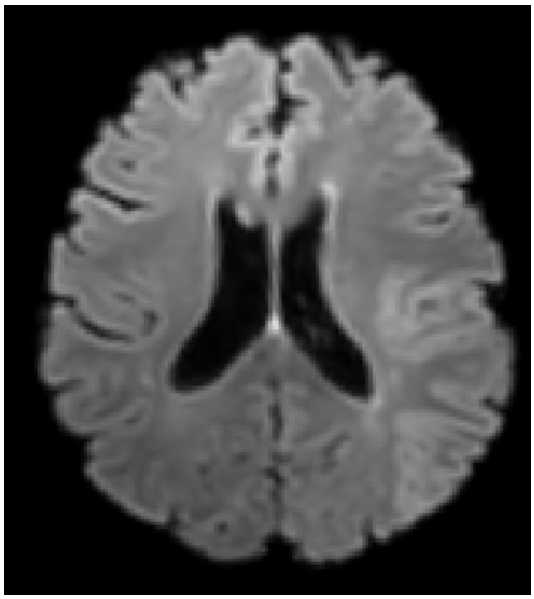

Figure 4.4 Example of a $T_2$ weighted FLAIR image from an acute ischaemic stroke patient.

### $T_2$ relaxation time parametric maps

As discussed in Chapter 3, Section 3.7.2, $T_2$ relaxometry maps are not the same as $T_2$w images. Figure 4.5 is an example of a $T_2$ map from the same ischaemic stroke patient in Figures 4.1, 4.2, 4.3 and 4.4. $T_2$ relaxation time maps are parametric, and so voxels in a $T_2$ map represent $T_2$ relaxation times, independent of proton-density and $T_1$ relaxation (Deoni, 2010). Due to the small dynamic range of $T_2$ relaxation times across the brain (Wansapura et al., 1999), the changes in $T_2$ are not generally visible on standard $T_2$ maps in the early hours of ischaemia (see Figure 4.9-parts A, B and C) (Rogers, McGarry et al. 2014). Therefore, to detect these early changes, the ischaemic region must first be identified with a diffusion-based image (i.e., DWI or ADC). $T_2$ relaxation time maps are not currently used in clinical settings; however, all scanner vendors can produce these automatically at no time cost if a multi-echo $T_2$ sequence is used.

Figure 4.5 Example of a $T_2$ relaxation time map from an acute ischaemic stroke patient.

### 4.2.3 Images based on $T_1$ relaxation contrast

The $T_1$ relaxation time is the main contributor to the contrast of $T_1$w images and the only contributor to the contrast of $T_1$ relaxation time maps. Preclinical studies have shown $T_1$ relaxation times increase within minutes of ischaemia onset (Calamante et al., 1999; Kettunen et al., 2000) due to factors such as compromised CBF (Kettunen et al., 2000), water accumulation (Barbier et al., 2005; Kato et al., 1985) and temperature drop (Kauppinen, 2014). $T_1$ shows a two-phase response to ischaemia which involves a rapid increase followed by a steadier increase over time (Calamante et al., 1999; Kettunen et al., 2000).

#### $T_1$ relaxation time parametric maps

As with $T_2$ relaxometry maps, changes in $T_1$ relaxation times in the early hours of ischaemia are not visible on relaxometry maps (Figure 4.6), and so ischaemic regions must first be identified with a diffusion-based image (DWI or ADC). $T_1$ relaxometry maps are not currently used in the assessment of acute ischaemic stroke, but as will be discussed in Chapter 5, preclinical studies suggest the $T_1$ relaxation times may be informative of stroke onset time and tissue status (Kauppinen, 2014; McGarry et al., 2016a; Rogers, McGarry et al., 2014).

In this thesis, $T_1$ relaxation time maps were computed in the preclinical study in Chapter 5 but were not acquired in the patient studies in Chapter 7 and Chapter 8, due to previous difficulties accurately computing $T_1$ maps from patient scans (McGarry, 2015). Figure 4.6 is an example of a $T_1$ map computed from $T_1$w images acquired at multiple flip angles, from an ischaemic stroke patient scanned five hours after symptom onset (McGarry, 2015).

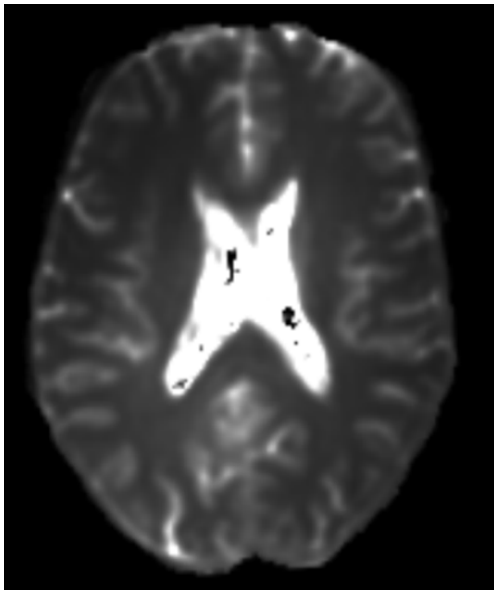

Figure 4.7 Example of a $T_1$ relaxation time map from an acute ischaemic stroke patient.

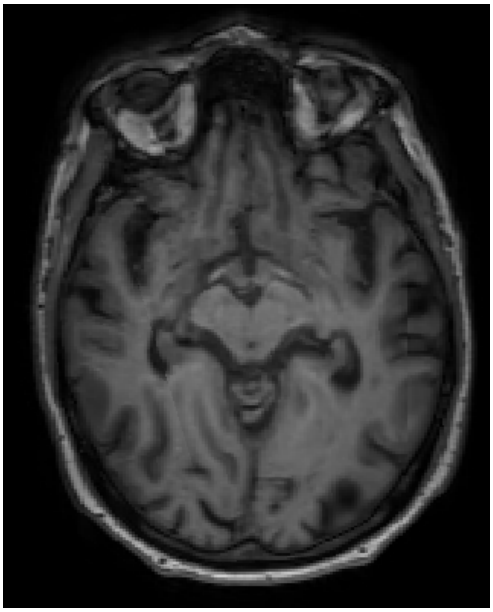

Figure 4.6 Example of a $T_1$ weighted image from an acute ischaemic stroke patient.

### $T_1$ weighted images ($T_1$w)

An example of a $T_1$w image is shown in Figure 4.7. Ischaemic tissue is typically isointense on $T_1$w images within the first six hours of ischaemia onset (e.g., Figure 4.9-parts A, B and C) but will become visible as hypointensities (e.g., Figure 4.9-part D) within sixteen hours due to the signal loss caused by the long $T_1$ relaxation of the accumulated fluid (i.e., vasogenic oedema) (Allen et al., 2012). Therefore, $T_1$w images are commonly considered not to be useful in the assessment of hyperacute ischaemic stroke (Wardlaw et al., 2013). However, isotropic volumetric 3D $T_1$w images are recommended for research purposes as sequences such as MPRAGE (magnetisation-prepared rapid gradient-echo) (Mugler & Brookeman, 1991) produce images with clear anatomical distinctions (e.g., Figure 4.8), that can be used to co-register other images to and determine precise locations of interest (Wardlaw et al., 2013).

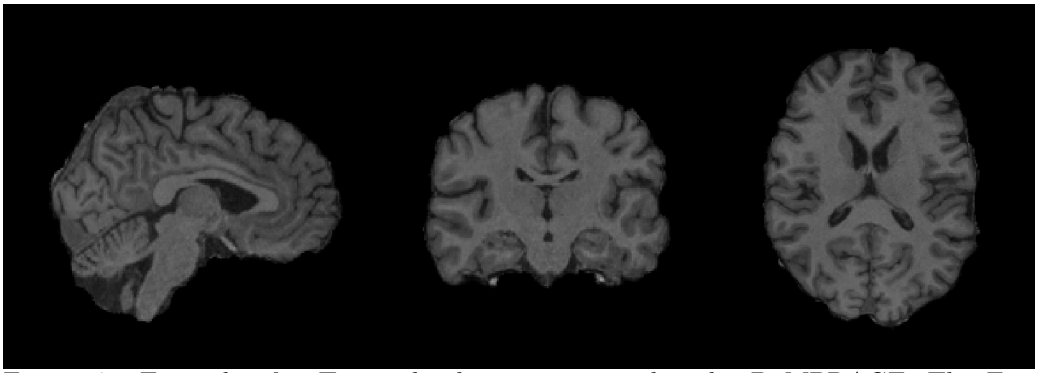

Figure 4.8 Example of a $T_1$ weighted image acquired with 3D MPRAGE. The Figure illustrates the great anatomical detail that can be acquired with a $T_1$ weighted sequence.

## 4.3 Summary of the relationships between pathophysiological and MR changes during acute ischaemic stroke

Figure 4.9 provides an illustrative summary of the relationship between different stages of oedema in the ischaemic brain and how they appear on MR images. This Figure and the following summary are intended as a rough guide to the relationships between changes in different MR signals and the pathophysiological changes in the ischaemic brain. It must be noted that there are no definitive time points for each specific stage of oedema, as the rate of development is a highly heterogeneous process which is specific to each patient. Therefore each stage, marked by different coloured boxes, is a rough indication of what the different stages oedema may look like and the approximate time frame in which the changes on the different images become visible. Each coloured box contains a set of MR images from a different ischaemic stroke patient at different times from symptom onset.

**A. DWI and ADC reveal cytotoxic oedema:** within minutes of stroke onset, ischaemic brain tissue undergoes cytotoxic oedema. The cellular swelling associated with cytotoxic oedema, means fluid in the tissue becomes less diffuse than normal. Thus when a diffusion-weighted sequence is used, the MR signal from the ischaemic tissue is high, and so appears bright on diffusion-weighted images. ADC values of ischaemic tissue are lower than normal brain tissue, and so ischaemic regions undergoing cytotoxic oedema are displayed as dark in ADC maps. Because there is not yet an increase in tissue water content, there are no visible changes in corresponding $T_2$w images, $T_2$w FLAIR images, $T_2$ relaxation time maps or $T_1$w images. The images in section **A.** are from a 49-year-old male patient with lacunar stroke (LACS), who was not thrombolysed and was scanned two hours and 55 minutes after symptom onset.

**B. Over subsequent hours, ionic oedema develops**: at this stage, water is still less diffuse than normal, but there begins to be a subtle increase in total tissue water content due to ionic oedema. As fluids have long $T_2$ relaxation times, these regions have a stronger signal, and therefore start to become subtly visible on $T_2$w images and $T_2$ relaxometry maps. These changes are not yet visible on $T_1$w images. The images in this section are from a 73-year-old male ischaemic stroke patient scanned five hours and 34 minutes after symptom onset, with partial anterior circulation stroke (PACS), who had been thrombolysed prior to the MRI scan.

**C. After approximately 4.5 hours, vasogenic oedema develops:** the blood-brain barrier breaks down, causing an increase in tissue water content. 4.5 hours is given in brackets as this is a rough estimate, and it is difficult to give precise timings. In the scans of the patient shown, the increase in water content is not visible on the $T_2$w images, but is distinctly visible on the FLAIR image, demonstrating why $T_2$w FLAIR images are prefered over standard $T_2$w images when examining acute ischaemic stroke patients. The changes are also not visible on the $T_2$ map or $T_1$w images. The images in this section are from 56-year-old male ischaemic stroke patient with PACS, scanned six hours and 50 minutes after symptom onset and had received thrombolysis before MRI.

**D. Within days and weeks following ischaemia onset a fluid-filled cavity remains:** this is visible on diffusion-weighted images as hyperintensities due to $T_2$ shine through. In contrast to the acute stages, the affected region is also hyperintense on the ADC image, reflecting the high diffusivity of water. The affected region is also visible as hyperintense on $T_2$w images and $T_2$ maps. A FLAIR scan was not available for this patient. The images in this section are from a male acute ischaemic stroke patient (age not recorded) with LACS, scanned three days after symptom onset and who had received thrombolysis as part of their treatment.

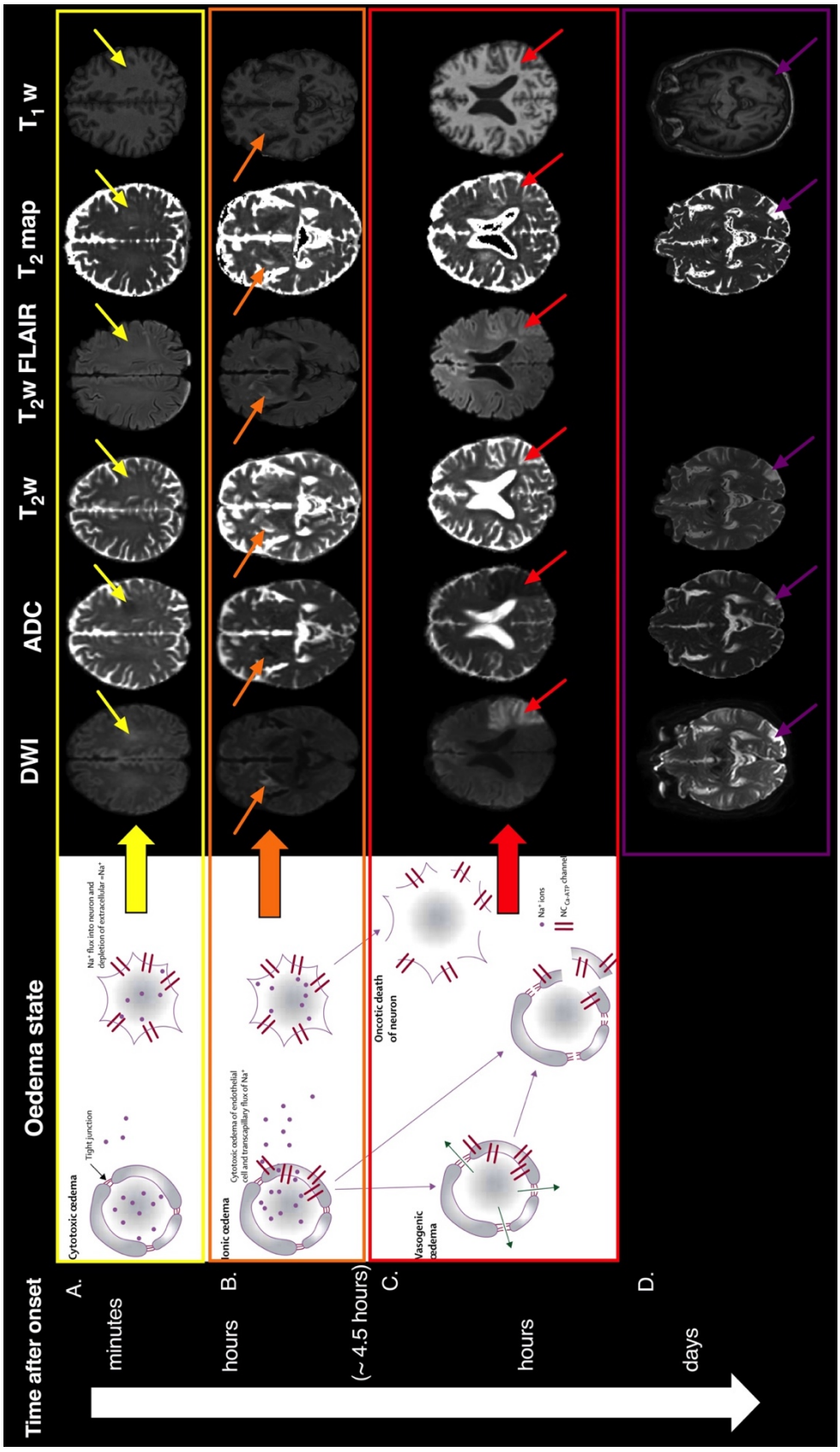


Figure 4.9 Summary of oedema progression during ischaemia in relation to MR images. The oedema section is the same figure shown in Chapter 2 and is reproduced from Simard et al. (2007) with permissions. 4.5 hours is written in brackets as it is an approximation as it is difficult to give precise timings of the visibility and onset of vasogenic oedema.

## 4.4 Estimating stroke onset time with MRI

The purpose of this Section is to contextualise the research Chapters of this thesis. The Section begins by introducing the supervised machine learning approaches that are used followed by an outline of the qualitative and quantitative MRI (qMRI) based stroke timing methods that have been proposed in the stroke imaging literature and the relevant studies. Next, a schematic illustration and further description of the two main quantitative approaches are provided to show how they relate to each other. This Section ends with an explanation of the rationale for the methods studied in this thesis, and recognition of potential alternative methods for applying qMRI to the problem of unknown onset time.

### 4.4.1 Supervised machine learning and stroke timing

The study of stroke onset time estimation using qMRI has predominantly taken a *supervised machine learning* approach, which is also adopted in the research Chapters of this thesis. Supervised machine learning involves developing algorithms that computers can use to extract patterns from existing data to generate predictive models that can be applied to new data (Kelleher & Tierney, 2018). Stroke timing studies, therefore, involve collecting MRI data from acute ischaemic stroke patients with a known time of symptom onset in order to develop a predictive model that estimates whether a patient with unknown onset time is within the rtPA treatment window.

Within the stroke timing literature, there are two main approaches to estimating stroke onset time using supervised machine learning. The method that has mainly been adopted in clinical research studies is to regard unknown onset time as a binary classification problem (e.g. Madai et al., 2016; McGarry et al., 2016b; Song et al., 2012; Thomalla et al., 2009; 2011). The binary approach aims to predict whether the patient is in one of two classes, either *within* or *beyond* the 4.5 hour

rtPA treatment window. This binary approach has been adopted for both visual (Thomalla et al., 2009; 2011) and quantitative based MRI methods (e.g. Madai et al., 2016; McGarry et al., 2016b; Song et al., 2012) which are discussed in Sections 4.4.2 and 4.4.3 of this Chapter respectively (note, the visual based binary method is not a machine learning technique as no computation is involved, but the same principles apply). The overall ability of binary approaches is typically assessed by calculating levels of specificity and sensitivity (described in Appendix A). A binary classification model with high specificity is essential to identify patients that are beyond the treatment window and would, therefore be at greater risk of harm by thrombolysis. High sensitivity is also imperative to identify as many patients as possible that could be eligible for thrombolytic therapy.

The second supervised machine learning approach, which has mainly been adopted in the preclinical research context, has involved developing predictive regression models that could estimate the time in minutes since ischaemia onset by inserting a measured qMRI parameter into the predictive model (Jokivarsi et al., 2010; McGarry et al., 2016a; Rogers, McGarry, et al., 2014). The overall ability of regression models for estimating stroke onset time can be evaluated by comparing the strength of the relationship between the qMRI parameter and time from ischaemia onset ($R^2$) and calculating the root mean square error (RMSE), which indicates the uncertainty of onset time estimations in ± minutes.

Both the binary and regression-based approaches rely on the observations that the MR signals in ischaemic tissue increase in a time-dependent manner (e.g., Jokivarsi et al., 2010; Madai et al., 2016; Rogers, McGarry & McGarry, 2014). For example, the $T_2$ relaxation time, which is the main contributor to signal in $T_2$w images, and a measurable parameter in $T_2$ maps has been shown to increase linearly with time from ischaemia onset in rats (e.g., Gröhn et al., 1998; Jokivarsi et al., 2010). In principle, a patient would be eligible to be considered for IV rtPA if they are classified as within the 4.5 hour treatment window, or if the estimated time from stroke onset is less than 270 minutes. Both the binary and regression-based

approaches to estimating stroke onset time are studied in the research Chapters of this thesis.

### 4.4.2 The visual based DWI/FLAIR mismatch method for stroke timing

Clinical studies investigating MRI for timing the ischaemic stroke have mainly focused on the binary, visual based *DWI/FLAIR mismatch* approach (Thomalla et al., 2009; 2011). The DWI/FLAIR mismatch is in keeping with the traditional approach to MRI, where the radiographer or clinician visually assesses the images and is not a machine learning approach as it does not involve computer based predictive modelling. According to the DWI/FLAIR mismatch approach, a patient is classified as within the 4.5 hour treatment window if they have a *DWI/FLAIR mismatch*, where ischaemic tissue is visible on diffusion weighted images (DWI +) but is isointense on $T_2$w FLAIR images (FLAIR -) (Thomalla et al., 2011). A patient is classified as beyond the treatment window if they have a *DWI/FLAIR match*, where ischaemic tissue is hyperintense on both DWI and FLAIR scans (DWI + and FLAIR +) (Thomalla et al., 2009, 2011). Examples of match and mismatch cases are shown in Figure 4.10.

The mismatch indicates tissue has undergone cytotoxic oedema due to hyperintense DWI but may still be salvageable because it has not evolved into vasogenic oedema, due to isointense FLAIR signal in the same region (Thomalla et al., 2009, 2011). The match indicates that the ischaemic tissue that is hyperintense on the DWI scan has undergone irreversible damage, because it is also hyperintense on the $T_2$w FLAIR scan (Thomalla et al., 2009, 2011). The reflection of the mismatch criteria for the indication of tissue salvageability and short ischaemia duration is supported by histological studies (Baird & Warach, 1998).

The DWI/FLAIR mismatch approach to stroke timing is appealing for clinical settings because of its perceived simplicity. The method involves viewing the images and does not require post-processing or mathematical calculations (Wouters et al., 2014). The DWI/FLAIR mismatch has also consistently been shown to have high specificity, and so successfully identifies the majority of patients that are beyond the treatment window (Etherton et al., 2018; Wouters et al., 2014). Recently, the WAKE-UP trial revealed patients with unknown onset given IV rtPA on the basis of the DWI/FLAIR mismatch showed improved outcome compared to those given placebo (Thomalla et al., 2018). This result suggests that DWI/FLAIR mismatch is a promising method for reducing the problem of unknown onset time (Thomalla et al., 2018).

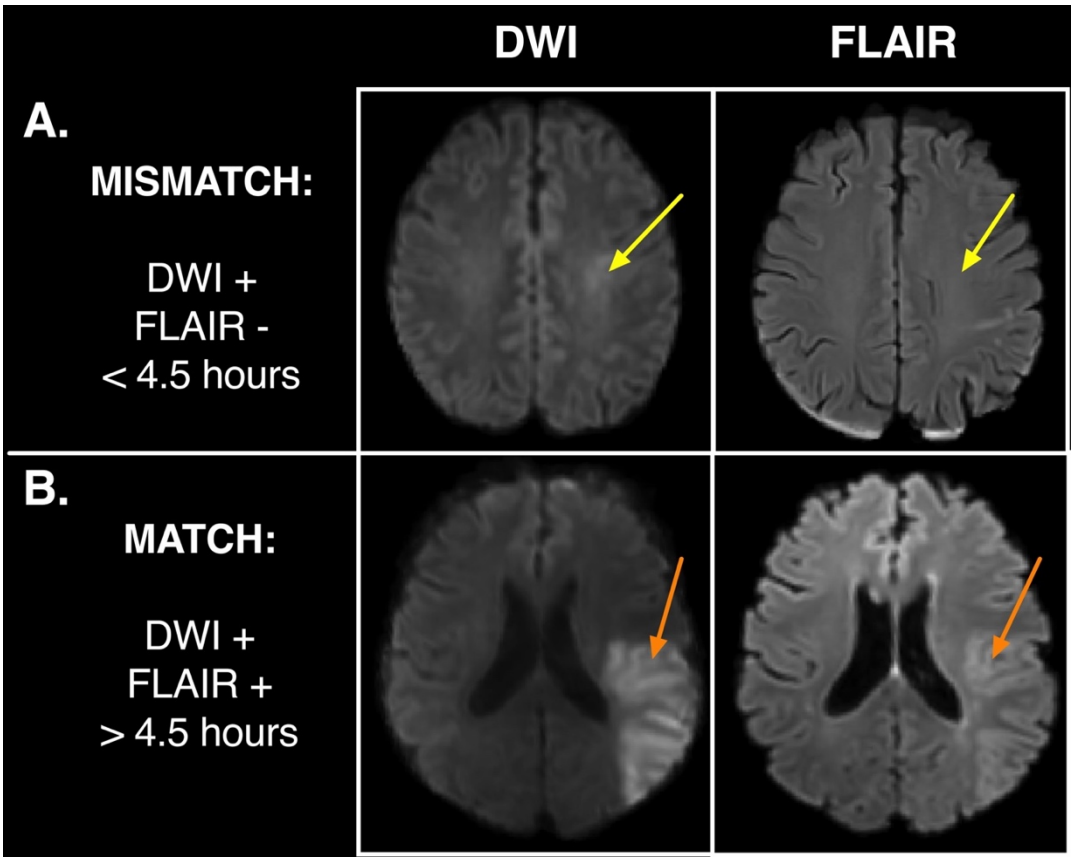


Figure 4.10 The qualitative, visual based DWI/FLAIR mismatch approach to onset time estimation. **A.** The patient is classified as within the 4.5 hour treatment window for IV thrombolysis if they show a DWI/FLAIR mismatch, where ischaemic tissue (indicated by yellow arrows) is visible on the diffusion weighted image (DWI +), but is not visible in the same region on the FLAIR image (FLAIR -). **B.** The patient is classified as beyond the 4.5 hour treatment window for IV thrombolysis if they show a DWI/FLAIR match (where ischaemic tissue (indicated by orange arrows) is visible on DWI (DWI +) and FLAIR (FLAIR +).

Although encouraging, the results of the WAKE-UP trial are not necessarily translatable to all clinical settings and presentations of stroke (Bunney & Ireland, 2019). The WAKE-UP trial was conducted in specialised and experienced stroke centres (with readily available diagnostic pathways and MRI) and only 37% of the patients screened for the WAKE-UP trial met the intervention criteria (Bunney & Ireland, 2019). Many patients excluded from the study did not have visible hyperintensities on DWI images, suggesting that they had had a transient ischaemic attack or stroke mimic (Bunney & Ireland, 2019). Smaller hospitals with less experience and equipment may struggle to effectively screen these more difficult patients (Bunney & Ireland, 2019).

Another predominant disadvantage of the DWI/FLAIR mismatch is that it has repeatedly been found to have low sensitivity, causing patients within the treatment window to be missed (Etherton et al., 2018; Wouters et al., 2014). A meta-analysis of DWI/FLAIR mismatch studies revealed a combined sensitivity of 0.62 (min: 0.38, max: 0.62) and specificity of 0.81 (min: 0.78, max: 0.89) for identifying patients scanned within 4.5 hours of symptom onset (Wouters et al., 2014). Low sensitivity is likely due to the high inter-rater and intra-rater variability (Wouters et al., 2014) and that many patients within 4.5 hours of symptom onset have visible FLAIR lesions (Emeriau et al., 2013). This high variability suggests that the DWI/FLAIR mismatch is not as simple as it appears on the outset.

Attempts to improve inter-rater agreement have been made. For example, one study colour coded FLAIR images to make subtle FLAIR hyperintensities more obvious, which improved inter-rater agreement (Kim et al., 2014). Although this finding suggests colour coding FLAIR images could improve the ability of the DWI/FLAIR mismatch to correctly classify patients, it also highlights the difficulty with relying on the visual assessment of MR images for onset time estimation. If interpretation can easily be influenced by how the image is perceived, then DWI/FLAIR mismatch cannot be considered a reliable method for which to base treatment decisions on. This point is especially important as the contrast and

quality of the images, and the experience of the rater in detecting changes on MR images, will vary between hospitals (Cheng et al., 2013; Galvonic et al., 2014).

### 4.4.3 Quantitative MRI based methods for stroke onset time estimation

The quantitative based approach for stroke onset time estimation is the main approach investigated in this thesis and for which machine learning methods are applicable. As discussed in Chapter 3 (Section 3.7) there are two main approaches in the stroke timing literature that come under the category of qMRI. The first is the *quantitative analysis of the signal intensities represented in weighted images* (Section 3.7.1) and the second, is *the parametric approach to qMRI* (Section 3.7.2) which involves mathematically parameterising MR signal intensities, before measuring them and transforming them into parametric images.

For both quantitative approaches, stroke timing involves quantifying the change in image intensities (i.e., signals present in weighted images, or the relaxation times of voxels in a parametric image, see Section 3.8) caused by ischaemia, by comparing intensities in the ischaemic region with intensities of the homologous tissue in the contralateral hemisphere. This comparison can be achieved by calculating the difference in image intensities (e.g., Siemonsen et al., 2009), calculating the ischaemic vs non-ischaemic image intensity ratio (e.g., Madai et al., 2016; McGarry et al., 2016b; Song et al., 2012) or computing the absolute percentage difference (e.g., McGarry et al., 2016a; Rogers, McGarry et al., 2014). As will be discussed in Chapter 8, the purpose of the contralateral hemisphere is to provide an approximation of the pre-ischaemic image intensity values. Both quantitative approaches are based on the finding that image intensities in ischaemic regions increase linearly with time from ischaemia onset (e.g., Jokivarsi et al., 2010; Cheng et al., 2013; Song et al., 2012). The goal of the binary approach to onset time estimation using qMRI is to identify a specific image intensity ratio threshold that

distinguishes between patients that are within and beyond the 4.5 hour rtPA treatment window. The regression based approach involves measuring the image intensity ratio at a given time point and inserting it into a regression equation in order to work back and estimate how long ago the stroke started in minutes.

### Estimating stroke onset time by quantifying signal intensities represented in weighted images

In an initial attempt to increase the sensitivity associated with the DWI/FLAIR mismatch and avoid low inter-rater and low intra-rater agreement altogether, the quantitative analysis of the signal intensities represented in the DWI or FLAIR images was proposed as a potentially more accurate approach to estimating onset time (Petkova et al., 2010; Song et al., 2012). However clinical studies have shown varying results, no consensus of the threshold that should be used, and little to no improvement on sensitivity compared to the visual DWI/FLAIR mismatch (e.g., Galinovic et al., 2014). For example, Song et al. (2012) reported a sensitivity of 0.78 and specificity of 0.67 for distinguishing between patients scanned before and after 4.5 hours from symptom onset using a FLAIR image intensity ratio. Petkova et al. (2010) reported the highest overall ability of the FLAIR image intensity ratio, but for the old treatment window of three hours, with sensitivity and specificity levels of 0.90 and 0.97 respectively. Madai et al. (2016), also reported high sensitivity and specificity levels for the 4.5 hour treatment window, with of 0.78 specificity and 0.75 sensitivity for DWI and 0.79 sensitivity and 0.89 specificity for FLAIR.

Other studies found less promising results for quantification of DWI and FLAIR image intensities. For example, Cheng et al. (2013) reported a moderate linear relationship of the FLAIR image intensity ratio with time from symptom onset and identified a threshold that distinguished between patients scanned before and after 4.5 hours from symptom onset with 0.85 specificity and 0.47 sensitivity and with no overall improvement on the ability of the visual DWI/FLAIR mismatch where

specificity was 0.78, and sensitivity was 0.58. Ebinger et al. (2010) did not find a relationship between FLAIR image intensity ratios and time from symptom onset and so could not identify a threshold to distinguish between patients within and beyond the thrombolysis treatment widow. In another attempt to improve the visual based DWI/FLAIR mismatch method, one study adopted a semi-quantitative method which involved quantitative measurements of FLAIR image intensities to support visual assessments (Galinovic et al., 2014). The semi-quantitative measure did not improve inter-rater agreement indicating that a quantitative analysis of $T_2$w FLAIR MR signals specifically would not be useful for estimating stroke onset time (Galvonic et al., 2014). This indication is supported by the results of Chapter 5 and Chapter 7 of this thesis.

### Estimating stroke onset time with the parametric approach to qMRI

At the start of this PhD (2015), only one clinical paper, by Siemonsen et al. (2009) had recognised the potential application of the parametric approach to qMRI for timing the ischaemic stroke as an alternative to the quantitative analysis of the signal intensities represented in weighted images. Much of the work on the parametric approach to qMRI for stroke timing was conducted in preclinical settings, dating back to the 1980s (e.g. Kato et al., 1985).

In their study of acute ischaemic stroke patients, Siemonsen et al. (2009) reported high accuracy of the $T_2$ relaxation time for identifying patients within the previous thrombolysis treatment window of three hours but did not test for the 4.5 hour window. In 2019, Knight, Damion and McGarry et al. (2019) reported higher accuracy of the $T_2$ relaxation time compared to $T_2$w image intensities for identifying stroke patients within the 4.5 hour treatment window, but sensitivity and specificity were not reported. The primary focus of the Knight, Damion and McGarry et al. (2019) paper was to demonstrate a potentially clinically applicable method for identifying elevated $T_2$ relaxation times in hyperacute ischaemic stroke

patients and was a side project involving the patient data analysed in this thesis. Therefore, the ability of $T_2$ based parameters for onset time estimation was not further investigated, as this analysis was reserved for Chapter 7 of this thesis (and its future publication).

The research adopting the regression based approach to stroke timing was mainly carried out in rat models of ischaemia, using hemispheric differences in qMRI parameters obtained from weighted and parametric images as well as distributional information as predictive parameters (discussed further in Chapter 5 and Chapter 8) (Jokivarsi et al., 2010; McGarry et al. 2016a; Rogers, McGarry et al., 2014). For example, in rat models of ischaemia, Jokivarsi et al. (2010) identified predictive linear regression models for the hemispheric difference in the $T_2$ relaxation time that could be used to estimate time from ischaemia onset in minutes. Further studies in rat models of ischaemia showed stronger relationships of relaxation time-based parameters with time from stroke onset, compared to image intensity ratios from weighted images (McGarry et al., 2016a; Rogers, McGarry et al., 2014). A relationship between hemispheric differences in $T_2$ and time from symptom onset had been reported in patients (Siemonsen et al., 2009) but a regression model was not used to assess its predictive ability. Since then, Duchaussoy et al. (2019) also reported a linear relationship between $T_2$ relaxation times and time from symptom onset in patients, but with no evaluation on performance.

### 4.4.4 Summary of qMRI based stroke timing methods

In the following summary of qMRI approaches to estimating stroke onset time, the reader is referred to the schematic illustration in Figure 4.11.

**Part A:** qMRI based approaches to timing the ischaemic stroke involves quantifying the difference in image intensities (i.e., the signal from weighted images, or the relaxation time from parametric maps) between the ischaemic region (shown as by the red region) and the homologous region in the non-ischaemic hemisphere (shown by the yellow region). The most common approach is to calculate the image intensity ratio, which is the mean voxel values of the ischaemic region, divided by the mean value in the non-ischaemic region.

**Part B:** The main approaches to onset time estimation are binary and regression based. Both are based on the underlying assumption that image intensity ratios of qMRI parameters increase linearly with time from stroke onset, which is illustrated by the dark blue trendline. This assumption has been based on extensive preclinical research, that the relaxation times which influence the signal intensities associated with weighted images, and are measured with the parametric approach to qMRI, increase linearly with time from onset (e.g., Calamante et al., 1999; Gröhn et al., 1998; Jokivarsi et al., 2010; Kettunen et al., 2000; Rogers, McGarry et al., 2014)

**Part C:** The binary approach involves identifying an optimal image intensity ratio that distinguishes between patients that are within and beyond the 4.5 hour treatment window. Patients whose image intensity ratio falls below the identified cut-off that corresponds to 4.5 hours, would be within the treatment window (indicated by shaded blue area). Patient's whose image intensity ratio exceeds the optimal ratio would be regarded as beyond the treatment window.

**Part D:** The regression based approach involves by measuring the image intensity ratio at a given time point and inserting it into a regression equation in order to work back and estimate how long ago the stroke started in minutes.

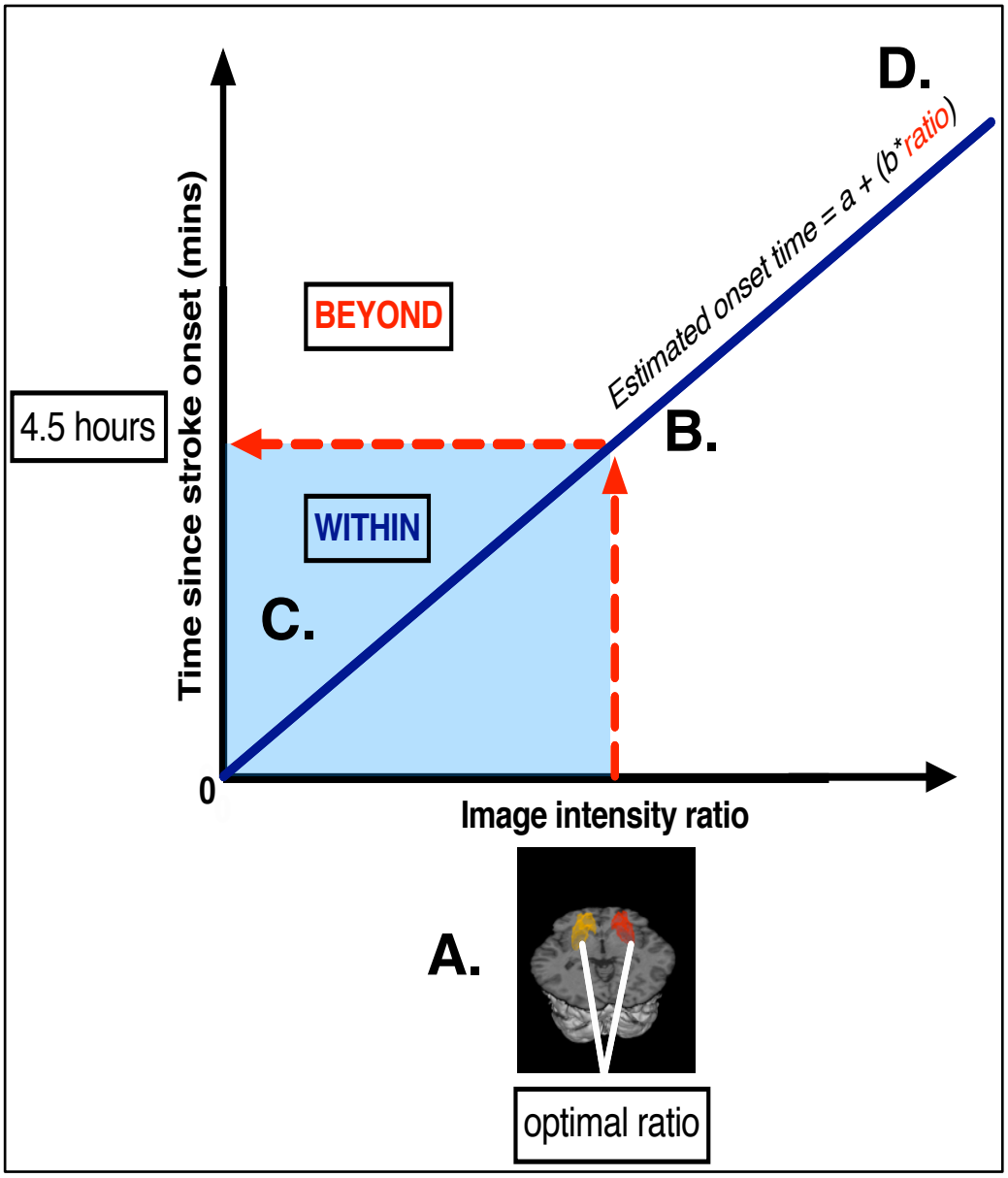


Figure 4.11 Schematic illustration of the binary and regression-based qMRI methods for estimating stroke onset time. Based on the assumption that the image intensity ratio has a linear relationship with time from stroke onset (**D.**), stroke onset time can be estimated by identifying an optimal image intensity ratio cut-off (**A.**) that distinguishes between scans performed before and after 4.5 hours from onset. A ratio below this threshold would indicate the patient is within the treatment window (**C.**). Alternatively, by measuring the image intensity ratio at a given time point, it can be inserted into the regression equation (**D.**) to work back and estimate how long ago the stroke started in minutes.

## 4.5 The rationale for the stroke timing methods studied in this thesis

The studies in this thesis focus primarily on *quantitative* approaches to onset time estimation and specifically establishing a linear relationship with qMRI parameters and time from ischaemia onset. The traditional visual based qMRI approach of the DWI/FLAIR mismatch was also studied as, despite its limitations (addressed Section 4.4.2), it is an active area of stroke timing research (e.g., Thomalla et al., 2018). The main motivation for studying the potential utility of *linear* relationships of qMRI parameters with time from stroke onset time was to keep in line with existing work and publications. At the start of the PhD, much of the previous preclinical and clinical stroke timing studies had focused on linear models. It had taken a long time to get the linear relationships of qMRI parameters that were observed in preclinical studies (e.g., Gröhn et al., 1998; Jokivarsi et al., 2010) to be investigated in clinical settings (e.g., Siemonsen et al., 2009; Song et al., 2012). It was therefore considered appropriate to continue this investigation in this thesis.

A further motivation for studying linear relationships was the simplicity of a linear model, which, in a clinical setting, is important. If a linear model for estimating onset time works well enough to successfully identify patients potentially eligible for rtPA, it would be unnecessary to overcomplicate the method by pursuing more complex models. Additionally, when applying machine learning to support clinical decisions, there is the issue of "*the black box*", where clinicians may be reluctant to incorporate a predictive model into their clinical practice if they do not know how it works (Zihni, Madai et al., 2020). Linear models and binary classification problems are familiar territories for researchers and clinicians alike, and therefore linear regression based models and binary classifiers may be more readily accepted into clinical practice. Indeed, a recent study by Zihni, Madai et al. (2020) showed traditional regression based machine learning methods performed comparably to more complex and advanced machine learning methods (tree boosting and multilayer perceptron) when using clinical parameters to predict stroke outcome. Although this would need to be tested in the context of stroke MRI, it suggests

that despite the limitations of simple models, they may be sufficient for clinical needs.

Despite the above advantages of seeking to establish a linear relationship, it is also recognised that qMRI stroke timing research should not be restricted to fitting linear models, especially as ischaemia is such a complex and heterogeneous disease state. Throughout the course of this PhD, it became evident that there may be more to the relationship of qMRI parameters and time from stroke onset, than a strictly linear one. qMRI studies in rats (Knight, McGarry et al., 2016; Norton et al., 2017), which are discussed in Chapter 8, highlighted the possibility of a non-linear relationship of the $T_2$ relaxation time with time from ischaemia onset. The possibility of a non-linear relationship of qMRI parameters was thus investigated in Chapter 8, by evaluating the predictive ability of polynomial regression models for onset time estimation. This involved including squared and cubed terms of the predictive variables in the original linear models, in order to accommodate non-linear relationships in the data (James et al., 2013).

It is also recognised that there are other machine learning methods that could be utilised in the study of onset time and acute ischaemic stroke. With the rapid advance of artificial intelligence in healthcare, the possibilities of machine learning approaches to support clinical decision making are endless (Zihni, Madai et al., 2020). The potential utility of other machine learning methods in stroke timing research was recognised during the data analysis of Chapter 7, and so Chapter 7 incorporates two additional supervised machine learning methods of analysis that had not previously been applied to qMRI stroke timing data, including logistic regression and precision-recall-gain (Flach & Kull, 2015).

Other approaches that are beyond the scope of this thesis, but would be worth investigating in future, include other supervised machine learning methods such as artificial neural networks and ensemble models such as and tree boosting, which

have been shown to perform better than traditional linear and logistic regression methods in other areas of predictive modelling in stroke related health care (Zihni & Madai et al., 2020). Also, if taking the *tissue clock* approach, rather than the *time-based* approach to reducing the problem of unknown onset time (outlined in Chapter 1), *unsupervised* machine learning techniques, such as principal components analysis or deep learning approaches, may also be informative when applied to qMRI data. This is because unsupervised approaches do not have a target attribute but seek to discover complex patterns in data sets and relationships between them that would otherwise be unknown, but maybe informative (Lundervold & Lundervold, 2019).

# Chapter 5
# Determining stroke onset time using quantitative relaxometric MRI: A study on accuracy, sensitivity and specificity in a rat model of focal permanent cerebral ischaemia

## 5.1 Abstract

Many ischaemic stroke patients are ineligible for thrombolytic therapy due to unknown time of symptom onset. Quantitative MRI (qMRI) has been proposed as a potential surrogate for stroke timing. In this study, rats were subjected to permanent middle cerebral artery occlusion (MCAo), and qMRI parameters were measured at hourly intervals at 4.7T and 9.4T for up to seven hours post MCAo. qMRI parameters included, image intensity ratios from the apparent diffusion coefficient maps (ADC), $T_2$ weighted images ($T_2$w), $T_1$ and $T_2$ relaxation time maps, as well as parameters representing the distribution of high $T_1$ or $T_2$ relaxation times ($f_1$, $f_2$ respectively) and both high $T_1$ and high $T_2$ relaxation times ($V_{overlap}$) within the ADC defined ischaemic region. The $T_2$ image intensity ratio, $f_2$ and $V_{overlap}$ qMRI parameters showed the strongest relationship with time from MCAo. Receiver operating characteristic (ROC) curves and areas under the ROC curves (AUC) showed the $T_2$ image intensity ratio, $f_2$ and $V_{overlap}$ were also the most successful at differentiating between scans performed before and after three hours from ischaemia onset (AUC $>$ 90%). At a specificity of 1, sensitivity was highest for $V_{overlap}$ (0.90) and $f_2$ (0.80). Overall results are promising for the potential use of qMRI indices based on relaxation times for the clinical assessment of stroke onset time.

## 5.2 Introduction

Ischaemic stroke patients are ineligible for thrombolytic treatment if the time of symptom onset is unknown (Powers et al., 2018). Common reasons include lack of a witness, being unaware of symptoms or *wake-up stroke* (Dekker et al., 2017; Thomalla et al., 2017). MRI is sensitive to hydrodynamic changes in brain parenchyma caused by ischaemia (Kauppinen, 2014). A growing body of evidence suggests quantitative data from these changes could be informative of tissue status and stroke onset time and therefore potentially aid decision-making for clinical treatment (e.g., Jokivarsi et al., 2010; Kauppinen, 2014; McGarry et al., 2016a, 2016b). Low sensitivity and ambiguity associated with relying on visual assessment of magnetic resonance (MR) images (e.g., DWI/FLAIR mismatch, Thomalla et al. 2009, 2011) prompted the investigation into the potential utility of quantitative MRI (qMRI) for clinical needs (e.g., Song et al., 2012).

Hemispheric differences in qMRI parameters including the apparent diffusion coefficient (ADC)(Petkova et al., 2010), signal intensities of $T_2$ weighted images ($T_2$w) with and without FLAIR (e.g., Madai et al., 2016; Petkova et al., 2010; Rogers, McGarry et al., 2014; Xu et al., 2014), the $T_1$ relaxation time (McGarry et al., 2016a) and the $T_2$ relaxation time (Jokivarsi et al., 2010; McGarry et al., 2016a; Rogers, McGarry et al., 2014; Siemonsen et al., 2009) have been shown to correlate with time from stroke onset, enabling onset time to be estimated with varying levels of accuracy. The relationships between these qMRI parameters and time from stroke onset are attributed to changes in tissue-water dynamics due to cytotoxic and vasogenic oedema (Chapter 3.2 and Kauppinen, 2014).

The time-dependency of the $T_1$ relaxation time in the ischaemic brain is less well characterised than for the $T_2$ relaxation time (McGarry et al., 2016a). $T_1$ increases gradually over time from stroke onset within regions of decreased diffusion (Calamante et al., 1999; Hoehn-berlarge et al., 1995; Kettunen et al., 2000). Pathophysiological mechanisms thought to underlie this $T_1$ increase are similar to

the increase in the $T_2$ relaxation time, including altered water dynamics and content in ischaemic tissue (Barbier et al., 2005; Kato et al., 1985; Kauppinen, 2014). The $T_1$ relaxation time is additionally influenced by the cerebral blood flow (CBF) and cerebral blood volume (CBV) (Calamante et al., 1999; Kettunen et al., 2000), temperature (Youl et al., 1992), pH (Kettunen et al., 2002) and tissue oxygen tension (Calamante et al., 1999). Thus, by combining data from the time courses of $T_1$ and $T_2$ in the ADC defined ischaemic region, one would expect to obtain a fuller picture of ischaemic pathology in brain tissue, which may aid in the estimation of stroke onset time and assessment of tissue viability (McGarry et al., 2016a).

Previous stroke timing studies in rat focal ischaemia also suggest that the distribution of relaxation times within the ischaemic region may serve as a proxy for stroke onset time (McGarry et al., 2016a, 2017; Rogers, McGarry et al., 2014). For example, the spatial distribution of elevated $T_2$ relaxation times (Rogers, McGarry et al., 2014) and volume of tissue with high $T_1$ or $T_2$ relaxation times (McGarry et al. 2016a) was initially smaller than the volume of total ischaemia delineated by ischaemic ADC but increased with ischaemia duration (McGarry et al., 2016a; Rogers, McGarry et al. 2014). Figure 5.1, reproduced and adapted from McGarry et al. (2016a), illustrates these changes and demonstrates how the heterogeneity of relaxation times within the ischaemic region, decreases over time. Based on these observations, qMRI surrogates for stroke timing were proposed, including $f_1$, $f_2$ (Knight, McGarry, et al., 2016a, 2017) and $V_{overlap}$ (McGarry et al., 2016a, 2017). $f_1$ and $f_2$ are the volumes of tissue with high $T_1$ or $T_2$ relaxation times as a percentage of total ischaemia volume, respectively and $V_{overlap}$ is the volume with both high $T_1$ and $T_2$ normalised by the whole-brain volume (McGarry et al., 2016a, 2017). Time from ischaemia onset time could be estimated in rats with uncertainties of ± 25 minutes, ± 34 minutes, ± 47 minutes using $V_{overlap}$, $f_2$ and $f_1$, respectively (McGarry et al., 2016a).

From a clinical perspective, a method for estimating stroke onset time must have high specificity to minimise potential adverse events of thrombolysis. High sensitivity is also essential to stratify as many patients as possible for thrombolysis. The abilities of the change in the ADC, $T_2$w, $T_1$ relaxation and $T_2$ relaxation times and the $f_1$, $f_2$ and $V_{overlap}$ parameters in estimating stroke onset time have been reported in preclinical (e.g., Jokivarsi et al., 2010; McGarry et al., 2016a, 2017; Xu et al., 2014) and clinical settings (e.g., Madai et al., 2016; Siemonsen et al., 2009) but performance of these parameters have not been compared. The objective of this study (McGarry et al.,2016b) was to compare the overall ability of these qMRI parameters as stroke timers in a defined rat model of ischaemic stroke.

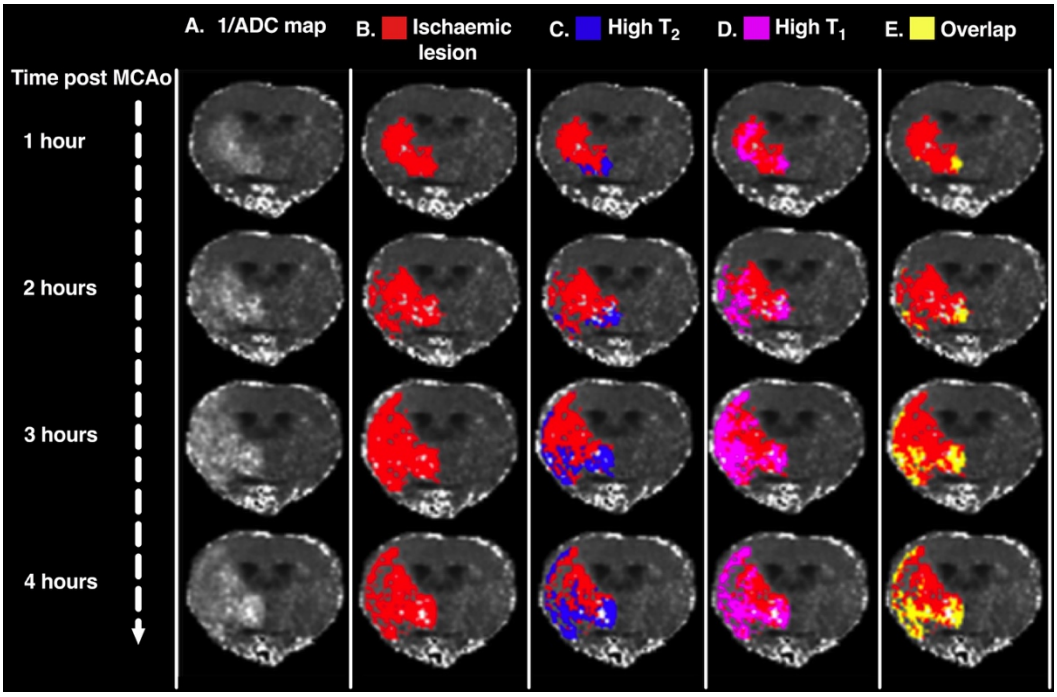


Figure 5.1 The spatial distribution of elevated relaxation times within the 1/ADC defined ischaemic lesion, at hourly intervals post MCAo. Bright voxels indicate decreased ADC values. Images in the Y direction are from the same rat at different scan times. The image remains the same from left to right. Images are a central slice from 1/ADC maps from a representative rat, overlaid with colour coded regions depicting regions with high relaxation times. Red regions indicate reduced ADC and therefore ischaemic tissue. Columns: **A.** 1/ADC map where hyperintense regions indicate ischaemia. **B.** Red voxels are the 1/ADC defined ischaemic regions of interest. **C.** Blue voxels represent reduced ADC and high $T_2$ relaxation times. **D.** Pink voxels represent reduced ADC and high $T_1$ relaxation times. **E.** Yellow voxels represent voxels with reduced ADC and voxels with both high $T_1$ and $T_2$ relaxation times. Relaxation times were identified as high if they exceeded the median relaxation time of the non-ischaemic VOI by more than one half-width at half maximum (see McGarry et al., 2016a). Figure reproduced and adapted from McGarry et al. (2016a).

## 5.3 Methods

The multi-parametric MRI images from previous rat stroke studies using 4.7T (Jokivarsi et al., 2010; Rogers, McGarry et al., 2014) and 9.4T MRI systems (Knight, McGarry et al., 2016; McGarry et al., 2016a, 2017) were combined and used in the data analyses of this study (McGarry et al., 2016b). Both studies were conducted on separate occasions at the A.I. Virtanen Institute for Molecular Sciences, Department of Neurobiology, the University of Eastern Finland, Kuopio. The 4.7T data was acquired by Dr Kimmo Jokivarsi and colleagues in 2008 (Jokivarsi et al., 2010) and the 9.4T data was acquired by Dr Kimmo Jokivarsi, Bryony McGarry and Harriet Rogers in 2014 (McGarry et al., 2016a, 2016b). The methods given for the animal model, MRI protocol and image processing are therefore identical to the methods described in the publications by Jokivarsi et al., (2010), Rogers, McGarry et al. (2014), Knight, McGarry et al. (2016) and McGarry et al. (2016a, 2016b, 2017). The methods employed in this study are also available in a video publication with a supporting manuscript (McGarry et al., 2017), which is accessible via: [https://www.jove.com/video/55277/a-magnetic-resonance-imaging-protocol-for-stroke-onset-time] or by scanning the QR code displayed below.

Although $T_1$ and $T_2$ relaxation times scale with magnetic field strength, combining data from 4.7T and 9.4T was not considered problematic as the net magnitude of $T_1$ and $T_2$ change due to ischaemia is independent of field strength during the first hours of stroke (McGarry et al., 2016a). For example, a previous study found that after ten minutes of ischemia, the change in the $T_1$ relaxation time was twofold greater at 9.4T than at 4.7T (Kettunen et al., 2000). However, at three hours post MCAo a change in $T_1$ at similar magnitudes has been determined, where at 4.7T,

$T_1$ increased by 9% (Moonen et al., 1991) and at 9.4T the increase was 6% (McGarry et al., 2016a). For $T_2$, at three hours post MCAo, the increase was 5% at both 4.7T (Jokivarsi et al., 2010) and 9.4T (McGarry et al., 2016a). These observations indicate that while the polarity of early changes and time-dependent kinetics of $T_1$ and $T_2$ relaxation times differ in ischaemic tissue, the increases in both relaxation times at clinically relevant time points are comparable and independent of magnetic field strength (McGarry et al., 2016a).

### 5.3.1 Animal model

Animal procedures were conducted according to European Community Council Directives 86/609/EEC guidelines and approved by the Animal Care and Use Committee of the University of Eastern Finland. Twelve male Wistar rats (300-400g) underwent permanent middle cerebral artery occlusion (MCAo) to induce focal ischaemia using the intraluminal thread model (Longa et al., 1989) where a nylon thread was advanced along the internal carotid artery until it blocked the blood flow from the middle cerebral artery (see McGarry et al., 2017 for a video demonstration). All rats were anaesthetised with isoflurane through a facemask (maintained at 1.5 – 2.4%) for the duration of the operation and MRI. Before MRI, arterial blood gases and pH were analysed (i-Stat CO, East Windsor, NJ). Breathing rate and rectal temperature were monitored, and core temperature maintained at 37°C with a water heating-pad under the torso. After MRI, rats were sacrificed via decapitation in deep isoflurane anaesthesia (McGarry et al. 2016a; 2017) or injection of saturated potassium chloride (KCl) (Jokivarsi et al., 2010, Rogers, McGarry et al., 2014).

### 5.3.2 MRI protocol

Multi-parametric MRI images were acquired using a horizontal 4.7T Magnex Scientific Inc (Yarnton, UK) magnet interfaced to a Varian Inova console (Palo

Alto, California), with a volume coil transmit/quadrature half-volume receive set up (Rapid Biomedical GmbH, Rimpar Germany) (Jokivarsi et al. 2010) and a 9.4T Agilent horizontal magnet (Agilent, Palo Alto, CA, USA) interfaced to a Varian direct drive system and equipped with an actively decoupled linear volume transmitter and quadrature receiver coil pair (RAPID Biomedical, GmbH, Rimpar Germany) (McGarry et al. 2016a, 2017).

The 4.7T MRI protocol included a spin-echo diffusion MRI sequence for quantification of ADC (TR = 1500ms, TE = 55ms, incorporating four bipolar gradients and four b-values 0 – 1370 $mm^{-2}$ s) and fast-spin multi-echo $T_2$ for quantification of $T_2$ relaxation times (5 echoes with 10ms inter-echo spacing starting at 10ms, TR = 2500ms). For both sequences, the images that were acquired were single slice, and field of view (FOV) was 2.56 cm x 2.56 cm covered by 64 x 128 points. This protocol was 24 minutes and for each rat (n = 7), was repeated every 30-60 minutes post MCAo. Therefore, maximum total imaging time for each rat was up to seven hours (Jokivarsi et al., 2010; McGarry et al. 2016a, 2017; Rogers, McGarry et al., 2014).

The 9.4T MRI protocol included **(a)** a 2D diffusion-weighted sequence for ADC quantification (TE = 36 ms, TR = 4000 ms, incorporating three bipolar gradients along each axis (duration of diffusion gradient = 5 ms) with three b-values: 0, 400, 1040 $mm^{-2}$ s), **(b)** the Carr-Purcell-Meiboom-Gill (CPMG) spin-echo multi-echo 2D $T_2$ sequence for quantification of $T_2$ relaxation times (12 echoes with 10ms inter-echo spacing starting at 10 ms, TR = 2000 ms) and **(c)** a 2D fast low angle shot (FLASH) $T_1$ (time from inversion to first FLASH sequence, = 7.58 ms, time between inversion pulses, = 10 s, TI = 600 ms, TR = 5.5 ms). For all sequences, 12 slices were acquired, and images were congruently sampled. FOV was 2.56 cm x 2.56 cm covered by 128 x 256 points, with 0.5 mm gap and 1 mm slice thickness. This protocol was 20 minutes and for each rat (n = 5), was repeated up to four times at hourly intervals post MCAo. Therefore, the maximum total imaging time for each rat was five hours (McGarry et al. 2016a, 2017).

### 5.3.3 Image processing

The following image processing steps were carried out using MATLAB release 2015b (The Mathworks, Natick, MA, USA) using functions written in-house by Knight, McGarry et al. (2016), which are available on the University of Bristol website (Wearn et al., 2017).

To preserve the signal to noise ratio (SNR), data were first filtered with a squared hamming window function in the phase and frequency-encode dimensions (Knight, McGarry et al. 2016; McGarry et al. 2016a, 2017). The hamming window is a smoothing function which increases SNR at the expense of resolution. It is applied to the $T_2$w images so that when the $T_2$ map is calculated, the $T_2$ values have smaller uncertainty and are closer to their true values even though the map is slightly blurred. The blurring was not considered a problem as it was much smaller than the size of the ischaemic region. It was necessary to apply the hamming window to the $T_2$w images rather than the $T_2$ maps, as any outlying $T_2$ values would be spread across the maps, resulting in inaccurate $T_2$ relaxation times.

Images used for the quantification of $T_2$w image intensities were the sum of weighted images acquired at each echo time (4.7T data: five images due to five echoes in the multi-echo $T_2$ protocol, and 9.4T data: 12 images due to 12 echoes in the multi-echo $T_2$ protocol). Relaxation time maps were computed using a mono-exponential fit in a logarithmic space. For $T_2$ data, hamming filtering was applied in k-space by a point-wise multiplication before inverse Fourier transform (Knight, McGarry et al., 2016). For diffusion and $T_1$, image-domain data was used, and squared-hamming filtering applied. $T_1$ fitting was performed according to methods given by Nekolla et al. (1992) however in order to speed up the process, magnitude data was used, and the lowest intensity point whose sign ($\pm$) cannot be known from the fitting, was excluded (Knight, McGarry et al. 2016; McGarry et al. 2017). ADC maps were calculated from diffusion-weighted data by the analytical solution to the Stejskal and Tanner (1965) diffusion equation (Knight, Mcarry et al., 2016).

To account for the fact that ischaemia causes an increase in $T_2$w image intensities, and $T_1$ and $T_2$ relaxation times, but causes ADC to decrease, reciprocal ADC maps (1/ADC) were calculated so that change in image intensities were all in the same direction.

### 5.3.4 Data analysis

Data analysis was performed using the Multi-image Analysis GUI (MANGO, Research Imaging Institute, UT Health Science Centre at San Antonio, TX, USA). Image intensity ratios of 1/ADC, $T_2$w, $T_1$ relaxation and $T_2$ relaxation times and the $f_1$, $f_2$ and $V_{\text{overlap}}$ parameters were computed for each rat at each time point available.

#### Computation of image intensity ratios (McGarry et al., 2016b)

Ischaemic regions were visually identified as hyperintense areas on 1/ADC images, all within the rat striatum. A typical example of the striatal hyperintensities on 1/ADC images at each time point post MCAo is shown in Figure 5.1. Figure 5.1 is adapted from McGarry et al., (2016a) and is of the 9.4T dataset used in this study. An example of the striatal hyperintensities in the 4.7T data set is shown in Figure 5.2. 1/ADC images were used to identify the ischaemic region because the bright voxels stand out more than the dark ischaemic voxels on normal ADC images. Regions of interest (ROI), 3 mm in diameter, were placed in the ischaemic and homologous regions of the non-ischaemic hemisphere and loaded onto corresponding weighted and relaxometry images (see Figure 5.2 for example). For 9.4T data, a representative central slice from the comparable brain region to the 4.7T data was chosen for analysis. Image intensity ratios of 1/ADC, $T_2$w, $T_1$ relaxation time and $T_2$ relaxation time images were calculated by dividing the mean value of the ischaemic ROI by the mean value in the non-ischaemic ROI. Use of non-ischaemic values was to eliminate inter-subject variation so that each rat served as its own control.

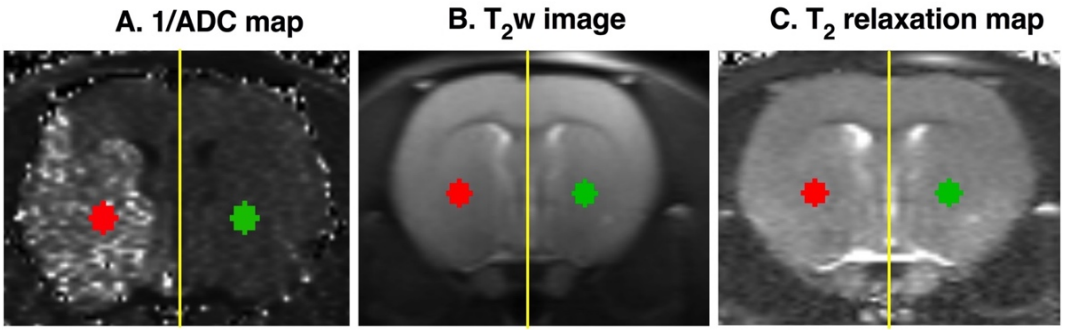


Figure 5.2 Example of 1/ADC map (A.) $T_2$w image (B.) and $T_2$ relaxation time map (C.) from a representative rat in the 4.7T data set. These images were acquired two hours after MCAo. The ischaemic region is clearly visible as hyperintensities on the 1/ADC map. The red circles are the ischaemic regions of interest (ROIs) the green circles are the non-ischaemic ROIs, which are the same as the ischaemic ROIs but have been reflected across the vertical axis, across the midline between the two hemispheres, which is indicated by the yellow line.

### Computation of $f_1$ and $f_2$

The $f$ parameter was initially introduced by Knight, McGarry et al. (2016) and represents the fraction of voxels within the ischaemic volume of interest (VOI) with high relaxation times. In this study, $f_1$ and $f_2$ are the number of voxels with high $T_1$ or $T_2$ relaxation times (respectively) relative to the number of voxels in the ADC defined ischaemic VOI, represented as a percentage (as per McGarry et al., 2016a, 2017). These parameters could not be computed for the 4.7T dataset as unlike the 9.4T data set which was 3D and imaged the whole brain, the 4.7T data set was 2D, and only one imaging slice through the ischaemic region was obtained per rat. Therefore, an ischaemic volume could not be calculated from the 4.7T images.

Computation of $f_1$ and $f_2$ first involved identifying ischaemic tissue and generating ischaemic volumes of interest (VOI) by applying Knight and McGarry et al.'s (2016) automatic ischaemic region detection method to 1/ADC images acquired for each rat at each time point. In brief, this involved identifying voxels with values in 1/ADC maps (where ischaemic voxels are bright with high values) that were higher

than average (one SD above the median) and eliminating voxels with unrealistically high $T_2$ voxels (above 200 ms, to exclude CSF) in order to generate binary masks.

The binary masks of the ischaemic region typically contained several distinct clusters of non-zero voxels as well as single voxels due to noise in the data. The masks were therefore filtered to remove clusters of voxels with a prescribed cluster size that were too small to realistically be ischaemic tissue (Knight, McGarry et al., 2016). The smallest acceptable cluster size was a user-defined parameter, which was set on a case by case basis (Knight, McGarry et al., 2016). In all cases, there was no ambiguity as to which voxels of the binary mask were ischaemic and which were due to noise, as the MCAo model used typically encompasses most of the rat striatum (see hyperintensities on 1/ADC maps in Figures 5.1 and 5.2). Homologous regions in the non-ischaemic hemisphere were identified by reflecting ischaemic VOIs about the vertical midline axis (see Figure 5.2).

Next, the number of voxels with high $T_1$ or $T_2$ relaxation times within the ischaemic VOI was determined by reflecting the ischaemic VOI onto the homologous region of the contralateral hemisphere to obtain the median $T_1$ or $T_2$ of the non-ischaemic tissue. As before, use of the non-ischaemic values was so that each rat served as its own control. A voxel within the ischaemic VOI was considered to have a 'high' relaxation time if its median value exceeded the median value of the non-ischaemic VOI by more than one half-width at half maximum (HWHM) of the distribution of relaxation times within the non-ischaemic VOI (Knight, McGarry et al., 2016) where HWHM is half of the difference between the two extreme values (full width at half maximum) of the independent variable (i.e., relaxation time in ms) when the dependent variable (number of voxels) is half of its maximum value.

As relaxation times have also been shown to decrease within the first hour after MCAo due to the negative blood oxygen level dependent (BOLD) effect (Gröhn et al., 2000; Jokivarsi et al., 2010; Rogers, McGarry et al., 2014) voxels with low

relaxation times were also identified (Knight, McGarry et al., 2016). A voxel in the ischaemic VOI was considered to have an unusually 'low' relaxation time if its median value was below the median value of the non-ischaemic VOI by more than one HWHM of the distribution of relaxation times within the non-ischaemic VOI (Knight, McGarry et al., 2016). The $f$ parameters were calculated as a percentage according to the following equation:

$$f_x = 100 * \left(\frac{N^{High} - N^{Low}}{N^{Lesion}}\right)$$

Where $x$ refers to the relaxation time ($T_1$ or $T_2$), $N^{High}$ refers to the number of 'high' relaxation time voxels in the ischaemic VOI, $N^{Low}$ is the number of 'low' relaxation time voxels in the ischaemic VOI (Knight, McGarry et al., 2016) and $N^{Lesion}$, is the total number of voxels within the ischaemic VOI (McGarry et al., 2016a, 2017).

### Computation of $V_{overlap}$

$V_{overlap}$ is the volume of tissue with both elevated $T_1$ and $T_2$ relaxation times within the ischaemic VOI, normalised by the whole brain volume and represented as a percentage (McGarry et al., 2016a, 2017). Different from $f_1$ and $f_2$, which shows elevated relaxation times within the ADC defined ischaemic region, $V_{overlap}$ shows how much of the overall rat brain has elevated relaxation times. $V_{overlap}$ was calculated for each rat and time-point as follows:

$$V_{overlap} = 100 * \left(\frac{N^{Overlap}}{N^{Wholebrain}}\right)$$

Where $N^{Overlap}$ is the number of voxels within the ADC defined ischaemic region with both high $T_1$ and $T_2$ (defined above). $N^{Wholebrain}$ is the total number of voxels within the whole rat brain, which was determined by manually creating a VOI

around the whole brain on $T_2$ relaxation time maps (McGarry et al., 2016a, 2017). Dividing by the whole brain volume was important to control for the fact that the brain swells (and therefore increases in size) during ischaemia due to the net increase in water content (ionic and vasogenic oedema). This has been demonstrated consistently in rat models of ischaemia (e.g., Gerriets et al., 2004).

### Signal to noise ratio (SNR)

SNR, the key image quality characteristic, was computed for the maps and summed weighted images using the dual acquisition approach described by Firbank et al., (1999). SNR was computed to account for the possibility that better performance could be due to better SNR rather than an inherent quality of the parameter studied. Also, to check the SNR was the same for scans acquired at the different field strengths. Firbank et al.'s (1999) SNR approach involved computing a difference image from sequential acquisitions (McGarry et al., 2016b). Here, difference images for all rats were computed by subtracting images acquired in the second hour post MCAo from images acquired in the first hour. SNR was computed using the following equation:

$$\mathrm{SNR}_{\mathrm{dual}} = \sqrt{2}\frac{S_1}{SD_{1-2}}$$

Where $S_1$ is the mean signal intensity from an ROI (6 mm x 6 mm) placed in the contralateral hemisphere, $SD_{1\text{-}2}$ is the standard deviation of the signal from the same ROI placed in the same region of the difference image. SNR values given in the results are averaged across rats.

## 5.3.5 Statistical analysis

Statistical analysis was performed using XLSTAT for Microsoft Excel and Prism 8.03 (GraphPad Software, La Jolla California, USA). Data were assessed for normality using the Shapiro-Wilk test (Shapiro & Wilk, 1965). The relationship of 1/ADC, $T_2$w, $T_1$, $T_2$, $f_1$, $f_2$ and $V_{\mathrm{overlap}}$ with time from ischaemia onset was assessed

using Pearson's correlations for normally distributed data and Spearman's correlations for non-normal data.

For a visual indication of the overall performance of each MRI parameter at discriminating between scans performed before and after three hours from ischaemia onset, receiver operating characteristic (ROC) curves were plotted (see Appendix A for description). Three hours was chosen as the time-point for comparison as both the 4.7T and 9.4T datasets contained this time-point and the number of scans before and after was similar (21 data points before three hours, 19 data points after three hours). For a numerical indication of the overall performance of MRI parameters, areas under the ROC curves (AUC) and their statistical difference from 0.5 (indicating no discriminative ability) were calculated and statistically compared using non-parametric methods that control for multiple comparisons (DeLong et al., 1988). The sensitivity levels of each parameter at a specificity level of 1, were also determined. All statistical tests were two-tailed with a significance level of $p < .05$.

## 5.4 Results

SNR was higher for weighted images than relaxation time maps but comparable across field strengths (Table 5.1) (McGarry et al., 2016b). Comparable SNR across field strength shows that combining data from two different field strengths could not have impacted the results.

Table 5.1 Signal to noise ratio of weighted images and relaxation time maps.

| | **Signal to Noise Ratio (SNR)** | |
|---|---|---|
| **Image** | **4.7 T** | **9.4 T** |
| **$T_2$w** | 31.4 (SD = 7.1) | 19.1 (SD=3.9) |
| **$T_2$ relaxation** | 90.5 (SD = 19.2) | 59.2 (SD = 23.0) |

*Note, standard deviation (SD) is given in brackets*

Non-normally distributed data included 1/ADC (w = 0.88, $p < 0.001$) and $f_1$ (w = 0.90, $p = 0.048$). Figure 5.3 shows all parameters correlated significantly with time from MCAo and that $V_{overlap}$ and $f_2$ showed the strongest relationships ($V_{overlap}$ $r$ = 0.93, $f_2$ $r$ = 0.91). Figure 5.4 shows the ROC curves and AUC values for all parameters. All AUC values were significant, demonstrating all parameters could be used to distinguish between scans performed before and after three hours from MCAo. $V_{overlap}$ and $f_2$ demonstrated the highest overall ability, as the AUCs for these parameters were comparable to each other ($p > 0.05$) and were significantly higher than the other parameters ($p < 0.05$) (McGarry et al., 2016b). The $T_2$ relaxation time ratio had the next highest overall performance, which was significantly higher than $f_1$, $T_2$w, $T_1$ and 1/ADC (McGarry et al., 2016b).

The low SNR of relaxation time maps compared to the weighted images (Table 5.1) shows that the better performance of the relaxation time based parameters (given below) was not attributable to higher signal and that despite higher SNR, which should boost performance, weighted images still performed poorly. This

suggests that the better performance of the relaxation time parameters is an inherent quality of these qMRI parameters.

Table 5.2 shows at a specificity of 1, $V_{overlap}$ and $f_2$ had the highest sensitivity levels and the sensitivity of $T_1$, $T_2$, 1/ADC and $T_2$w were low (McGarry et al., 2016b). Thresholds for identifying strokes less than or equal to three hours at these specificity and sensitivity levels are also shown in Table 5.2. For example, a $V_{overlap}$ measurement of greater than 1.83% indicates that the scan was performed after three hours from onset (due to specificity of 1) and most measurements less than or equal to 1.83% indicates the scan was performed within three hours of onset. However, due to the sensitivity of 0.90, 10% of the measurements that were less than 1.83% could have been after three hours. A $T_2$ image intensity ratio (mean ischaemic $T_2$ / mean non-ischaemic $T_2$) greater than 0.99 indicates that the scan was performed after three hours (due to specificity of 1) and most measurements equal to or less than 0.99 indicates the scan was performed within three hours of onset. However, due to the sensitivity of 0.39, 61% of the measurements could have been after three hours.

Table 5.2 Sensitivity of qMRI parameters and corresponding cut-off values when specificity is maximum (McGarry et al., 2016b).

| **qMRI parameter** | **Threshold** | **Specificity (95% CI)** | **Sensitivity (95% CI)** |
|---|---|---|---|
| $V_{overlap}$ | 1.83 % | 1 (0.65 – 1) | 0.90 (0.57 – 1.00) |
| $f_2$ | 69.71 % | 1 (0.65 – 1) | 0.80 (0.48 – 0.95) |
| $f_1$ | 84.09 % | 1 (0.65 – 1) | 0.50 (0.24 – 0.76) |
| $T_2$ | 0.99 | 1 (0.85 – 1) | 0.39 (0.24 – 0.56) |
| $T_2w$ | 1.00 | 1 (0.85 – 1) | 0.29 (0.16 – 0.47) |
| $T_1$ | 0.99 | 1 (0.65 – 1) | 0.10 (0.00 – 0.43) |
| 1/ADC | 0.79 | 1 (0.77 – 1) | 0.00 (0.00 – 0.12) |

*Note, CI = 95% confidence interval. Thresholds for $f_1$, $f_2$ and $V_{overlap}$ are percentages, where $f_1$ and $f_2$ are the respective volumes of high $T_1$ or $T_2$ within the ADC defined ischaemic region as a percentage of the* size *of the ischaemic volume. $V_{overlap}$ is the percentage of voxels with both high $T_1$ and high $T_2$ within the ischaemic volume relative to the whole-brain size. 1/ADC, $T_2$, $T_2$ and $T_2w$ thresholds are the image intensity ratios (mean ischaemic image intensity/ mean non-ischaemic image intensity).*

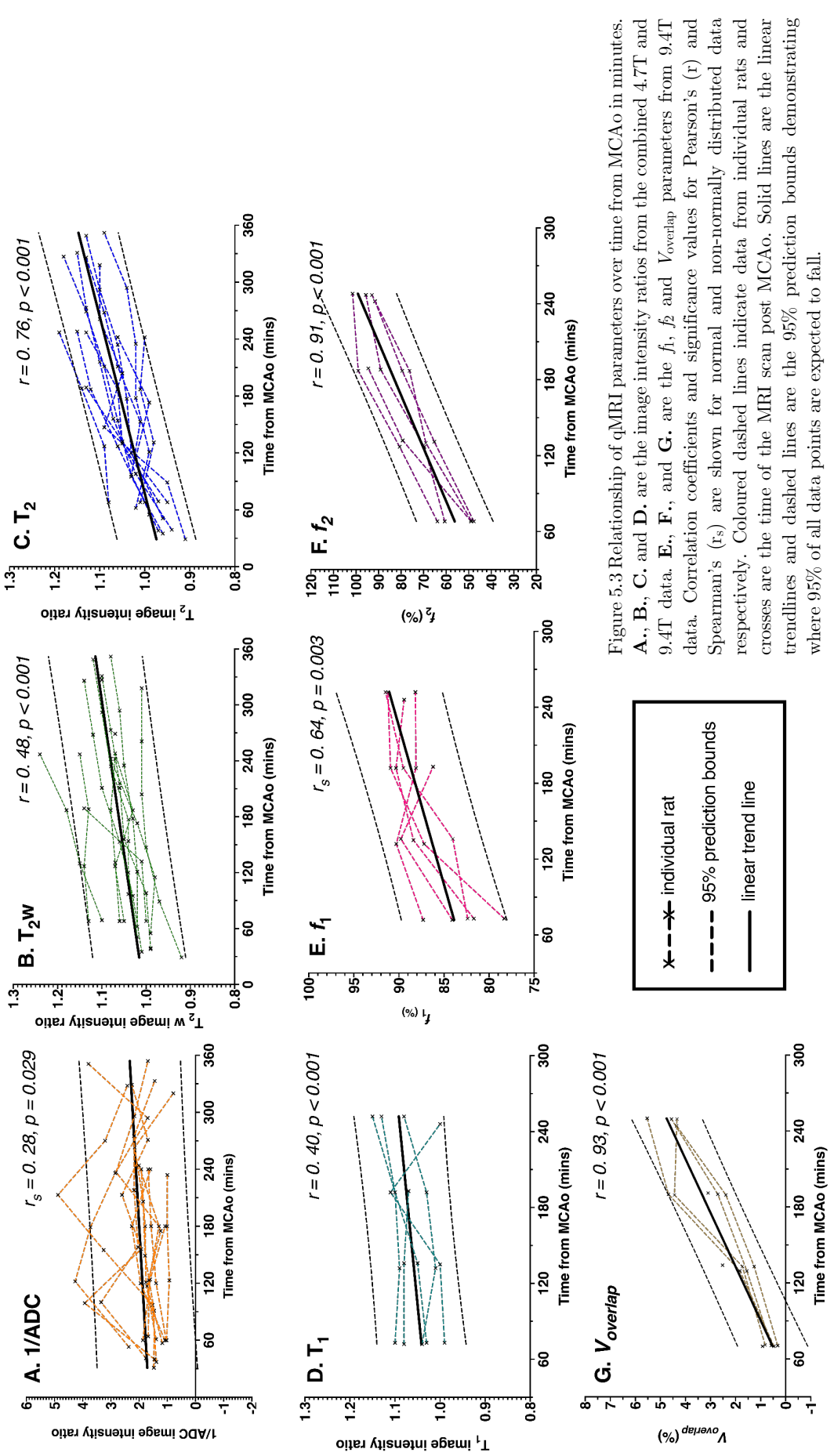


Figure 5.3 Relationship of qMRI parameters over time from MCAo in minutes. **A.**, **B.**, **C.** and **D.** are the image intensity ratios from the combined 4.7T and 9.4T data. **E.**, **F.**, and **G.** are the $f_1$, $f_2$ and $V_{overlap}$ parameters from 9.4T data. Correlation coefficients and significance values for Pearson's (r) and Spearman's ($r_s$) are shown for normal and non-normally distributed data respectively. Coloured dashed lines indicate data from individual rats and crosses are the time of the MRI scan post MCAo. Solid lines are the linear trendlines and dashed lines are the 95% prediction bounds demonstrating where 95% of all data points are expected to fall.

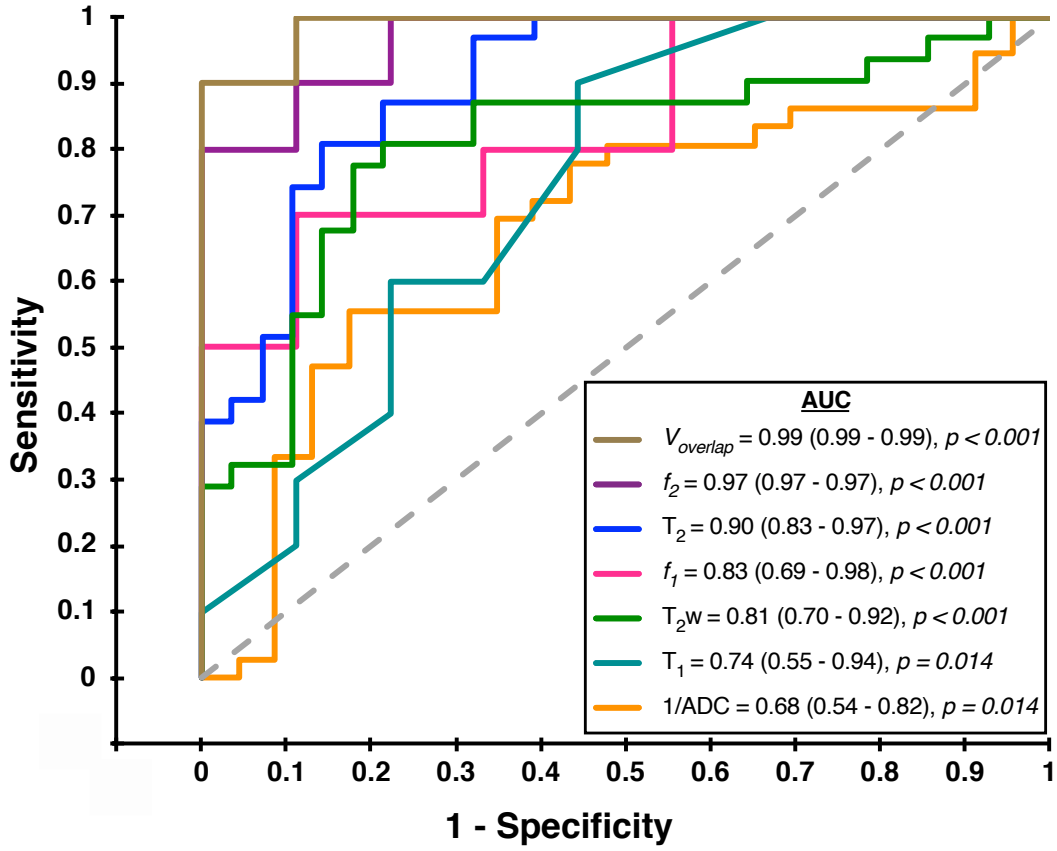


Figure 5.4 ROC curves and associated AUC values showing the overall ability of qMRI parameters for distinguishing between MRI scans performed before and after three hours from MCAo in ischaemic rats. AUC values are displayed for each qMRI parameter with 95% confidence intervals in brackets. Lines closer to the grey dashed 0.5 reference line indicate parameters with poor overall ability. Figure adapted from McGarry et al. (2016b).

## 5.5 Discussion

The study compared the overall ability of qMRI parameters for estimating stroke onset time in rat models of ischaemia (McGarry et al., 2016b). qMRI parameters involving $T_2$ relaxation times had the highest overall ability, as $V_{overlap}$, $f_2$, and the $T_2$ image intensity ratio demonstrated the strongest relationships with time from ischaemia onset. These qMRI parameters also had the highest overall accuracy for distinguishing between scans performed before and after three hours from onset (McGarry et al., 2016b). The data suggest qMRI is a potential tool for identifying ischaemic stroke patients with an unknown onset time that are still within the treatment window, which may aid decision making for pharmacotherapy (McGarry et al., 2016b).

This study agrees with previous studies that quantitative MR relaxation times are more accurate for stroke onset determination than signal intensities in respective relaxation-weighted images (Rogers, McGarry et al., 2014; McGarry et al., 2016a). The high overall ability of parameters derived from relaxation times in this study (demonstrated by high AUCs) is likely due to the fact that fitting signal intensities to the MR relaxation equations removes inherent variations caused by technical factors such as magnetic field inhomogeneities, and proton-density (McGarry et al., 2016a, also discussed in Chapter 3 Section 3.7.2). A further benefit of $V_{overlap,}$ $f_1$ and $f_2$ is their insensitivity to magnetic field variation within the ischaemic region (McGarry et al., 2016a, 2016b). SNR was higher for summed weighted images suggesting poor SNR cannot account for the inferior performance of signal intensities from weighted images (McGarry et al. 2016b).

The results argue that $V_{overlap}$ and $f_2$, which represent the distribution of elevated relaxation times within ADC defined ischaemic regions, may perform better in onset time estimation than relaxation-based image intensity ratios (McGarry et al., 2016b). The relationship of these distribution-based parameters with time from stroke onset, reflects the transition of the ischaemic region from compromised

tissue, to irreversible infarction (McGarry et al., 2016a, 2016b). As illustrated in Figure 5.1, in the initial hours, the ischaemic region is composed of voxels with heterogenous relaxation times. In the absence of reperfusion, the extent of irreversible damage, and therefore the number of voxels with elevated relaxation times will increase.

Given the different pathophysiological mechanisms reflected by $T_1$ and $T_2$ (Kauppinen, 2014), $V_{overlap}$ may also serve as an indicator of tissue viability (McGarry et al., 2016a). Where voxels with decreased ADC, high $T_1$ and high $T_2$, indicates irreversibly damaged tissue (McGarry et al., 2016a) and voxels with decreased ADC and 'normal' $T_1$ and $T_2$ indicate potentially viable tissue (McGarry et al. 2016a; Rogers, McGarry et al., 2014). This conclusion (McGarry et al., 2016a) is supported by the fact that prolonged $T_1$ and $T_2$ relaxation times in the ischaemic brain were shown to signify the transition to necrosis by histological methods (Calamante et al., 1999). $T_1$ and $T_2$ are influenced by total tissue water content (Barbier et al., 2005; Kato et al., 1985), and so, $V_{overlap}$ may represent tissue with irreversible vasogenic oedema (McGarry et al., 2016a).

It is worth noting; however, that quantification of $V_{overlap}$ and $f_2$ could be problematic in a clinical setting. The rat brain is comprised mainly of grey matter (GM) (Zhang & Sejnowski, 2000) and so in this study, it was safe to assume that an increase in relaxation times relative to the non-ischaemic hemisphere was caused by ischaemia. The human brain, however, is a combination of GM and white matter (WM), which due to difference in structure, metabolism, haemodynamics and electrophysiology, have different baseline $T_2$ relaxation times (Wansapura et al., 1999), and sensitives to ischaemia (Berner et al., 2016). CBF thresholds for the ischaemic core have been shown to be higher in GM than WM in patients (Bristow et al., 2005; Chen et al., 2019) and anoxic depolarisation (associated with cytotoxic oedema), was shown to decrease faster in GM in ischaemic cats (Kumura et al., 1999). As these factors both contribute to changes in ADC (Sotak, 2004) and $T_2$

relaxation (Knight, McGarry et al., 2016), the criteria for defining 'high $T_2$' caused by ischaemia will differ between tissue types.

ADC does not differentiate between tissue type (Serner, 2001), therefore applying one criterion across the whole ADC defined ischaemic region to identify high and low relaxation times as was done in this study, will not be informative. It would not be clear whether voxels identified as having high or low $T_2$ represent voxels from a different tissue type or voxels that have changed due to ischaemia. Ischaemic GM and WM would, therefore, need to be analysed separately in patients (addressed in Chapter 8) which may be challenging in a clinical setting. Although the methods employed for calculating $V_{overlap}$ and $f_2$, in this study are not necessarily directly translatable to human stroke patients, results suggest that examining the distribution of relaxation times within regions of reduced ADC, could be informative of stroke onset time and therefore merits further investigation.

Although the $T_2$ ratio demonstrated high overall ability at distinguishing between scans performed before and after three hours from ischaemia onset, compared to $V_{overlap}$ and $f_2$, the sensitivity of $T_2$ was low (Table 5.2). Applying the cut-off of a $T_2$ ratio greater or less than 0.99, meant all scans performed after three hours were identified (ratio $> 0.99$), but at the expense of only identifying 39% of scans performed before three hours (ratio $< 0.99$). The low sensitivity is likely due to including $T_2$ data from early time points. As seen in Figure 5.3, several data points had a ratio of less than one, indicating a decrease in $T_2$. This decrease is consistent with studies in rat models of ischaemia, where $T_2$ decreased within the first 90 minutes, before increasing over time (Calamante et al., 1999; Gröhn et al., 2000). The $T_2$ shortening is attributed to the negative BOLD effect described in Chapter 3, Section 3.2.2 (Calamante et al., 1999; Gröhn et al., 2000). The subsequent normalisation and increase in $T_2$ reflect the reduction or normalisation of the oxygen extraction fraction (OEF) due to a decline in the cerebral metabolic rate of oxygen ($CMRO_2$) (Calamante et al., 1999).

By including $T_2$ ratios from early time points in the analysis, the sensitivity levels of $T_2$ reported in this study are unlikely to be representative of the performance of the $T_2$ ratio in patients. To date, a decrease in $T_2$ due to ischaemia has not been captured in patients. Duchaussoy et al. (2019) were the first to quantify $T_2$ relaxation time ratios in hyperacute ischaemic patients as early as 30 minutes from symptom onset. None of the patients had a $T_2$ ratio below one, but several within the first 90 minutes had a ratio of one or close to it. Even so, a decline in $T_2$ would not be problematic for onset time estimation, as it would suggest that the patient is within the 4.5 hour treatment window for thrombolysis (Rogers, McGarry et al., 2014). In support, patients without hyperintensities in $T_2$w FLAIR images were found to be within three hours of symptom onset (Thomalla et al., 2009). Thus, the low sensitivity reported here should not discourage investigation of the $T_2$ ratio as a method for stroke timing in patients.

The sensitivity was zero for ADC and very low for $T_2$w image intensity ratios (McGarry et al., 2016b). In clinical acute stroke cases, ADC was deemed to carry no timing information, but rather serve as an early MRI index of ischaemia per se (Burgess & Kidwell, 2011; Kauppinen, 2014). Similarly, the low sensitivity of $T_2$w image intensities was reported clinically (Ebinger et al., 2010; Wouters et al., 2014). Thus, ADC or $T_2$w image intensity ratios can be regarded as poor indices for stroke timing, but instead are important for stroke diagnosis (McGarry et al., 2016b). The low sensitivity of the $T_1$ relaxation time compared to the other relaxation-based parameters is likely due to the more gradual changes in $T_1$ over time (McGarry et al., 2016a), illustrated by the gradual slope and low correlation coefficient in Figure 5.3. In contrast to $T_2$, which increases rapidly following the initial shortening (Gröhn et al., 2000; Jokivarsi et al., 2010), the $T_1$ relaxation time has a two-phase response to ischaemia (McGarry et al. 2016a), where $T_1$ increases rapidly within the first 25 minutes post occlusion, followed by a more gradual change (Calamante et al., 1999). This two-phase response and subtle changes in $T_1$ may make it less suitable for onset time estimation in clinics.

To conclude, from the multiple qMRI parameters studied here, $V_{overlap}$ $f_2$, and the $T_2$ image intensity ratio quantified in the ADC defined ischaemic region provide the most accurate estimates of stroke onset time. The current preclinical data encourage investigation into qMRI indices based on absolute relaxation times (not weighted images), including image intensity ratios and distributions within the ischaemic region, as surrogates for stroke timing in clinical settings. A common concern regarding qMRI for stroke timing in clinical settings is the long scan times required for multi-echo $T_2$ and inversion recovery $T_1$, which increases the possibility of motion-induced artefacts and would delay treatment. However, methods for fast $T_1$ and $T_2$ relaxation time mapping is now possible in clinically available systems. With the advent of magnetic resonance fingerprinting (Ma et al., 2013, Chapter 3 Section 3.7.3), which provides many quantitative MR results simultaneously, the future of qMRI for clinical use is promising (McGarry et al. 2016a, 2016b).

Overall, the results of this Chapter suggest that qMRI parameters involving image intensity ratios of the $T_2$ relaxation time, as well as the distribution of $T_2$ relaxation times are informative of stroke onset time in rats. These results, therefore, warrant an investigation into the ability of these parameters for estimating onset time in hyperacute ischaemic stroke patients.

# Chapter 6
# Translation of preclinical findings to clinical presentations of hyperacute ischaemic stroke

The overarching goal of the preclinical MRI study in Chapter 5 was to investigate the potential utility of qMRI parameters for estimating stroke onset time, under controlled conditions, in an experiment that would be difficult and unethical to emulate in patients. A comprehensive study that investigates all possible qMRI parameters at multiple time points after ischaemia onset would not have been possible in patients due to the time-critical nature of treating hyperacute stroke patients and their vulnerable clinical state. Additionally, the pathophysiology of cerebral ischaemia is highly variable as it is influenced by several factors such as the anatomical location, cause and severity of the ischaemia (i.e. degree of drop in local CBF), the presence of pre-existing systemic disease(s), and the age, body temperature, and arterial blood profiles of the patient (Macrae, 1992). These factors can be controlled in rats, but in a patient study, would introduce variability into the data that could confound statistical evaluation (Macrae, 1992). Use of the intraluminal thread model to induce middle cerebral artery occlusion (MCAo) ensured consistent location, size and severity of ischaemia across rats (Longa et al., 1989) in the vascular territory that is most commonly affected in patients (Mohr et al., 1986). The potential confound of pre-existing diseases was also avoided by

studying young rats, and the core temperature, breathing rate, and arterial blood gases were monitored.

Rats are considered suitable subjects for studying ischaemia because the cerebrovascular anatomy is similar to that of a human, including the presence of a circle of Willis (Durukan & Tatlisumak, 2007; Tamura et al., 1981). However, there are also fundamental differences in the physiology and anatomy of the rat and human brain that limit how far results from rats are translatable to humans (Macrae, 1992). The most notable difference is that the rat brain is 86% grey matter (GM), whereas the human brain is approximately half GM and half white matter (WM) (Zhang & Sejnowski, 2000). Therefore, the conclusions drawn from studies of rat models of ischaemia are regarded as only representative of GM.

Although the ischaemic cascade in GM and WM is similar as both start with the exhaustion of ATP followed by the loss of ion homeostasis (Macrae, 1992), it is unlikely that the same mechanisms damage these tissue types because of their extremely different compositions (Goldberg & Ransom, 2003). For example, GM has more neuronal cell bodies, and synapses than WM (Goldberg et al., 1987) and WM has no synapses, more axons and glia (Goldberg & Ransom, 2003). GM has twice the metabolic rate of WM (Clarke & Sokolof, 1999; Nishizaki et al., 1988) and up to three times the CBF and CBV requirements than WM has (Helenius et al., 2003; Simon et al., 2005). As discussed in Chapter 5, GM also has higher CBF thresholds for ischaemia (Bristow et al., 2005; Chen et al., 2019) and a faster decrease in anoxic depolarisation (Kumura et al., 1999). Ischaemic lesions have also been shown to extend preferentially within WM of patients (Berner et al., 2016). Replicating the ischaemic damage seen in WM of humans has not been straightforward in animal studies, and where it has been successful the methods used are not considered representative of how ischaemia is induced in the human brain (Sozmen et al., 2012).

Given the differences between rats and humans outlined above, preclinical findings cannot be relied on for deciding which methods to use in the clinic but can be used to inform the design of pilot studies in patients, which will ultimately inform the design of larger-scale clinical studies. Chapter 5 and the previous preclinical and clinical MRI studies of stroke timing referenced in Chapter 4 (Section 4.4), informed the design of the pilot studies in the following chapters of this thesis. The overall goal of the pilot studies in Chapter 7 and Chapter 8 was to explore potential relationships between $T_2$ based MRI parameters and time from stroke onset in hyperacute ischaemic stroke patients, with the view to generating specific hypotheses that could be investigated in future patient studies.

The focus was specifically on $T_2$ based qMRI parameters due to the encouraging results of $T_2$ relaxation times in Chapter 5 and previous preclinical studies (Jokivarsi et al., 2010; McGarry et al., 2016a, 2016b; Rogers, McGarry et al., 2014) as well as the clinical study by Siemonsen et al. (2009). Although DWI and $T_2$w signal intensities did not perform well for estimating stroke onset time in Chapter 5, these were also included in the study in Chapter 7, because of the considerable attention they have received in the clinical stroke timing literature (e.g., see Wouters et al., 2014 and Etherton et al., 2018 for reviews). $T_2$ based parameters were also considered the most feasible for the acute stroke setting as DWI and $T_2$w imaging (without and without FLAIR) are already part of stroke protocols, for the respective identification and assessment of ischaemic regions (Mair & Wardlaw 2014). These sequences can be run in a few minutes, and most clinical MRI scanners also produce $T_2$ relaxation time maps from the weighted images at no extra time cost if a multi-echo $T_2$ sequence is used.

The $T_1$ relaxation time was not included in the pilot studies because it showed poor performance in rats in Chapter 5, and as discussed, the two-phase response to ischaemia could make it less suitable for stroke timing than $T_2$. Additionally, quantifying $T_1$ using the inversion recovery approach (outlined in Chapter 4, Section 4.2.3) requires long repetition times (TR), which make it unsuitable for

emergency clinical settings (Deoni et al., 2003; Pykett et al., 1983). We previously trialled quantifying $T_1$ relaxation times using the DESPOT$_1$ (Deoni et al., 2003) methods for fast $T_1$ mapping (McGarry, 2015) which involves averaging $T_1$ weighted images acquired at two or more flip angles, with a short and constant TR. However, we were unable to accurately and consistently measure $T_1$ in the human brain using a similar approach in the Philips Achieva platform (McGarry, 2015) due to difficulties selecting the correct flip angles, and in-homogeneities in the $B_1$ field (Deoni et al., 2008).

The MRI protocol for the patient studies of Chapter 7 and Chapter 8, therefore included:

- A multi b-value DWI sequence for visually locating ischaemic tissue and for quantifying DWI image intensities.
- The trace of diffusion tensor, to quantify ADC and generate ischaemic volumes of interest (VOI).
- Multi-echo $T_2$ for quantification of $T_2$w image intensities and computation of $T_2$ relaxation time maps. $T_2$w images also enabled tissue to be segmented into GM and WM for separate analysis in Chapter 8.
- 3D $T_1$w to register all other images to and to ensure that the same region was being compared.

# Chapter 7
# A pilot study comparing $T_2$ relaxation-based MRI stroke timing methods in hyperacute ischaemic stroke patients

## 7.1 Abstract

$T_2$ relaxation-based MRI signals may identify acute ischaemic stroke patients with an unknown symptom onset time that are within the 4.5 hour time-window for intravenous (IV) thrombolytic therapy. This pilot study compared the ability of visual and quantitative MRI based stroke timing methods in a cohort of hyperacute ischaemic stroke patients.

Thirty-five patients underwent 3T MRI (< 9 hours symptom onset). Diffusion-weighted (DWI), apparent diffusion coefficient (ADC), $T_1$ weighted ($T_1$w), $T_2$ weighted ($T_2$w) and $T_2$ relaxation time ($T_2$), images were acquired from all 35 patients. $T_2$ weighted FLAIR (FLAIR) images were acquired for 17 of these patients (sub-cohort). Image intensity ratios of the average intensities in ischaemic and non-ischaemic reference regions were calculated for ADC, DWI, $T_2$w, $T_2$ relaxation, and FLAIR images and optimal image intensity ratio cut-offs were determined. DWI and FLAIR images were assessed visually for DWI/FLAIR mismatch.

The $T_2$ relaxation time image intensity ratio was the only parameter that correlated significantly with time from symptom onset (r = 0.49, $p = 0.003$), had a significant area under the ROC curve (AUC = 0.77, $p < .0001$) and an optimal cut-off ($T_2$ ratio = 1.072) that accurately differentiated between patients within (< 1.072) and beyond (> 1.072) the 4.5 hour treatment window without compromising sensitivity (0.74) and specificity (0.74). There was a trade-off between sensitivity and specificity for ADC, DWI and $T_2$w image intensity ratios. Multiple logistic regression revealed no benefit of combining ADC, DWI, $T_2$w, and $T_2$ ratios. In the sub-cohort of patients with the additional FLAIR scans, areas under the precision-recall-gain curve (AUPRG) and $F_1$ scores showed that the $T_2$ relaxation time ratio (AUPRG = 0.60, $F_1$ = 0.73) performed considerably better than the FLAIR ratio (AUPRG = 0.39, $F_1$ = 0.57) and the visual DWI/FLAIR mismatch ($F_1$ = 0.25).

It was concluded that when exploiting $T_2$ MRI in ischaemic stroke, quantification of the $T_2$ relaxation time should be the preferred method because it is more adept at predicting whether a patient is within the IV thrombolysis treatment window than the alternatives considered here. The use of the quantified parameter also eliminates the presence of unwanted contributions to the signal that often affect weighted signal intensities. The $T_2$ relaxation time is, therefore, a controllable MRI variable, which may provide a more reliable stroke timer.

## 7.2 Introduction

Unknown time of symptom onset due to *wake-up stroke* or lack of witness is a common contraindication for reperfusion therapies for ischaemic stroke (Etherton et al., 2018). Intraarterial administration of thrombolytic agents is considered safe within six hours of onset but is not routine (Berkhemer et al., 2015) and patients with large vessel occlusion (LVO) can now be considered for mechanical thrombectomy if symptom onset was within the last 24 hours (Nogueira et al., 2018; Powers et al., 2018). For the many patients without LVO, intravenous (IV) rtPA is the only alternative. The current European licensing limit for IV rtPA is 4.5 hours (Fiehler et al.,2016; Powers et al., 2018) as the administration of IV rtpa after this time point is associated with increased risk of haemorrhage (Hacke et al., 2008) Multiparametric MRI reveals pathophysiological changes in the ischaemic brain parenchyma, enabling diagnosis, insight into the extent of on-going tissue damage, and inference of stroke duration (for a comprehensive review see Kauppinen, 2014). MRI may, therefore, aid treatment stratification of ischaemic stroke patients with unknown symptom onset time by identifying patients that (a) are likely to be within the 4.5 hour IV rtPA treatment window or (b) have sufficient viable tissue that would suggest they may benefit from reperfusion therapy regardless of onset time (Biggs et al., 2019; Etherton et al., 2018). This study focused on imaging methods aimed at achieving (a).

MRI contrasts, including diffusion-weighted imaging (DWI) or the parametric measure of diffusion, the apparent diffusion coefficient (ADC), are extremely sensitive to ischaemia. Studies using rodent models showed DWI signals increase and ADC values decrease sharply within minutes of ischaemia onset at the same cerebral blood flow (CBF) threshold for catastrophic energy failure (Busza et al., 1992; Gröhn et al., 2000). Regions with low ADC, therefore, reflect tissue undergoing cytotoxic oedema and the associated cellular changes (Kauppinen, 2014). The wide dynamic range of ADC provides an excellent contrast to the non-ischaemic brain, and so is useful for diagnosing ischaemia and localising affected brain tissue (Burgess & Kidwell, 2011; Kauppinen, 2014). However, ADC values in

patients remain consistently low for several days after the insult (Schlaug et al., 1997), making it an unsuitable parameter for stroke timing. Preclinical studies have shown that the $T_1$ and $T_2$ relaxation times that contribute to the signal of weighted images typically acquired in the clinic, such as DWI, $T_2$ weighted ($T_2$w) and $T_2$w FLAIR, also change early during ischaemia but, compared to ADC, changes are small (Kauppinen, 2014). $T_1$ and $T_2$ relaxation times have been shown to have linear time dependency in rat stroke models (Chapter 5, Jokivarsi et al., 2010; McGarry et al., 2016a, 2016b) and, for $T_2$ this has been translated to human stroke (Damion, Knight, McGarry et al., 2019; Duchaussoy et al., 2019; Siemonsen et al., 2009), suggesting quantification of $T_2$ may be a suitable method for stroke timing.

As outlined in Chapter 4, the $T_2$ relaxation-based signal changes that occur in DWI and FLAIR images after stroke have also been exploited for stroke timing using visual (Thomalla et al., 2011) and quantitative methods (e.g., Song et al., 2012). For both approaches, if the signal in the ischaemic region in the FLAIR image (identified by DWI or ADC) is deemed not to be hyperintense, it is likely that the patient is within the 4.5 hour treatment window and thus potentially eligible for rtPA. For the visual DWI/FLAIR mismatch approach (see Chapter 4, Section 4.4.2), the presence of a *mismatch* where ischaemia is visible on DWI but not FLAIR scans indicates patient eligibility (Thomalla et al., 2011). For the quantitative approach, eligibility is determined by whether the ratio of image intensity values between ischaemic and non-ischaemic reference regions is below a specific optimal cut-off (e.g., Song et al., 2012, Chapter 4). This approach has been studied using image intensities from ADC, DWI, $T_2$w, FLAIR and $T_2$ relaxation images in animal models of ischaemia (Chapter 5, McGarry et al., 2016b, Xu et al., 2014) and ischaemic stroke patients (Knight, Damion, McGarry et al., 2019; Madai et al., 2016; Song et al., 2012; Wouters et al., 2018) but the overall performance of these parameters has not been directly compared in hyperacute stroke patients.

The recent results of the 'WAKE-UP' stroke trial (Thomalla et al., 2018) in which patients with DWI/FLAIR mismatch treated with IV rtPA showed an 11.5%

increased favourable outcome compared to placebo, have provided further impetus for investigating the clinical benefit and application of MRI for timing the ischaemic stroke. Potential stroke timing methods must be able to successfully discriminate between patients within and beyond the 4.5 hour rtPA time-window. High sensitivity is essential to identify as many patients as possible that are eligible for rtPA, and high specificity is also imperative in order to avoid potentially harmful treatment. In this pilot study (McGarry et al., 2020), the performance of quantitative and visual MRI based stroke timing methods derived from the same cohort of hyperacute ischaemic stroke patients was compared. The focus was on image intensity ratios of ADC, DWI, $T_2$w, $T_2$ relaxation and FLAIR images, and the DWI/FLAIR mismatch.

## 7.3 Methods

### 7.3.1 Patients

Patients were recruited from North Bristol NHS Trust Frenchay and Southmead Hospitals (Bristol), Queen Elizabeth University Hospital (Glasgow) and University of Oxford Radcliffe Department of Medicine's Acute Vascular Imaging Centre (Oxford). Time of witnessed symptom onset, National Institute Health Stroke Scale (NIHSS), and the attending physician's stroke classification according to the Oxford Community Stroke Project Classification (Bamford et al., 1991) were recorded on admission. Before enrolment, all patients received NCCT scans and were treated according to the standard-of-care protocol, including administration of IV rtPA if eligible. Thrombectomy was not offered at any site.

Patients, or their legal representative, provided informed consent. Enrolled patients had MRI scans within nine hours of symptom onset. Exclusion criteria after enrolment included: withdrawal from involvement in the study after initial consent, early termination of scan due to claustrophobia, unclear diagnosis, uncertainty regarding symptom onset time and error in scan protocol. Imaging related exclusion criteria included: no evident ischaemia on ADC images, movement artefacts, evidence of bilateral stroke, bias field problems in weighted images and presence of extensive white matter hyperintensities (WMH) on $T_2$w images (see Figure 7.1 for example). It was important to remove these imaging factors from the dataset as the non-ischaemic tissue would provide an unreliable estimate of pre-ischaemic MR values. Exclusion of patients according to the above criteria was agreed upon by three raters with experience in MRI and stroke (RD, RAK, BLM). WMHs, or *leukoaraiosis,* are visible as white spots on $T_2$w images of the brain (Wardlaw et al., 2015). These hyperintensities are presumed to have a vascular origin and are common in older subjects and patients with stroke and dementia (Wardlaw et al., 2015). WMHs were considered extensive if both parenchymal and periventricular WMHs were present. An example of an excluded case is shown in Figure 7.1.

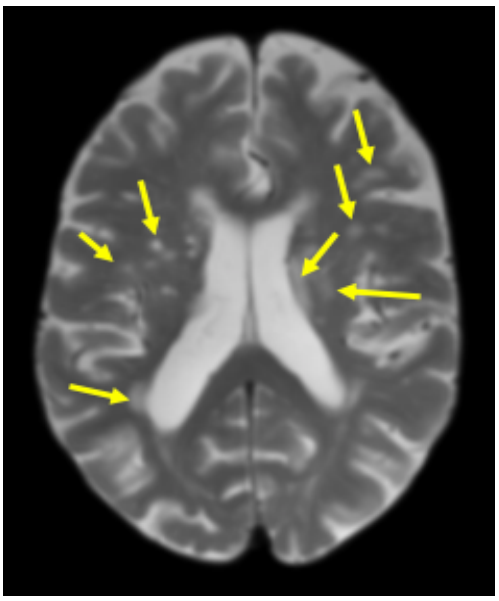

Figure 7.1 Example of a $T_2$ weighted image with extensive white matter hyperintensities., indicated by the yellow arrows.

The study received ethical approval from the South West Frenchay Research Ethics Committee (ref 13/SW/0256), Scotland A REC (ref 16/SS/0223) and UK National Research Ethics Service committees (refs 12/SC/0292 and 13/SC/0362) for participants in Bristol, Oxford and Glasgow, respectively. Ethical approval allowed patients to be in the scanner for up to 20 minutes at Bristol and up to 30 minutes at Oxford and Glasgow. The total scan time allowed included set up of the patient and localisers as well as the MRI protocol. The study was carried out in accordance with the Declaration of Helsinki.

Table 7.1 MRI acquisition parameters.

| | Sequence | TR (ms) | TE (ms) | Resolution ($mm^3$) | | | Acquisition time (minutes: seconds) |
|---|---|---|---|---|---|---|---|
| **Multi-echo $T_2$** | | | | | | | |
| Bristol | GRASE | 3000 | 20,40,60,80,100 | 0.6 x 0.6 x 2.3 | - | - | 3:09 |
| Glasgow | TSE | 12500 | 9.5,66,123 | 1.7 x 1.7 x 2.0 | - | - | 2:03 |
| Oxford | TSE | 12000 | 7.7,77,177 | 1.8 × 1.7 × 2.0 | - | - | 1:50 |
| | | | | | **TI (ms)** | **Flip angle** | |
| **3D $T_1$w:** | | | | | | | |
| Bristol | FFE | 6.84 | 3.18 | 1.0 x 1.0 x 1.1 | - | 8° | 4.54 |
| Glasgow | MP RAGE | 2200 | 2.28 | 0.9 x 0.9 x 0.9 | 900 | 9° | 5.07 |
| Oxford | MP RAGE | 1800 | 4.55 | 1.5 x 1.5 x 1.0 | 900 | 8° | 2.06 |
| **$T_2$w FLAIR:** | | | | | | | |
| Glasgow | TSE | 10000 | 93 | 0.9 x 0.9 x 5.0 | 2500 | 150° | 3.02 |
| Oxford | TSE | 9000 | 96 | 1.9 x 1.9 x 2.0 | 2500 | 150° | 2.08 |
| | | | | | **b value, $s/mm^2$ (multiplicity)** | **Gradient directions** | |
| **Diffusion:** | | | | | | | |
| Bristol | SE-EPI | 3009 | 60.5 | 1.2 x 1.2 x 4.4 | 0(1), 1000(3) | 3 | 0.37 |
| Glasgow | SE-EPI | 8000 | 90 | 0.9 x 0.9 x 2.0 | 0(3), 1000(20) | 20 | 3.03 |
| Oxford | SE-EPI | 5300 | 91 | 1.8 x 1.8 x 5.0 | 0(1), 1000(1) | 3 | 1.00 |

*Note. Parameters include: time of echo (TE), time of repetition (TR), time of inversion (TI), Gradient and Spin Echo (GRASE), Turbo Spin Echo (TSE), radiofrequency spoiled incoherent gradient echo ($T_1$ FFE), 3D $T_1$w Magnetisation Prepared Rapid Acquisition Gradient Echo (MP RAGE), slice selective $T_2$w Fluid Attenuated Inversion Recovery ($T_2$w FLAIR), Spin-Echo Echo Planar Imaging (SE-EPI), milliseconds (ms), millimetres (mm), seconds (s).*

### 7.3.2 MRI

All sites used a 3T MRI scanner with a 32-channel head coil (Bristol: Philips Achieva, Glasgow: Siemens Magnetom Prisma, Oxford: Siemens Magnetom Verio). The MRI protocol detailed in Table 7.1 included: multi *b*-value diffusion for computation of diffusion-weighted and ADC images, multi-echo $T_2$ for computation of $T_2$ relaxation and $T_2$w images, and 3D $T_1$w images for anatomical reference and registration. The approved scan time at Oxford and Glasgow enabled the acquisition of $T_2$w FLAIR as well.

### 7.3.3 Image processing and analysis

Image processing and analysis steps are illustrated in Figure 7.2 and are described in detail below. These methods were developed and implemented by Knight, Damion, McGarry et al., (2019) and Damion, Knight, McGarry et al., (2019) and programs used included MATLAB release 2016b (The MathWorks, Inc., Natick, MA, US), FSL (FMRIB, Oxford, UK), MANGO version 4.1 (Research Imaging Institute, UT Health Science Center, San Antonio, USA) and SPM12 (Wellcome Trust Centre for Neuroimaging).

#### Image registration

To ensure correct alignment between voxels across all images and that the midline of the brain was consistently defined, for each patient, $T_1$w, ADC, DWI, $T_2$w, $T_2$ relaxation and FLAIR images were brain extracted using FSL BET (Smith, 2002) and registered to the same space. This involved non-linear registration of the ADC images to the $T_2$w image space using FSL FNIRT via the diffusion $S_0$ image and the echo summed $T_2$w image. If $T_1$w images were available, the $T_2$w image space was linearly registered (six-degrees of freedom) to the $T_1$w image space, which was subsequently registered to the MNI frame at $1mm^3$ isotropic resolution using FSL FLIRT (Jenkinson & Smith, 2001). Where $T_1$w images were not available, the $T_2$w

image space was, instead, directly registered (linearly) to the MNI frame at 1 $mm^3$ isotropic resolution. All images were then linearly registered to the MNI frame using the registration maps (or combination of) generated by previous stages. The quality of co-registration across all image types was assessed visually by two independent assessors using SPM12. All images were deemed to be acceptably co-registered.

## Image computation

For diffusion data using three orthogonal diffusion-sensitising gradients at a common *b*-value, orientation independent ADC images were calculated using:

$$ADC = -\ln(S_1 S_2 S_3 / S_0^3)/3b$$

Where $S_0$ is the signal without diffusion weighting, $b$ is the *b*-value and $S_1$, $S_2$, $S_3$ are signal intensities at the three orthogonal directions.

For diffusion-weighted data with 20 independent diffusion-gradient directions ($b$ = 1000 $mm^2$ $s^{-1}$) and three $b$ = 0 images, ADC values were obtained from mean diffusivity maps, which were computed using FSL DTIFIT. Effective diffusion-weighted images were created for $b$ = 1000 $mm^2/s$ using the registered $S_0$ and ADC images via:

$$DWI = S_0 e^{(-1000 \times ADC)}$$

Echo-summed $T_2$w images were computed by summing all echoes of the TE series, followed by bias correction using FSL FAST (Zhang et al., 2001). Calculation of $T_2$ relaxation images involved fitting a mono-exponential decay on a voxel-wise basis (described in more detail in Chapter 3, Section 3.7.2).

.

### Identification of ischaemic tissue

The definition of ischaemic voxels was those with ADC values $> 0.2 - 0.4$ $\mu m^2/ms$ and $< 0.55 - 0.6$ $\mu m^2/ms$ as well as ADC values less than one half-width half-maximum from the median ADC of non-ischaemic tissue (Knight, Damion, McGarry et al. 2019). Limits of $T_2 > 30$ ms and $< 200$ ms were also applied to reduce CSF contribution (Knight, Damion, McGarry et al. 2019). These criteria were used to create binary masks to define ischaemic volumes of interest (VOI).

To ensure that all ischaemic regions were correctly identified by this automatic procedure, the location and size of the binary masks in relation to the hypointense regions on the ADC images were visually inspected by Dr Michael Knight and Dr Robin Damion. In some cases, the binary masks included small clusters of random voxels that were not close to the ischaemic region (due to spurious signals). In such cases, the masks were refined by removing all but the largest contiguous cluster, or clusters, in the cases where there was more than one ischaemic region (Knight, Damion, McGarry et al., 2019). The smallest acceptable cluster size was a user-defined parameter, which was set on a case by case basis (Knight, Damion, McGarry et al., 2019).

Selection of non-ischaemic reference VOIs required reflecting the ischaemic VOI about the midline of axial slices (medial/lateral), applying the above $T_2$ limits and manually editing if CSF was visible within the VOI. VOIs with visible CSF containing volumes were evident as hyperintense regions near the ventricles, which was further confirmed by clear tails present in histograms of the signal distribution within the VOI. In such cases, VOIs were manually refined using the MANGO multi-image analysis GUI, which enables the areas corresponding to the histogram tails to be automatically selected and deleted from the VOI.

### Computation of image intensity ratios

To approximate changes in image intensities due to ischaemia, image intensity ratios were calculated for each patient and image type, which involved dividing the mean value in the ischaemic VOI by the mean value in the non-ischaemic reference VOI. Pre-ratio values were in milliseconds (ms) for $T_2$ relaxation images, $\mu m^2$/ ms for ADC, and signal intensities (SI, which as explained in Chapter 3, Section 3.7.1 are the arbitrary numbers that represent the signal strength) for weighted images (DWI, $T_2$w, FLAIR). The purpose of computing ratios instead of using hemispheric differences in mean values (as per Siemonsen et al., 2009) was to reduce concerns that may arise from differences in pulse sequences, structures and parameters between imaging sites.

### Visual DWI/FLAIR mismatch

Four independent raters with experience in stroke MRI assessed DWI and FLAIR images. Raters were blinded to clinical details and asked to identify cases showing a *match* (visible hyperintensities in the same region on DWI and FLAIR), a *mismatch* (visible hyperintensity on DWI, not FLAIR) or cases they were uncertain about (no response) For an example of match and mismatch cases see Figure 4.10 (Chapter 4, Section 4.4.2). Raters viewed and windowed the images according to personal preference. An arbitrator with over 25 years of experience in stroke MRI assessed images where there was uncertainty or disagreement between raters. Final classification as match or mismatch was based on majority classification, or the arbitrator's adjudication when there was a 2-2 split in opinion.

Figure 7.2 Summary of image processing steps. **1.** All images were registered to the same space. **2.** ADC and $T_2$ limits defined the ischaemic volumes of interest (VOI). **3.** Non-ischaemic reference VOIs were created by reflecting the ischaemic VOI across the sagittal midline applying ADC and $T_2$ limits and manually editing if necessary. **4.** Image intensity ratios were determined by dividing the average image intensity of the ischaemic VOI by the average image intensity in the non-ischaemic VOI. Image intensity refers to the signal intensity values represented in the weighted images as well as relaxation times and ADC values represented in the parametric maps. Images shown are from the same patient (time from onset = 6 hours 49 minutes, age = 59, thrombolysed before MRI, NIHSS = 13) and are representative of the image quality of scans acquired for all patients.

### 7.3.4 Statistical analysis

Data from all 35 patients and the sub-cohort of the 17 patients with the additional FLAIR scans were analysed separately. This separation was to allow for a fair comparison of the performance of FLAIR with other MRI classifiers. Statistical analysis was carried out using GraphPad Prism version 8.02 (GraphPad Software, La Jolla California USA), MedCalc Statistical Software version 19.0.5 (MedCalc Software bvba, Ostend, Belgium) and MATLAB release 2019a (The MathWorks, Inc., Natick, MA, US).

Data were assessed for normality using the Shapiro-Wilk test (Shapiro & Wilk, 1965). The difference between the average ADC values in the ischaemic VOI between thrombolysed and non-thrombolysed patients was assessed using unpaired t-tests. The relationships of image intensity ratios with time from symptom onset were assessed using Pearson's correlations for normally distributed data and Spearman's and Kendall's correlations for non-normal data. Randolph's free-marginal Fleiss Kappa calculator (Randolph, 2005, 2008) was used to measure the agreement between the four DWI/FLAIR mismatch raters. All statistical tests were two-tailed with a significance level of $p < 0.05$. 95% confidence intervals (CI) were calculated as ± 1.96 * the standard error (SE) unless otherwise stated. The performance of MRI classifiers was compared using measures of accuracy (accuracy, sensitivity/recall, specificity), correctness (positive and negative predictive values), and probability (logistic regression) (described in Appendix A).

#### All patients

For a visual indication of the overall performance of MRI classifiers, Receiver Operating Characteristic (ROC) curves were plotted. For a numerical indication of overall performance, areas under the ROC curves (AUC) were calculated and statistically compared using non-parametric methods that control for multiple comparisons (DeLong et al., 1988). Optimal image intensity ratio cut-offs were

derived by the maximum Youden J Index, which identifies the cut-off that minimises misclassification by giving equal weight to sensitivity and specificity (Youden, 1950). Accuracy, sensitivity, specificity, positive predictive value (PPV) and negative predictive values (NPV) associated with these cut-offs were also calculated.

For further insight into the predictive performance of MRI classifiers, a logistic regression analysis using MATLAB's Classification Learner app was also performed. Predictive generalised linear models were produced for individual image intensity ratios (i.e., ADC ratio, DWI ratio, $T_2$w ratio, $T_2$ relaxation time ratio separately) as well as a combination of all of the image intensity ratios. Predictive generalised linear models took the form of:

$$Y = \alpha + \beta_1\chi_1 + \beta_2\chi_2 + \beta_3\chi_3 + \beta_4\chi_4 \ldots$$

Where, $Y$ is the predicted log odds of the patient being within the treatment window ($Y = 1$ for onset time $< 270$ minutes, $Y = 0$ for onset time $> 270$ minutes), $\alpha$ is the estimated intercept, $\beta_1$ is the estimated regression coefficient, $\chi_{1\ldots n}$ are the predictors (e.g. image intensity ratio of ADC, DWI, $T_2$w, $T_2$) (Peng et al., 2002). The probability of being within the treatment window ($P$) could thus be calculated as:

$$P = \frac{e^{(\alpha + \beta_1\chi_1 + \beta_2\chi_2 + \beta_3\chi_3 + \beta_4\chi_4 \ldots)}}{1 + e^{(\alpha + \beta_1\chi_1 + \beta_2\chi_2 + \beta_3\chi_3 + \beta_4\chi_4 \ldots)}}$$

Where the closer P is to 1, the higher the probability that the patient is within the 4.5 hour treatment window.

For a visual indication of the predictive power of the models, probability plots for each qMRI parameter (i.e., ADC ratio, DWI ratio, $T_2$w ratio, $T_2$ relaxation time ratio) were generated. This involved calculating the probability of each patient being within the thrombolysis treatment window (P) and plotting these probabilities against the image intensity ratio of each patient, to produce the curves, shown in Figure 7.6 of the Results (where the x-axis is the image intensity ratio of the individual patient, and the y-axis is the estimated P). P for each patient was calculated by solving the probability equation above using the coefficients of the generalised linear models from the logistic regression (shown in Table 7.3 of the Results Section) and the image intensity ratio obtained from the individual patient. For comparison, the true classification of each patient (Y = 1 indicates within the treatment window, and Y = 0 indicates beyond the treatment window) was also plotted against the image intensity ratio (X-axis), to give two parallel lines that correspond to the dichotomous outcomes (Figure 7.6 of the Results Section).

The overall performance of the models was evaluated by comparing the significance of the chi-squared statistic ($\chi^2$) and comparing the Akaike information criterion (AIC) values (Akaike, 1974) corrected for sample size ($AIC_c$, see Appendix A), where a low $AIC_c$ indicates a high-quality model (Symonds & Moussalli, 2011). For the combined model, the significance level of the t-statistic associated with each of the estimated coefficients ($\beta$) was used to assess the extent of the contribution of each parameter to the model.

### Sub-cohort with FLAIR MRI

Different methods of evaluation were applied to the sub-cohort of patients with the additional FLAIR scans due to the imbalance in class sizes (n = 5 with onset times less than 4.5 hours, n = 12 with onset times greater than 4.5 hours). In datasets where there is a class imbalance, traditional ROC curves and AUCs are not recommended as they place more weight on the larger class and portray an overly optimistic view of overall performance (Berrar & Flach, 2012; Davis & Goadrich,

2006). Instead, in cases where there is low prevalence in the positive compared to the negative class (i.e., five patients within the treatment window in this study) it has been recommended to use performance metrics such as precision/PPV and recall/sensitivity, which do not use the true negative contingency class in their definitions (Berrar & Flach, 2012; Davis & Goadrich, 2006; Ozenne et al., 2015). Flach and Kull's (2015) precision-recall-gain (PRG) approach performs well in class-imbalanced data sets while maintaining the benefits associated with ROC analysis, and so this method was used instead of traditional precision-recall approaches (Davis & Goadrich, 2006) and ROC analysis (see Flach & Kull, 2015 and Appendix A).

For a visual indication of the overall performance of MRI classifiers, precision-recall-gain curves (PRG) were plotted and for a numerical indication, areas under the PRG curves (AUPRG) were calculated using open-source MATLAB software (see http://people.cs.bris.ac.uk/~flach/PRGcurves//). An AUPRG of zero indicates a trivial (random) classifier, and positive and negative AUPRGs indicate more and less optimal classifiers, respectively. In order to compare the performance of image intensity ratios with the visual DWI/FLAIR mismatch, $F_1$ scores (Rijsbergen, 1979) were calculated for the DWI/FLAIR mismatch and image intensity ratio cut-offs. The $F_1$ score gives equal weighting to the importance of precision and recall and is considered an appropriate evaluation measure for imbalanced data sets (Bekkar & Djemaa, 2013). For each parameter, the image intensity ratio with the highest $F_1$ score was chosen for comparison.

## 7.4 Results

Sixty-eight patients were enrolled in the study. Thirty were not included in the final analysis due to: bilateral stroke (n = 4), extensive WMHs (n =2) for which the mirror-reference approach cannot be applied, no clear ischaemia on ADC scans (n = 11), uncertainty over stroke diagnosis (n = 3 ), movement artefacts (n = 1), ADC or $T_2$ not acquired (n = 4 ), vague onset time (n = 3), MRI declined after consent (n = 1) and the early termination of scanning due to claustrophobia (n = 1).

A summary of the clinical and imaging characteristics of all 35 patients and the sub-cohort of 17 patients with FLAIR scans are shown in Table 7.2. On average, the MRI protocol lasted eight minutes at Bristol, 14 minutes at Glasgow and seven minutes at Oxford. Results for Shapiro-Wilk tests, Pearson's, Spearman's and Kendall's correlations are given in Appendix B (Table B1). Mean ADC values ($\mu m^2/ms$) in ischaemic and non-ischaemic-reference VOIs were consistent with previous reports in patients (Sener, 2001). There was no difference between average ADC values in ischaemic VOIs between thrombolysed and non-thrombolysed patients, for all 35 patients (thrombolysed mean = 0.50, SD = 0.05 vs non-thrombolysed mean = 0.54, SD = 0.05, t(33) = 2.02, $p = 0.052$) and the sub-cohort with FLAIR scans (thrombolysed mean = 0.49, SD = 0.06 vs non-thrombolysed mean = 0.54 SD = 0.02, t(15) = 1.35, $p = 0.197$)

Table 7.2 Clinical and imaging characteristics.

| | **All patients** | **Sub-cohort with FLAIR** |
|---|---|---|
| **Patients, n (%):** | 35 | 17 |
| **Female, n (%):** | 13 (37.1 %) | 3 (17.6%) |
| **Age, median (min - max):** | 68 (31 - 85) | 67 (49 - 85) |
| **NIHSS*, median (min - max):** | 8 (1 - 28) | 8 (1 - 28) |
| **Study site:** | | |
| Bristol | 17 (48.6%) | 0 |
| Oxford | 5 (14.3%) | 4 (23.5%) |
| Glasgow | 13 (37.1%) | 13 (75.5%) |
| **Stroke type †, n (%):** | | |
| LACS | 12 (34.3%) | 6 (35.3%) |
| PACS | 12 (34.3%) | 9 (52.9%) |
| POCS | 3 (8.6%) | 0 |
| TACS | 8 (22.9%) | 2 (11.8%) |
| **Left hemisphere, n (%):** | 16 (45.7%) | 9 (52.9%) |
| **Thrombolysis:** | | |
| Patients received rtPA, n (%) | 26 (74.3%) | 14 (82.4%) |
| Median time from onset to rtPA, hours:mins (min-max) | 2:05 (1:02 - 3:55) | 2:32 (1:05 - 3:55) |
| Median time from rtPA to MRI, hours:mins (min-max) | 3:37 (0:29 - 7:18) | 4:20 (1:10 - 7:18) |
| **Time from onset to MRI:** | | |
| All patients, median hours:mins (min-max) | 5:34 (2: 25 - 9:29) | 6:46 (2:28 - 9:29) |
| 0 – ≤ 4.5 hours: | | |
| patients, n (%) | 16 (45.7%) | 5 (29.4%) |
| median hours:mins (min-max) | 3:22 (2:25 – 4:25) | 3:00 (2:28 – 3:10) |
| > 4.5 – ≤ 9.5 hours: | | |
| patients, n (%) | 19 (54.3%) | 12 (70.6%) |
| median hours:mins (min-max) | 6:55 (5:08 – 9:29) | 6:59 (5:34 – 9:29) |
| **VOI characteristics:** | | |
| Median ADC defined ischaemic volume, mL (min-max) | 1.99 (0.04 - 54.6) | 5.50 (0.11 – 25.01) |
| Median ischaemic ADC, $\mu m^2$/ms (min-max) | 0.53 (0.39 - 0.58) | 0.51 (0.39 - 0.58) |
| Median non-ischaemic ADC, $\mu m^2$/ms (min-max) | 0.77 (0.36 - 1.00) | 0.79 (0.69 - 0.89) |

Note. rtPA = recombinant tissue plasminogen activator. *Scores on the National Institutes of Health Stroke Scale (NIHSS) range from 0 - 42, higher scores indicate greater deficit. †Strokes classified according to the Oxford Stroke Classification Scale (Bamford et al., 1991). LACS = Lacunar, PACS= Partial Anterior Circulation, POCS = Posterior Circulation, TACS = Total Anterior Circulation. VOI = volume of interest. ADC = apparent diffusion coefficient. mL = millilitres, ms = milliseconds.

### 7.4.1 All 35 patients

The $T_2$ relaxation time intensity ratio was the only parameter that correlated significantly with time from symptom onset (Figure 7.3). All correlation coefficients are shown in Appendix B (Table B1).

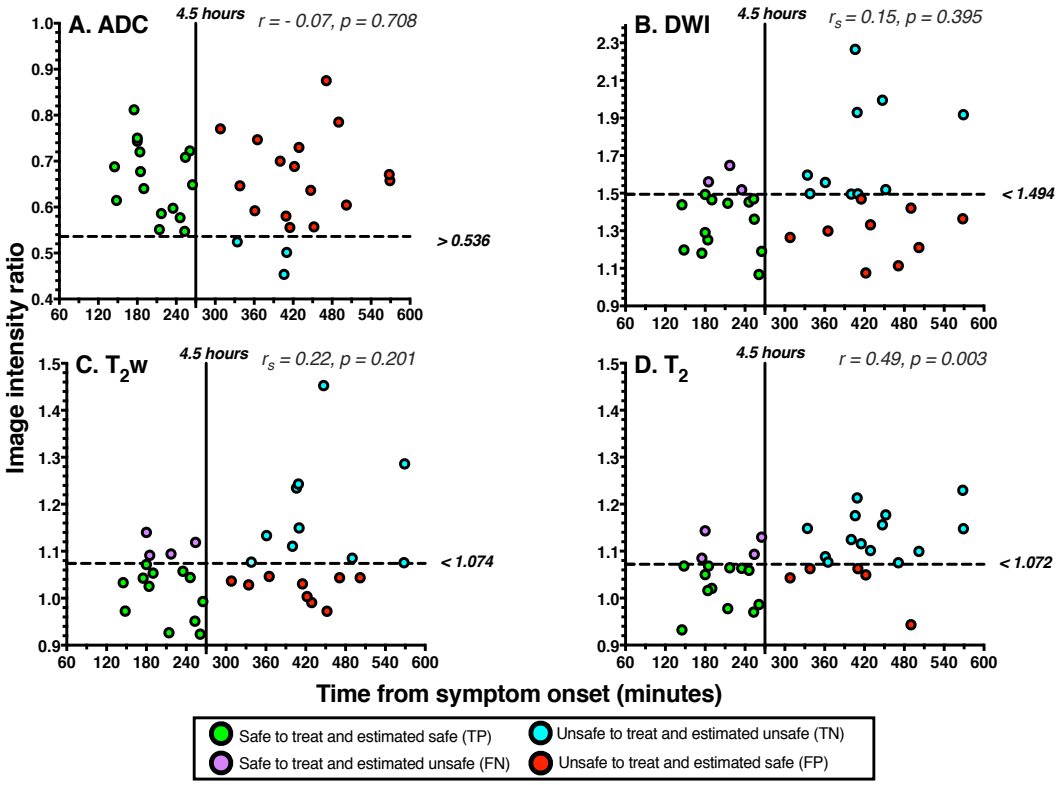


Figure 7.3 Relationship of image intensity ratios with time from symptom onset for **A.** ADC, **B.** DWI, **C.** $T_2$w and **D.** the $T_2$ relaxation time. Correlation coefficients and p values are shown for each parameter. Pearson's correlation coefficients (r) are shown for ADC and $T_2$ as they were normally distributed. Spearman's rank correlation coefficients ($r_s$) are shown for DWI and $T_2$w as they were not normally distributed. Horizontal dashed lines represent optimal image intensity ratio cut-offs identified by the maximum Youden J index, which are labelled to the right of each Figure. Vertical solid lines represent the 4.5 hour thrombolysis treatment-window cut-off. Data points represent individual patients and are colour-coded according to the classification instructed by the optimal image intensity ratios. Green indicates a true positive case (TP), blue indicates a true negative case (TN), purple indicates a false negative case (FN) and red indicates a false positive case (FP). Data is from all 35 patients.

The $T_2$ relaxation time image intensity ratio also showed the highest overall ability at distinguishing between patients scanned before and after 4.5 hours as the ROC curve was closer to the top left-hand corner of the ROC graph, and it was the only parameter with a significantly high AUC (Figure 7.4). There was no statistical difference between the AUCs of any of the parameters (statistics shown in Appendix B, Table B2).

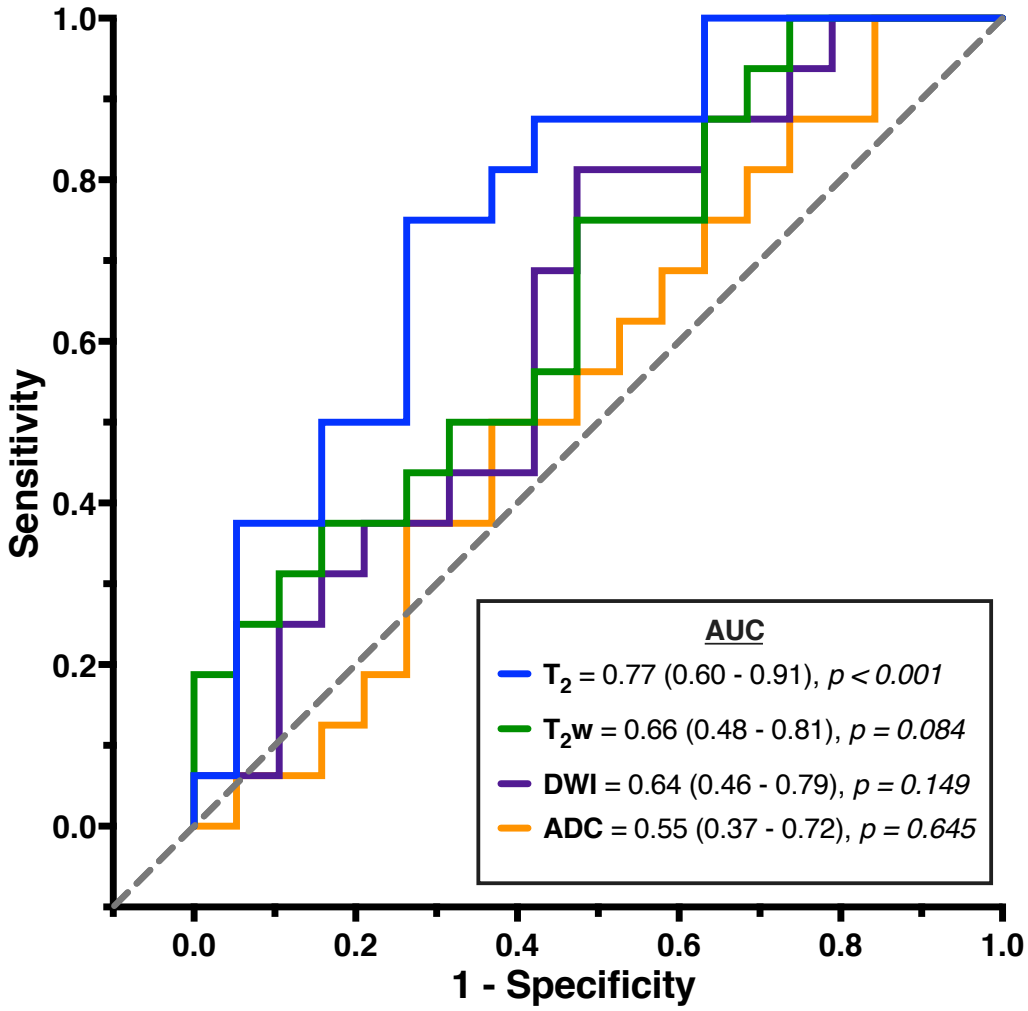


Figure 7.4 ROC curves showing the overall ability of image intensity ratios for distinguishing between ischaemic stroke patients scanned before or after 4.5 hours from symptom onset. Lines closer to the grey dashed 0.5 reference line indicates parameters with poor overall ability. The closer the line to the top left-hand corner of the ROC graph, the higher the overall ability. AUC and p values are displayed for each MRI parameter with 95% binomial exact confidence intervals in brackets. An AUC with $p > 0.05$ indicates an AUC that does not significantly differ from an AUC of 0.5 and therefore performs no better than chance. Results are from all 35 patients.

Figure 7.5 shows accuracy, sensitivity and specificity values for optimal image intensity ratio cut-offs. As seen, the $T_2$ relaxation time ratio had the highest accuracy, and the sensitivity and specificity levels were high and comparable. For ADC, DWI and $T_2$w there was a trade-off, where most patients within the thrombolysis time-window were correctly identified (high sensitivity) but at the expense of falsely regarding many patients beyond the time-window as within it (low specificity). With these optimal image intensity-ratio cut-offs, PPVs were calculated for $T_2$ (70.59% CI: 51.79 – 84.28), ADC (50.0% CI: 45.15 - 54.85), DWI (59.09 % CI: 45.97 – 71.03), and $T_2$w (57.14% CI: 43.43 – 69.84), and indicate that the $T_2$ ratio has the highest probability of correctly predicting whether a patient that is identified by this parameter as being within the treatment window, is actually within the window. Except for ADC, where NPV = 100%, NPVs were comparable for DWI (76.92% CI = 52.46 – 86.6), $T_2$w (71.43% CI = 49.16 – 86.6) and $T_2$ (77.78% CI = 58.97 – 89.50). The performance of image intensity ratio cut-offs is further illustrated in Figure 7.3, which shows how patients were classified when cut-offs were applied.

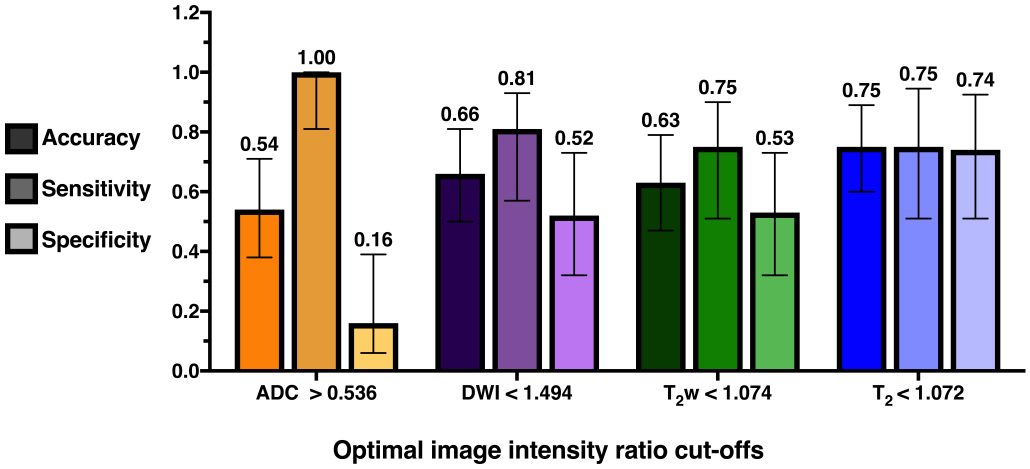


Figure 7.5 Accuracy, sensitivity and specificity of optimal image intensity ratio cut-offs identified by the maximum Youden J index. For each parameter, the first bar represents the accuracy, the second represents sensitivity, and the third represents specificity. Corresponding values are labelled above the error bars, which represent the 95% confidence intervals. Results are from all 35 patients.

Derived from logistic regressions, Figure 7.6 depicts that the probability that a patient is within the treatment window is higher when the DWI, $T_2$w and $T_2$ ratios are smaller and that the $T_2$ relaxation time ratio offers the highest probability (up to 90%). As the ADC values decrease during ischaemia, higher ADC ratios indicate a higher probability of being within the treatment window. However, of those plots displayed in Figure 7.6, the results of the regressions indicate that only the $T_2$ relaxation time and the $T_2$w ratios were significant predictors of whether the patient was within the treatment window (Table 7.3).

Table 7.3 also shows that the combined model involving all four image intensity ratios significantly predicted the probability of a patient being within the treatment window, but not to the same extent as the single-parameter regressions on the $T_2$w ratio and, in particular, the $T_2$ relaxation time ratio. Closer examination of the contribution of each parameter in the combined model (p values, Table 7.3) shows that the intercept was the only significant contributor to the model and that the $T_2$ ratio, though not significant, had the most dominant contribution ($p = 0.068$). Overall, the $T_2$ relaxation time ratio only model was the best predictor of whether a patient was within or beyond the treatment window and compared to other models, it was the most significant and had the lowest $AIC_c$.

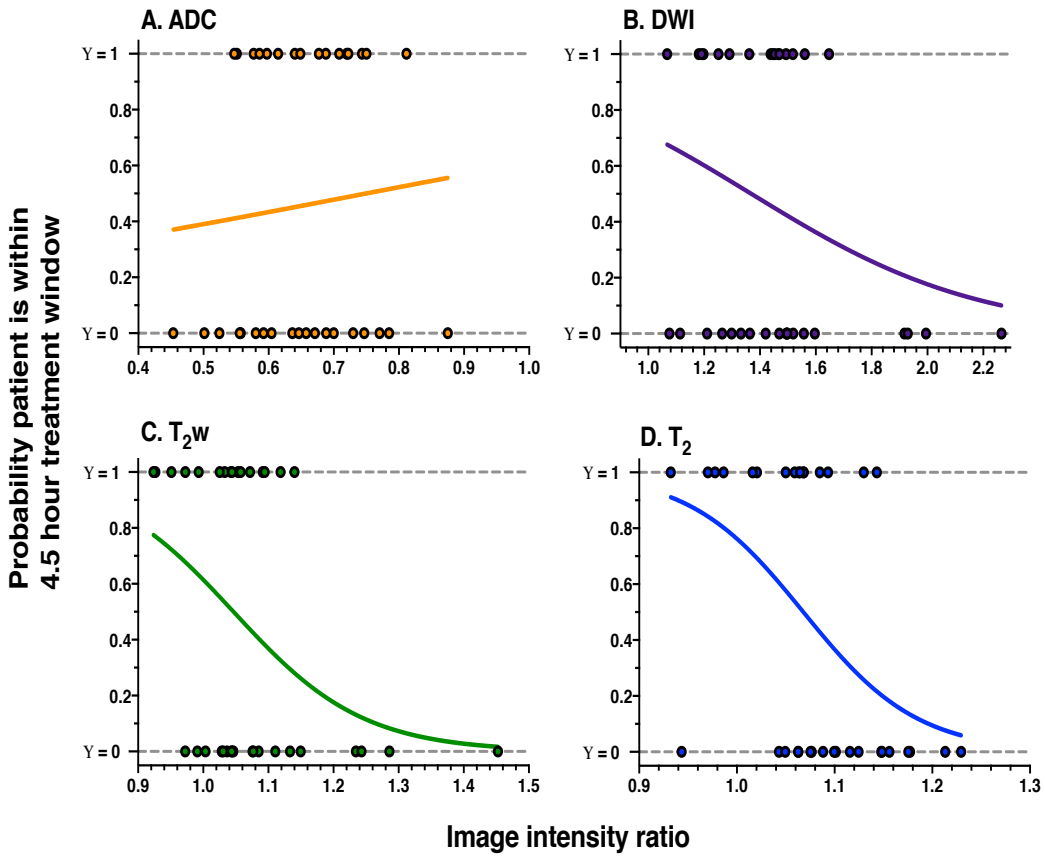


Figure 7.6 Probability plots for **A.** ADC, **B.** DWI, **C.** $T_2$w, and **D.** $T_2$ relaxation time image intensity ratios, derived from all 35 patients. The curves are the logistic fits that model the probability of a patient being within the 4.5 hour thrombolysis treatment window (y-axis) as a function of the image intensity ratio (x-axis). Dots represent image intensity ratios of individual patients that are within (Y = 1) or beyond (Y = 0) the treatment window.

Table 7.3 Information for the logistic regression analysis.

| Model | β (SE) | t-statistic | p | Overall model evaluation | | | |
|---|---|---|---|---|---|---|---|
| | | | | $\chi^2$ | df | p | AIC |
| **ADC** | | | | 0.24 | 33 | 0.626 | 52.03 |
| ADC ratio | 1.79 (3.68) | 0.49 | 0.627 | - | - | - | - |
| Intercept | -1.34(2.43) | -0.55 | 0.582 | - | - | - | - |
| **DWI** | | | | 2.76 | 33 | 0.097 | 49.50 |
| DWI ratio | -2.44(1.61) | -1.51 | 0.130 | - | - | - | - |
| Intercept | 3.34 (2.33) | 1.44 | 0.150 | - | - | - | - |
| **$T_2$w** | - | - | - | 5.38 | 33 | 0.020* | 46.88 |
| $T_2$w ratio | -10.05 (5.29) | -1.90 | 0.057 | - | - | - | - |
| Intercept | 10.514 (5.58) | 1.88 | 0.060 | - | - | - | - |
| **$T_2$** | | | | 8.41 | 33 | 0.004* | 43.85 |
| $T_2$ ratio | -17.13 (7.09) | -2.42 | 0.016* | - | - | - | - |
| Intercept | 18.3 (7.64) | 2.39 | 0.017* | - | - | - | - |
| **Combined** | | | | 9.75 | 30 | 0.045* | 48.52 |
| Intercept | 22.05 (10.23) | 2.15 | 0.031* | - | - | - | - |
| ADC ratio | -0.07 (5.90) | -0.01 | 0.990 | - | - | - | - |
| DWI ratio | 0.72 (3.52) | 0.21 | 0.837 | - | - | - | - |
| $T_2$w ratio | -7.57 (8.78) | -0.86 | 0.389 | - | - | - | - |
| $T_2$ ratio | -14.05 (7.69) | -1.83 | 0.068 | - | - | - | - |

Note. $\beta$ is the estimated coefficient of the ratio or intercept, SE is the estimated standard error of $\beta$, t-statistic = $\beta$ divided by the SE, $p$ is the significance level, * indicates $p < .05$, $\chi^2$ is the chi-squared statistic, $df$ = degrees of freedom, AIC = Akaike information criterion.

### 7.4.2 Sub-cohort with FLAIR MRI

The agreement between raters of the DWI/FLAIR mismatch was intermediate to good, with a free marginal Fleiss' kappa value of 0.59 (CI = 0.36 – 0.82), and 72.8% agreement (Randolph, 2005). All image intensity ratios did not correlate significantly with time from symptom onset (Appendix B Table B1), likely due to the small number of patients in the sub-cohort (Table 7.2). Figure 7.7 shows the PRG curves and associated AUPRGs. The AUPRGs were highest for the $T_2$ relaxation time ratio and DWI ratio, suggesting both parameters have good overall ability at identifying patients within the thrombolysis treatment window. However, the $T_2$ relaxation time curve was closest to the top right-hand corner of the graph, possibly suggesting a superior ability to the $T_2$w ratio. The AUPRGs were lowest for the $T_2$w and FLAIR ratios, demonstrating poor overall ability. Superior performance of $T_2$ relaxation compared to other parameters was also reflected by the $F_1$ score which was highest for the $T_2$ relaxation time ratio (0.73, CI = 0.52 - 0.94), lower for the ADC (0.59, CI = 0.35 – 0.82), DWI (0.67, CI = 0.44 – 0.89), $T_2$w (0.59, CI = 0.35 - 0.82) and FLAIR (0.57 CI = 0.34 – 0.81) ratios, and very low for the DWI/FLAIR mismatch (0.25, CI = 0.15 – 0.35).

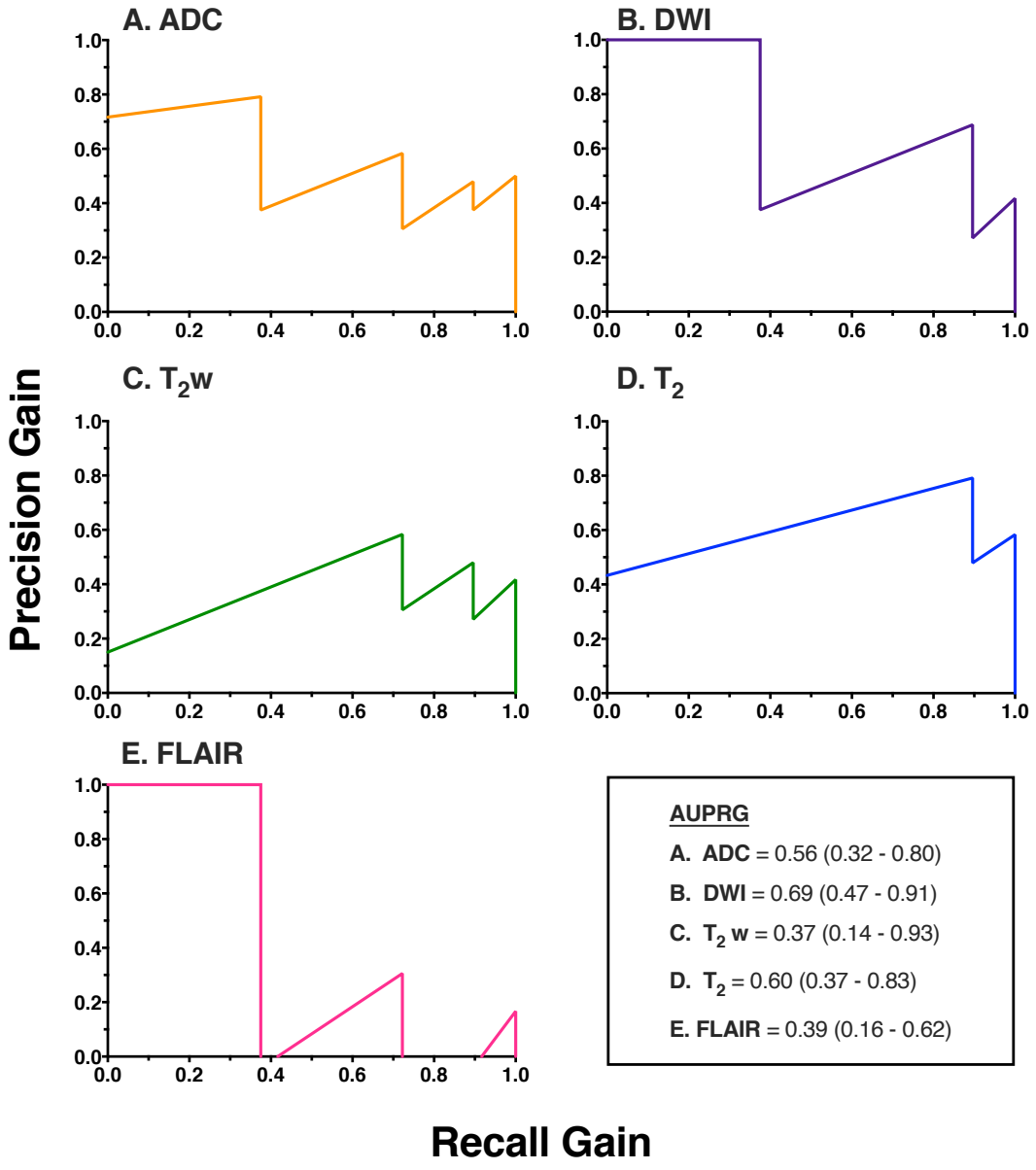


Figure 7.7 Precision-recall-gain (PRG) curves and areas under the PRG (AUPRG) curves from the sub-cohort of patients with additional FLAIR scans. The y-axis shows precision-gain, and the x-axis shows recall-gain values. Lines closest to the top right of the graph indicate parameters with high overall ability to identify patients scanned before 4.5 hours. An AUPRG of zero indicates a trivial classifier, and positive and negative AUPRGs indicate more and less optimal classifiers, respectively. AUPRG values are given, with 95% confidence intervals in brackets.

## 7.5 Discussion

In this study, the overall performance of quantitative and visual MRI based methods for estimating stroke onset time, in the same cohort of hyperacute stroke patients was compared (McGarry et al., 2020). The $T_2$ relaxation time ratio outperformed ADC, DWI, $T_2$w, FLAIR image intensity ratios and the visual DWI/FLAIR mismatch, and combining ADC, DWI, $T_2$w and $T_2$ ratios showed no benefit. Results, therefore, suggest that the acquisition of $T_2$ relaxation times, with ADC for identification of the ischaemic region, may be sufficient for estimating stroke onset time (McGarry et al., 2020).

The results of this study support recent conclusions drawn from preclinical (Chapter 5, McGarry et al., 2016a; Rogers, McGarry et al., 2014) and clinical studies (Damion, Knight, McGarry et al., 2019; Duchaussoy et al., 2019) that the $T_2$ relaxation time detects brain ischaemia and estimates onset time more accurately than MRI parameters derived from weighted images (McGarry et al., 2020). Studies in rat models of ischaemia reported strong relationships of the $T_2$ relaxation with time from stroke onset (Chapter 5, McGarry et al., 2016a, 2016b) and that onset time estimates made with $T_2$ had a lower margin of error than when intensities of weighted images were used (McGarry et al., 2016a; Norton et al., 2017; Rogers, McGarry et al., 2014). The $T_2$ relaxation time also demonstrated higher overall ability at differentiating between scans performed before and after three hours from ischaemia onset in rat models (Chapter 5, McGarry et al., 2016b).

As will be discussed further in the General Discussion of this thesis (Chapter 9), this study adds to knowledge in stroke timing literature by providing the first direct comparison of the performance of the parametric approach to qMRI (i.e., ADC and the $T_2$ relaxation time) as a method for stroke timing with commonly researched timing methods based on the signals in weighted images (i.e., the DWI/FLAIR mismatch, DWI ratio, $T_2$w ratio, FLAIR ratio). Previous to this study, there had been a range of clinical studies on the performance of individual MRI based stroke

timing, for example, separate studies on DWI/FLAIR mismatch (e.g., Aoki et al., 2010; Thomalla et al., 2011, 2018), the DWI image intensity ratio (e. g., Chen et al., 2019; Emeriau et al., 2016; Wouters et al., 2018), the FLAIR image intensity ratio (e.g., Song et al., 2012; Wouters et al., 2016) and the $T_2$ relaxation time ratio (e.g., Duchaussoy et al., 2019; Damion, Knight, McGarry et al., 2019; Knight, Damion, McGarry et al., 2019; Siemonsen et al., 2009). There had also been studies comparing one or more approaches, for example, the performance of the visual based DWI/FLAIR mismatch versus the performance of signal intensity ratios represented in weighted images (e.g., Cheng et al., 2013; Emeraiu et al., 2016; Madai et al., 2016; Petkova et al., 2010) and the strength of the correlation of FLAIR image intensity ratio compared to the $T_2$ relaxation time ratio (Duchaussoy et al., 2019). Thus, before this study, it was not clear which MRI stroke timing method should be studied further. As a result of this study, it is now clear that the $T_2$ relaxation time requires further study as a stroke timing parameters.

Patient studies have shown the $T_2$ relaxation time to have a strong linear relationship with time from symptom onset and high overall ability at distinguishing between patients within and beyond the thrombolysis time-window (Duchaussoy et al., 2019; Knight, Damion, McGarry et al., 2019; Siemonsen et al., 2009). In this study, the AUC of the $T_2$ relaxation time ratio shows that 77% of the time a randomly selected patient scanned within 4.5 hours of symptom onset had a lower $T_2$ than a randomly selected patient scanned at a time later than 4.5 hours. Similarly, previous patient studies have reported 76% using hemispheric differences in $T_2$ relaxation times at 1.5T for a three hour time-window (Siemonsen et al., 2009), and at 3T for a 4.5 hour time-window, 71% using the $T_2$ change (difference) and 81% using a user-independent technique to quantify $T_2$ changes (Knight, Damion, McGarry et al., 2019).

The potential utility of FLAIR imaging for estimating onset time has received considerable attention within the stroke imaging literature (e.g., see Etherton et al., 2018 for review) but has only recently been directly compared to the $T_2$

relaxation time (Duchaussoy et al., 2019). Results by Duchaussoy et al. (2019) and from this study, suggest that the $T_2$ relaxation time will provide a more accurate estimation of stroke onset time than FLAIR-based approaches. Duchaussoy et al. (2019) reported a stronger relationship for $T_2$ relaxation with time from symptom onset compared to FLAIR image intensities ($T_2$: $r = 0.65$ vs FLAIR: $r = 0.18$) in a cohort of stroke patients scanned within 4.5 hours of symptom onset. Here these findings were extended by showing that the stronger relationship with time also applies when scans performed up to nine hours from symptom onset are considered (all patients: $r = 0.49(T_2)$; sub-cohort: $r = 0.35(T_2)$, $r_s = 0.25$(FLAIR). This extension across a longer time frame is important because it is well recognised that the signal of FLAIR images does not increase much within the first 4.5 hours of symptom onset (the premise of the DWI/FLAIR mismatch approach). Therefore, the low correlation of FLAIR with time reported by Duchaussoy et al. (2019) could just be representative of the limited time frame for which FLAIR was measured. Furthermore, although in early 2020, the licencing limit for rtPA is still 4.5 hours, as IA rtPA and mechanical thrombectomy start to become more routine practice in hospitals, there will be greater need to identify patients within six hours of symptom onset for IA rtPA. (Berkhemer et al., 2015) and between six and 24 hours for thrombectomy (Nogueira et al., 2018; Powers et al., 2018).

In further support of previous research, in the sub-cohort of patients with additional FLAIR scans, the $T_2$ relaxation time ratio demonstrated a much higher overall ability than the FLAIR ratio at identifying patients scanned within the thrombolysis treatment window. The ability of the FLAIR ratio and the DWI/FLAIR mismatch approach was comparatively weak, which is in accordance with previous studies that have reported low sensitivity of FLAIR-based methods (e.g., Ebinger et al., 2010; and see Wouters et al., 2014 and Etherton et al., 2018 for reviews). The changes in $T_2$ relaxation that occur during early ischaemia reflect the radical changes in water dynamics caused by anoxic depolarisation, whereby water is shifted from the extracellular to intracellular compartment, followed by the time-dependent breakdown of intracellular macromolecules (Knight, McGarry

et al., 2016). The same pathophysiological factors that cause changes in $T_2$ relaxation therefore also contribute to the signal of images with a $T_2$ weighted component, which will explain why other patient studies have reported a relationship for DWI and FLAIR image intensities with time from symptom onset (e.g., Chen et al., 2019; Wouters et al., 2018).

It is likely that the relationships of the DWI ratio and FLAIR ratios with time from symptom onset were not detected in this study because it was not powered to detect a relationship in these specific parameters. Wouters et al. (2018) reported a moderate correlation of the FLAIR ratio with time from symptom onset ($r = 0.4$, $p < 0.01$) in a clinical cohort scanned in the same time frame as the present study (within nine hours of symptom onset). Based on Wouters et al.'s (2018) r value, a priori power analysis (see Appendix A for the power analysis output) showed that to be able to detect the same strong relationships with 90% probability and $p < 0.05$, at least 61 FLAIR scans within nine hours of onset would be required. Whereas, based on Siemonsen et al.'s (2009) correlation of $T_2$ differences ($r = 0.5$, within six hours of onset) and the present study's correlation of the $T_2$ image intensity ratio ($r = 0.5$ within 9 hours of onset), to be able to detect a relationship of $T_2$ with time, with 90% probability and $p < 0.05$, at least 37 patients would be required. This power analysis suggests the present study, which had 35 patients, was powered to detect the relationship with $T_2$ over time, but not FLAIR and further indicates $T_2$ is a more robust parameter for onset time estimation, as it is a more easily detectable qMRI parameter.

Despite the complexity of contributions to the measured $T_2$ relaxation time, being a single quantitative parameter, it is a more accurate measure of stroke onset time (and, possibly, of pathophysiological changes in ischaemia) than image intensities from weighted images which are also influenced by other factors such as proton-density, $T_1$ relaxation, pulse sequence parameters, and inhomogeneities in $B_0$ and $B_1$. The increase in $T_1$ relaxation during ischaemia would decrease the $T_2$w and FLAIR signals in ischaemic regions unless the images are acquired with very long

TR (>10000 ms at 3T) (McGarry et al., 2016a), which may explain why $T_2$w and FLAIR ratios did not increase significantly in this study. Bias field problems are particularly problematic in weighted images and would result in a misrepresentation of the change in MR signals due to ischaemia. The benefit of quantifying the $T_2$ relaxation time is that in computing the $T_2$ images, sources of error described above are removed. Thus, using $T_2$ relaxation instead of weighted images for stroke timing utilises the dependence of $T_2$ on ischaemia while removing confounding factors, making it a potentially more reliable stroke timer.

This study has some limitations that require consideration. Firstly, it was a pilot study with a modestly sized unselected cohort of people with stroke symptoms, consisting of strokes of varying size and severity, that occurred in different vascular territories and tissue types. Recent results suggest the time dependency of $T_2$ during the first nine hours of stroke does not differ between grey and white matter (Damion, Knight, McGarry et al., 2019) but it is currently unclear whether this is true for different vascular territories. A previous study found the size of the ischaemic region to be a mediating factor in the relationship of DWI image intensity ratios with time from onset (Madai et al., 2016). It is, therefore, possible that the wide range of ischaemic regions sizes included in this study introduced some variability in the data, which could underlie the weak correlations of some of the parameters. Other clinical variables, which could not be accounted for in this study, may also affect the relationship of image intensity ratios over time. For example, collateral status has been shown to influence the relationship of FLAIR image intensities with time from symptom onset (Wouters et al., 2016).

Secondly, due to the clinical nature of the study, the majority of MRI scans were acquired after thrombolysis was administered (74.3% all patients and 82.4% in sub-cohort), which is not representative of patients with an unknown onset time. Nevertheless, it is unlikely that rtPA will have had a significant impact on $T_2$ values within the ischaemic region as the average ADC values in ischaemic VOIs of the thrombolysed patients were not significantly different to the low ADC values of

non-thrombolysed patients. Preclinical data suggests that if the ADC remains low following reperfusion, $T_2$ continues to increase with time (Kettunen et al.., 2002). Additionally, a recent patient study showed rtPA does not alter net water uptake in the ischaemic region (Broocks et al., 2020) and so by extension, $T_2$, which also reflects net water uptake, should not be altered. Furthermore, in a recent analysis of the patient cohort studied here, the size of ADC defined ischaemic VOIs increased in 11 out of 19 thrombolysed patients between the initial ($<$ 9 hours onset) and follow-up scans (24+ hours), suggesting that ADC remained low long after rtPA, and thus rtPA would have had minimal or no effect on $T_2$ in the ischaemic region (Damion, Knight, McGarry et al., 2019). However, to truly support this point, more information about blood flow would be needed.

Given the above limitations, further investigation in a larger patient cohort is required. Such a study would enable more FLAIR scans so that the FLAIR image intensity ratio and DWI/FLAIR mismatch can be compared fully with other parameters. Additional scans should be acquired that offer information on collateral status to determine the effects of thrombolysis, and whether it mediates the relationship of other MR parameters with time from onset. A more extensive study would also allow separation of data analysis into different vascular territories and the size of ischaemic tissue and should involve validation of results in an unseen test data set.

In conclusion, this study suggests that the $T_2$ relaxation time is the most accurate and reliable measure for estimating stroke onset time and that relying on weighted images as a method for stroke timing may be problematic. It also suggests that quantifying ADC for identification of ischaemic tissue and quantifying $T_2$ for onset time estimation will be sufficient, and other parameters are not needed. In terms of clinical practice and feasibility, quantifying ADC and $T_2$ relaxation times for onset time estimation requires minimal image processing. The MRI protocol adopted here is based on commonly available pulse sequences provided by all MRI vendors. Diffusion and multi-echo $T_2$ are quick and easy to acquire ($\sim$ 5 minutes

maximum, in total, in this study), and most scanners automatically produce ADC and $T_2$ relaxation time images.

With the advent of magnetic resonance fingerprinting (MRF) (Ma et al., 2013; Chapter 3 Section 3.7.3) under-sampled image acquisition of both ADC and $T_2$ parameters could result in even shorter acquisition times, which is imperative in emergencies such as ischaemic stroke where 'time is brain' (Saver, 2006). The clinical feasibility of using MRF for the assessment of hyperacute stroke patients has recently been demonstrated, where 2D $T_1$ and FLAIR images and $T_1$ and $T_2$ relaxation time maps were acquired simultaneously within four minutes and 24 seconds (Duchaussoy et al., 2019). It typically takes about one minute to acquire a full NCCT head scan but given all the extra information that can be obtained with MRF, the extra three to four minutes would be a worthwhile trade-off. The post-processing steps used in this Chapter were exploratory and not designed for a clinical setting. However fast and automatic delineation of ischaemic regions on ADC images is already widely available (e.g., Straka et al., 2010) and at the University of Bristol, we have recently proposed a user-independent method for quantifying the impact of stroke on the human brain which has the potential to be easily automated for a clinical setting (Knight, Damion, McGarry et al., 2019).

# Chapter 8
# An investigation of reference-independent stroke timing using the $T_2$ relaxation time distribution in ADC defined ischaemic regions in a clinical cohort

## 8.1 Abstract

The results of the previous chapters in this thesis suggest that quantifying the change in the $T_2$ relaxation time due to ischaemia can provide an estimate of stroke onset time. However, the methods considered are dependent on non-ischaemic voxels as a reference for pre-ischaemic $T_2$ values, which may be problematic due to inherently varying $T_2$ relaxation times across the brain and common neurological co-morbidities in stroke patients. Studies in rats suggest the distribution of $T_2$ relaxation times within the ADC defined ischaemic region is informative of stroke onset time (e.g., Chapter 5, McGarry et al., 2016a; Rogers, McGarry et al., 2014) and so a *reference-independent* method based on the $T_2$ distribution has been suggested as a potential proxy for stroke timing (Norton et al., 2017). This study examined the distribution of $T_2$ relaxation times within ischaemic regions of hyperacute ischaemic stroke patients. The goal was to establish which, if any, distributional parameters have a relationship with time from stroke onset and could, therefore, provide a means to develop a *reference-independent* timing tool for human stroke.

ADC and $T_2$ relaxation time data from 23 ischaemic stroke patients, with onset time less than nine hours and low ADC defined ischaemic region greater than 0.5 ml were analysed. Ischaemic and non-ischaemic volumes of interest (VOI) were segmented into grey matter (GM) and white matter (WM) VOIs and analysed separately. Probability distributions that best described the empirical distribution of $T_2$ relaxation times within the VOIs were identified. For each patient and VOI type, the parameters of the probability distributions were estimated and used to design linear regression models. Linear regression models incorporating the standard deviation (SD) of $T_2$ and the *reference-dependent* $T_2$ image intensity ratio, were also created for comparison. All regressors were trained and tested using leave one out cross-validation (LOOCV).

For whole ischaemic regions, the *reference-dependent* $T_2$ image intensity ratio was the only variable that had a relationship with time from symptom onset. The

*reference-dependent* and *reference-independent* regressors were not significant for ischaemic WM. Significant regression models for GM included a second-order polynomial with parameters of the Burr type X11 distribution as predictor variables (*reference-independent*) and a multiple linear regression model with the $T_2$ mean, SD and image intensity ratio as predictor variables (*reference-dependent*). Overall results suggest, that reference-independent distributional parameters in GM may be informative of stroke onset time in patients and that the reference-dependent approach applied to the whole ADC defined ischaemic region is more accurate and may, therefore, be more suitable for clinical settings.

## 8.2 Introduction

Quantitative MRI (qMRI) could be used to identify ischaemic stroke patients with an unknown onset time that are within the treatment time window for thrombolysis. As described in Chapter 4 (Section 4.4), patient eligibility may be determined in a binary fashion, where a patient is deemed to be within the 4.5 hour treatment window if the measured qMRI parameter (e.g., image intensity ratio or the $f_2$ parameter defined in Chapter 5) is below a certain threshold (applied in Chapters 5 and 7) or if the predictive probability is high (applied in Chapter 7). Alternatively, the amount of time that has passed since stroke onset can be estimated by inserting the measured qMRI parameter into a linear regression model (e.g., Jokivarsi et al., 2010; McGarry et al., 2016a; Norton et al., 2017; Rogers, McGarry et al., 2014). For both approaches, results of previous research (Duchaussoy et al., 2019; McGarry et al., 2016a, 2016b; Rogers, McGarry et al., 2014; Siemonsen et al., 2009) and Chapters 5 and 7 suggest that compared to methods that rely on intensities of weighted images, the $T_2$ relaxation time is a more robust MRI variable, which may provide a more reliable stroke timer.

Despite the $T_2$ relaxation time showing superior ability to the other MRI parameters considered in this thesis, the ability to estimate stroke onset time was not perfect, and there is still room for improvement. For example, in Chapter 7, the optimal $T_2$ relaxation time cut-off was the most accurate at differentiating between patients scanned before and after 4.5 hours from symptom onset, but the accuracy of 75% meant 25% of patients were still misclassified. As discussed in Chapter 7, several factors may contribute to errors in estimates of onset time, including vascular territory, size of the ischaemic region, collateral status, clinical characteristics, and common neurological co-morbidities in aged stroke patients.

As described in Chapter 4 (Section 4.4) the standard approach for estimating stroke onset time using the $T_2$ relaxation time typically involves estimating the change in $T_2$ due to ischaemia by using the non-ischaemic voxels in the *mirror-reference*

region as an indication of pre-ischaemic or 'normal' $T_2$ values (e.g., Chapter 5; Chapter 7; McGarry et al., 2016a, 2016b; Siemonsen et al., 2009; Song et al., 2012). However, an accurate estimate of pre-ischaemic $T_2$ will be challenging to obtain due to lack of perfect anatomical symmetry between hemispheres and inherently varying relaxation times across the brain (Knight, McCann, Tsivos, Coulthard et al., 2016; Wansapura et al., 1999). $T_2$ relaxation anisotropy, where the measured $T_2$ depends on the positioning of the patients head relative to the applied magnetic field, is likely to be another source of error, especially in WM (Knight et al., 2015). As these variations in $T_2$ are larger than the changes caused by ischaemia, the increase in $T_2$ due to ischaemia cannot be calculated with certainty, which will contribute to errors in estimates of stroke onset time (Knight, Damion, McGarry et al., 2019; Norton et al., 2017). Even in rat models of ischaemia, where, structurally, the brain is relatively homogenous consisting mainly of grey matter (GM) (Zhang & Sejnowski, 2000), Norton et al. (2017) found the placement of the mirror-reference region influenced the overall precision of onset time estimates in rats, resulting in larger uncertainties in stroke timing than have been reported previously (e.g., McGarry et al., 2016a; Rogers, McGarry et al., 2014).

Preclinical studies in rats point to the possibility that the distribution of relaxation times within ADC defined ischaemic regions, which can be considered an indicator of the heterogeneity of tissue state, is more informative of stroke onset time than the change in average $T_2$ relaxation time (e.g., Chapter 5; McGarry et al., 2016a, 2016b; Rogers, McGarry et al., 2014). In Chapter 5 (McGarry et al. 2016b), the distributional parameters $f_1$, $f_2$ and $V_{overlap}$, which represent the volume of tissue with high relaxation times relative to the size of the ADC defined ischaemic region demonstrated better overall ability at distinguishing between scans performed before and after three hours from ischaemia onset than image intensity ratios. Rogers, McGarry et al. (2014) also found that by quantifying the spatial distribution of significantly elevated $T_2$ relaxation times within the ischaemic region, an estimate of 4.5 hours since ischaemia onset had an uncertainty of ± 26 minutes, compared to ± 35 minutes when using the change in $T_2$. However, as with

the reference-dependent approach, these studies also relied on the non-ischaemic mirror-reference voxels to determine which voxels were comparatively 'high' in the ischaemic region

Norton et al. (2017) developed a stroke timing method in rats that avoids the need for a non-ischaemic reference by exploiting the information of the empirical distributions of $T_2$ within ADC defined ischaemic regions. This method involved finding a probability distribution that best described the empirical distribution of the $T_2$ relaxation time within the ischaemic region and using the parameters associated with the probability distribution to design linear regression models that could be used to estimate stroke onset time (Norton et al., 2017). A third-order polynomial regression model with parameters of the log-logistic probability distribution as predictive variables was a significant predictor of time since MCAo (Norton et al., 2017). This reference-independent regressor provided more accurate estimates of stroke onset time than the reference-dependent approach (Norton et al., 2017). A third-order polynomial includes squared and cubed terms of the predictive variables used in the linear model, which accounts for nonlinear relationships in the data (James et al., 2013). Norton et al.'s (2017) study, therefore, suggests distribution based qMRI parameters are related to onset time, but unlike the image intensity ratios studied in Chapter 5 and Chapter 7, this relationship is not necessarily linear.

Madai et al. (2016) suggested another reference-independent approach for estimating stroke onset time, which involved quantifying the standard deviation (SD) of diffusion weighted image intensities within the DWI bright ischaemic region. Using this method, ischaemic stroke patients scanned before and after 4.5 hours of symptom onset were identified with 85% accuracy. The explanation for this result was similar to the explanation given for $f_2$ in Chapter 5. The DWI SD is a reflection of heterogeneity of ischaemic tissue, where, in the earlier hours, the DWI SD is large as the ischaemic region contains a combination of voxels with bright and duller signals indicating infarcted and normal tissue respectively (Madai

et al., 2016). As the ischaemic region progresses to infarction, the number of bright voxels relative to the number of duller voxels increase, therefore lowering the SD (Madai et al., 2016). Given that the $T_2$ relaxation time contributes to the signal of DWI, and in the previous Chapters $T_2$ was more informative of stroke onset time than DWI, the $T_2$ SD could also be informative of stroke onset time. Motivated by the encouraging results of distribution-based methods for estimating onset time discussed above, this study examined the distribution of $T_2$ relaxation times within the ischaemic tissue of hyperacute ischaemic stroke patients. The primary aims were to:

**a)** Identify the probability distributions that best describe the distribution of $T_2$ relaxation times within the whole ADC defined ischaemic region as well as ischaemic regions segmented into GM and WM tissue types. As much of the $T_2$ distribution-based work for onset time estimation has been conducted in rats (e.g., McGarry et al., 2016a, 2016b, 2017; Norton et al., 2017.) GM and WM were studied separately because human GM is closer to the cell composition of the rat brain (Zhang & Sejnowski, 2000). Also, as discussed in Chapter 6 the evolution of ischaemic injury differs between tissue types due to differences in structure, metabolism, haemodynamics and electrophysiology (Berner et al., 2016; Kumura et al., 1999).

**b)** For whole, GM only and WM only ischaemic regions, create linear regression models using the estimated parameters of the probability distributions identified in a) as well as the $T_2$ SD as variables, to determine which, if any, aspects of the $T_2$ distribution, have a relationship with time from symptom onset.

**c)** Compare the performance of the distribution-based *reference-independent* regression models created in b), with linear regression models based on the *reference-dependent* $T_2$ image intensity ratio.

The ultimate goal was to study whether $T_2$ distributional parameters could provide a means to develop distribution-based reference-independent timing tools for human stroke.

## 8.3 Methods

### 8.3.1 Patient recruitment and MRI protocol

The MRI data from the 35 patients in Chapter 7 were also used in this study. Therefore, details regarding recruitment, ethics, MRI protocol, image computation and identification of ischaemic regions, are also applicable here.

### 8.3.2 Image processing

#### Volumes of interest

The steps involved in creating ischaemic volumes of interest (VOI) encompassing the whole ischaemic region, ischaemic GM only and ischaemic WM only, are illustrated in Figure 8.1 and are described in detail in the Figure caption. To summarise, as outlined in the methods of Chapter 7, ischaemic volumes of interest (VOI) were generated using ADC and relaxation time limits according to methods given by Knight, McGarry et al. (2016) (Figure 8.1-part A). Non-ischaemic VOIs were created as described in Chapter 7, by reflecting the ischaemic VOIs about the sagittal midline (see Figure 7.2, in Chapter 7) and applying the same $T_2$ limits to minimise CSF contribution.

In order to analyse GM and WM within the ischaemic region separately, the ischaemic and non-ischaemic VOIs were further segmented into GM and WM VOIs by subtracting GM and WM masks from the ischaemic and non-ischaemic VOIs (Figure 8.1). This process involved computing GM and WM binary masks from the echo summed $T_2$w images according to methods given by Damion, Knight, McGarry et al. (2019). The segmentation process involved running FSL FAST (FMRIB's Automated Segmentation Tool, Zhang et al., 2001) on the echo summed $T_2$w images and specifying four tissue types for segmentation (GM, WM, CSF, spurious tissue, Figure 8.1-partB). The $T_2$w images were used for tissue type

segmentation because as outlined in Chapter 4 (Section 4.2.2), $T_2$w images are insensitive to early ischaemia, and so appear as they would before ischaemia onset. This pre-ischaemic representation of MR signals means the ability of FAST to differentiate between tissue types would not be impacted by ischaemia and so resulting masks (Figure 8.1-part C) should correctly represent GM and WM regions. The $T_1$w subcortical segmentation aspect of Damion, Knight, McGarry et al.'s (2019) segmentation procedure was not applied in this study as it had not been developed at the time of data analysis.

Once the separate GM and WM masks were produced (Figure 8.1-part C), ischaemic WM VOIs were created by subtracting the GM mask from the ischaemic VOI (Figure 8.1-part D), and the ischaemic GM VOIs were created by subtracting the WM mask from the ischaemic VOI (Figure 8.- part E). VOIs were then applied to the $T_2$ relaxation time maps to extract distributional information of the $T_2$ relaxation time within ischaemic GM and ischaemic WM, respectively (Figure 8.1-part D). To generate non-ischaemic VOIs for GM and WM, the same procedure was followed but applied to the non-ischaemic VOIs that were generated in Chapter 7. The GM and WM segmentation masks and the GM and WM ischaemic and non-ischaemic VOIs were visually inspected to ensure they were accurately segmented and correctly placed. Figure 8.2 shows examples of the contiguous VOIs from three patients.

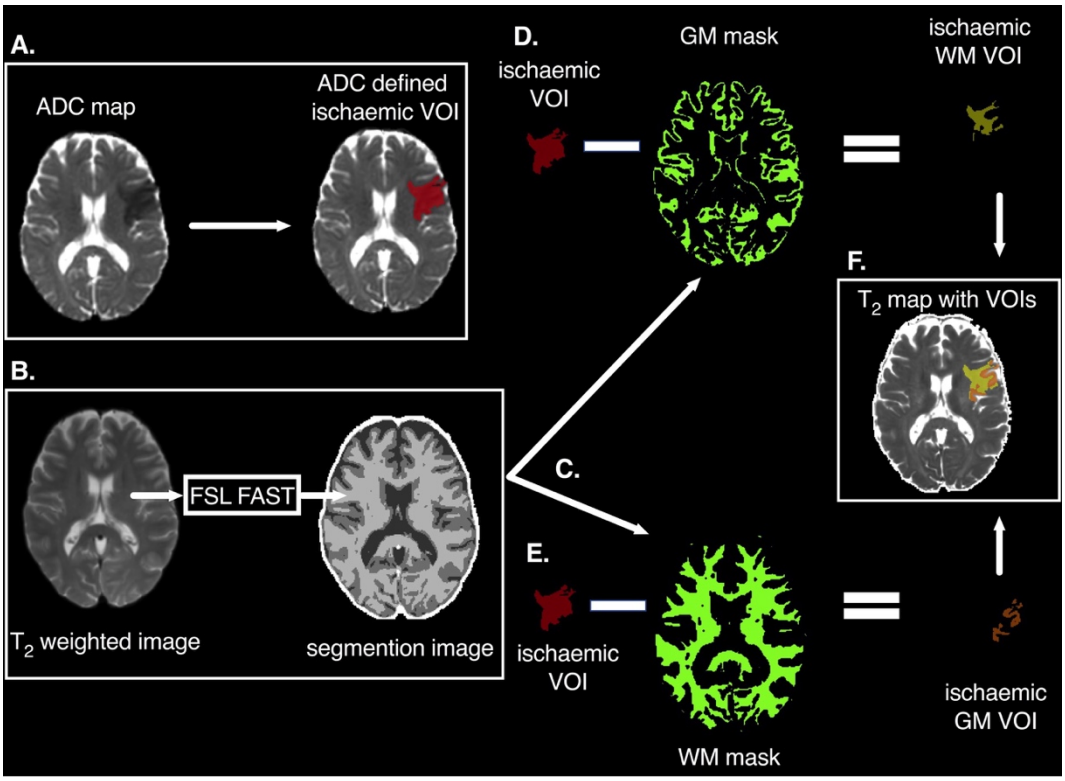


Figure 8.1 Illustration of the procedure followed to produce VOIs containing ischaemic WM only and ischaemic GM only. he ischaemic VOIs (represented as red) were generated using the methods described in Chapter 7 where ischaemic voxels were defined as those with ADC values $> 0.2 - 0.4$ $\mu m^2$/ms and $< 0.55 - 0.6$ $\mu m^2$/ ms, ADC values less than one half-width half-maximum from the median ADC of non-ischaemic tissue, and $T_2 > 30$ ms and $< 200$ ms.

**A.** FSL FAST (FMRIB's Automatic Segmentation Tool) was applied to $T_2$w images to produce binary masks for four tissue types. Where the darkest grey represents CSF, the middle shade of grey represents GM, the lightest grey represents WM, and white indicates spurious signals. $T_2$w images were used because they are insensitive to early ischaemia, and so provide an indication of the pre-ischaemic brain.

**B.** The tissue type masks produced from FSL FAST were separated, and only the GM and WM masks were used for the rest of the analysis.

**C.** Ischaemic VOIs containing only WM were created by subtracting the GM binary masks from the ischaemic VOI binary mask, to produce a separate WM ischaemic VOI (represented as yellow).

**D.** Ischaemic VOIs containing only GM were created by subtracting the WM binary masks from the ischaemic VOI binary mask, to produce a separate GM ischaemic VOI (represented as orange).

**E.** The ischaemic GM VOI and ischaemic WM VOI could then be loaded on to $T_2$ relaxation time maps, to extract $T_2$ information within ischaemic GM and ischaemic WM respectively.

To generate non-ischaemic VOIs for GM and WM, the same procedure was followed but applied to the non-ischaemic VOIs that were generated in Chapter 7.

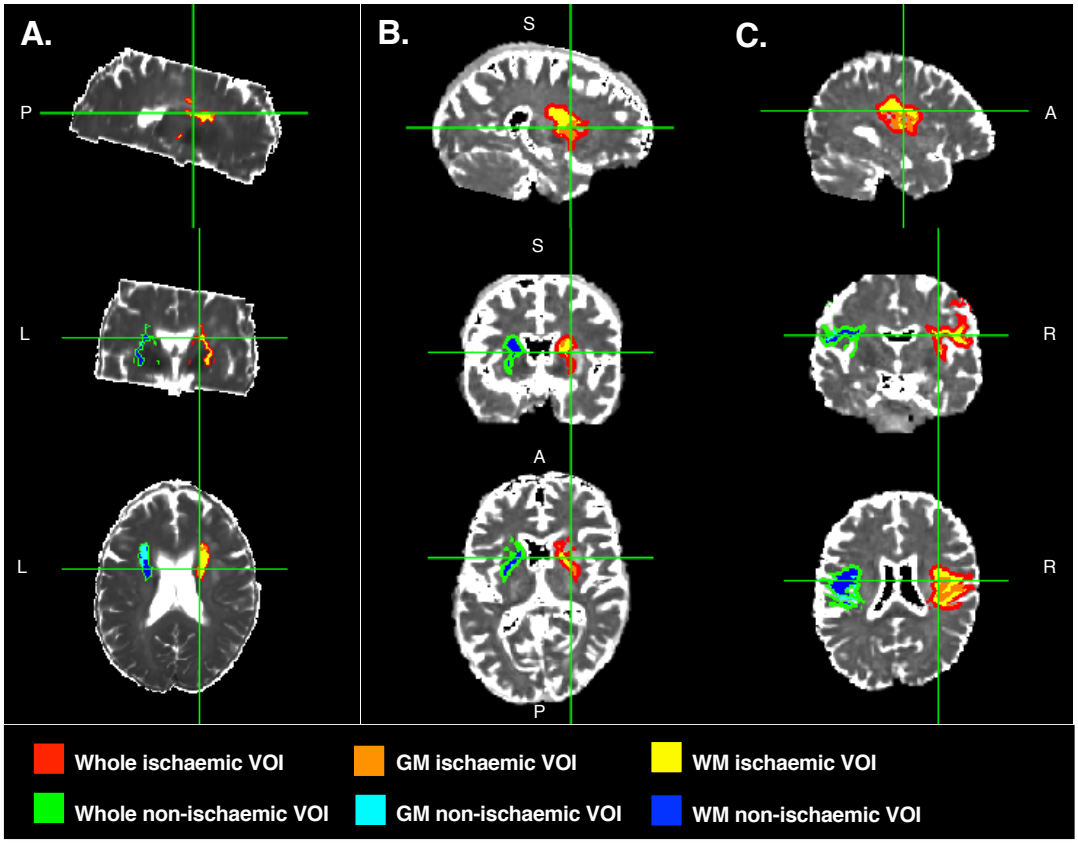


Figure 8.2 Examples of contiguous VOIs containing the whole ischaemic region, only GM and only WM, from three patients with different onset times. VOIs are overlaid on the $T_2$ relaxation time maps. **A.** 69-year-old female patient with right total anterior circulation stroke (TACS), thrombolysed, NIHSS on admission = 21, time from symptom onset to MRI = 184 minutes, scanned at the Bristol site. **B.** 71-year-old male patient with right partial anterior circulation stroke (PACS), thrombolysed, NIHSS on admission = 7, time from symptom onset to MRI = 334 minutes, scanned at the Glasgow site. **C.** 64-year-old male patient with right TACS, thrombolysed, NIHSS on admission = 9, time from symptom onset to MRI = 452 minutes, scanned at the Glasgow site.

### 8.3.3 Data selection

To ensure VOIs contained enough voxels to model the distribution of $T_2$ relaxation times, only VOIs greater than 0.5 $mm^3$ were included in the analysis. Patients were also excluded if the $T_2$ MRI data did not cover the whole ischaemic region. This was sometimes the case for patients scanned at Bristol, as due to the shorter time allowed for scanning, radiographers applied the multi-echo $T_2$ sequence only to regions affected by ischaemia (identified by DWI) rather than the whole brain. Total slice coverage was limited to 32 slices, which sometimes did not cover the whole ischaemic region. This was not considered a problem for quantifying image intensity ratios in Chapter 7 as average $T_2$ relaxation times could still be extracted. However, an ischaemic VOI covering only part of the ischaemic region on $T_2$ maps could distort the estimates of the $T_2$ distribution parameters. As the leave-one-out cross-validation (LOOCV) technique used to train and test the regression models is sensitive to outliers (James et al., 2013), the distribution of onset times within the datasets was also assessed using box and whisker plots and patients with outlying onset times were not included in the analysis.

### 8.3.4 Data analysis

#### Identification of probability distributions

Methods for investigating the relationship of $T_2$ distributions with time from stroke onset were carried out as closely to Norton et al.'s (2017) methods as possible. MATLAB scripts, which called upon the 'fitmethis' script available for free download(https://uk.mathworks.com/matlabcentral/fileexchange/40167-fitmethis) and the MATLAB release 2016b Statistics and Distribution toolbox and Distribution Fitting App, were created to identify which probability distributions best described the empirical distributions of $T_2$ relaxation times within the ischaemic VOIs.

To summarise, for each patient, the scripts created histograms of the $T_2$ relaxation times within the whole, GM and WM ischaemic VOIs, which were area normalised to represent the probability densities. All distributions available in the MATLAB statistics and distribution toolbox (see Appendix C for list) were then fitted to the data by maximum likelihood estimation and compared with the empirical $T_2$ distributions. For each patient and VOI type, the three probability distributions with the lowest Akaike information criteria scores (AIC) (Akaike, 1974) indicating a good fit, were recorded (see Appendix A for an explanation of AIC). To keep the analysis as simple and clear as possible, rather than investigating all potential probability distributions, across patients, the two most commonly identified probability distributions were chosen as those that best described the distribution of $T_2$ relaxation times within the whole, GM and WM ischaemic VOIs.

### Training and testing linear regression models

The parameters of the best fitting probability distributions were estimated for each patient and VOI type, via maximum likelihood estimation and used collectively to estimate the coefficients of linear regression models as well as second and third-order polynomial regression models. With no validation cohort available, leave one out cross-validation (LOOCV) was used to determine, train and test the regression models using the MATLAB release 2019a Regression Learner app. LOOCV involves iteratively separating the data into a training set containing the data from all patients, but one, and a test set, containing the data of the remaining patient, until each patient data set has served as a test set (James et al., 2013). For each iteration or 'fold' of the LOOCV, the root mean square error (RMSE) with respect to the actual onset time, was calculated.

Linear regression models that included individual parameters of the probability distributions such as shape, scale and location, as well as the $T_2$ mean and SD, were also created to examine whether these individually had a relationship with time from symptom onset. For comparison, reference-dependent linear regression

models were also created for each VOI type, which included the $T_2$ image intensity ratio as a predictive variable. As described in Chapter 7 and illustrated in Figure 7.2, the computation of image intensity ratios involved dividing the mean $T_2$ relaxation time of the ischaemic VOI by the mean $T_2$ relaxation time of the non-ischaemic VOI.

The relationship of the $T_2$ distributional parameters with the size of the ADC defined ischaemic region (number of voxels within the VOI) was also assessed using Pearson's and Spearman's correlations for normal and non-normally distributed data. Normality was determined by significant Shapiro -Wilk results ($p < .05$). As the $T_2$ data at each time point were obtained from different patients, and therefore ischaemic regions of different sizes, this stage of the analysis was to determine whether the size of the ischaemic region would be a potential confound in any relationship of distributional parameters with time from symptom onset.

### Model evaluation

The performance of regression models was evaluated by a) the significance and size of the $R^2$, b) the size of the AICc corrected for sample size (AICc), where the model with the lowest AICc indicates a better quality model relative to the other models from the same data set (Symonds & Moussalli, 2011) and c), calculating the average RMSE across folds of the LOOCV to indicate how well the model would perform when applied to new data. The RMSE is the uncertainty of the onset time estimates in minutes (±).

## 8.4 Results

Following the exclusion criteria outlined in the Methods section (Section 8.3), a total of 23 patients were included in the analyses. Of those excluded, nine patients had ischaemic VOIs less than $< 0.5$ mm$^3$, two were identified as outliers with onset times of 568 and 569 minutes, and the $T_2$ maps of one patient did not cover the whole ischaemic region. Ten of the remaining patients had GM VOIs less than 0.5mm$^3$ so were not included in GM analysis, and two had WM VOIs less 0.5 mm$^3$, so were not included in the WM analysis. Table 8.1 shows the clinical and imaging characteristics of the patients included in the analysis of the whole, GM and WM VOIs.

Table 8.1 Clinical and imaging characteristics of patients included in the analysis of the whole ADC defined ischaemic region, ischaemic GM and WM VOIs.

| | **Whole lesion (full cohort)** | **GM (sub cohort)** | **WM (sub cohort)** |
|---|---|---|---|
| **Patients, n (% full cohort):** | 23 (100%) | 13 (56.5%) | 21 (91.3%) |
| **Female, n (%):** | 8 (34.8%) | 4 (30.8%) | 6 (42.9%) |
| **Age in years** | 67 (31 – 85) | 67 (31 – 81) | 67 (31 -82) |
| **NIHSS*** | 7 (1 – 21) | 9 (1 – 21) | 7 (1 - 21) |
| **Study site, n (%):** | | | |
| Bristol | 10 (43.5%) | 5 (38.5%) | 9 (42.9%) |
| Oxford | 4 (17.4%) | 2 (15.4%) | 3 (14.3%) |
| Glasgow | 9 (39.1%) | 6 (46.1%) | 9 (42.9%) |
| **Stroke type †, n (%):** | | | |
| LACS | 7 (30.4%) | 1 (7.7%) | 5 (23.8%) |
| PACS | 7 (30.4%) | 5 (38.5%) | 8 (38.1%) |
| POCS | 2 (8.7%) | 2 (15.4%) | 2 (9.5%) |
| TACS | 6 (26.1%) | 5 (38.5%) | 6 (28.6%) |
| **Left hemisphere, n (%):** | 10 (43.5%) | 6 (46.2%) | 10 (47.6%) |
| **Thrombolysis:** | | | |
| Patients received rtPA, n (%) | 19 (82.6%) | 12 (92.3%) | 17 (81.1%) |
| Time from onset to rtPA | 2:00 (1:02 - 3:54) | 1:13 (1:02 - 3:54) | 2:00 (1:02 - 3:54) |
| Time from rtPA to MRI | 3:53 (0:29 - 5:53) | 4:15 (0:38 - 5:53) | 4:27 (0:29 - 5:53) |
| **Time from onset to MRI:** | 5:34 (2:25 - 7:51) | 6:46 (2:28 - 7:51) | 5:38 (2:25 - 7:51) |
| **VOI characteristics:** | | | |
| ADC defined ischaemic volume (mL) | 6.87 (0.59 - 32.44) | 5.54 (0.58 - 12.48) | 3.21 (0.62 - 19.49) |
| % ischaemic GM | 23.12 (0 - 75) | 38.47 (12.77 - 75) | 23.12 (0 - 75) |
| % ischaemic WM | 75.11 (21.77 - 100) | 58.60 (21.77 -87.19) | 75.11 (21.77 - 100) |

*Note. Values given are medians with minimum and maximum values in brackets. n = number. rtPA = recombinant tissue plasminogen activator. *Scores on the National Institutes of Health Stroke Scale (NIHSS) range from 0 - 42, higher scores indicate greater deficit. †Strokes are classified according to the Oxford Stroke Classification Scale (Bamford et al., 1991). LACS = Lacunar, PACS= Partial Anterior Circulation, POCS = Posterior Circulation, TACS = Total Anterior Circulation. Times are in hours and minutes (hours: minutes). VOI = volume of interest. ADC = apparent diffusion coefficient. mL = millilitres, ms = milliseconds. % GM and % WM are the percentage of the respective tissue types with the whole ADC defined ischaemic region.*

### 8.4.1 $T_2$ Distributions

The fitted probability distributions over plots of the empirical distributions of $T_2$ relaxation times within whole ischaemic VOIs, GM ischaemic VOIs and WM ischaemic VOIs are shown in Figures 8.3, 8.4 and 8.5 respectively. Histograms of $T_2$ relaxation times within the non-ischaemic VOIs are shown for comparison. To give a representation of the distributions at regular time intervals, the distributions shown in the Figures are from separate patients, with time from symptom onset closest to the nearest hour. In some instances, there was only one patient scanned close to the hourly interval (whole ischaemic VOI: six and eight hours, GM VOI: two, four, five and hours, WM VOI: two hours, five hours, six hours, eight hours) and in other cases, no patients were scanned within the specific hourly interval (WM VOI: six hours). The shapes of the distributions were inspected for each patient and VOI type, including the ones that are not shown in the Figures. The distributions shown in the Figures are representative of the other patients scanned within that time frame. Cases that appeared to show a different distribution to the other were included in the Figures, and these are highlighted in the Results (Section 8.4.2).

Within the whole dataset, there were two patients with data from all three VOI types where the size of the GM and VOIs relative to each other were comparable. The fitted probability distributions over plots of the empirical distributions of the relaxation times within whole, GM and WM ischaemic VOIs of these patients are shown in Figure 8.6. There were no patients scanned at three hours for which the GM and WM VOIs were similar sizes and so are the same patients shown in Figure 8.2. The patient scans shown in Figure 8.6 are also the same patients shown in Figure 8.2.

### Whole ischaemic VOIs

The $T_2$ distributions within whole ischaemic VOIs were best described by the Generalised Extreme Value (GEV) (Mathworks 2019a; McFadden, 1978) and Burr type X11 (Mathworks 2019b; Rodriguez, 1977) probability distributions (Figure 8.3. and Figure 8.6- parts A, D, G). Of the 23 VOIs analysed, 15 had GEV in the top three distributions, and 15 had Burr in the top three distributions. Of these, seven had both GEV and Burr in the top three, six were Burr only, and eight were GEV only.

The three-parameter GEV probability distribution takes the form of:

$$y = f(x|k,\mu,\sigma) = \left(\frac{1}{\sigma}\right)\exp\left(-\left(1+k\frac{(x-\mu)}{\sigma}\right)^{-\frac{1}{k}}\right)\left(1+k\frac{(x-\mu)}{\sigma}\right)^{-1-\frac{1}{k}}$$

$$for$$

$$1+k\frac{(x-\mu)}{\sigma}$$

Where $k$, μ and σ denote the shape, location and scale parameters.

The three-parameter Burr type X11 probability distribution takes the form of:

$$f(x|\alpha,c,k) = \frac{\frac{kc}{\alpha}\left(\frac{x}{\alpha}\right)^{c-1}}{\left(1+\left(\frac{x}{\alpha}\right)^{c}\right)^{k+1}}$$

$$where\ x>0, \alpha>0, c>0, k>0.$$

Where α is the scale parameter, and c and k are the shape parameters.

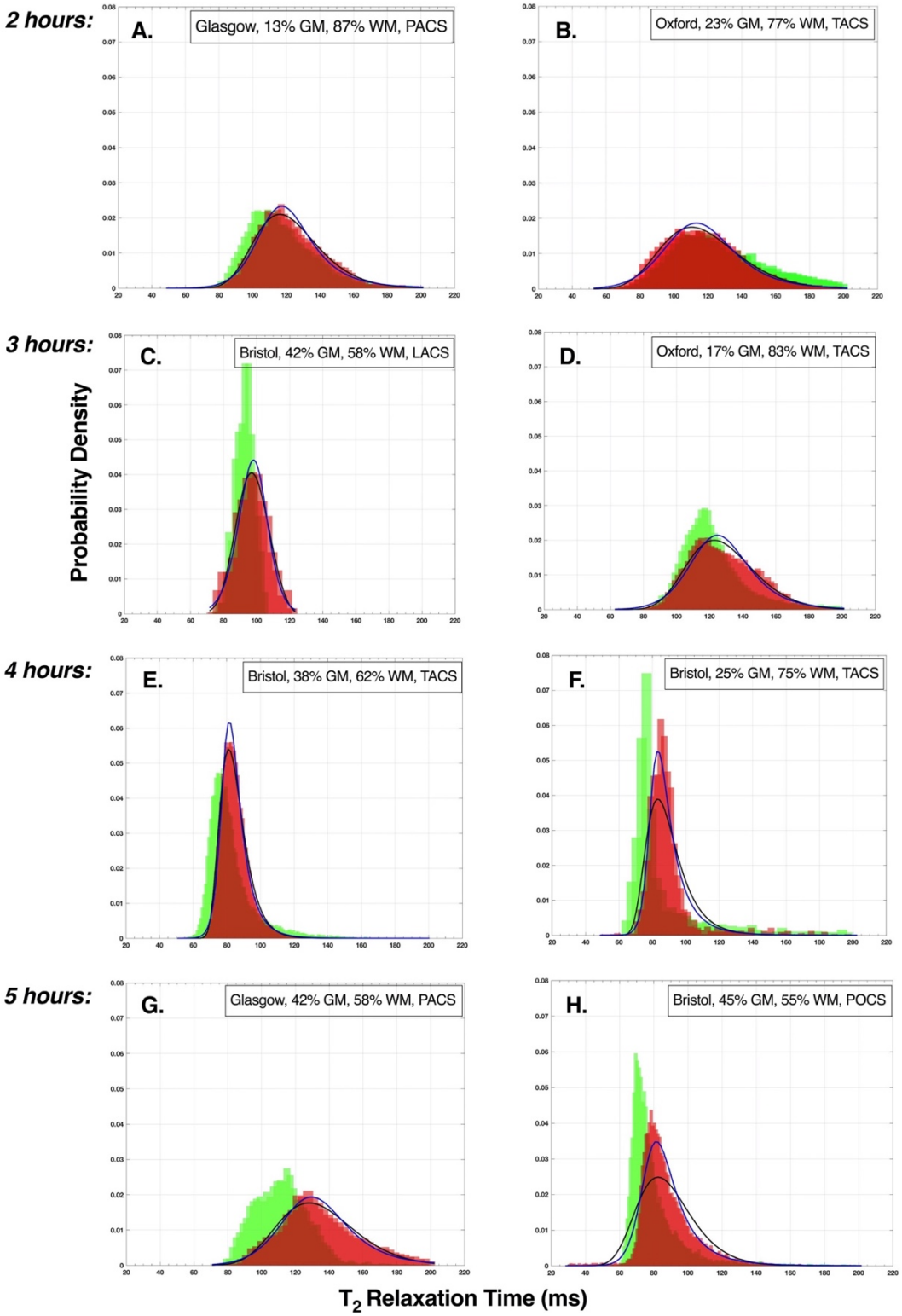
2 hours:
3 hours:
4 hours:
5 hours:
A.
Glasgow, 13% GM, 87% WM, PACS
B.
Oxford, 23% GM, 77% WM, TACS
C.
Bristol, 42% GM, 58% WM, LACS
D.
Oxford, 17% GM, 83% WM, TACS
E.
Bristol, 38% GM, 62% WM, TACS
F.
Bristol, 25% GM, 75% WM, TACS
G.
Glasgow, 42% GM, 58% WM, PACS
H.
Bristol, 45% GM, 55% WM, POCS
Probability Density
T2 Relaxation Time (ms)

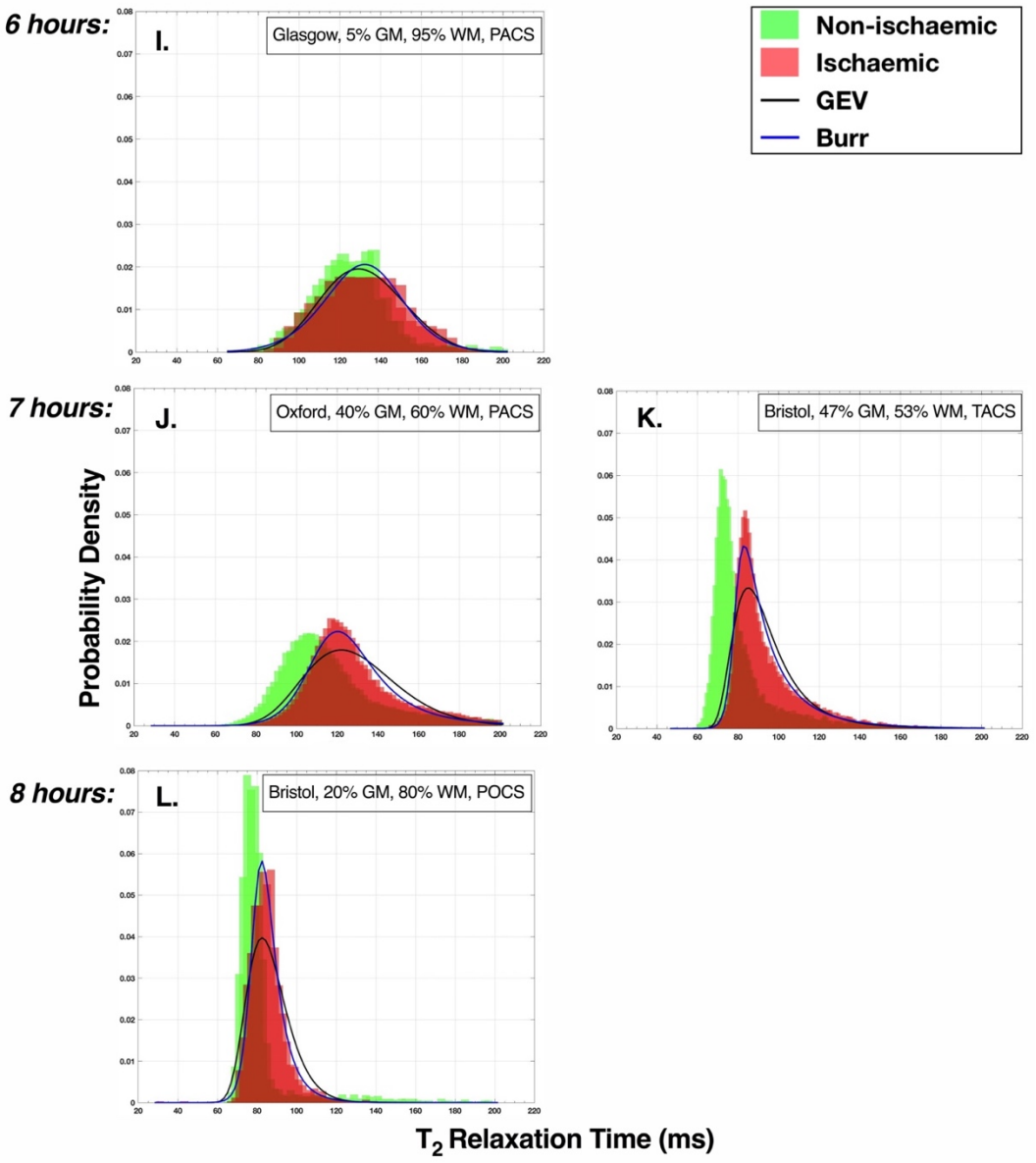


Figure 8.3 Fitted generalised extreme value (GEV) and Burr type X11 probability distributions over histograms of empirical $T_2$ relaxation times within whole ischaemic VOIs. Each histogram is from a different patient, and plots are grouped according to time from symptom onset, rounded to the nearest hour. In each plot, histograms of the $T_2$ relaxation times in the non-ischaemic contralateral VOI are shown for comparison. Scan site, percentage of grey matter (GM) and white matter (WM) within the ADC defined ischaemic region and stroke type are shown. The x axis is the $T_2$ relaxation time in ms (20 – 220 ms) and the y axis is the probability density (0 - 0.1).

**A.** 68-year-old male patient with right partial anterior circulation stroke (PACS), not thrombolysed, NIHSS on admission = 11, time from symptom onset to MRI = 148 minutes, scanned at Glasgow.

**B.** 82-year-old male with left total anterior circulation stroke (TACS), thrombolysed, NIHSS on admission = 19, time from symptom onset to MRI = 145 minutes, scanned at Oxford.

**C.** 54-year-old female with Lacunar Stroke (LACS), thrombolysed, NIHSS on admission = 2, scanned at Bristol.

**D.** 81-year-old male with right TACS, thrombolysed, NIHSS on admission = 8, time from symptom onset to MRI = 185 minutes, scanned at Oxford.

**E.** 63-year-old female with right TACS, thrombolysed, NIHSS on admission = 17, time from symptom onset to MRI = 235 minutes, scanned at Bristol.

**F.** 66-year-old male with left PACS, thrombolysed, NIHSS on admission = 3, time from symptom onset to MRI = 265 minutes, scanned at Bristol.

**G.** 71-year-old male with left PACS, thrombolysed, NIHSS on admission = 7, time from symptom onset to MRI = 334 minutes, scanned at Glasgow.

**H.** 80-year-old male with right posterior circulation stroke (POCS), thrombolysed, NIHSS on admission = 5, time from symptom onset = 338 minutes, scanned at Bristol.

**I.** 76-year-old male with left PACS, thrombolysed, NIHSS on admission = 2, time from symptom onset to MRI = 361 minutes, scanned at Glasgow.

**J.** 56-year-old male with left PACS, thrombolysed, NIHSS on admission = 10, time from symptom onset to MRI = 410 minutes, scanned at Oxford.

**K.** 45-year-old male with right TACS, thrombolysed, NIHSS on admission = 18, time from symptom onset to MRI = 415 minutes, scanned at Bristol.

**L.** 31-year-old female with left POCS, thrombolysed, NIHSS on admission = 2, time from symptom onset to MRI = 471 minutes, scanned at Bristol.

### Ischaemic GM VOIs

The $T_2$ distributions within ischaemic GM VOIs were also best described by the GEV and Burr type X11 probability distributions (Figure 8.4 and Figure 8.6-parts B, E, H). Of the 13 GM VOIs analysed, 12 had GEV in the top three distributions, and six had Burr in the top three distributions. Six VOIs were described by both Burr and GEV; six were described by GEV only, two of which did not fit Burr at all so could not be used to train the Burr based regressors.

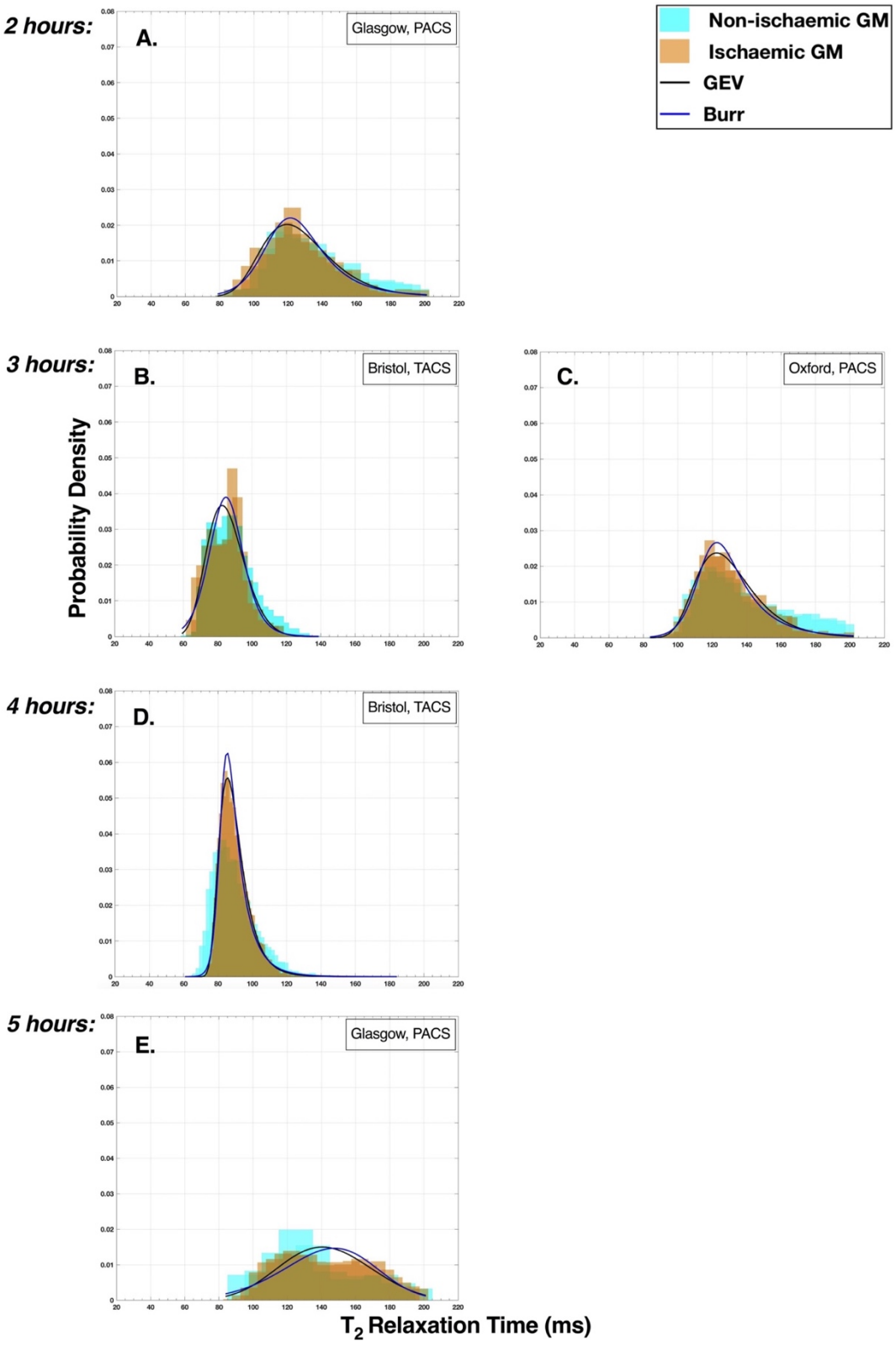
2 hours:
A.
Glasgow, PACS
Non-ischaemic GM
Ischaemic GM
GEV
Burr
3 hours:
B.
Bristol, TACS
C.
Oxford, PACS
Probability Density
4 hours:
D.
Bristol, TACS
5 hours:
E.
Glasgow, PACS
T2 Relaxation Time (ms)

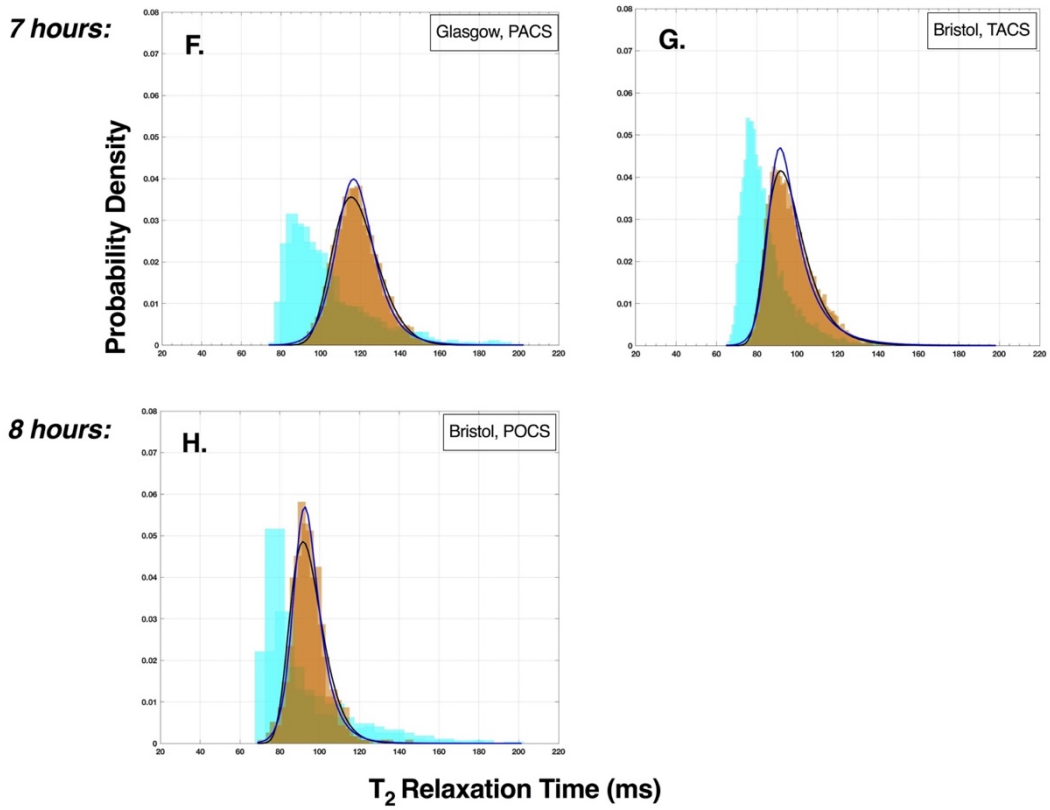


Figure 8.4 Fitted generalised extreme value (GEV) and Burr type X11 probability distributions over histograms of empirical $T_2$ relaxation times within ischaemic grey matter (GM) VOIs. Each histogram is from a different patient, and plots are grouped according to time from symptom onset, rounded to the nearest hour. There were no patients in the GM group scanned six hours from symptom onset. Scan site and stroke type are shown. In each plot, histograms of the $T_2$ relaxation times in the non-ischaemic contralateral VOI are shown for comparison. The x axis is the $T_2$ relaxation time in ms (20 – 220 ms) and the y axis is the probability density (0 - 0.1).

**A.** 68-year-old male with right partial anterior circulation stroke (PACS), not thrombolysed, NIHSS on admission = 11, time from symptom onset to MRI = 148 minutes, scanned at Glasgow.

**B.** 69-year-old female with right total anterior circulation stroke (TACS), thrombolysed, NIHSS on admission = 21, time from symptom onset to MRI = 184 minutes, scanned at Bristol.

**C.** 81-year-old male with right TACS, thrombolysed, NIHSS on admission = 8, time from symptom onset to MRI = 185 minutes, scanned at Oxford.

**D.** 63-year-old female with right TACS, thrombolysed, NIHSS on admission = 17, time from symptom onset to MRI = 235 minutes, scanned at Bristol.

**E.** 71-year-old male with left PACS, thromblysed, NIHSS on admission = 7, time from symptom onset to MRI = 334 minutes, scanned at Glasgow.

**F.** 59-year-old male with left PACS, thrombolysed, NIHSS on admission = 13, time from symptom onset to MRI = 409 minutes, scanned at Glasgow.

**G.** 45-year-old male with right TACS, thrombolysed, NIHSS on admission = 18, time from symptom onset to MRI = 415 minutes, scanned at Bristol.

### Ischaemic WM VOIs

The $T_2$ distributions within ischaemic WM VOIs were best described by the GEV and log-logistic (Fisk, 1961; Mathworks, 2019c) probability distributions (Figure 8.5 and Figure 8.6-part C, F, I). Of the 21 WM VOIs included in the analysis, 12 had GEV in the top three distributions, nine had log-logistic in the top three, two VOIs fitted both distributions, and two did not fit either. The two-parameter log-logistic probability distribution takes the form of:

$$f\ (x|\mu,\sigma) = \frac{1}{\sigma}\frac{1}{x}\frac{\exp(z)}{[1+\exp\ (z)]^2}$$

$$where\ z = \frac{\log(x) - \mu}{\sigma}$$

Where μ denotes the log-median value and σ denotes the distributional shape.

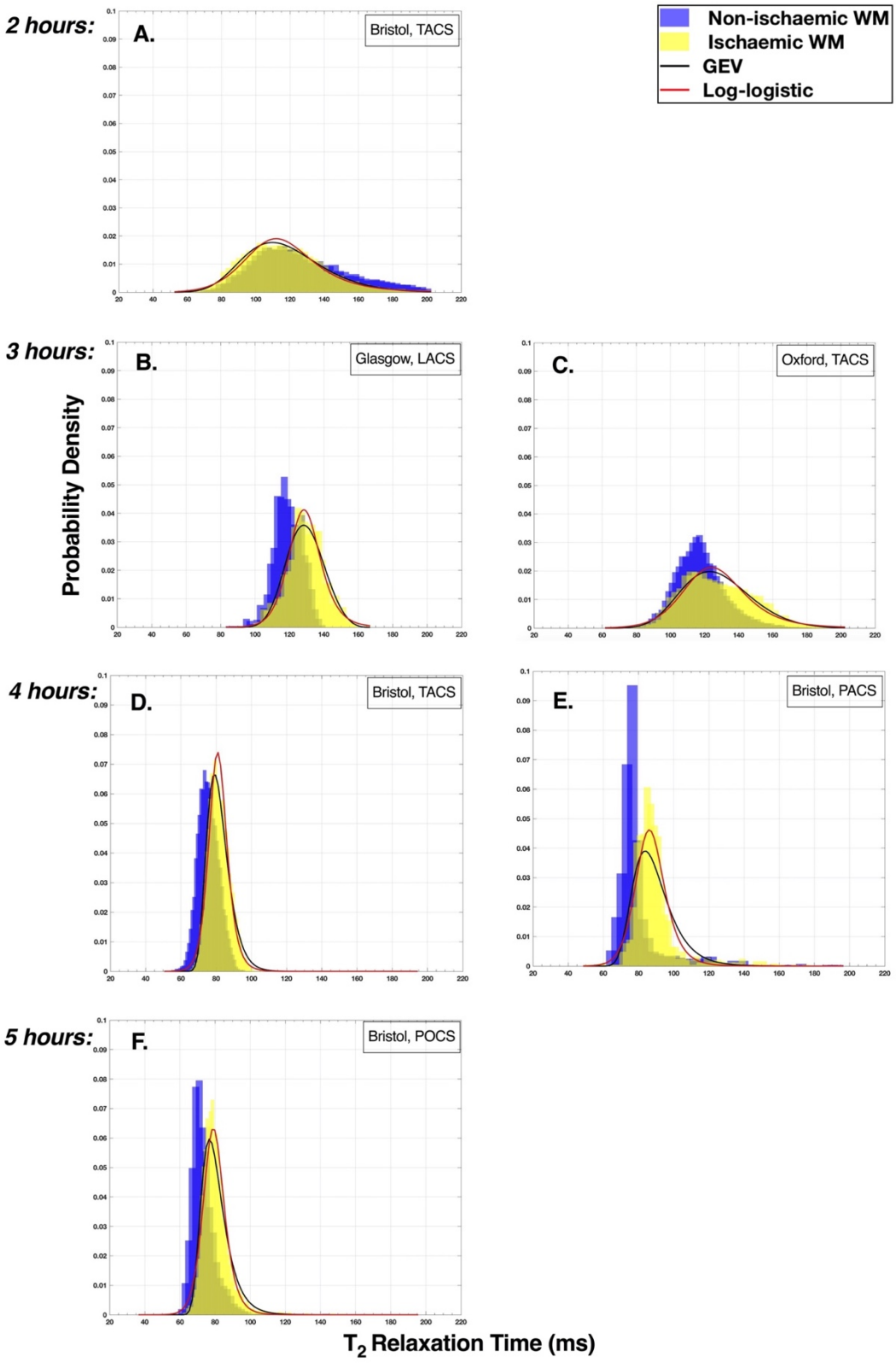
2 hours:
A.
Bristol, TACS
Non-ischaemic WM
Ischaemic WM
GEV
Log-logistic
3 hours:
B.
Glasgow, LACS
C.
Oxford, TACS
Probability Density
4 hours:
D.
Bristol, TACS
E.
Bristol, PACS
5 hours:
F.
Bristol, POCS
T2 Relaxation Time (ms)

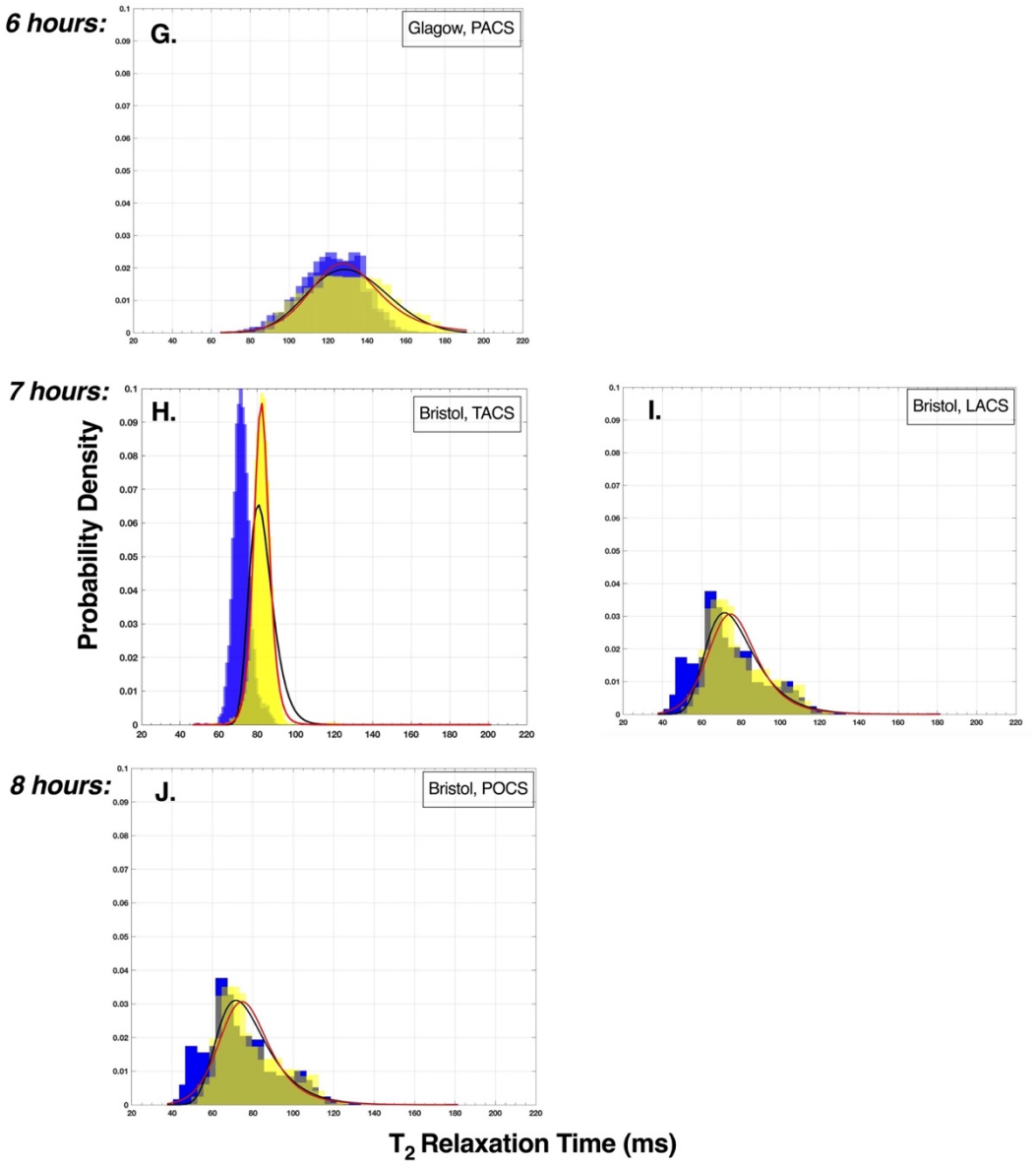


Figure 8.5 Fitted generalised extreme value (GEV) and log-logistic probability distributions over histograms of empirical $T_2$ relaxation times within ischaemic white matter (WM) VOIs. Each histogram is from a different patient, and plots are grouped according to time from symptom onset, rounded to the nearest hour. There were no patients in the GM group scanned six hours from symptom onset. Scan site and stroke type are shown. In each plot, histograms of the $T_2$ relaxation times in the non-ischaemic contralateral VOI are shown for comparison. The x axis is the $T_2$ relaxation time in ms (20 – 220 ms) and the y axis is the probability density (0 - 0.1).

**A.** 82-year-old male with left total anterior circulation stroke (TACS), thrombolysed, NIHSS on admission = 19, time from symptom onset to MRI = 145 minutes, scanned at Oxford.

**B.** 49-year-old male with right lacunar stroke (LACS), not thrombolysed, NIHSS on admission = 19, time from symptom onset to MRI = 175 minutes, scanned at Glasgow.

**C.** 81-year-old male with right TACS, thrombolysed, NIHSS on admission = 8, time from symptom onset = 185 minutes, scanned at Oxford.

**D.** 63-year-old female with right TACS, thrombolysed, NIHSS on admission = 17, time from symptom onset to MRI = 235 minutes, scanned at Bristol.

**E.** 66-year-old male with left partial anterior circulation stroke (PACS), thrombolysed, NIHSS on admission = 3, time from symptom onset to MRI = 265 minutes, scanned at Bristol.

**F.** 65-year-old female with left PACS, not thrombolysed, NIHSS on admission = 3, time from symptom onset to MRI = 261 minutes, scanned at Bristol.

**G.** 80-year-old male with right posterior circulation stroke (POCS), thrombolysed, NIHSS on admission = 5, time from symptom onset to MRI = 338 minutes, scanned at Bristol.

**H.** 76-year-old male with left PACS, thrombolysed, NIHSS on admission = 2, time from symptom onset to MRI = 361 minutes, scanned at Glasgow.

**I.** 45-year-old male with right TACS, thrombolysed, NIHSS on admission = 18, time from symptom onset to MRI = 415 minutes, scanned at Bristol.

**J.** 53-year-old male with right LACS, not thrombolysed, NIHSS on admission = 1, time from symptom onset to MRI = 422 minutes, scanned at Bristol.

**K.** 31-year-old female with left POCS, thrombolysed, NIHSS on admission = 2, time from symptom onset to MRI = 471 minutes, scanned at Bristol.

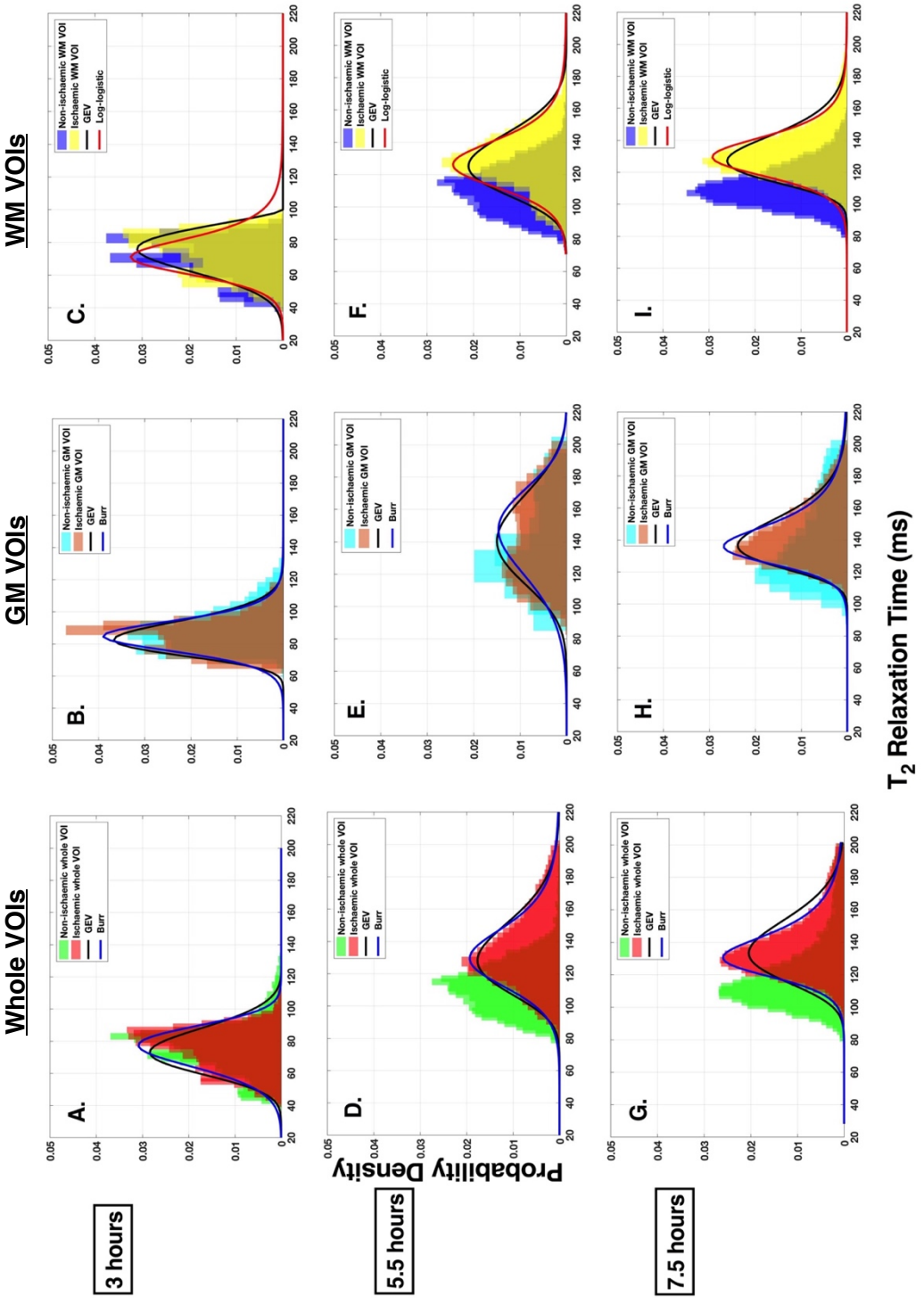
Whole VOIs
GM VOIs
WM VOIs
3 hours
5.5 hours
7.5 hours
Probability Density
T2 Relaxation Time (ms)
A.
B.
C.
D.
E.
F.
G.
H.
I.
Non-ischaemic whole VOI
Ischaemic whole VOI
Non-ischaemic GM VOI
Ischaemic GM VOI
Non-ischaemic WM VOI
Ischaemic WM VOI
GEV
Burr
Log-logistic

Figure 8.6 (shown on the left-hand side). Fitted probability distributions over histograms of empirical $T_2$ relaxation times within ischaemic whole (A, D, G), GM (B, E,H) and WM (C,F I) VOIs from three example patients (also in Figure 8.2) scanned at different times after symptom onset (to the nearest half hour). Histograms of $T_2$ relaxation times within the non-ischaemic VOIs are shown for comparison. **A. B.** and **C.** are from a 69-year-old female patient with right total anterior circulation stroke (TACS), thrombolysed, NIHSS on admission = 21, time from symptom onset to MRI = 184 minutes, scanned at the Bristol site, ischaemic VOI = 17% GM, 83% WM. **D. E.** and **F.** are from a 71-year-old male patient with right partial anterior circulation stroke (PACS), thrombolysed, NIHSS on admission = 7, time from symptom onset to MRI = 334 minutes, scanned at the Glasgow site, ischaemic VOI = 41% GM, 59% WM. **G. H.** and **I.** are from a 64-year-old male patient with right TACS, thrombolysed, NIHSS on admission = 9, time from symptom onset to MRI = 452 minutes, scanned at the Glasgow site, ischaemic VOI = 37% GM, 63% WM. The $T_2$ distributions within the non-ischaemic reference VOIs are shown for comparison. The x axis is the $T_2$ relaxation time in ms (20 – 220 ms) and the y axis is the probability density (0 - 0.1).

### 8.4.2 Observations from the probability distributions

The following observations were made from the histograms shown in Figures 8.3, 8.4, 8.5 and 8.6. What these observations may mean and why they are interesting are considered in the Discussion of this Chapter.

- For all VOI types, the $T_2$ distributions display a right shift over time, showing more voxels with longer $T_2$ relaxation times in the later hours of ischaemia.
- In Figure 8.6, there is a bimodal distribution of $T_2$ relaxation times within ischaemic VOIs of the patient scanned at approximately three hours from symptom onset (Figure 8.6-parts A, B and C, and Figure 8.4-part B ), and the patient scanned at approximately five and a half hours from symptom onset (Figure 8.6-parts D, E and F and Figure 8.4-part E). The bimodal distribution is not present in the patient scanned at the later time from symptom onset (Figure 8.6-parts G, H and I), or any of the other patients in the study dataset.
- The $T_2$ values within VOIs of Bristol patients are shorter than the $T_2$ values within VOIs of the patients scanned at Glasgow and Oxford.

### 8.4.3 Linear regression models

The linear regression results for whole ischaemic VOIs, ischaemic GM VOIs and ischaemic WM VOIs are given in Tables 8.2, 8.3, and 8.4, respectively. Figure 8.7 illustrates the predictive abilities of the distribution-based reference-independent regressors and the reference-dependent regressors. Correlational analyses showed no relationship between VOI size and any of the $T_2$ parameters studied in the regression models, for whole ischaemic VOIs, GM VOIs and WM VOIs (see Appendix C, Table 1C for Shapiro Wilk, Spearman's and Pearson's Correlations results). It was therefore concluded that the size of the ADC defined ischaemic region was not a confounding factor in the regression results.

To summarise the results, which are described in more detail below, overall, GM was the only VOI type for which the $T_2$ distributional parameters showed a relationship with time from symptom onset. Reference-dependent models incorporating the $T_2$ ratio were the most accurate models for estimating onset time in GM and whole ischaemic VOIs. None of the reference-dependent and reference-independent regressors for WM were significant.

#### Whole ischaemic region regression models

Reference-independent regression models which incorporated parameters of the GEV and Burr type X11 probability distributions, or the $T_2$ SD, as predictive variables were not significant. Therefore, $T_2$ distributional parameters within the whole ischaemic VOIs were not related to time from symptom onset. The reference-dependent $T_2$ image intensity ratio was the only parameter studied that showed a relationship with time from symptom onset. The linear regression model with the $T_2$ image intensity ratio as the predictive variable outperformed all of the whole ischaemic VOI based regressors as the $R^2$ was moderate and highly significant ($R^2 = 0.39$, $p = 0.001$), it had the lowest $AIC_c$ value (275.49) and one of the lowest average RMSE across LOOCV folds (± 92 minutes). The regression equation was:

$$\text{Stroke onset time (minutes)} \approx (1052.3 \pm 285.3)\text{rT}_{2\ \text{ischaemic}} - (828.1 \pm 308.5)$$

Where $\text{rT}_{2\ \text{ischaemic}}$ is the $T_2$ relaxation time image intensity ratio obtained from the whole ischaemic and whole non-ischaemic VOIs.

A four-parameter linear regression model incorporating the $T_2$ ratio, mean $T_2$, $T_2$ SD and one constant term was also significant with a high $R^2$ and significance level ($R^2 = 0.49$, $p = 0.008$), a low $AIC_c$ value (278.62) and low average RMSE (± 91 minutes). However, upon further investigation, the constant term and $T_2$ ratio were the only significant variables in the model ($p < 0.05$), showing that the $T_2$ ratio was the only variable that was related to onset time.

## GM regression models

Reference-independent regression models with parameters associated with the GEV and Burr type X11 probability distributions as predictive variables were not significant. However, including a quadratic term into the Burr distribution-based regression model, improved the fit, and produced a significant seven-parameter second-order polynomial regression model (including one constant term) with a high $R^2$ of 0.95, and average RMSE of ± 121 minutes. All variables significantly contributed to the model ($p < 0.001$). The equation for the regression model was:

$$\text{Stroke onset time (minutes)} \approx$$

$$-(572.9 \pm 242.9)\alpha_{GMT2} - (79.3 \pm 25.4)c_{GMT2} + (96.1 \pm 15.1)k_{GMT2} - (572.9 \pm 242.9)\alpha_{GMT2}{}^2 + (0.368 \pm 0.115)c_{GMT2}{}^2 - (1.9 \pm 0.32)k_{GMT2}{}^2 + (2932.9 \pm 1288.9)$$

Where $\alpha_{GMT2}$, $c_{GMT2}$, and $k_{GMT2}$ are the estimated scale, first shape and second shape Burr type X11 distributional parameters for $T_2$ within ischaemic GM.

A linear regression model incorporating the reference-dependent $T_2$ ratio as the sole predictive variable was also significant ($R^2 = 0.32$, $p = 0.043$, average RMSE = ±106 minutes, AICc = 159.21). Where,

Stroke onset time (minutes) ≈

$$\text{Stroke onset time (minutes)} \approx (884.3 \pm 386.0)\text{rT}_{2\ \text{GM}} - (828.1 \pm 308.5)$$

Where $\text{rT}_{2\ \text{GM}}$ is the $T_2$ relaxation time image intensity ratio obtained from the ischaemic and non-ischaemic GM VOIs.

However, including the $T_2$ mean and $T_2$ SD in addition to the $T_2$ ratio, produced a significant model ($p = 0.024$) that, compared to the $T_2$ ratio in isolation, had with a higher $R^2$ (0.63), lower RMSE (± 94 minutes) and comparable AICc (159.02). All variables significantly contributed to the model ($p < .001$). The equation for the regression model was:

Stroke onset time (minutes) ≈

$$(751.3 \pm 319.8)\ \text{rT}_{2\ \text{GM}} + (5.01 \pm 1.9)\ \text{MT}_{2\ \text{ischaemicGM}} -$$

$$(18.8 \pm 7.2)\text{SDT}_{2\ \text{ischaemicGM}} - (730 \pm 331.2)$$

Where $\text{rT}_{2\ \text{GM}}$ is the $T_2$ ratio of the GM VOIs, $\text{MT}_{2\ \text{ischaemicGM}}$ is the mean $T_2$ relaxation time within the ischaemic GM VOI, and $\text{SDT}_{2\ \text{ischamicGM}}$ is the $T_2$SD of the ischaemic GM VOI.

Table 8.2 Statistics of regression models and evaluation metrics for the whole ischaemic region VOIs.

| **Variables included** | | **Statistics of regression models** | | | | **Evaluation statistics** | |
|---|---|---|---|---|---|---|---|
| **in regression models** | *df* | *F* | $R^2$ | *p* | RMSE (± mins) | AICc | Average RMSE (± mins) |
| GEV (μ ,σ, k) | 19 | 0.97 | 0.13 | 0.428 | 115 | 289.33 | 121 |
| GEV 2nd order | 16 | 0.48 | 0.15 | 0.812 | 124 | 300.02 | 216 |
| GEV 3rd order | 13 | 0.47 | 0.24 | 0.873 | 130 | 314.28 | 263 |
| μ (location) | 21 | 0.78 | 0.04 | 0.386 | 115 | 286.13 | 119 |
| σ (scale) | 21 | 1.18 | 0.05 | 0.290 | 116 | 285.72 | 114 |
| k (shape) | 21 | 0.41 | 0.02 | 0.531 | 122 | 286.54 | 116 |
| | | | | | | | |
| Burr (α, c, k) | 19 | 0.81 | 0.11 | 0.502 | 116 | 289.82 | 149 |
| Burr 2nd order | 16 | 0.74 | 0.22 | 0.629 | 119 | 298.24 | 2981 |
| Burr 3rd order | 13 | 1.08 | 0.43 | 0.439 | 113 | 307.91 | 1088 |
| α (scale) | 21 | 0.16 | 0.01 | 0.698 | 117 | 286.80 | 121 |
| c (shape) | 21 | 0.40 | 0.02 | 0.439 | 116 | 286.54 | 114 |
| k (shape) | 21 | 1.56 | 0.07 | 0.225 | 113 | 285.33 | 114 |
| | | | | | | | |
| $T_2$ mean | 21 | 0.93 | 0.04 | 0.347 | 115 | 285.98 | 118 |
| $T_2$ SD | 21 | 1.60 | 0.07 | 0.219 | 113 | 285.28 | 118 |
| $T_2$ ratio | 21 | 13.60 | 0.39 | 0.001* | 91 | 275.49 | 92 |
| $T_2$ mean and SD | 20 | 0.77 | 0.07 | 0.476 | 116 | 287.93 | 122 |
| $T_2$ mean, SD and ratio | 19 | 5.30 | 0.46 | 0.008* | 95 | 278.62 | 91 |

*Note.* Variables included in the linear regression models are the parameters associated with the probability distributions listed. 2nd order models include parameters of the distributional model as well as parameters of the model squared. 3rd order models include parameters of the distributional model, and parameters the model squared and cubed. VOI = volume of interest, df = degrees of freedom, F = F-statistic vs. constant model, p = significance level, GEV = Generalized Extreme Value, RMSE = root mean square error rounded to the nearest minute, average RMSE is the average RMSE across folds from leave-one-out cross-validation, $AIC_c$ = Akaike information criteria corrected for sample size. * denotes statistically significant model as $p < 0.05$.

Table 8.3 Statistics of regression models and evaluation metrics for GM VOIs

| **Variables included in regression models** | **Statistics of regression models** | | | | **Evaluation statistics** | | |
|---|---|---|---|---|---|---|---|
| | *df* | *F* | $R^2$ | *p* | RMSE (± mins) | AICc | Average RMSE (± mins) |
| GEV (μ ,σ, k) | 9 | 0.21 | 0.07 | 0.888 | 128 | 171.21 | 145 |
| GEV 2nd order | 6 | 0.42 | 0.30 | 0.844 | 136 | 190.94 | 332 |
| GEV 3rd order | 3 | 0.79 | 0.70 | 0.655 | 614 | 273.25 | 124 |
| μ (location) | 11 | 0.51 | 0.04 | 0.490 | 117 | 163.70 | 125 |
| σ (scale) | 11 | 0.14 | 0.01 | 0.718 | 119 | 164.13 | 119 |
| k (shape) | 11 | 0.04 | 0.00 | 0.848 | 119 | 164.24 | 125 |
| | | | | | | | |
| Burr (α, c, k) | 7 | 0.93 | 0.29 | 0.474 | 125 | 147.09 | 178 |
| Burr 2nd order | 4 | 11.7 | 0.95 | 0.016* | 45.3 | 155.32 | 121 |
| Burr 3rd order | 1 | 118 | 0.99 | 0.071 | 12 | inf | 4201 |
| α (scale) | 9 | 1.32 | 0.13 | 0.279 | 122 | 140.11 | 133 |
| c (shape) | 9 | 0.46 | 0.05 | 0.513 | 127 | 141.07 | 127 |
| k (shape) | 9 | 1.39 | 0.13 | 0.268 | 121 | 140.04 | 171 |
| | | | | | | | |
| $T_2$ mean | 11 | 0.93 | 0.78 | 0.356 | 115 | 163.23 | 121 |
| $T_2$ SD | 11 | 0.00 | 0.00 | 0.971 | 119 | 164.28 | 128 |
| $T_2$ ratio | 11 | 5.25 | 0.32 | 0.043* | 98 | 159.21 | 106 |
| $T_2$ mean and SD | 10 | 3.47 | 0.41 | 0.071 | 96 | 160.90 | 105 |
| $T_2$ mean, SD and ratio | 9 | 5.20 | 0.63 | 0.024* | 80 | 159.02 | 94 |

Note. Variables included in the linear regression models are the parameters associated with the probability distributions listed. 2nd order models include parameters of the distributional model as well as parameters of the model squared. 3rd order models include parameters of the distributional model, and parameters the model squared and cubed. VOI = volume of interest, df = degrees of freedom, F = F-statistic vs. constant model, p = significance level, GEV = Generalized Extreme Value, RMSE = root mean square error rounded to the nearest minute, average RMSE is the average RMSE across folds from leave-one-out cross-validation, $AIC_c$ = Akaike information criteria corrected for sample size. * denotes statistically significant model as $p < 0.05$.

Table 8.4 Statistics of regression models and evaluation metrics for WM VOIs

| **Variables included in regression models** | **Statistics of regression models** | | | | | **Evaluation statistics** | |
|---|---|---|---|---|---|---|---|
| | *df* | *F* | $R^2$ | *p* | RMSE (± mins) | AICc | Average RMSE (± mins) |
| GEV (μ ,σ, k) | 17 | 0.91 | 0.14 | 0.456 | 114 | 264.55 | 129 |
| GEV 2nd order | 14 | 0.63 | 0.21 | 0.704 | 120 | 274.78 | 271 |
| GEV 3rd order | 11 | 0.75 | 0.38 | 0.659 | 120 | 289.10 | 1120 |
| μ (location) | 19 | 0.39 | 0.02 | 0.542 | 115 | 261.43 | 120 |
| σ (scale) | 19 | 0.03 | 0.00 | 0.869 | 116 | 261.82 | 124 |
| k (shape) | 19 | 0.91 | 0.46 | 0.353 | 113 | 260.88 | 121 |
| Log-logistic (μ,σ) | 18 | 1.70 | 0.16 | 0.211 | 109 | 260.97 | 118 |
| Log-logistic 2nd order | 16 | 0.81 | 0.20 | 0.535 | 115 | 267.30 | 195 |
| Log-logistic 3rd order | 14 | 1.02 | 0.30 | 0.453 | 113 | 272.20 | 145 |
| μ (location) | 19 | 0.64 | 0.03 | 0.433 | 114 | 261.16 | 119 |
| σ (scale) | 19 | 2.06 | 0.10 | 0.167 | 110 | 259.69 | 118 |
| $T_2$ mean | 19 | 0.07 | 0.03 | 0.492 | 115 | 261.32 | 119 |
| $T_2$ SD | 19 | 0.07 | 0.00 | 0.800 | 116 | 261.78 | 123 |
| $T_2$ ratio | 19 | 2.43 | 0.11 | 0.136 | 109 | 259.33 | 123 |
| $T_2$ mean, SD | 18 | 0.83 | 0.08 | 0.453 | 114 | 262.75 | 128 |
| $T_2$ mean, SD, ratio | 17 | 0.96 | 0.15 | 0.433 | 113 | 264.39 | 137 |

Note. Variables included in the linear regression models are the parameters associated with the probability distributions listed. 2nd order models include parameters of the distributional model as well as parameters of the model squared. 3rd order models include parameters of the distributional model, and parameters the model squared and cubed. VOI = volume of interest, df = degrees of freedom, F = F-statistic vs. constant model, p = significance level, GEV = Generalized Extreme Value, RMSE = root mean square error rounded to the nearest minute, average RMSE is the average RMSE across folds from leave-one-out cross-validation, $AIC_c$ = Akaike information criteria corrected for sample size. * denotes statistically significant model as $p < 0.05$.

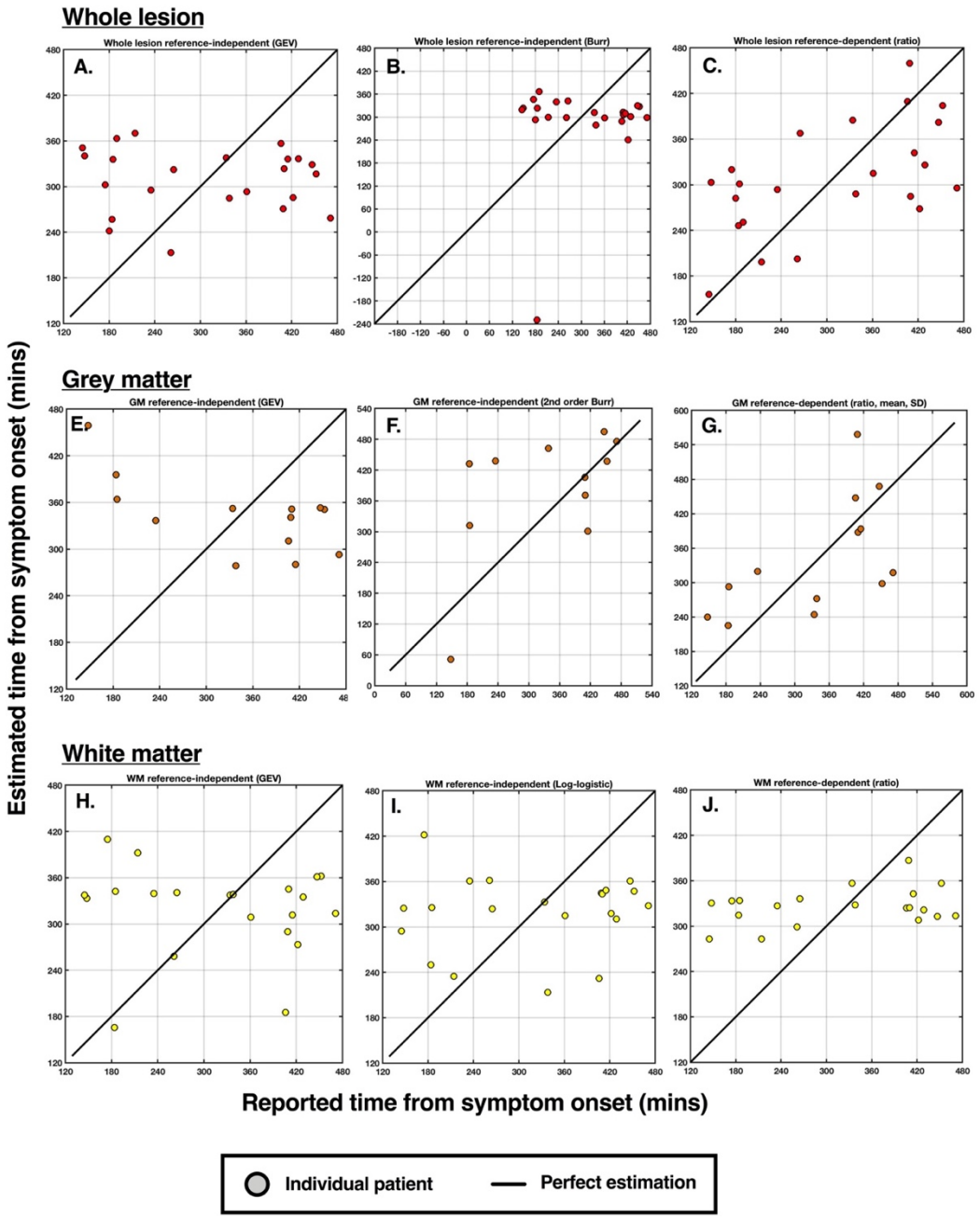


Figure 8.7 Reported symptom onset time vs estimated time of stroke onset plots illustrating the performance of $T_2$ based reference-independent and reference-dependent regression models for whole ischaemic (**A.**, **B.**, **C.**), GM (**E.**, **F.**, **G.**) and WM (**H.**, **I.**, **J.**) VOIs.

**A.** Whole VOI reference-independent regressor with parameters of the GEV probability distribution as variables.

**B.** Whole VOI reference-independent regressor with the parameters of the Burr type X11 probability distribution as variables.

**C.** Whole VOI reference-dependent regressor with the $T_2$ ratio as the predictive variable.

**D.** GM VOI reference-independent regressor with parameters of the GEV probability distribution as predictive variables.

**E.** GM VOI reference-independent second-order polynomial with the parameters of the Burr type X11 probability distribution as variables.

**F.** GM VOI reference-dependent regressor with the $T_2$ ratio, mean $T_2$ and $T_2$ SD as variables.

**G.** WM VOI reference-independent regressor with parameters of the GEV probability distribution as variables.

**H.** WM VOI reference-independent regressor, with the parameters of the log-logistic probability distribution as variables.

**I.** WM VOI reference-dependent regressor with the $T_2$ ratio as the predictive variable.

## 8.5 Discussion

The study examined the distributions of $T_2$ relaxation times within ADC defined ischaemic regions of hyperacute ischaemic stroke patients. The aim was to determine whether characteristics of the $T_2$ distributions would correlate with stroke onset time and therefore provide a means to develop reference-independent timing tools for human stroke. GM was the only tissue type for which distributional parameters demonstrated a relationship with time from symptom onset. Despite concerns over finding an accurate non-ischaemic reference in the contralateral hemisphere, the simple reference-dependent $T_2$ image intensity ratio from the whole ischaemic VOI provided the most accurate estimates of stroke onset time.

The finding that distributional parameters within GM VOIs showed a significant relationship with time from symptom onset is consistent with Norton et al.'s (2017) results in rat models of ischaemia, where ischaemic regions were almost exclusively GM. Norton et al. (2017) found a third-order polynomial regression model with the $T_2$ location ($\mu$) and scale ($\sigma$) parameters associated with the log-logistic probability distribution as variables, was significantly related to time from ischaemia onset. In the present study, a second-order polynomial regressor including the $T_2$ scale (c, k) and shape ($\alpha$) parameters associated with the Burr type X11 probability distribution as variables, was significantly related to time from symptom onset. The squared (this study) and cubed (Norton et al., 2017) variables included in the regressors from both studies, suggests that, at least for GM, the relationship between $T_2$ distribution-based parameters and time from symptom onset is not necessarily linear.

Interestingly, Siemonsen et al. (2009) also reported a quadratic trend of hemispheric differences in the $T_2$ relaxation time in ischaemic regions containing both GM and WM in ischaemic stroke patients. Accordingly, the mathematical *cytotoxic oedema dissociation model* (CED model), which describes the combined spatiotemporal progression of ADC and $T_2$ in rat cerebral ischaemia predicts a nonlinear

development of the $T_2$ distribution in early time points where the width of the $T_2$ distribution is initially narrow, then becomes broader and longer than average, before narrowing again (Knight, McGarry et al., 2016). It is assumed that this change in distribution reflects the gradual change of oedema states in the ischaemic region, as not all voxels are equally affected by ischaemia (Knight, McGarry et al., 2016).

The initially narrow distribution shows that most of the voxels within the ischaemic region have similar 'normal' $T_2$ relaxation times because at this stage water content has not changed (i.e., cytotoxic oedema). The broader distribution that follows reflects the transition to the ionic oedema and vasogenic oedema states, where total water content, and therefore $T_2$, begins to increase. As the development of ionic and vasogenic oedema is gradual and will happen at different rates within the ischaemic tissue, some voxels will have very long $T_2$ relaxation times reflecting increased water content (vasogenic oedema), some will have long $T_2$ relaxation times but longer than normal (reflecting more subtle water uptake from ionic oedema), or normal, pre ischaemic relaxation times (reflecting cytotoxic oedema). The eventual re-narrowing of the $T_2$ distribution in the later hours of ischaemia reflects the final state of vasogenic oedema, where all voxels within the ischaemic region have increased water content, and so the majority of voxels have similarly long $T_2$ relaxation times. Thus, the relationship of $T_2$ based parameters with time from stroke onset may be more complex and dynamic than first assumed. It is difficult to determine from the dataset in this study whether the transition of the $T_2$ distribution described above (from narrow to broad to narrow again) also applies to patients because the ischaemic VOIs differed considerably in size and location. However, it is worth investigating other potential nonlinear fits to the data when investigating $T_2$ based methods for stroke onset time estimation.

The GEV and log-logistic probability distributions provided the best fit to the $T_2$ distributions within ischaemic WM of patients, but parameters associated with these distributions showed no relationship with time from symptom onset. The time

dependency of GM, but not WM distributional parameters, could be due to inherent functional and structural differences between the tissue types. For example, imaging studies of patients suggest WM is generally more resistant to ischaemia, as WM tended to contain more 'at risk' tissue than GM even at later time points (Falcao et al., 2004; Koga et al., 2005). WM has half the metabolic demands of GM (Helenius et al., 2003; Simon et al., 2005) and up to one-third of the CBF and CBV requirements that GM has (Clarke & Sokolof, 1999; Nishizaki et al., 1988). Thus, lack of oxygen will be less detrimental to WM, resulting in slower progression to irreversible infarction than GM (Matute et al., 2013). Consequently, changes in the heterogeneity of the ischaemic region and therefore $T_2$ distributional parameters, may not be pronounced enough with the first six hours to demonstrate a relationship with time. The six hour time period studied here may also explain why the WM $T_2$ image intensity ratio was not a significant predictor of stroke onset time but was in a previous study with a larger cohort of strokes scanned within nine and a half hours of onset (Damion, Knight, McGarry et al., 2019).

Additionally, WM is structurally more complicated than GM, and so damage and stress are likely to alter its magnetic environment in a different way to GM (Knight, McCann, Tsivos, Coulthard, et al., 2016). For example, WM contains fibre tracts, for which the $T_2$ relaxation time is directionally dependent, termed '$T_2$ anisotropy' (Knight et al., 2015). Longer $T_2$ in the head-foot direction and WM corticospinal tracts and shorter $T_2$ in the anterior thalamic radius of elderly participants has also been observed (Knight, McCann, Tsivos, Coulthard, et al., 2016). Given this variation, it is likely that the $T_2$ distribution within WM differs depending on anatomy and may, therefore, explain why $T_2$ distributions were not related to onset time in this study as the regressors were trained on $T_2$ data from strokes occurring in different territories. A study with a larger cohort would enable ischaemic regions in different anatomical regions to be studied separately.

Aside from containing only ischaemic GM, another difference between previous studies investigating the $T_2$ distributions over time (e.g., Chapter 5; McGarry et al., 2016a; Norton et al., 2017) is that that the majority of patients received thrombolysis (Chapter 7, Section 7.4, Table 7.1) whereas the rats in the previous studies were not thrombolysed. As discussed in Chapter 7, it is unlikely that thrombolysis affected the average $T_2$ over time as the formation of ischaemic brain oedema is not affected by rtPA (Broocks et al., 2019). Siemonsen et al. (2012) also found no difference between $T_2$ values in ischaemic growth regions and surviving tissue regions in thrombolysed and non-thrombolysed patients. However, it is not clear how thrombolysis would affect distributional parameters. The location and scale parameters of the log-logistic distribution changed with time from stroke onset in GM of non-reperfused rats (Norton et al., 2017), but thrombolysis could be responsible for these parameters not changing in WM, especially as thrombolysis is more effective in WM than GM (Tisserand et al., 2014).

The hypothesis that the SD of $T_2$ within the ADC defined ischaemic region would provide timing information in acute stroke patients was based on Madai et al.'s (2016) finding that the SD of DWI image intensities differentiated between patients within and beyond the thrombolysis treatment window with high accuracy. However, this hypothesis was not supported in the present study. The relationship of the DWI SD, but not $T_2$ SD, with time from symptom onset, could be because the DWI signal eliminates signal from mobile species such as water and is, therefore, less likely to be influenced by CSF than $T_2$ relaxometry maps. The DWI signal intensity would, therefore, be also sensitive to changes in the $T_2$ distribution caused by ischaemia.

Furthermore, although in Chapter 7 it was concluded that a range of confounding factors that influence intensities of weighted images contribute to errors in onset time estimates, it may be that when examining the heterogeneity of the ischaemic region, these factors are beneficial. The DWI signal is essentially the composite of the ADC and the $T_2$ relaxation time, and therefore, the signal reflects a

combination of cytotoxic oedema (ADC) and vasogenic oedema ($T_2$). The DWI image intensity ratio is not ideal for estimating onset time because the decrease in ADC counteracts the increase in $T_2$, causing a weak relationship with time. Also, Madai et al. (2016) found the ADC SD and $T_2$w FLAIR SD studied separately, did not predict onset time, suggesting it is something about the combination of ADC and $T_2$ that makes DWI unique for reflecting changes in the heterogeneity of ischaemic tissue. The change in the DWI SD overtime may be similar to $f_2$, reflecting the change in $T_2$ relative to the change in ADC. It was beyond the scope of this study to examine the distribution of DWI signal intensities in relation to stroke onset time, but this should be investigated in future.

There are a few limitations to this study, related to having a small data set that imposed restrictions on the analysis and inference of results. Firstly, in the absence of a test dataset to validate the regression models, LOOCV was applied to estimate how well they could potentially perform with new data (James et al., 2013). LOOCV is useful for small datasets as it means all of the available data is used to train the model, and therefore benefits from low bias (James et al., 2013). However, because the performance of the model is only tested on one dataset, LOOCV is sensitive to fluctuations in the data, which can result in a high variance in the estimates of the model's prediction accuracy (James et al. 2013; Varoquax, 2018). Therefore, estimates of the overall performance of the regression models given by the average RMSEs provide an initial indication of the ability to estimate onset time but should not be considered conclusive.

Secondly, Norton et al.'s (2017) reference-independent approach to stroke timing required finding the probability distribution that 'best described' the empirical distributions of $T_2$ relaxation times within ADC defined ischaemic regions. In the current study, 'best described' was operationally defined as the two probability distributions that commonly had the lowest AIC values across patients. Therefore, the identified probability distributions did not fit the empirical $T_2$ distributions of all of the patients. For example, in the WM VOI dataset, some VOIs fitted the

Burr type X11 probability distribution only, some, the GEV distribution only, some fitted both and a few fitted neither. Therefore, including data in the GEV based regression model, that did not have a good fit to the GEV probability distribution, could have contributed to higher uncertainties in onset time estimates. The fact that a singular distributional model did not fit the $T_2$ distribution of all ischaemic VOIs in the same group could also reflect the more complex structure of the human brain compared to the rat brain.

Further to the point above, the present study was conducted on the assumption that the distributions of relaxation times within ischaemic regions would be unimodal, as this was observed previously in rat models of ischaemia (Knight, McGarry et al. 2016; Norton et al. 2017). However, a bimodal distribution was observed in the ischaemic VOIs of two patients in this study (Figure 8.6- parts A, B, C, E and F). This observation raises two interesting possibilities. Firstly, the presence of a bimodal $T_2$ distribution may be indicative of onset time, as bimodality was present in the earlier scan times (3 hours and 5.5 hours) and not in the later scan time (7.5 hours). However, a bimodal distribution was not present in the data of the other patients. It is not clear why these particular patients had bimodal distributions, but a larger dataset would help clarify this.

Secondly, although the rest of the dataset did not contain a bimodal distribution, the two cases in Figure 8.6 highlight the possibility that $T_2$ distributional information within the ischaemic region is not necessarily reducible to a unimodal distribution. Therefore, in future studies, before deciding on which distributional models and associated parameters best describe the $T_2$ distribution, the probability distributions of $T_2$ for each patient should first be tested for multi-modality. One approach would be to use the Müller and Sawitzi (1991) excess-mass test which indicates the presence of a mode where the excess of the probability mass is concentrated. In cases where a multi-modal distribution is present, the appropriate models to be tested for fitting can be selected.

An additional limitation is that the multi-echo $T_2$ pulse sequences and parameters needed for computation of $T_2$ relaxometry maps differed between sites. The only multi-echo $T_2$ sequence available on the Philips scanner in Bristol was a gradient and spin-echo sequence (GRASE), which involves alternating 180-degree RF pulses and gradient pulses to generate multiple echoes (Caruthers et al., 1998; Elster 1993). The resulting signal is therefore influenced by both $T_2$ relaxation due to the spin-echo component, as well as $T_2^*$ due to the gradient-echo component (Caruthers et al., 1998; Elster 1993). Whereas the only multi-echo $T_2$ sequence available on the Siemens scanners at Glasgow and Oxford was a turbo-spin-echo sequence (TSE), and so $T_2^*$ did not contribute to signal. The contribution of $T_2^*$ could have made the $T_2$ results from Bristol noisier (Carneiro et al., 2006).

Additionally, compared to GRASE, the TSE sequences involved longer TRs and fewer TEs with longer echo-spacing (Chapter 7, Section 7.3, Table 7.1), which produced inherently longer $T_2$ values in ischaemic and non-ischaemic regions. The difference in the average $T_2$ between sites is evident in Figure 8.6 where the peak of the $T_2$ distributions of ischaemic and non-ischaemic VOIs are further to the right in the two patients from Glasgow (D, E, F and G, H, I) compared to the patient from Bristol (A, B, C). Quantifying $T_2$ relaxation times is more reliable than quantifying intensities from weighted images because $T_2$ relaxation times are reproducible across sites and repeated imaging sessions (Deoni et al., 2008), but only if the same $T_2$ sequence is used. Thus, combining the $T_2$ distribution data from the three sites could have mitigated any relationship between $T_2$ distributional parameters and time from symptom onset. Separating the data according to the site would be an essential next step to determine whether pulse sequence parameters affect the $T_2$ distribution. If so, a standardisation method that ensures $T_2$ is sensible across all scans would be required. However, given that the purpose of quantifying image intensity ratios for the reference-dependent approach was to reduce concerns associated with different pulse sequences, quantifying the image intensity ratio for onset time estimation may be the more straightforward option.

To conclude, this study suggests that $T_2$ distributional parameters may be informative of onset time in strokes occurring in GM, but not in WM or strokes affecting both tissue types. The relationship of $T_2$ distributional parameters with time from stroke onset was studied to determine whether the $T_2$ distribution could provide a reference-independent means for onset time estimation. A reference-independent approach would avoid sources of error associated with reference-dependent methods for stroke timing. However, this study suggests that the distribution-based reference-independent approach has its own sources of error, such as sensitivity to tissue type, anatomical location and pulse sequences, that would limit its utility in a clinical setting. Considering these issues and that the $T_2$ image intensity ratio from the whole ischaemic VOI provided the most accurate estimate of stroke onset time, the reference-dependent approach may be more suitable for clinical settings.

Sources of error associated with the reference-dependent approach are still a concern, but these could be addressed by improving methods for defining the reference volume. For example, Knight, Damion, McGarry et al. (2019) recently developed the user-independent, *spherical reference approach,* that exploits the insensitivity of $T_2$w signal intensities to ischaemia to approximate pre-ischaemic $T_2$ relaxation times. In brief, the spherical reference approach involves measuring the mean $T_2$ relaxation time of normal brain tissue in a reference sphere (of a given radius) centred around a voxel contralateral to the ischaemic region and measuring the $T_2$w signal intensity value of a voxel in the ischaemic region. The pre-ischaemic reference $T_2$ relaxation time is estimated by conditioning the mean $T_2$ relaxation time by the $T_2$w intensity value. This spherical-reference method was more accurate at estimating stroke onset time in patients than the standard mirror-reference approach (used in Chapters 5 and 7 and other studies, e.g., Siemonsen et al., 2009; Song et al., 2012), and for a more detailed explanation, the reader is referred to the paper published by Knight, Damion, McGarry et al. (2019).

# Chapter 9
# General Discussion

The aim was to explore the ability of time-based qMRI methods for estimating stroke onset time in preclinical models of ischaemia and hyperacute ischaemic stroke patients. The overall goal was to identify which, if any, parameter(/s) should be examined further in more extensive clinical studies. This Chapter begins by summarising the main conclusions and the questions that emerged from the three research chapters (Chapter 4, Chapter 6, Chapter 7). These summaries are then drawn together to form an overarching conclusion, followed by a discussion outlining the original contributions of this thesis. Conclusions are then discussed in the context of up-to-date stroke timing literature (up to February 2020) and how they support or complement the ongoing qMRI research efforts for alleviating the problem of unknown onset time issue in clinics. Limitations of the research studies in this thesis are subsequently addressed, and the Chapter ends with recommendations for further work.

## 9.1 Summary of the conclusions drawn from the research chapters

### Chapter 5 (preclinical study): The $T_2$ relaxation time ratio and $T_2$ distributions estimate ischaemia onset time more accurately than image intensity ratios from weighted images in rat models of ischaemia

Chapter 5 was a preclinical MRI study that investigated the accuracy, sensitivity and specificity of qMRI parameters in distinguishing between scans performed before and after three hours from ischaemia onset (McGarry et al., 2016b). The study enabled a direct and unambiguous comparison between qMRI parameters, under controlled conditions, without being compromised by the short MRI scan time for patients. The purpose was to identify the qMRI parameters that could also be used in patients and therefore inform the design of the pilot studies in Chapters 7 and 8. The main conclusions drawn from the preclinical study were that qMRI indices based on the $T_2$ relaxation time are more accurate, sensitive and specific than any quantitative parameters from weighted images and that the distributional information of the $T_2$ relaxation times ($f_2$) or distributional information of $T_1$ and $T_2$ combined ($V_{overlap}$) may be more informative of onset time than the relaxation time ratios. These conclusions support previous preclinical studies that showed relaxation-based qMRI parameters had smaller margins of error when used to estimate stroke onset time than qMRI parameters based on intensities of weighted images (McGarry et al., 2016a; Rogers, McGarry et al., 2014). An additional conclusion was that the $T_1$ relaxation time ratio is unlikely to be suitable for stroke timing in clinics because it had low sensitivity, which is likely due to the more gradual, two-phase response to ischaemia (Calamante et al., 1999; Kettunen et al., 2000).

The questions that emerged from Chapter 5 were: **a)** whether the $T_2$ relaxation time-based image intensity ratios based on the non-ischaemic reference would identify hyperacute ischaemic stroke patients scanned within or beyond the 4.5 hour treatment window. **b)** whether distributional information of the $T_2$ relaxation time within the ADC defined ischaemic region would also be informative of stroke onset time in patients. These questions were subsequently addressed in Chapters 7 and 8.

## Chapter 7 (clinical study): The $T_2$ relaxation time image intensity ratio is a more accurate and reliable indicator of time from symptom onset in hyperacute ischaemic stroke patients than image intensity ratios from weighted images.

Chapter 7 was a pilot study of hyperacute ischaemic stroke patients, which compared the ability of visual and quantitative MRI methods for stroke timing. The $T_2$ relaxation time was the only qMRI parameter that showed a significant linear relationship with time from symptom onset, had the highest ability at differentiating between scans performed within and beyond 4.5 hours of onset (without compromising sensitivity and specificity) and the highest probability of correctly predicting whether a patient was scanned within 4.5 hours. The predictive ability by MRI variables was not improved by including ADC, DWI, $T_2$w and $T_2$ ratios in the same model, suggesting that acquiring ADC (for identification of ischaemic regions) and $T_2$ (for onset time estimation) would be sufficient. $T_2$ also demonstrated better ability at identifying patients within the treatment window compared to the visual DWI/FLAIR mismatch and the FLAIR image intensity ratio. This finding supports previous conclusions concerning the low sensitivity associated with FLAIR-based stroke timing methods (Ebinger et al., 2010; Etherton et al. 2018).

In line with conclusions from Chapter 5, the main conclusion from Chapter 7 was that quantification of the $T_2$ relaxation time is a more accurate method for stroke

timing than quantification of intensities of weighted images. The main question that emerged from Chapter 7 was whether the results would be supported in a more extensive study, which would enable acquisition of more FLAIR scans and the potential influence of factors such as vascular territory and collateral flow (i.e., with additional angiography scans) to be studied.

### Chapter 8 (clinical study): $T_2$ distributional parameters in ischaemic GM may be a reference-independent indicator of onset time, but the reference-dependent method may be more accurate and more applicable for patients.

Chapter 8 was a pilot study of hyperacute ischaemic stroke patients that investigated which probability distributions best described the empirical distributions of $T_2$ relaxation times within ADC defined whole, GM and WM ischaemic regions. Also, whether any of the distribution characteristics could potentially provide a reference-independent stroke timing tool for human stroke as has been suggested in a rat stroke model (Norton et al. 2017). The $T_2$ in whole ischaemic regions and GM ischaemic regions was best described by the Burr type X11 and the generalised extreme value (GEV) probability distributions. The $T_2$ in WM ischaemic regions was best described by the GEV and log-logistic distributions. However, the only distributional parameters that showed a relationship with time from symptom onset were the shape $\alpha$ and scale ($c$,$k$) parameters of the Burr type X11 probability distribution in GM, in the form of a second-order polynomial regression model.

The main conclusions drawn from Chapter 8 were that $T_2$ distributional parameters from GM, but not WM or whole ischaemic regions, may be informative of stroke onset time, but the relationship of GM $T_2$ with time may not be linear. Tentatively, the ischaemic GM $T_2$ distribution characteristics is a potential reference-independent stroke timer. Additionally, the reference-dependent image intensity approach applied to the whole ischaemic region (used in Chapter 5 and Chapter 7)

may be more suitable for clinical settings because it provided the most accurate estimate of stroke onset time. Also, the reference-independent distribution-based approach is likely to be influenced by tissue type, anatomical location and the MRI pulse sequences used to acquire $T_2$ maps. The main question raised from Chapter 8, for future work, was whether the lack of timing information of the $T_2$ distributional parameters in WM and whole ischaemic regions was due to a) the small sample sizes, b) inherent complexities of WM, c) combining distributions from different vascular territories, or d) the use of different multi-echo $T_2$ pulse sequences (i.e. GRASE and TSE).

## 9.2 Main conclusion

The collective results of the studies in this thesis strongly suggest that future imaging research efforts dedicated to reducing the problem of unknown onset time should focus on quantifying the $T_2$ relaxation time within the ADC defined ischaemic region. This is because the $T_2$ relaxation time was demonstrated to be a more reliable and accurate estimator of onset time than image intensities from weighted images in both rat models of ischaemia and hyperacute stroke patients.

## 9.3 Original contributions

### First direct comparisons of potential MRI stroke timers

The studies in this thesis were the first of their kind. At the start of this PhD (2015), the $T_2$ relaxation time as an estimator of stroke onset time was mainly the focus of preclinical research (e.g. Jokivarsi et al., 2010; McGarry et al., 2016a, 2016b), and the study by Siemonsen et al. (2009) was the only published study that investigated $T_2$ in hyperacute ischaemic stroke patients for the purpose of stroke timing. Much of the focus within the stroke timing literature was on the potential ability of the visual-based DWI/FLAIR mismatch (Thomalla et al., 2011),

and quantification of the FLAIR image intensity ratio (e.g., Song et al., 2012; Petkova et al., 2010). With the exception of Wu et al. (2011), in 2015 (and even now in 2020), comprehensive, often-cited MRI stroke timing review papers have not mentioned $T_2$ relaxometry as a potential method for onset time estimation (e.g., Biggs et al., 2019; Etherton et al., 2018; Huang et al., 2019; Kang et al., 2012; Wouters et al., 2014), despite the large amount of preclinical work indicating the potential utility of MR relaxometry in stroke timing (e.g., Calamante et al., 1999; Gröhn et al., 1998; Hoehn-berlage et al., 1995; Jokivarsi et al., 2010; Rogers, McGarry et al., 2014). Until the publication of McGarry et al. (2016b) (Chapter 5), there had not been a direct comparison of DWI, ADC, $T_2$w, and $T_2$ ratios as qMRI stroke timers in rat models. Until now (Chapter 7) there has not been a direct comparison of all of these qMRI parameters with the FLAIR image intensity ratio and the DWI/FLAIR mismatch for stroke timing in patients. Also, the heterogeneity of $T_2$ within ADC defined ischaemic regions had not been studied in hyperacute ischaemic stroke patients (Chapter 8), only in rats (Knight, McGarry et al., 2016; McGarry et al., 2016a; Rogers, McGarry et al., 2014; Norton et al., 2017).

## Existing $T_2$ based MRI stroke timing methods can be improved by parametrising $T_2$ weighted MRI data

The main conclusion of this thesis also suggests that the scientific community focused on improving stratification of stroke patients with unknown onset time to treatment, are on the right track using $T_2$ based MR signal intensities represented in weighted images to estimate onset time ( i.e., DWI and $T_2$w with/without FLAIR). However, the results also suggest that the ability of $T_2$ based MRI data for estimating onset time can be improved by adopting the parametric approach to quantitative MRI (Chapter 3, Section 3.7.2). The studies here have demonstrated that by transforming weighted images to their parametric counterparts (i.e., DWI to ADC and $T_2$w images to $T_2$ relaxation time maps), ischaemia can be identified early-on and onset time can be estimated more reliably and accurately. The MR data that is represented in parametric maps (e.g., ADC values in ADC maps, and

$T_2$ relaxation times in $T_2$ maps) are essentially a purer, more refined form of the signal intensities studied in the corresponding weighted images (e.g., DWI, $T_2$w or $T_2$w FLAIR) because they are not impacted by uncontrollable sources of variance (e.g., magnetic field inhomogeneities, $T_1$ relaxation and PD). By taking this parametric approach, the recommended MRI stroke protocol incorporating DWI, $T_2$w, $T_2$w FLAIR and $T_2^*$w images (Mair & Wardlaw, 2014) can still be used at no extra scan time as DWI and ADC are always provided together in clinical practice, and most MRI scanners can automatically produce $T_2$ maps from multi-echo $T_2$ sequences. It would also be possible to acquire all these images almost as quickly as it would take for a patient to have a NCCT scan if magnetic resonance fingerprinting, which involves the simultaneous acquisition of multiple parameters (Ma et al., 2013, see Chapter 3, Section 3.7.3), becomes a routine in clinical MRI scanners.

## Demonstration that preclinical MRI of stroke is translatable to clinical MRI of stroke

The successful translation of preclinical MRI findings (Chapter 5; Jokivarsi et al., 2010; McGarry et al., 2016a, 2016b; Rogers, McGarry et al., 2014; Norton et al., 2017) to clinical presentations of hyperacute ischaemic stroke (Chapters 7 and 8) shows that MRI observations made in animal models of stroke are directly relevant to human stroke. This is because the MRI and data analysis techniques used in the rat (Chapter 5) and patient (Chapters 7 and 8) studies and the parallel research in patients at the University of Bristol (Damion, Knight, McGarry et al., 2019; Knight, Damion, McGarry et al., 2019) were all developed in preclinical projects (Knight, McGarry et al., 2016; McGarry et al., 2016a, 2016b, 2017; Norton et al., 2017). This translation and other recent research (e.g., Bertoglio et al., 2017) demonstrates that preclinical MRI data are crucial guides for advancing clinical imaging to benefit patient management of stroke and other neurological conditions. This demonstrated translation, therefore, also justifies the use of animal models in future MRI research of common human diseases.

## First application of Precision-Recall-Gain analysis in MRI stroke timing research

Another original contribution of this thesis is that the study in Chapter 7 (McGarry et al., 2020) raises awareness of the problem of class imbalance in MRI stroke timing research, and is the first study to apply Precision-Recall-Gain (Flach & Kull, 2015) as a more appropriate method of evaluation to address the problem. As discussed in Chapter 4, Section 4.4, the majority of clinical MRI stroke timing studies treat the problem of unknown onset time as a binary classification problem and evaluate the performance of different MRI based timing methods using ROC curves, the area under ROC curves and by calculating the accuracy, sensitivity and specificity. However, as highlighted in Chapter 8 (McGarry et al., 2020), these performance metrics are only appropriate if the class distribution is evenly weighted (i.e., a comparable number of patients within 4.5 hours and beyond 4.5 hours). If there are more patients in one class than the other (i.e., more scanned within the treatment window than beyond it) than the evaluation metrics will be biased toward the class with a higher number of patients.

At the time of writing this Discussion (early 2020), out of all the MRI stroke timing studies that assessed the same MRI based methods that were studied in this thesis (DWI/FLAIR mismatch, FLAIR ratio, DWI ratio, ADC ratio), only one (Petkova et al., 2010) had an evenly weighted class distribution (63 scanned within three hours of onset, and 67 scanned after). Most studies included more patients within the treatment window than beyond (e.g., Emeriau et al., 2013, 2016; Madai et al., 2016; Thomalla et al., 2011; Wouters et al., 2018) and others did not specify the class distribution (e.g., Cheng et al., 2013; Siemonsen et al., 2009). Authors of stroke timing studies have confidently reported evaluation metrics whilst being unaware of the impact of an imbalanced class distribution on these metrics and their resulting conclusions. For example, in a clinical study, Madai et al. (2016) reported high accuracy, sensitivity and specificity levels for DWI/FLAIR mismatch, the DWI ratio and FLAIR ratio, but these results were based on a dataset that had 63 patients within the 4.5 hour thrombolysis treatment window

and 19 beyond it. Therefore, results would have overestimated the overall accuracy and sensitivity of these classifiers, giving an unrealistic representation of the ability to correctly identify patients within the rtPA treatment window. Overrepresentation of sensitivity is critical, because as discussed in Chapter 4, Section 4.4.2, it is one of the predominant limitations of the visual DWI/FLAIR mismatch.

The class imbalance problem also applies to studies that examine the relationship of qMRI parameters with time from symptom onset. For example, Ebinger et al. (2010) reported no relationship between the FLAIR image intensity ratio and time from symptom onset; however, the cohort included 72 patients scanned within 4.5 hours from symptom onset and 22 patients scanned after. It is already well established that $T_2$w FLAIR signals image do not change much within the first 4.5 hours (hence why DWI/FLAIR mismatch indicates patients within 4.5 hours), so if the majority of points in the correlation were from this early time point, it is not surprising there was no overall correlation. Similarly, Cheng et al. (2013) reported a strong relationship of the FLAIR image intensity ratio with time from symptom onset, but the majority of patients were scanned between four and 12 hours from symptom onset, which would have biased the strength of the correlation as the size of the FLAIR ratio would have been greater for a larger proportion of the dataset.

In order to fully understand the ability of MRI based methods for timing the ischaemic stroke, this work encourages future stroke timing studies to either a) ensure that the dataset is comprised of an equal number of patients within and beyond the specified treatment window or b) to apply methods, such as precision-recall-gain that can account for the class imbalance (Flach and Kull, 2015).

## 9.4 Relevance to stroke timing literature in early 2020

Recently published MRI studies adopting supervised machine learning and unsupervised deep learning techniques for stroke onset time estimation (Ho et al., 2019; Lee et al., 2020) are of particular relevance to the thesis results. *Supervised machine learning* involves developing algorithms that computers can use to extract patterns from existing data to generate predictive models that can be applied to new data (Kelleher & Tierney, 2018). Deep learning is a form of machine learning, that is *unsupervised,* where computers discover complex patterns in large data sets that would otherwise be unknown (Lundervold & Lundervold, 2019). The machine learning studies distinguished between patients scanned before and after 4.5 hours from symptom onset using MRI based descriptive (e.g., image intensities) and morphological features (e.g., the diameter of the ischaemic region) (Lee et al., 2020), as well as latent features identified via deep learning (Ho et al., 2019), as predictive variables. Lee et al. (2020) reported an AUC of 0.83, a sensitivity of 0.75 and specificity 0.83, whereas, with the addition of deep learning features, Ho et al. (2019) obtained an AUC of 0.77, sensitivity and specificity of 0.79.

What is interesting about the above machine learning results is that 34 predictive features across three images types (FLAIR, ADC, DWI, b-value of 1000) (Lee et al., 2020) and 486 predictive features across four image types (DWI, ADC, FLAIR, PWI) (Ho et al., 2019) were required to achieve similar predictive ability to the one reported for the $T_2$ relaxation time alone in Chapter 7 (AUC of 0.77, sensitivity of 0.75, specificity of 0.75). Thus, as discussed in Chapter 7, ADC and $T_2$ alone are robust enough to estimate stroke onset time in a clinically applicable manner, without the support of additional predictive MRI variables. However, it is also worth considering that, given the poor performance of weighted images demonstrated in Chapters 5 and 6, if Lee et al. (2020) and Ho et al. (2019) 's models including descriptive, morphological and deep features, can achieve such high levels of predictive ability using weighted images, perhaps similar models using $T_2$ maps, will improve the ability of the $T_2$ relaxation time as a stroke timer.

The studies in this thesis were designed in accordance with thrombolysis guidelines for hyperacute ischaemic stroke patients with unknown onset time, where chronological time was (and still is) the main barrier to treating patients with unknown onset time with rtPA (Biggs et al., 2019; Powers et al., 2018). However, between the start and end of this PhD research project (2015 – 2019), there has been a move toward exploration of patient-specific, instead of guideline-based, stroke treatment. For example, in 2018, the European Union's Horizon 2020 funded a four-year project, *Precise 4Q* (precise4q.eu), which is focused on developing predictive machine learning methods that would enable individualised stroke treatment, including using MRI parameters for treatment stratification of hyperacute stroke patients.

Many authors (e.g., Etherton et al., 2018; Wang & Wang, 2019) are encouraging the use of imaging as a *tissue clock* (outlined in Chapter 1) for patient-specific treatment decisions due to the accumulating evidence that some patients benefit from reperfusion-based therapies after 4.5 hours (reviewed by Etherton et al., 2018; Wang and Wang, 2019). For example, the DAWN trial showed patients with large vessel occlusion, a *clinical-core mismatch* (significant clinical deficit, small infarct volume identified via perfusion CT or DWI), and onset time between six and 24 hours, benefited from mechanical thrombectomy (Nogueira et al., 2018). The EXTEND trial (Ma et al., 2019) also showed patients with ischaemic stroke and salvageable brain tissue (identified via perfusion CT or MRI) that awoke with symptoms or whose time of symptom onset was between four and a half hours to nine hours, and received rtPA, were more likely to have no or minor neurological deficits than patients given a placebo. Thus, for some patients, penumbral tissue may exist longer than 4.5 hours after symptom onset.

In the future, treatment guidelines for reperfusion therapies may shift from the chronological time-based to the patient-specific tissue-based approach (Etherton et al., 2019; Wang and Wang, 2019). Rather than relying on a uniform time window, clinicians would tailor treatment decisions according to the status of the individual

patient's brain (Demeestere et al., 2020). In this situation, ADC and $T_2$ relaxation time MRI will remain highly relevant in clinics and will be extremely useful for stratification of acute ischaemic stroke patients to treatment. This is because, as suggested by Rogers, McGarry et al. (2014) and McGarry et al. (2016a), and discussed in Chapter 5, the combination of ADC and $T_2$ also provides an opportunity to identify potentially salvageable tissue. Reduced ADC indicates cytotoxic oedema, and therefore potentially viable tissue, and elevated $T_2$ in regions of reduced ADC represents tissue destined for infarction (Gröhn et al., 2000). Regardless of onset time if the low ADC region is more extensive than elevated $T_2$, reperfusion therapy may reduce stroke lesion size (McGarry et al., 2016a; Rogers, McGarry et al., 2014).

Inspired by the studies by Rogers, McGarry et al., (2014) and McGarry et al. (2016a) that produced images showing the spatial distributions of changes in relaxation times caused by ischaemia (e.g., Figure 5.1 in Chapter 5), the *spherical reference approach* (which was being developed during the period of this thesis), prepares images of the change in $T_2$ relaxation time due to ischaemia in images from patients as well as providing a user-independent approach for estimating onset time (Knight, Damion, McGarry et al., 2019. Although the spherical reference approach needs validating, it would enable the benefits of ADC and the $T_2$ relaxation time for reducing the problem of unknown onset that were identified in this thesis to be studied in the context of the tissue clock approach to treatment stratification of acute ischaemic stroke patients.

## 9.5 Limitations

The main limitations of the studies in Chapters 7 and 8 are the small patient sample sizes. The sample size for the preclinical study in Chapter 5 may sound small. However, the rats were genetically homogenous, and of the same sex and the experimental conditions, including the severity of ischaemia, was strictly controlled.

These factors could not be controlled in the patients. The patient studies were conducted on MRI data from three UK hospitals, between the years 2014 and 2018 and so data analysis was limited to the reality of what could feasibly be collected in hospitals where emergency MRI of hyperacute stroke patients was not necessarily a routine practice. Therefore, the studies were not designed to be powered to test a specific hypothesis; instead, the purpose was to explore which qMRI parameter(/s) should be examined in a larger-scale clinical study.

The small patient sample also highlights a problem that is specific to imaging of hyperacute stroke patients in the UK. It took four years to scan 68 stroke patients by MRI, 38 of these with low ADC verified acute ischaemia. The majority of scans were acquired from the Queen Elizabeth Hospital in Glasgow, which is actively engaged in clinical research of stroke patients and is equipped with a research-dedicated MRI system. Except for six scans from Oxford, which is also a clinical stroke facility, the rest of the scans were acquired at Southmead Hospital in Bristol, where emergency MRI is not routine, and the MRI scanner was located two floors above the accident and emergency department. Patients were only scanned if the MRI radiographers could fit the patient into the overbooked MRI schedule, and if the correct staff were available (i.e., clinicians and research nurses involved in the study and the porters to transport the patients to the MRI scanner).

Unfortunately, the situation at Southmead Hospital is typical of most NHS hospitals, and although clinicians are most likely aware of the benefits of MRI for treatment stratification of acute stroke patients, they have to work with what is available. Therefore, it is recognised that although the thesis results are promising for improving the stratification of acute ischaemic stroke patients to treatment, MRI cannot solve the problem of unknown onset time alone. Other methods for when MRI is not available are needed. For example, recent studies indicate that it may now be possible to estimate stroke onset time using NCCT (in a similar way to the reference-dependent qMRI approaches) (Mair et al., 2017; Minnerup et al., 2016). Studies quantifying the change in CT signal (Hounsfield units = HU) caused

by ischaemia (Mair et al., 2017) and using the HUs to approximate the percentage water uptake (Minnerup et al., 2016), identified patients within 4.5 hours of symptom onset with high sensitivity and specificity. However, the insensitivity of NCCT to early ischaemia poses a substantial challenge for this approach, as the location of ischaemic tissue cannot be identified as easily as with ADC or DWI (Chalela et al., 2007; Fiebach et al., 2002).

One of the main consequences of a low number of stroke patients scanned is that it is difficult to draw reliable and generalisable clinical conclusions (Varoquaux, 2018). The studies in this thesis used predictive models to assess the ability of qMRI parameters to estimate stroke onset time. However, in order to draw reliable conclusions, a much larger sample size is required so that the data can be split into a training set to develop the models, and a test dataset to validate their performance (Lee et al., 2020; Varoquax, 2018). With no test data set available, leave one out cross-validation (LOOCV) was used in Chapter 8 to approximate how well the regression models would perform on new data. Although LOOCV is better than no validation, when applied to small data sets, cross-validation methods can strongly underestimate estimates of prediction accuracy (Varoquax, 2018). Varoquax (2018) estimated that in order to be 90% confident in the measures of prediction accuracies from cross-validation techniques in neuroimaging studies (e.g., average RMSE of ± minutes across folds in Chapter 8), at least 1000 samples would be needed. Therefore, with a sample size of 23 patients in Chapter 8, the estimated predictive accuracies reported should not be taken as definitive and only as an indication of which probability distribution best describes the $T_2$ distribution and how well these distributional characteristics could potentially perform when estimating onset time. This point is especially important to consider for Chapters 5 and 7 as validation methods were not used, and so the reported performance of the qMRI parameters will be biased toward the data set that the results are based on (James et al., 2013; Kelleher & Tierney, 2018).

As highlighted in the discussions of Chapters 7 and 8, a further consequence of the small sample size was that it was not possible to account for all of the potential sources of variability, which may affect qMRI measurements and therefore estimates of onset time. For example, strokes that occurred in different vascular territories (PACS, LACS, TACS, LOCS) were grouped in the analysis. However, focal cerebral ischaemia is a highly variable disease state, and the pathophysiological effects, and the rate at which infarction spreads, will differ according to the vascular territory involved, due to differences in local blood supply and metabolism (Macrae et al., 1992; Wang & Wang, 2019). As qMRI parameters are sensitive to these pathophysiological changes, the differing rates could, in turn, influence the rate and extent of changes in MRI signals. Lumping MRI data from all vascular territories into the same analysis may, therefore, have confounded estimates of stroke onset time. Additionally, as suggested in Chapter 8, the $T_2$ distributions within ischaemic regions may also differ according to the vascular territory involved. The inclusion of lacunar infarcts (LACS 34% in Chapter 7, and 30% in Chapter 8), which are small infarcts in deep cerebral WM, basal ganglia, or the pons, could have been a particular source of error, as compared to cortical ischaemic strokes, lacunar strokes are thought to have different pathophysiological causes and consequences (Wardlaw, 2005). Basal ganglia regions also have higher iron concentrations, and so $T_2$ relaxation times are inherently shorter than other regions (Schenker et al., 1993).

An inherent limitation of stroke timing studies is that they are reliant on knowing the exact time of ischaemia onset. In rats, the exact time of ischaemia onset is precise, whereas, in patients, the time of the first symptoms is used to approximate the time of ischaemia onset. However, the CBF thresholds for loss of function and ischaemia are known to be different (Hossmann, 1989, 1994). Indeed, there could be a delay in the onset of symptoms after the ischaemic event, which may be common for lacunar strokes (Nakamura et al., 1999). Additionally, if multiple emboli and arterial branches were involved, there could have been multiple ischaemic events, for which the onset times would be different. Therefore, the time

of symptom onset recorded for the patients in this study may not be representative of the time of the first ischaemic event, which could have introduced some variability into the data and explain why some patients were misclassified.

Another limitation of the clinical studies in this thesis was the use of two different multi-echo pulse sequences for the computation of $T_2$ maps and $T_2$w images (GRASE in Bristol, TSE in Oxford and Glasgow). The advantage of the parametric approach to qMRI is that the measured values are repeatable and reproducible across sites, but that is providing the same pulse-sequence is used (Deoni et al., 2008). For quantifying image intensity ratios combining data from GRASE and TSE sequences was not considered a problem because ratios are comparable. However as discussed in Chapter 8, given the contribution of $T_2^*$ to the spin-echo from the GRASE sequence, combining data could have introduced variability into the $T_2$ distribution data, making it difficult to draw any concrete conclusions.

The use of two versions of multi-echo $T_2$ pulse sequences in the clinical studies was not intended in the initial design of the study and was a result of combining data from a clinical MRI scanner with data from a research specific MRI scanner. The clinical study was designed to be conducted in Bristol only, and the only multi-echo $T_2$ sequence in the clinical package of the Bristol's Philips MRI scanner was the GRASE sequence. For the purposes of estimating onset time, the use of GRASE and the small contribution of $T_2^*$ to the spin-echo was seen as insignificant. However, due to difficulties with recruiting enough patients within the Dunhill Medical Trust funding time window (2014 – 2018), Oxford and Glasgow were included as additional sites into the study These sites had Siemens research scanners that did not have a GRASE equivalent, and so TSE was used. In future studies, it would not be difficult to ensure the same multi-echo sequence is used in scanners from different vendors. All MRI scanners can perform multi-echo TSE, and so it would be a matter of ensuring that the correct package is available at all sites before beginning the study.

## 9.6 Recommendations for further work

Although this thesis demonstrated that $T_2$ MRI relaxation times are more accurate than image intensity ratios for onset time estimation, the accuracies reported are still not high enough to confidently base treatment decisions on, as accuracy was 77% in Chapter 7, and the smallest margins of error were ± 90 minutes in Chapter 8. The following suggestions for future studies may help to improve the accuracy of $T_2$ as a proxy for onset time. These suggestions are based on the questions that emerged from the research Chapters, the discussed limitations, and inspiration from research in other areas of clinical imaging.

### Studies focused on improving the detection of elevated $T_2$ caused by ischaemia

The potential utility and success of the $T_2$ relaxation time in aiding treatment decisions of hyperacute ischaemic stroke patients and patients with other conditions is reliant on the ability to accurately measure $T_2$ in the first place. Throughout this thesis, it has been argued that the benefit of quantifying $T_2$ relaxation times, is that, unlike image intensities from weighted images, measuring relaxation times facilitates unbiased comparison between scans from the same and different patients in different sessions and scanners (Deoni et al., 2008; 2010; Tofts, 2005). Additionally, the extent of the change in $T_2$ values caused by ischaemia is unlikely to be influenced by the pulse-sequences used (Damion, Knight, McGarry et al., 2019; Knight, Damion, McGarry et al., 2019). However, as highlighted in Chapter 8, the absolute $T_2$ values will vary because of significant $T_2$ anisotropy imposed by tissue microstructure (Knight et al., 2015; Knight, McCann, Tsivos, Dillon, et al., 2016) as well as the use of different pulse sequences (e.g. $T_2$ was shorter with GRASE than with TSE). These sources of variation are a potential cause for concern, as could result in errors when measuring $T_2$, which could potentially confound estimates of onset time and the extent of high $T_2$ within the ischaemic region. When quantifying $T_2$ for clinical use, one needs to be confident that the observed changes in $T_2$ are due to ischaemia and do not have biological and/or

MRI technical basis. Thankfully, low ADC is a guidance for the presence of acute ischaemia.

A *test-retest* study where a patient or a healthy elderly participant, is scanned multiple times with the same protocol with the same scanner, would enable the minimum and maximum variation in $T_2$ between scans to be estimated (i.e., by calculating the coefficient of variation). Knowing the repeatability limits of $T_2$ relaxation times within healthy tissue and ischaemic tissue would enable one to determine the extent to which the measured $T_2$ values can be classified as 'normal' or 'elevated' (Jansen et al., 2007). This estimate could then be included in predictive models for onset time estimation and accounted for when quantifying the extent of $T_2$ change due to ischaemia. Similar methods have been adopted in clinical imaging research using relaxation times for identifying cartilage degeneration (e.g., Hannila et al., 2015; Williams et al., 2011) and breast cancer (e.g., Aliu et al., 2014).

Another avenue for improving the measurement of the $T_2$ relaxation time and thus improving the ability to detect $T_2$ change due to ischaemia would be to invest in methods that increase the signal to noise ratio (SNR). For instance, by engineering improved hardware and pulse sequences and performing studies using ultra-high-field MRI. Achieving a higher SNR enables imaging with smaller voxel sizes, and increased spatial resolution, which in turn results in increased sensitivity to changes in the signal caused by pathology (Filippi et al., 2014; Schindler et al., 2017). For example, studies at 7T and 8T detected more incidences of WM ischaemia than 1.5T and 3T (Kangarlu et al., 2007; Mistry et al., 2011). Another example is in this thesis, as the overall accuracy of qMRI parameters was higher in the preclinical study in Chapter 5, compared to the patient study in Chapter 7. Aside from the more controlled conditions, the use of ultra-high-field scanners in the preclinical study (4.7T and 9.4T) compared to the clinical studies (3T) would likely have contributed to this higher accuracy. Therefore, studying $T_2$ at ultra-high field could enable better detection of $T_2$ changes caused by ischaemia and a clearer picture of

the $T_2$ heterogeneity within the ischaemic region, which could ultimately enable more accurate estimates of onset time.

### A study specifically investigating the $T_2$ characteristics in white matter

The clinical work in this thesis had the advantage of being informed by preclinical studies. It was clear from studies and Chapter 5 (McGarry et al., 2016b) and previous preclinical work (e.g., Jokivarsi et al., 2010; Rogers, McGarry et al., 2014) that the $T_2$ relaxation time increases during ischaemia and so is also likely to be suitable for stroke timing in patients. Also, that the $T_2$ distribution in ischaemic GM may be informative of onset time (Norton et al., 2017). These observations were supported in the clinical studies in Chapter 7 (McGarry et al., 2020) and Chapter 8. For the studies in this thesis, especially Chapter 8, there was not this advantage of supporting preclinical research on the $T_2$ in WM specifically. This is because, as discussed in Chapter 6 and Chapter 8, WM ischaemia is difficult to induce in rats when there is so little WM available in the brain. WM also has different ischaemic pathology to GM, and as a tissue type, is structurally more complex. The $T_2$ relaxation times have only been studied specifically in WM in acute ischaemic stroke patients by Damion, Knight, McGarry et al. (2019) who showed a relationship of the $T_2$ relaxation time within WM specifically. There was no prior work indicating what to expect about the distribution of $T_2$ relaxation times  The sample size for ischaemic WM in Chapter 8 was too small (n = 21) and too variable (i.e., WM ischaemic regions in multiple vascular territories and of different sizes) to draw a definitive conclusion regarding the lack of relationship between $T_2$ distributional parameters and time from symptom onset that was observed. Thus, there is a need for further studies investigating the distributional parameters of WM specifically.

Given that this thesis demonstrated that preclinical MRI of ischaemia is translatable to the clinical MRI of ischaemia, it would also be advantageous if

preclinical work specifically into WM ischaemia was possible. However, as rodents are poor models for WM ischaemic pathology, higher species that have a similar composition of GM and WM to humans would be needed (Kauppinen, 2014). For example, others have successfully studied WM ischaemia in cats (e.g., Matsumiya et al., 1990), baboons (e.g., Bell et al., 1985) and dogs (e.g., Xu et al., 2014). However, there are several factors that suggest a preclinical study of higher species is not the optimal way forward. For example, in labs that study rodents, it is fairly easy and inexpensive to care and look after a large number of animals (Sommer, 2007). However, this is not the case for higher-level species (Sommer, 2007). Therefore, unless there is a large research budget, there would not be much improvement on the small sample sizes in clinical studies such as Chapter 8. Additionally, because of the cognitive and emotional similarities to humans, there are also the important ethical contentions surrounding studying higher-level species to consider (Cook & Tymianski, 2012). The brains of higher-level species are also structurally and physiologically more complex than rodent brains, and so the variabilities that could be avoided by studying rodents (e.g., location, size, severity of ischaemia), are not necessarily avoidable when studying higher species, and the different methods for inducing ischaemia have their own complications (reviewed by Cook & Tymiansk, 2012).

Another way to gain insight into the $T_2$ distribution in WM is to study subcortical lacunar strokes (LACs) in patients. This is because, LACs only affect WM, specifically deep cerebral white matter, the basal ganglia, or pons, and are caused by the occlusion of a single small perforating artery supplying subcortical brain regions (Bamford, 1991; Wardlaw, 2005). LACs are caused by the occlusion of a single small perforating artery supplying subcortical brain regions (Bamford, 1991; Wardlaw, 2005). Thus, studying LACs in patients, would have the benefits of studying ischaemia in GM of rats, as one artery is occluded (i.e., the MCA in rats and a small perforating artery in patients) and due to the location that is affected, there is little blood supply from surrounding regions, thus controlling for the variability in the MRI data that could be induced by collateral blood supply (i.e.,

Wouters et al., 2016). LACs constitute one fifth of all strokes (Sudlow & Warlow, 1997) and so it would be possible to obtain a large enough sample size (i.e., 39 patients based on the power analysis in Chapter 7). Thus, studying patients with LACS would enable the distribution of $T_2$ in WM to be studied in isolation and in a context that has some of the benefits of a preclinical study (i.e., control over sample size, affected region, collateral blood supply) but avoids the complications associated with conducting preclinical studies in higher-level species (Cook & Tymiansk, 2012).

### A more extensive, hypothesis-driven study

The next step for investigating the ability of $T_2$ for reducing the problem of unknown onset is to design and conduct a larger, more extensive study that is powered to directly test whether the $T_2$ relaxation time is the more accurate and reliable method for estimating stroke onset time. Also, to address the questions that could not be addressed in this thesis, such as whether different vascular territories have different $T_2$ distribution characteristics and whether thrombolysis influences onset time estimation. A more extensive study would also enable predictive models to be developed and tested on separate data sets to provide a more reliable indication of their ability to estimate stroke onset time.

If funding, feasibility, and practicalities were not obstacles, a more extensive study could involve:

- Acquiring enough data to be able to study $T_2$ image intensity ratios and the distributions of $T_2$ relaxation times in the ischaemic regions of different vascular territories separately. The power analysis conducted in Chapter 7 suggested that at least 37 patients would be needed to have 90% confidence in identifying a relationship with time from symptom onset. Therefore at least 37 patients of each stroke subtype would be required. Validation test-tests of a similar size per territory would also be acquired. As discussed earlier in this Chapter,

studying lacunar strokes in isolation would enable further insight into the $T_2$ distribution of ischaemic WM.

- Acquiring enough data to be able to compare sensitivity and specificity of the $T_2$ relaxation time with the DWI/FLAIR mismatch and FLAIR image intensities, as due to the imbalanced dataset in Chapter 7, a comparison of specificity was not possible. According to the power calculations in Chapter 7, this would require data from at least 67 patients to be able to confidently identify a relationship of the FLAIR image intensity ratio with time from symptom onset. Again, a validation test set of a similar size would also be required.

- The addition of a perfusion-weighted imaging (PWI) sequence to approximate the collateral status. Collateral status was previously shown to modify the relationship of the FLAIR image intensity ratio with time from symptom onset, where the relationship of FLAIR was less dependent on time from symptom onset in patients with good collateral flow than patients with poor collateral flow (Wouters et al., 2016). It would, therefore, be important to determine whether the same is true for the $T_2$ relaxation time when assessing the ability of $T_2$ to estimate stroke onset time.

- The addition of sodium magnetic resonance spectroscopy (MRS) to the imaging protocol. Extensive clinical and preclinical studies suggest that MRS is more informative of tissue viability in acute ischaemic stroke than MRI (see Fagan, 2012 for a review) because compared to hydrogen (studied in MRI) sodium is more immediately related to the ischaemic cascade due to the collapse of the ionic gradients. Regions with increased sodium are thought to reflect the irreversibly damaged core, whilst regions with normal or decreased sodium levels indicate hypoperfused potentially viable tissue (Fagan, 2012). MRS data could, therefore, be compared to regions of decreased ADC and elevated $T_2$ to

determine whether ADC and $T_2$ could be informative of tissue status and thus be used to assist with the patient-specific *tissue clock* approach to the problem of unknown onset time. As has been argued throughout this thesis, parameterising MR signals is the key to obtaining more reliable information about pathophysiology in ischaemic stroke research. As MRS is parametric, MRS may overcome the difficulties that have been encountered when trying to approximate tissue viability with perfusion-weighted images mentioned in Chapter 1 (Dani et al., 2011; Demeestere et al., 2020; González et al., 2013). MRS may therefore be a more reliable indicator of the viability of tissue with regions of low ADC and high $T_2$ than PWI.

Adding MRS is the most ambitious aspect of this suggestion for future research as it would involve an MR research scanner with two tubes (one hydrogen and one sodium), broad transmit-receive coils, specialised radiofrequency coils and a specifically optimised pulse sequence (Fagan, 2012) that are not currently available in hospital scanners. However, MRF including spectroscopy, involving the simultaneous acquisition of sodium density images, PD weighted, $T_1$ relaxation time maps and $T_2$ relaxation time maps, has recently been achieved (Yu et al., 2020), suggesting this proposed study may be possible in future.

### Machine learning

At the International Society for Magnetic Resonance Imaging in Medicine (ISMRM) conference in May 2019 (Montreal, Canada), it was apparent that MRI research is moving toward use of artificial intelligence (AI) enabled precision medicine. AI-based MRI medical research involves using supervised and unsupervised machine learning methods to develop predictive models that could aid clinicians in their diagnoses and treatment decisions. The potential benefits of machine learning in medical imaging was recently demonstrated in breast cancer research (Yala et al., 2019). Predictive models which included latent texture and density information of mammograms (identified using deep learning algorithms)

resulted in significantly higher accuracy for risk discrimination than genomic and clinical information alone (Yala et al., 2019). If such improvement can be achieved by applying deep learning to simple mammographic images, then it is likely that applying deep learning to multiparametric MRI data could be extremely beneficial when developing predictive models for many disease states, given that it already provides so much more information about different pathologies (Kuhl, 2019). Indeed, deep learning was shown to be beneficial in stroke timing research, as by including latent features extracted from PWI, the accuracy of identifying patients with 4.5 hours improved by 10% (Ho et al., 2019).

Machine learning approaches, especially those involving deep learning, require extensive data sets (Lundervold & Lundervold, 2019) and so, if, or when the $T_2$ relaxation time is more routinely acquired, and enough $T_2$ data from hyperacute ischaemic stroke patients is available, deep learning methods could be investigated for $T_2$ based stroke timing. Deep learning algorithms may also offer further insights into the heterogeneity of $T_2$ within the ischaemic region. In the future, if appropriately applied and understood, advanced machine learning techniques could help further unlock the currently untapped potential of quantitative relaxometric MRI for improving the stratification of hyperacute ischaemic stroke patients to treatment.

# References

Aguiar de Sousa, D., von Martial, R., Abilleira, S., Gattringer, T., Kobayashi, A., Gallofré, M., Fazekas, F., Szikora, I., Feigin, V., Caso, V., & Fischer, U. (2019). Access to and delivery of acute ischaemic stroke treatments: A survey of national scientific societies and stroke experts in 44 European countries. *European Stroke Journal*, *4*(1), 13–28.

Akaike, H. (1974). A new look at the statistical model identification. *IEEE Transactions on Automatic Control*, *19*(6), 716–723.

Aliu, S. O., Jones, E. F., Azziz, A., Kornak, J., Wilmes, L. J., Newitt, D. C., Suzuki, S. A., Klifa, C., Gibbs, J., Proctor, E. C., Joe, B. N., & Hylton, N. M. (2014). Repeatability of quantitative MRI measurements in normal breast tissue. *Translational Oncology*, *7*(1), 130–137.

Allen, L. M., Hasso, A. N., Handwerker, J., & Farid, H. (2012). Sequence-specific MR imaging findings that are useful in dating ischaemic stroke. *RadioGraphics*, *32*(5), 1285–1297.

Anderson, T. R., Jarvis, C. R., Biedermann, A. J., Molnar, C., & Andrew, R. D. (2005). Blocking the anoxic depolarization protects without functional compromise following simulated stroke in cortical brain slices. *Journal of Neurophysiology*, *93*(2), 963–979.

Aoki, J., Kimura, K., Shibazaki, K., & Sakamoto, Y. (2013). Negative Fluid-Attenuated Inversion Recovery- Based Intravenous Thrombolysis Using Recombinant Tissue Plasminogen Activator in Acute Stroke Patients with Unknown Onset Time. *Cerebrovascular Diseases Extra*, *3*(1), 35–45.

Astrup, J., Siesjö, B. K., & Symon, L. (1981). Thresholds in cerebral ischemia—the ischaemic penumbra. *Stroke*, *12*(6), 723–725.

Astrup, J., Symon, L., Branston, N. M., & Lassen, N. A. (1977). Cortical evoked potential and extracellular K+ and H+ at critical levels of brain ischemia. *Stroke; a Journal of Cerebral Circulation*, *8*(1), 51–57.

Baird, A. E., & Warach, S. (1998). Magnetic resonance imaging of acute stroke. *Journal of Cerebral Blood Flow & Metabolism*, *18*(6), 583–609.

Bamber, D. (1975). The area above the ordinal dominance graph and the area below the receiver operating characteristic graph. *Journal of Mathematical Psychology*, *12*(4), 387–415.

Bamford, J., Sandercock, P., Dennis, M., Warlow, C., & Burn, J. (1991). Classification and natural history of clinically identifiable subtypes of cerebral infarction. *The Lancet*, *337*(8756), 1521–1526.

Barbier, E. L., Liu, L., Grillon, E., Payen, J.F., Lebas, J.F., Segebarth, C., & Rémy, C. (2005). Focal brain ischemia in rat: Acute changes in brain tissue $T_1$ reflect acute increase in brain tissue water content. *NMR in Biomedicine*, *18*(8), 499–506.

Baron, J. C. (2001). Mapping the ischaemic penumbra with PET: A new approach. *Brain*, *124*(1), 2–4.

Bekkar, M., & Djemaa, D. H. K. (2013). Evaluation measures for models assessment over imbalanced data sets. *Journal of Information Engineering and Applications,* 3(10), 27-38.

Bell, B. A., Symon, L., & Branston, N. M. (1985). CBF and time thresholds for the formation of ischemic cerebral edema, and effect of reperfusion in baboons. *Journal of Neurosurgery*, *62*(1), 31–41.

Berkhemer, O. A., Fransen, P. S. S., Beumer, D., van den Berg, L. A., Lingsma, H. F., Yoo, A. J., Schonewille, W. J., Vos, J. A., Nederkoorn, P. J., Wermer, M. J. H., van Walderveen, M. A. A., Staals, J., Hofmeijer, J., van Oostayen, J. A., Lycklama à Nijeholt, G. J., Boiten, J., Brouwer, P. A., Emmer, B. J., de Bruijn, S. F., ... Dippel, D. W. J. (2015). A randomized trial of intraarterial treatment for acute ischaemic stroke. *New England Journal of Medicine*, *372*(1), 11–20.

Berner, L.P., Cho, T. H., Haesebaert, J., Bouvier, J., Wiart, M., Hjort, N., Klærke, M. I., Derex, L., Thomalla, G., Pedraza, S., Østergaard, L., Baron, J. C., Nighoghossian, N., & Berthezène, Y. (2016). MRI assessment of ischaemic lesion evolution within white and gray matter. *Cerebrovascular Diseases*, *41*(5–6), 291–297.

Berrar, D., & Flach, P. (2012). Caveats and pitfalls of ROC analysis in clinical microarray research (and how to avoid them). *Briefings in Bioinformatics*, *13*(1), 83–97.

Bertoglio, D., Verhaeghe, J., Dedeurwaerdere, S., & Gröhn, O. (2017). Neuroimaging in animal models of epilepsy. *Neuroscience*, *358*, 277–299.

Biggs, D., Silverman, M. E., Chen, F., Walsh, B., & Wynne, P. (2019). How should we treat patients who wake up with a stroke? A review of recent advances in management of acute ischaemic stroke. *The American Journal of Emergency Medicine*, *37*(5), 954–959.

Birenbaum, D., Bancroft, L. W., & Felsberg, G. J. (2011). Imaging in acute stroke. *Western Journal of Emergency Medicine*, *12*(1), 67–76.

Blink, E. (2004). *Basic MRI Physics*. http://www.mri-physics.net/textuk.html

Bloembergen, N., Purcell, E. M., & Pound, R. V. (1948). Relaxation effects in nuclear magnetic resonance absorption. *Physical Review*, *73*(7), 679–712.

Boulby, P. A. & Rugg-Gunn, F. (2003). $T_2$: the transverse relaxation time. In Tofts, P.S. (2005 Eds*), Quantitative MRI of the brain: measuring changes caused by disease (pp. 143- 201).* John Wiley & Sons.

Bristow, M. S., Simon, J. E., Brown, R. A., Eliasziw, M., Hill, M. D., Coutts, S. B., Frayne, R., Demchuk, A. M., & Mitchell, J. R. (2005). MR perfusion and diffusion in acute ischaemic stroke: Human gray and white matter have different thresholds for infarction. *Journal of Cerebral Blood Flow & Metabolism*, *25*(10), 1280–1287.

Broocks, G., Kniep, H., Kemmling, A., Flottmann, F., Nawabi, J., Elsayed, S., Schön, G., Thomalla, G., Fiehler, J., & Hanning, U. (2020). Effect of intravenous alteplase on ischaemic lesion water homeostasis. *European Journal of Neurology*, *27*(2):376-383.

Brown, M. A., & Semelka, R. C. (2011). *MRI: Basic Principles and Applications*. John Wiley & Sons.

Bunney, G. & Ireland, A. (2019). *Rise and shine: a review of the WAKE-UP trial. A peer reviewed web publication, NUEM Blog, expert commentary by Richards, C.* Retrieved from http://www.nuemblog.com/blog/wake-up-trial.

Burdette, J. H., Elster, A. D., & Ricci, P. E. (1999). Acute cerebral infarction: quantification of spin-density and $T_2$ shine-through phenomena on diffusion-weighted MR images. *Radiology*, *212*(2), 333–339.

Burgess, R. E., & Kidwell, C. S. (2011). Use of MRI in the assessment of patients with stroke. *Current Neurology and Neuroscience Reports*, *11*(1), 28–34.

Burke, J. F., Kerber, K. A., Iwashyna, T. J., & Morgenstern, L. B. (2012). Wide variation and rising utilization of stroke magnetic resonance imaging: Data from 11 states. *Annals of Neurology*, *71*(2), 179–185.

Busza, A. L., Allen, K. L., King, M. D., Bruggen, N. van, Williams, S. R., & Gadian, D. G. (1992). Diffusion-weighted imaging studies of cerebral ischemia in gerbils: Potential relevance to energy failure. *Stroke*, *23*(11), 1602–1612.

Calamante, F., Lythgoe, M. F., Pell, G. S., Thomas, D. L., King, M. D., Busza, A. L., Sotak, C. H., Williams, S. R., Ordidge, R. J., & Gadian, D. G. (1999). Early changes in water diffusion, perfusion, $T_1$, and $T_2$ during focal cerebral ischemia in the rat studied at 8.5 T. *Magnetic Resonance in Medicine*, *41*(3), 479–485.

Carneiro, A. A. O., Vilela, G. R., Araujo, D. B. de, & Baffa, O. (2006). MRI relaxometry: methods and applications. *Brazilian Journal of Physics*, *36*(1A), 9–15.

Caruthers, S. D., Jara, H., & Melhem, E. R. (1998). MR imaging: Some applications of GRASE. *Medica Mundi, 42*(3), 6.

Chalela, J. A., Kidwell, C. S., Nentwich, L. M., Luby, M., Butman, J. A., Demchuk, A. M., Hill, M. D., Patronas, N., Latour, L., & Warach, S. (2007). Magnetic resonance imaging and computed tomography in emergency assessment of patients with suspected acute stroke: A prospective comparison. *The Lancet*, *369*(9558), 293–298.

Chen, M. M., Chen, P. M., Hailey, L., Mortin, M., Rapp, K., Agrawal, K., Huisa, B., Modir, R., Meyer, D. M., Hemmen, T., & Meyer, B. C. (2019). Mapping a reliable stroke onset time course using signal intensity on DWI scans. *Journal of Neuroimaging*, *29*(4),476-480.

Cheng, B., Brinkmann, M., Forkert, N. D., Treszl, A., Ebinger, M., Köhrmann, M., Wu, O., Kang, D.-W., Liebeskind, D. S., Tourdias, T., Singer, O. C., Christensen, S., Luby, M., Warach, S., Fiehler, J., Fiebach, J. B., Gerloff, C., & Thomalla, G. (2013). Quantitative measurements of relative fluid-attenuated inversion recovery (FLAIR) signal intensities in acute stroke for the prediction of time from symptom onset. *Journal of Cerebral Blood Flow & Metabolism*, *33*(1), 76–84.

Clarke, D. D., & Sokoloff, L. (1999). Circulation and energy metabolism of the brain. In G.S. Siegel & B. Agranoff (Eds.), *Basic neurochemistry: molecular cellular and medical aspects* ($6^{th}$ ed., pp. 637-69).

Cook, D. J., & Tymianski, M. (2012). Nonhuman Primate Models of Stroke for Translational Neuroprotection Research. *Neurotherapeutics*, *9*(2), 371–379.

Currie, S., Hoggard, N., Craven, I. J., Hadjivassiliou, M., & Wilkinson, I. D. (2013). Understanding MRI: Basic MR physics for physicians. *Postgraduate Medical Journal*, *89*(1050), 209–223.

Damion, R. A., Knight, M. J., McGarry, B. L., Bosnell, R., Jezzard, P., Harston, G. W., Carone, D., Kennedy, J., El-Tawil, S., Elliot, J., Muir, K. W., Clatworthy, P., & Kauppinen, R. A. (2019). Quantifying $T_2$ relaxation time changes within lesions defined by apparent diffusion coefficient in grey and white matter in acute stroke patients. *Physics in Medicine & Biology*, *64*(9), 095016.

Dani, K. A., Thomas, R. G. R., Chappell, F. M., Shuler, K., MacLeod, M. J., Muir, K. W., Wardlaw, J. M., & on behalf of the Translational Medicine Research Collaboration Multicentre acute stroke imaging study. (2011). Computed tomography and magnetic resonance perfusion imaging in ischaemic stroke: Definitions and thresholds. *Annals of Neurology*, *70*(3), 384–401.

Davis, J., & Goadrich, M. (2006). The relationship between Precision-Recall and ROC curves. *Proceedings of the 23rd International Conference on Machine Learning - ICML '06*, 233–240.

Dekker, L., Hund, H., Lemmens, R., Boiten, J., & van den Wijngaard, I. (2017). Unknown onset ischaemic strokes in patients last-seen-well >4.5 h: Differences

between wake-up and daytime-unwitnessed strokes. *Acta Neurologica Belgica*, *117*(3), 637–642.

DeLong, E. R., DeLong, D. M., & Clarke-Pearson, D. L. (1988). Comparing the areas under two or more correlated receiver operating characteristic curves: A nonparametric approach. *Biometrics*, *44*(3), 837–845.

Demeestere, J., Wouters, A., Christensen, S., Lemmens, R., & Lansberg, M. G. (2020). Review of perfusion imaging in acute ischaemic stroke: From time to tissue. *Stroke*, *51*(3):101-1024.

Deoni, S.C.L, Peters, T. M., & Rutt, B. K. (2004). High-resolution $T_1$ and $T_2$ mapping of the brain in a clinically acceptable time with $DESPOT_1$ and $DESPOT_2$. *Magnetic Resonance in Medicine*, *53*(1), 237–241.

Deoni, S.C.L, Rutt, B. K., & Peters, T. M. (2003). Rapid combined $T_1$ and $T_2$ mapping using gradient recalled acquisition in the steady state. *Magnetic Resonance in Medicine*, *49*(3), 515–526.

Deoni, S.C.L. (2010). Quantitative relaxometry of the brain. *Topics in Magnetic Resonance Imaging*, *21*(2), 101–113.

Deoni, S C.L., Williams, S. C. R., Jezzard, P., Suckling, J., Murphy, D. G. M., & Jones, D. K. (2008). Standardized structural magnetic resonance imaging in multicentre studies using quantitative $T_1$ and $T_2$ imaging at 1.5 T. *NeuroImage*, *40*(2), 662–671.

Deoni, S.C.L. (2019, May). *Quantitative MRI: relaxometry sunrise session. Beyond the phenomenological single compartment model.* Marques, J, Kozerke, S. & Hancu, I (Chairs), International Society for Magnetic Resonance in Medicine conference, Montréal, Canada: https://www.ismrm.org/19/program_files/SM08.htm

Dirnagl, U., Iadecola, C., & Moskowitz, M. A. (1999). Pathobiology of ischaemic stroke: An integrated view. *Trends in Neurosciences*, *22*(9), 391–397.

Doyle, K. P., Simon, R. P., & Stenzel-Poore, M. P. (2008). Mechanisms of ischaemic brain damage. *Neuropharmacology*, *55*(3), 310–318.

Duchaussoy, T., Budzik, J.-F., Norberciak, L., Colas, L., Pasquini, M., & Verclytte, S. (2019). Synthetic $T_2$ mapping is correlated with time from stroke onset: A future tool in wake-up stroke management? *European Radiology*, *29*(12):7019-7026.

Durukan, A., & Tatlisumak, T. (2007). Acute ischaemic stroke: Overview of major experimental rodent models, pathophysiology, and therapy of focal cerebral ischemia. *Pharmacology, Biochemistry, and Behavior*, *87*(1), 179–197.

Dzialowski, I., Weber, J., Doerfler, A., Forsting, M., & von Kummer, R. (2004). Brain tissue water uptake after middle cerebral artery occlusion assessed with CT. *Journal of Neuroimaging*, *14*(1), 42–48.

Ebinger, M., Galinovic, I., Rozanski, M., Brunecker, P., Endres, M., & Fiebach, J. B. (2010). Fluid-attenuated inversion recovery evolution within 12 hours from stroke onset: A reliable tissue clock? *Stroke*, *41*(2), 250–255.

Elliott, W. J. (1998). Circadian variation in the timing of stroke onset A meta-analysis. *Stroke*, *29*(5), 992–996.

Elster, A. D. (1988). An index system for comparative parameter weighting in MR imaging. *Journal of Computer Assisted Tomography*, *12*(1), 130–134.

Elster, A. D. (1993). Gradient-echo MR imaging: Techniques and acronyms. *Radiology*, *186*(1):1-8.

Emeriau, S., Serre, I., Toubas, O., Pombourcq, F., Oppenheim, C., & Pierot, L. (2013). Can diffusion-weighted imaging–fluid-attenuated inversion recovery mismatch (Positive diffusion-weighted imaging/negative fluid-attenuated inversion recovery) at 3 Tesla identify patients with stroke at $<$4.5 hours? *Stroke*, *44*(6), 1647–1651.

Emeriau, S., Benaïssa, A., Toubas, O., Pombourcq, F., & Pierot, L. (2016). Can MRI quantification help evaluate stroke age? *Journal of Neuroradiology*, *43*(2), 155–162.

Etherton, M. R., Barreto, A. D., Schwamm, L. H., & Wu, O. (2018). Neuroimaging paradigms to identify patients for reperfusion therapy in stroke of unknown onset. *Frontiers in Neurology*, *9*.327.

Fagan, A. J. (2012). How can sodium MRI techniques help us understand acute stroke? *Imaging in Medicine*, *4*(3), 367–379.

Falcao, A. L. E., Reutens, D. C., Markus, R., Koga, M., Read, S. J., Tochon-Danguy, H., Sachinidis, J., Howells, D. W., & Donnan, G. A. (2004). The resistance to ischemia of white and gray matter after stroke. *Annals of Neurology*, *56*(5), 695–701.

Fiebach, J. B., Schellinger, P. D., Jansen, O., Meyer, M., Wilde, P., Bender, J., Schramm, P., Jüttler, E., Oehler, J., Hartmann, M., Hähnel, S., Knauth, M., Hacke, W., & Sartor, K. (2002). CT and diffusion-weighted MR imaging in randomized order: Diffusion-weighted imaging results in higher accuracy and lower interrater variability in the diagnosis of hyperacute ischaemic stroke. *Stroke; a Journal of Cerebral Circulation*, *33*(9), 2206–2210.

Fiehler, J., Cognard, C., Gallitelli, M., Jansen, O., Kobayashi, A., Mattle, H. P., Muir, K. W., Mazighi, M., Schaller, K., & Schellinger, P. D. (2016). European recommendations on organisation of interventional care in acute stroke (EROICAS). *International Journal of Stroke*, *11*(6), 701–716.

Fiehler, J., Foth, M., Kucinski, T., Knab, R., von Bezold, M., Weiller, C., Zeumer, H., & Röther, J. (2002). Severe ADC decreases do not predict irreversible tissue damage in humans. *Stroke; a Journal of Cerebral Circulation*, *33*(1), 79–86.

Filippi, M., Evangelou, N., Kangarlu, A., Inglese, M., Mainero, C., Horsfield, M. A., & Rocca, M. A. (2014). Ultra-high-field MR imaging in multiple sclerosis. *J Neurol Neurosurg Psychiatry*, *85*(1), 60–66.

Firbank, M. J., Coulthard, A., Harrison, R. M., & Williams, E. D. (1999). A comparison of two methods for measuring the signal to noise ratio on MR images. *Physics in Medicine and Biology*, *44*(12), N261-264.

Fisk, P. R. (1961). The Graduation of Income Distributions. *Econometrica*, *29*(2), 171–185.

Flach, P., & Kull, M. (2015). Precision-Recall-Gain Curves: PR analysis done right. In C. Cortes, N. D. Lawrence, D. D. Lee, M. Sugiyama, & R. Garnett (Eds.), *Advances in Neural Information Processing Systems 28* (pp. 838–846). Curran Associates, Inc.

Galinovic, I., Puig, J., Neeb, L., Guibernau, J., Kemmling, A., Siemonsen, S., Pedraza, S., Cheng, B., Thomalla, G., Fiehler, J., & Fiebach, J. B. (2014). Visual and region of interest–based inter-rater agreement in the assessment of the diffusion-weighted imaging– fluid-attenuated inversion recovery mismatch. *Stroke*, *45*(4), 1170–1172.

Gerriets, T., Stolz, E., Walberer, M., Müller, C., Kluge, A., Bachmann, A., Fisher, M., Kaps, M., & Bachmann, G. (2004). Noninvasive quantification of brain edema and the space-occupying effect in rat stroke models Using magnetic resonance imaging. *Stroke*, *35*(2), 566–571.

Goldberg, M. P., Weiss, J. H., Pham, P. C., & Choi, D. W. (1987). N-methyl-D-aspartate receptors mediate hypoxic neuronal injury in cortical culture. *The Journal of Pharmacology and Experimental Therapeutics*, *243*(2), 784–791.

Goldberg M. P., & Ransom B R. (2003). New light on white matter. *Stroke*, *34*(2), 330–332.

González, R. G., Copen, W. A., Schaefer, P. W., Lev, M. H., Pomerantz, S. R., Rapalino, O., Chen, J. W., Hunter, G. J., Romero, J. M., Buchbinder, B. R., Larvie, M., Hirsch, J. A., & Gupta, R. (2013). The Massachusetts General Hospital acute stroke imaging algorithm: An experience and evidence based approach. *Journal of NeuroInterventional Surgery*, *5*(suppl 1), i7–i12.

Gröhn, O. H. J., Kettunen, M. I., Mäkelä, H. I., Penttonen, M., Pitkänen, A., Lukkarinen, J. A., & Kauppinen, R. A. (2000). Early detection of irreversible cerebral ischemia in the rat using dispersion of the magnetic resonance imaging relaxation time, $T_{1\rho}$. *Journal of Cerebral Blood Flow & Metabolism*, *20*(10), 1457–1466.

Gröhn, O. H. J., Lukkarinen, J. A., Oja, J. M. E., van Zijl, P. C. M., Ulatowski, J. A., Traystman, R. J., & Kauppinen, R. A. (1998). Noninvasive detection of cerebral hypoperfusion and reversible ischemia from reductions in the magnetic resonance imaging relaxation time, $T_2$. *Journal of Cerebral Blood Flow & Metabolism*, *18*(8), 911–920.

Gowland, P. A. & Stevenson, V. L. (2003). $T_1$: the longitudinal relaxation time. In Tofts, P. S. (2005 Eds*), Quantitative MRI of the brain: measuring changes caused by disease (pp. 111- 141).* John Wiley & Sons.

Haase, A. (1990). Snapshot FLASH MRI. Applications to $T_1$, $T_2$, and chemical-shift imaging. *Magnetic Resonance in Medicine*, *13*(1), 77–89.

Hacke, W., Kaste, M., Bluhmki, E., Brozman, M., Dávalos, A., Guidetti, D., Larrue, V., Lees, K. R., Medeghri, Z., Machnig, T., Schneider, D., von Kummer, R., Wahlgren, N., Toni, D., & ECASS investigators. (2008). Thrombolysis with alteplase 3 to 4.5 hours after acute ischaemic stroke. *The New England Journal of Medicine*, *359*(13), 1317–1329.

Hahn, E. L. (1950). Spin echoes. *Physical Review*, *80*(4), 580–594.

Hahn, E. L. (1960). Detection of sea-water Motion by nuclear precession. *Journal of Geophysical Research*, *65*, 776.

Hajnal, J. V., Bryant, D. J., Kasuboski, L., Pattany, P. M., De Coene, B., Lewis, P. D., Pennock, J. M., Oatridge, A., Young, I. R., & Bydder, G. M. (1992). Use of fluid attenuated inversion recovery (FLAIR) pulse sequences in MRI of the brain. *Journal of Computer Assisted Tomography*, *16*(6), 841–844.

Hannila, I., Lammentausta, E., Tervonen, O., & Nieminen, M. T. (2015). The repeatability of $T_2$ relaxation time measurement of human knee articular cartilage. *Magnetic Resonance Materials in Physics, Biology and Medicine*, *28*(6), 547–553.

Hansen, A. J., & Zeuthen, T. (1981). Extracellular ion concentrations during spreading depression and ischemia in the rat brain cortex. *Acta Physiologica Scandinavica*, *113*(4), 437–445.

Helenius, J., Perkiö, J., Soinne, L., Østergaard, L., Carano, R. a. D., Salonen, O., Savolainen, S., Kaste, M., Aronen, H. J., & Tatlisumak, T. (2003). Cerebral hemodynamics in a healthy population measured by dynamic susceptibility contrast MR imaging. *Acta Radiologica (Stockholm, Sweden: 1987)*, *44*(5), 538–546.

Hendrick, J., E. (2005). *Glossary of MR Terms* (5th ed.). American College of Radiology.

Hess, D. C., Wechsler, L. R., Clark, W. M., Savitz, S. I., Ford, G. A., Chiu, D., Yavagal, D. R., Uchino, K., Liebeskind, D. S., Auchus, A. P., Sen, S., Sila, C. A., Vest, J. D., & Mays, R. W. (2017). Safety and efficacy of multipotent adult

progenitor cells in acute ischaemic stroke (MASTERS): A randomised, double-blind, placebo-controlled, phase 2 trial. *The Lancet. Neurology*, *16*(5), 360–368.

Heiss, W. D., & Rosner, G. (1983). Functional recovery of cortical neurons as related to degree and duration of ischemia. *Annals of Neurology*, *14*(3), 294–301.

Ho, K. C., Speier, W., Zhang, H., Scalzo, F., El-Saden, S., & Arnold, C. W. (2019). A machine learning approach for classifying ischaemic stroke onset time from imaging. *IEEE Transactions on Medical Imaging*, *38*(7), 1666–1676.

Hoehn-berlarge, M., Eis, M., Back, T., Kohno, K., & Yamashita, K. (1995). Changes of relaxation times ($T_1$, $T_2$) and apparent diffusion coefficient after permanent middle cerebral artery occlusion in the rat: Temporal evolution, regional extent, and comparison with histology. *Magnetic Resonance in Medicine*, *34*(6), 824–834.

Hossmann, K. A. (1994). Viability thresholds and the penumbra of focal ischemia. *Annals of Neurology*, *36*(4), 557–565.

Hossmann, K. A. (1996). Periinfarct depolarizations. *Cerebrovascular and Brain Metabolism Reviews*, *8*(3), 195–208.

Hossmann, K. A. (1989). The pathophysiology of experimental brain edema. *Neurosurgical Review*, *12*(4), 263–280.

Huang, X., Alakbarzade, V., Khandanpour, N., & Pereira, A. C. (2019). Management of a wake-up stroke. *Practical Neurology*, *19*(4), 326–331.

Iwasawa, E., Ichijo, M., Ishibashi, S., & Yokota, T. (2016). Acute development of collateral circulation and therapeutic prospects in ischaemic stroke. *Neural Regeneration Research*, *11*(3), 368–371.

James, G. Witten, D., Hasite, T., Tibshirani, R. (2013). *An introduction to statistical learning.* Springer.

Jansen, J. F. A., Kooi, M. E., Kessels, A. G. H., Nicolay, K., & Backes, W. H. (2007). Reproducibility of quantitative cerebral $T_2$ relaxometry, diffusion tensor

imaging, and $^{1}$H magnetic resonance spectroscopy at 3.0 Tesla: *Investigative Radiology*, *42*(6), 327–337.

Jenkinson, M., & Smith, S. (2001). A global optimisation method for robust affine registration of brain images. *Medical Image Analysis*, *5*(2), 143–156.

Johnson, C. O., Nguyen, M., Roth, G. A., Nichols, E., Alam, T., Abate, D., Abd-Allah, F., Abdelalim, A., Abraha, H. N., Abu-Rmeileh, N. M., Adebayo, O. M., Adeoye, A. M., Agarwal, G., Agrawal, S., Aichour, A. N., Aichour, I., Aichour, M. T. E., Alahdab, F., Ali, R., Murray, C. J. L. (2019). Global, regional, and national burden of stroke, 1990–2016: A systematic analysis for the global burden of disease study 2016. *The Lancet Neurology*, *18*(5), 439–458.

Jokivarsi, K. T., Hiltunen, Y., Gröhn, H., Tuunanen, P., Gröhn, O. H., & Kauppinen, R. A. (2010). Estimation of the onset time of cerebral ischemia using $T_{1\rho}$ and $T_2$ MRI in rats. *Stroke*, *41*(10), 2335–2340.

Jones, T. H., Morawetz, R. B., Crowell, R. M., Marcoux, F. W., FitzGibbon, S. J., DeGirolami, U., & Ojemann, R. G. (1981). Thresholds of focal cerebral ischemia in awake monkeys. *Journal of Neurosurgery*, *54*(6), 773–782.

Juchem, C., & de Graaf, R. A. (2017). $B_0$ magnetic field homogeneity and shimming for in vivo magnetic resonance spectroscopy. *Analytical Biochemistry*, *529*, 17–29.

Kang, D. W., Kwon, J. Y., Kwon, S. U., & Kim, J. S. (2012). Wake-up or unclear-onset strokes: Are they waking up to the world of thrombolysis therapy? *International Journal of Stroke*, *7*(4), 311–320.

Kangarlu, A., Bourekas, E. C., Ray-Chaudhury, A., & Rammohan, K. W. (2007). Cerebral cortical lesions in multiple sclerosis detected by MR imaging at 8 Tesla. *American Journal of Neuroradiology*, *28*(2), 262–266.

Kato, H., Kogure, K., Ohtomo, H., Tobita, M., Matsui, S., Yamamoto, E., & Kohno, H. (1985). Correlations between proton nuclear magnetic resonance imaging and retrospective histochemical images in experimental cerebral infarction. *Journal of Cerebral Blood Flow & Metabolism*, *5*(2), 267–274.

Kauppinen, R. A. (2014). Multiparametric magnetic resonance imaging of acute experimental brain ischaemia. *Progress in Nuclear Magnetic Resonance Spectroscopy*, *80*, 12–25.

Kelleher, J. D., & Tierney, B. (2018). *Data science.* The MIT Press.

Kettunen, M. I., Gröhn, O. H. J., Silvennoinen, M. J., Penttonen, M., & Kauppinen, R. A. (2002). Effects of intracellular pH, blood, and tissue oxygen tension on $T_{1\rho}$ relaxation in rat brain. *Magnetic Resonance in Medicine*, *48*(3), 470–477.

Kettunen, M. I., Gröhn, O. H. J., Lukkarinen, J. A., Vainio, P., Silvennoinen, M. J., & Kauppinen, R. A. (2000). Interrelations of $T_1$ and diffusion of water in acute cerebral ischemia of the rat. *Magnetic Resonance in Medicine*, *44*(6), 833–839.

Kim, B. J., Kim, Y. H., Kim, Y. J., Ahn, S. H., Lee, D. H., Kwon, S. U., Kim, S. J., Kim, J. S., & Kang, D.-W. (2014). Color-coded fluid-attenuated inversion recovery images improve inter-rater reliability of fluid-attenuated inversion recovery signal changes within acute diffusion-weighted image lesions. Stroke, 45(9), 2801–2804.

Kingsley, P. B., & Monahan, W. G. (2004). Selection of the optimum b factor for diffusion-weighted magnetic resonance imaging assessment of ischaemic stroke. *Magnetic Resonance in Medicine*, *51*(5), 996–1001.

Klatzo, I. (1967). Presidental address. neuropathological aspects of brain edema. *Journal of Neuropathology and Experimental Neurology*, *26*(1), 1–14.

Knight, M. J., Damion, R. A., McGarry, B. L., Bosnell, R., Jokivarsi, K. T., Gröhn, O. H. J., Jezzard, P., Harston, G. W. J., Carone, D., Kennedy, J., El-Tawil, S., Elliot, J., Muir, K. W., Clatworthy, P., & Kauppinen, R. A. (2019). Determining $T_2$ relaxation time and stroke onset relationship in ischaemic stroke within apparent diffusion coefficient-defined lesions. A user-independent method for quantifying the impact of stroke in the human brain. *Biomedical Spectroscopy and Imaging*, *8*(1–2), 11–28.

Knight, M. J., McCann, B., Tsivos, D., Coulthard, E., & Kauppinen, R. A. (2016). Quantitative $T_1$ and $T_2$ MRI signal characteristics in the human brain: Different patterns of MR contrasts in normal ageing. *Magma, 29*(6):833-842.

Knight, M. J., McCann, B., Tsivos, D., Dillon, S., Coulthard, E., & Kauppinen, R. A. (2016). Quantitative $T_2$ mapping of white matter: Applications for ageing and cognitive decline. *Physics in Medicine and Biology*, *61*(15), 5587–5605.

Knight, M. J., McGarry, B. L., Rogers, H. J., Jokivarsi, K. T., Gröhn, O. H., & Kauppinen, R. A. (2016). A spatiotemporal theory for MRI $T_2$ relaxation time and apparent diffusion coefficient in the brain during acute ischaemia: Application and validation in a rat acute stroke model. *Journal of Cerebral Blood Flow & Metabolism*, *36*(7), 1232–1243.

Knight, M. J., Wood, B., Couthard, E., & Kauppinen, R. (2015). Anisotropy of spin-echo $T_2$ relaxation by magnetic resonance imaging in the human brain in vivo. *Biomedical Spectroscopy and Imaging*, *4*(3), 299–310.

Koga, M., Reutens, D. C., Wright, P., Phan, T., Markus, R., Pedreira, B., Fitt, G., Lim, I., & Donnan, G. A. (2005). The existence and evolution of diffusion-perfusion mismatched tissue in white and gray matter after acute stroke. *Stroke*, *36*(10), 2132–2137.

Kuhl, C. (2019, May). *Mansfield lecture: Predict – Then Act! Moving towards tailored prevention.* L., Wald (Chair), International Society for Magnetic Resonance in Medicine conference, Montréal, Canada: https://www.ismrm.org/19/program_files/Plenary_Mansfield.htm

Kumura, E., Graf, R., Dohmen, C., Rosner, G., & Heiss, W. D. (1999). Breakdown of calcium homeostasis in relation to tissue depolarization: Comparison between gray and white matter ischemia. *Journal of Cerebral Blood Flow and Metabolism: Official Journal of the International Society of Cerebral Blood Flow and Metabolism*, *19*(7), 788–793.

Le Bihan, D., Turner, R., Douek, P., & Patronas, N. (1992). Diffusion MR imaging: Clinical applications. *American Journal of Roentgenology*, *159*(3), 591–599.

Lee, H., Lee, E.-J., Ham, S., Lee, H. B., Lee, J. S., Kwon, S. U., Kim, J. S., Kim, N., & Kang, D. W. (2020). Machine learning approach to identify stroke within 4.5 hours. *Stroke*, *51*(3), 860 – 866.

Lees, K. R., Emberson, J., Blackwell, L., Bluhmki, E., Davis, S. M., Donnan, G. A., Grotta, J. C., Kaste, M., von Kummer, R., Lansberg, M. G., Lindley, R. I.,

Lyden, P., Murray, G. D., Sandercock, P. A. G., Toni, D., Toyoda, K., Wardlaw, J. M., Whiteley, W. N., Baigent, C., ... del Zoppo, G. J. (2016). Effects of Alteplase for Acute Stroke on the Distribution of Functional Outcomes: A Pooled Analysis of 9 Trials. *Stroke*, *47*(9), 2373–2379.

Li, L., Binney, L. E., Luengo-Fernandez, R., Silver, L. E., Rothwell, P. M., & Study, O. V. (2019). Temporal trends in the accuracy of hospital diagnostic coding for identifying acute stroke: A population-based study. European Stroke Journal. https://doi.org/10.1177/2396987319881017

Longa, E. Z., Weinstein, P. R., Carlson, S., & Cummins, R. (1989). Reversible middle cerebral artery occlusion without craniectomy in rats. *Stroke; a Journal of Cerebral Circulation*, *20*(1), 84–91.

Lundervold, A. S., & Lundervold, A. (2019). An overview of deep learning in medical imaging focusing on MRI. *Zeitschrift Für Medizinische Physik*, *29*(2), 102–127.

Ma, D., Gulani, V., Seiberlich, N., Liu, K., Sunshine, J. L., Duerk, J. L., & Griswold, M. A. (2013). Magnetic resonance fingerprinting. *Nature*, *495*(7440), 187–192.

Ma, H., Campbell, B. C. V., Parsons, M. W., Churilov, L., Levi, C. R., Hsu, C., Kleinig, T. J., Wijeratne, T., Curtze, S., Dewey, H. M., Miteff, F., Tsai, C.-H., Lee, J.T., Phan, T. G., Mahant, N., Sun, M.-C., Krause, M., Sturm, J., Grimley, R., ... EXTEND Investigators. (2019). Thrombolysis guided by perfusion imaging up to 9 hours after onset of stroke. *The New England Journal of Medicine*, *380*(19), 1795–1803.

Maas, M. B., Lev, M. H., Ay, H., Singhal, A. B., Greer, D. M., Smith, W. S., Harris, G. J., Halpern, E., Kemmling, A., Koroshetz, W. J., & Furie, K. L. (2009). Collateral vessels on CT angiography predict outcome in acute ischaemic stroke. *Stroke*, *40*(9), 3001–3005.

Macrae, M. I. (1992). New models of focal cerebral ischaemia. *British Journal of Clinical Pharmacology*, *34*(4), 302–308.

Madabhushi, A., & Udupa, J. K. (2005). New methods of MR image intensity standardization via generalized scale. *Medical Physics, 33* (9), 3426-3434.

Madai, V. I., Wood, C. N., Galinovic, I., Grittner, U., Piper, S. K., Revankar, G. S., Martin, S. Z., Zaro-Weber, O., Moeller-Hartmann, W., von Samson-Himmelstjerna, F. C., Heiss, W. D., Ebinger, M., Fiebach, J. B., & Sobesky, J. (2016). Clinical-radiological parameters improve the prediction of the thrombolysis time window by both MRI signal intensities and DWI-FLAIR mismatch. *Cerebrovascular Diseases*, *42*(1–2), 57–65.

Mair, G., & Wardlaw, J. M. (2014). Imaging of acute stroke prior to treatment: Current practice and evolving techniques. *The British Journal of Radiology*, *87*(1040), 20140216.

Mair, Grant, Sandercock, P., & Wardlaw, J. (2017, May). *Feasibility of Using Brain Attenuation Changes on CT to Accurately Predict Time of Ischaemic Stroke Onset*. Poster presented at the European Stroke Organisation Conference in Prague, Czech Republic.

Malone, K., Amu, S., Moore, A. C., & Waeber, C. (2019). The immune system and stroke: From current targets to future therapy. *Immunology & Cell Biology*, *97*(1), 5–16.

MathWorks. (2019a). *Generalised extreme value distribution.* Website. https://www.mathworks.com/help/stats/generalized-extreme-value-distribution-1.html

MathWorks. (2019b). *Burr type X11 Distribution.* Website.https://www.mathworks.com/help/stats/burr-type-xii-distribution.html

Mathworks. (2019c). *Loglogistic Distribution.* Website. https://www.mathworks.com/help/stats/loglogistic-distribution.html

Matute C., Domercq M., Pérez-Samartín A., & Ransom B. R. (2013). Protecting white matter from stroke injury. *Stroke*, *44*(4), 1204–1211.

Matsumiya N, Koehler R C, & Traystman R J. (1990). Consistency of cerebral blood flow and evoked potential alterations with reversible focal ischemia in cats. *Stroke*, *21*(6), 908–916.

McFadden, D. (1978). *Modeling the Choice of Residential Location.* Transportation Research Record, (673), 72 – 77.

McGarry, B. L. (2015). *Investigating quantitative MRI as a method for the treatment stratification of stroke patients with unknown onset time* [Masters by research thesis, University of Bristol]. University of Bristol Arts and Social Sciences Library Research Repository.

McGarry, B. L., Rogers, H. J., Knight, M. J., Jokivarsi, K. T., Sierra, A., Gröhn, O. H., & Kauppinen, R. A. (2016a). Stroke onset time estimation from multispectral quantitative magnetic resonance imaging in a rat model of focal permanent cerebral ischemia. *International Journal of Stroke*, *11*(6), 677–682.

McGarry, B. L., Rogers, H. J., Knight, M. J., Jokivarsi, K. T., Gröhn, O. H. J., & Kauppinen, R. A. (2016b). Determining stroke onset time using quantitative MRI: high accuracy, sensitivity and specificity obtained from magnetic resonance relaxation times. *Cerebrovascular Diseases Extra*, *6*(2), 60–65.

McGarry, B. L., Jokivarsi, K. T., Knight, M. J., Grohn, O. H. J., & Kauppinen, R. A. (2017). A magnetic resonance imaging protocol for stroke onset time estimation in permanent cerebral ischemia. *JoVE (Journal of Visualized Experiments)*, *127*, e55277–e55277.

McGarry, B. L., Damion, R. A., Chew, I., Knight. M. J., Harston, G. J., Carone, D. Jezzard, P., Sitaram, A, Muir, W. K. Clatworthy, P. L., & Kauppinen, R. A. (2020). A comparison of $T_2$ relaxation-based MRI stroke timing methods in hyperacute ischaemic stroke patients: A pilot study. Journal of Central Nervous System and Disease, recommended for publication subject to minor revisions, 26th May 2020.

McRobbie, D. W., Moore, E. A., Graves, M. J., & Prince, M. R. (2006). *MRI from Picture to Proton*. Cambridge University Press.

Meschia, J. F., & Brott, T. (2018). Ischaemic stroke. *European Journal of Neurology*, *25*(1), 35–40.

Milford, D., Rosbach, N., Bendszus, M., & Heiland, S. (2015). Mono-exponential fitting in $T_2$ relaxometry: relevance of offset and first echo. *PLOS ONE*, *10*(12), e0145255.

Minnerup, J., Broocks, G., Kalkoffen, J., Langner, S., Knauth, M., Psychogios, M. N., Wersching, H., Teuber, A., Heindel, W., Eckert, B., Wiendl, H., Schramm, P., Fiehler, J., & Kemmling, A. (2016). Computed tomography–based quantification of lesion water uptake identifies patients within 4.5 hours of stroke onset: A multicenter observational study. *Annals of Neurology*, *80*(6), 924–934.

Mistry, N., Tallantyre, E. C., Dixon, J. E., Galazis, N., Jaspan, T., Morgan, P. S., Morris, P., & Evangelou, N. (2011). Focal multiple sclerosis lesions abound in 'normal appearing white matter'. *Multiple Sclerosis*, *17*(11), 1313–1323.

Mohr, J. P., Gautier, J. C., Hier, D., & Stein R. W. (1986). Middle cerebral artery. In H. J. M. Barnett, B.M. Stein, J.P. Mohr, F.M. Yatsu (Eds), *Stroke, Vol 1, pathophysiology, diagnosis and management* (pp.377 – 450). Churchill Livingstone.

Moonen, C. T., Pekar, J., de Vleeschouwer, M. H., van Gelderen, P., van Zijl, P. C., & DesPres, D. (1991). Restricted and anisotropic displacement of water in healthy cat brain and in stroke studied by NMR diffusion imaging. *Magnetic Resonance in Medicine*, *19*(2), 327–332.

Moseley, M. E., Cohen, Y., Mintorovitch, J., Chileuitt, L., Shimizu, H., Kucharczyk, J., Wendland, M. F., & Weinstein, P. R. (1990). Early detection of regional cerebral ischemia in cats: Comparison of diffusion- and $T_2$-weighted MRI and spectroscopy. *Magnetic Resonance in Medicine*, *14*(2), 330–346.

Mugler, J. P., & Brookeman, J. R. (1991). Rapid three-dimensional $T_1$-weighted MR imaging with the MP-RAGE sequence. *Journal of Magnetic Resonance Imaging*, *1*(5), 561–567.

Muir, K. W., Buchan, A., von Kummer, R., Rother, J., & Baron, J. C. (2006). Imaging of acute stroke. *The Lancet Neurology*, *5*(9), 755–768.

Mukherjee, P., Berman, J. I., Chung, S. W., Hess, C. P., & Henry, R. G. (2008). Diffusion tensor MR imaging and fiber tractography: Theoretic underpinnings. *AJNR. American Journal of Neuroradiology*, *29*(4), 632–641.

Muller, D. W., & Sawitzki, G. (1991). Excess mass estimates and tests for Multimodality. *Journal of the American Statistical Association*, *86*(415), 738–746. JSTOR.

Nakamura, K., Saku, Y., Ibayashi, S., & Fujishima, M. (1999). Progressive motor deficits in lacunar infarction. *Neurology*, *52*(1), 29–33.

Nekolla, S., Gneiting, T., Syha, J., Deichmann, R., & Haase, A. (1992). $T_1$ maps by k-space reduced snapshot-FLASH MRI. *Journal of Computer Assisted Tomography*, *16*(2), 327–332.

Nishizaki, T., Yamauchi, R., Tanimoto, M., & Okada, Y. (1988). Effects of temperature on the oxygen consumption in thin slices from different brain regions. *Neuroscience Letters*, *86*(3), 301–305.

Nogueira, R. G., Jadhav, A. P., Haussen, D. C., Bonafe, A., Budzik, R. F., Bhuva, P., Yavagal, D. R., Ribo, M., Cognard, C., Hanel, R. A., Sila, C. A., Hassan, A. E., Millan, M., Levy, E. I., Mitchell, P., Chen, M., English, J. D., Shah, Q. A., Silver, F. L., ... Jovin, T. G. (2018). Thrombectomy 6 to 24 hours after stroke with a mismatch between deficit and infarct. *New England Journal of Medicine*, *378*(1), 11–21.

Norrving, B., Barrick, J., Davalos, A., Dichgans, M., Cordonnier, C., Guekht, A., Kutluk, K., Mikulik, R., Wardlaw, J., Richard, E., Nabavi, D., Molina, C., Bath, P. M., Stibrant, S., K., Rudd, A., Drummond, A., Planas, A., & Caso, V. (2018). Action plan for stroke in europe 2018–2030. *European Stroke Journal*, *3*(4), 309–336.

Norton, T. J. T., Pereyra, M., Knight, M. J., McGarry, B. M., Jokivarsi, K. T., Gröhn, O. H. J., & Kauppinen, R. A. (2017). Stroke Onset Time Determination Using MRI Relaxation Times without Non-Ischaemic Reference in A Rat Stroke Model. *Biomedical Spectroscopy and Imaging*, *6*(1–2), 25–35.

O'Collins, V. E., Macleod, M. R., Donnan, G. A., Horky, L. L., van der Worp, B. H., & Howells, D. W. (2006). 1,026 experimental treatments in acute stroke. *Annals of Neurology*, *59*(3), 467–477.

OECD (Organisation for Economic Cooperation and Development). (2018). *Number of magnetic resonance imaging (MRI) units in selected countries as of 2017 (per million population).* Website.

https://www.statista.com/statistics/282401/density-of-magnetic-resonance-imaging-units-by-country/

Ozenne, B., Subtil, F., & Maucort-Boulch, D. (2015). The precision–recall curve overcame the optimism of the receiver operating characteristic curve in rare diseases. *Journal of Clinical Epidemiology*, *68*(8), 855–859.

Peng, C. Y. J., Lee, K. L., & Ingersoll, G. M. (2002). An introduction to logistic regression analysis and reporting. *The Journal of Educational Research*, *96*(1), 3–14.

Petkova, M., Rodrigo, S., Lamy, C., Oppenheim, G., Touzé, E., Mas, J.-L., Méder, J.F., & Oppenheim, C. (2010). MR imaging helps predict time from symptom onset in patients with acute stroke: Implications for patients with unknown onset time. *Radiology*, *257*(3), 782–792.

Plewes, D. B., & Kucharczyk, W. (2012). Physics of MRI: A primer. *Journal of Magnetic Resonance Imaging*, *35*(5), 1038–1054.

Powers, W. J., Rabinstein, A. A., Ackerson, T., Adeoye, O. M., Bambakidis, N. C., Becker, K., Biller, J., Brown, M., Demaerschalk, B. M., Hoh, B., Jauch, E. C., Kidwell, C. S., Leslie-Mazwi, T. M., Ovbiagele, B., Scott, P. A., Sheth, K. N., Southerland, A. M., Summers, D. V., & Tirschwell, D. L. (2018). 2018 guidelines for the early management of patients with acute ischaemic stroke: A guideline for healthcare professionals from the American Heart Association/American Stroke Association. *Stroke*, *49*(3).

Puig, J., Blasco, G., Daunis-I-Estadella, J., Thomalla, G., Castellanos, M., Soria, G., Prats-Galino, A., Sánchez-González, J., Boada, I., Serena, J., & Pedraza, S. (2013). Increased corticospinal tract fractional anisotropy can discriminate stroke onset within the first 4.5 hours. *Stroke*, *44*(4), 1162–1165.

Pykett, I. L., Rosen, B. R., Buonanno, F. S., & Brady, T. J. (1983). Measurement of spin-lattice relaxation times in nuclear magnetic resonance imaging. *Physics in Medicine and Biology*, *28*(6), 723.

Rajsic, S., Gothe, H., Borba, H. H., Sroczynski, G., Vujicic, J., Toell, T., & Siebert, U. (2019). Economic burden of stroke: A systematic review on post-stroke care. *The European Journal of Health Economics*, *20*(1), 107–134.

Randolph, J. J. (2005). *Free-Marginal Multirater Kappa (multirater K[free]): An Alternative to Fleiss' Fixed-Marginal Multirater Kappa*. Retrieved from https://eric.ed.gov/?id=ED490661

Randolph, J. J. (2008). Online kappa calculator. Website: http://justusrandolph.net/kappa/

Rehncrona, S., Rosén, I., & Smith, M. L. (1985). Effect of different degrees of brain ischemia and tissue lactic acidosis on the short-term recovery of neurophysiologic and metabolic variables. *Experimental Neurology*, *87*(3), 458–473.

Rijsbergen, C. J. V. (1979). *Information Retrieval* (2nd ed.). Butterworth-Heinemann.

Rizzo, S., Botta, F., Raimondi, S., Origgi, D., Fanciullo, C., Morganti, A. G., & Bellomi, M. (2018). Radiomics: The facts and the challenges of image analysis. *European Radiology Experimental*, *2*(36), 2 – 8.

Rodriguez, R. N. (1977). A guide to the burr type XII distributions. *Biometrika*, *64*(1), 129–134.

Rogers, H. J., McGarry, B. L., Knight, M. J., Jokivarsi, K. T., Gröhn, O. H. J., & Kauppinen, R. A. (2014). Timing the ischaemic stroke by $^{1}$H-MRI: Improved accuracy using absolute relaxation times over signal intensities. *NeuroReport*, *22;25*(15):1180-5.

Roldan-Valadez, E., Gonzalez-Gutierrez, O., & Martinez-Lopez, M. (2012). Diagnostic performance of PWI/DWI MRI parameters in discriminating hyperacute versus acute ischaemic stroke: Finding the best thresholds. *Clinical Radiology*, *67*(3), 250–257.

Rosenberg, G. A. (1999). Ischaemic brain edema. *Progress in Cardiovascular Diseases*, *42*(3), 209–216.

Sacco, R. L., Kasner, S. E., Broderick, J. P., Caplan, L. R., Connors, J. J. B., Culebras, A., Elkind, M. S. V., George, M. G., Hamdan, A. D., Higashida, R. T., Hoh, B. L., Janis, L. S., Kase, C. S., Kleindorfer, D. O., Lee, J.-M., Moseley, M. E., Peterson, E. D., Turan, T. N., Valderrama, A. L., ... Council on nutrition, physical activity and metabolism. (2013). An updated definition of stroke for the

21st century: A statement for healthcare professionals from the American Heart Association/American Stroke Association. *Stroke*, *44*(7), 2064–2089.

Sandercock, P., Wardlaw, J. M., Lindley, R.I., Dennis, M. Cohen, G., Murray, G., ... Arauz, A. (2012).The benefits and harms of intravenous thrombolysis with recombinant tissue plasminogen activator within 6 h of acute ischaemic stroke (the third international stroke trial [IST-3]): a randomised controlled trial. *The Lancet, 379 (9843),* 2352 – 63.

Saver, J. L. (2006). Time is brain—quantified. *Stroke*, *37*(1), 263–266.

Schaefer, P. W., Grant, P. E., & Gonzalez, R. G. (2000). Diffusion-weighted MR Imaging of the Brain. *Radiology*, *217*(2), 331–345.

Schenker, C., Meier, D., Wichmann, W., Boesiger, P., & Valavanis, A. (1993). Age distribution and iron dependency of the $T_2$ relaxation time in the globus pallidus and putamen. *Neuroradiology*, *35*(2), 119–124.

Schindler, M. K., Sati, P., & Reich, D. S. (2017). Insights from ultra-high field imaging in multiple sclerosis. *Neuroimaging Clinics of North America*, *27*(2), 357–366.

Schlaug, G., Siewert, B., Benfield, A., Edelman, R. R., & Warach, S. (1997). Time course of the apparent diffusion coefficient (ADC) abnormality in human stroke. *Neurology*, *49*(1), 113–119.

Schneider, T., Kissela Brett, Woo Daniel, Kleindorfer Dawn, Alwell Kathleen, Miller Rosemary, Szaflarski Jerzy, Gebel James, Khoury Jane, Shukla Rakesh, Moomaw Charles, Pancioli Arthur, Jauch Edward, & Broderick Joseph. (2004). Ischemic stroke subtypes: a population-based study of incidence rates among blacks and whites. *Stroke*, *35*(7), 1552–1556.

Sener, R. N. (2001). Diffusion MRI: Apparent diffusion coefficient (ADC) values in the normal brain and a classification of brain disorders based on ADC values. *Computerized Medical Imaging and Graphics*, *25*(4), 299–326.

Shapiro, S. S., & Wilk, M. B. (1965). An analysis of variance test for normality (complete samples). *Biometrika*, *52*(3–4), 591–611.

Siemens Healthcare Limited. (2020). *MR Fingerprinting: a giant leap for precision medicine. Website.* https://www.siemens-healthineers.com/en-uk/magnetic-resonance-imaging/technologies-and-innovations/mr-fingerprinting

Siemonsen, S., Löbel, U., Sedlacik, J., Forkert, N. D., Mouridsen, K., Østergaard, L., Thomalla, G., & Fiehler, J. (2012). Elevated $T_2$-values in MRI of stroke patients shortly after symptom onset do not predict irreversible tissue infarction. *Brain*, *135*(6), 1981–1989.

Siemonsen, S., Mouridsen, K., Holst, B., Ries, T., Finsterbusch, J., Thomalla, G., Ostergaard, L., & Fiehler, J. (2009). Quantitative $T_2$ values predict time from symptom onset in acute stroke patients. *Stroke; a Journal of Cerebral Circulation*, *40*(5), 1612–1616.

Siemund, R., Cronqvist, M., Andsberg, G., Ramgren, B., Knutsson, L., & Holtås, S. (2009). Cerebral perfusion imaging in hemodynamic stroke: Be aware of the pattern. *Interventional Neuroradiology*, *15*(4), 385–394.

Simard, J. M., Kent, T. A., Chen, M., Tarasov, K. V., & Gerzanich, V. (2007). Brain oedema in focal ischaemia: Molecular pathophysiology and theoretical implications. *The Lancet Neurology*, *6*(3), 258–268.

Simon, J. E., Bristow, M. S., Lu, H., Lauzon, M. L., Brown, R. A., Manjón, J. V., Eliasziw, M., Frayne, R., Buchan, A. M., Demchuk, A. M., & Mitchell, J. R. (2005). A novel method to derive separate gray and white matter cerebral blood flow measures from MR imaging of acute ischaemic stroke patients. *Journal of Cerebral Blood Flow & Metabolism*, *25*(9), 1236–1243

Smith, S. M. (2002). Fast robust automated brain extraction. *Human Brain Mapping*, *17*(3), 143–155.

Sommer, C. J. (2017). Ischemic stroke: Experimental models and reality. *Acta Neuropathologica*, *133*(2), 245–261.

Song, S. S., Latour, L. L., Ritter, C. H., Wu, O., Tighiouart, M., Hernandez, D. A., Ku, K. D., Luby, M., & Warach, S. (2012). A pragmatic approach using magnetic resonance imaging to treat ischaemic strokes of unknown onset time in a thrombolytic trial. *Stroke*, *43*(9), 2331–2335.

Sotak, C. H. (2004). Nuclear magnetic resonance (NMR) measurement of the apparent diffusion coefficient (ADC) of tissue water and its relationship to cell volume changes in pathological states. *Neurochemistry International*, *45*(4), 569–582.

Sozmen, E. G., Hinman, J. D., & Carmichael, S. T. (2012). Models that matter: White matter stroke models. *Neurotherapeutics*, *9*(2), 349–358.

Stejskal, E. O., & Tanner, J. E. (1965). Spin diffusion measurements: Spin echoes in the presence of a time-dependent field gradient. *The Journal of Chemical Physics*, *42*(1), 288–292.

Straka, M., Albers, G. W., & Bammer, R. (2010). Real-time diffusion-perfusion mismatch analysis in acute stroke. *Journal of Magnetic Resonance Imaging: JMRI*, *32*(5), 1024–1037.

Sudlow C.L.M., & Warlow C.P. (1997). Comparable Studies of the Incidence of Stroke and its Pathological Types. *Stroke*, *28*(3), 491–499.

Symonds, M. R. E., & Moussalli, A. (2011). A brief guide to model selection, multimodel inference and model averaging in behavioural ecology using Akaike's information criterion. *Behavioral Ecology and Sociobiology*, *65*(1), 13–21.

Tamura, A., Graham, D. I., McCulloch, J., & Teasdale, G. M. (1981). Focal cerebral ischaemia in the rat: 1. Description of technique and early neuropathological consequences following middle cerebral artery occlusion. *Journal of Cerebral Blood Flow & Metabolism*, *1*(1), 53–60.

Thomalla, G., Boutitie, F., Fiebach, J. B., Simonsen, C. Z., Nighoghossian, N., Pedraza, S., Lemmens, R., Roy, P., Muir, K. W., Ebinger, M., Ford, I., Cheng, B., Galinovic, I., Cho, T.-H., Puig, J., Thijs, V., Endres, M., Fiehler, J., Gerloff, C., & WAKE-UP Investigators. (2017). Stroke with unknown time of symptom onset: Baseline clinical and magnetic resonance imaging data of the first thousand patients in WAKE-UP (Efficacy and safety of MRI-based thrombolysis in wake-up stroke: A randomized, doubleblind, placebo-controlled trial). *Stroke*, *48*(3), 770–773.

Thomalla, G., Cheng, B., Ebinger, M., Hao, Q., Tourdias, T., Wu, O., Kim, J. S., Breuer, L., Singer, O. C., Warach, S., Christensen, S., Treszl, A., Forkert, N. D., Galinovic, I., Rosenkranz, M., Engelhorn, T., Köhrmann, M., Endres, M., Kang, D. W., ... Gerloff, C. (2011). DWI-FLAIR mismatch for the identification of

patients with acute ischaemic stroke within 4·5 h of symptom onset (PRE-FLAIR): A multicentre observational study. *The Lancet Neurology*, *10*(11), 978–986.

Thomalla, G., Fiebach, J. B., Østergaard, L., Pedraza, S., Thijs, V., Nighoghossian, N., Roy, P., Muir, K. W., Ebinger, M., Cheng, B., Galinovic, I., Cho, T.-H., Puig, J., Boutitie, F., Simonsen, C. Z., Endres, M., Fiehler, J., Gerloff, C., & WAKE-UP investigators. (2014). A multicenter, randomized, double-blind, placebo-controlled trial to test efficacy and safety of magnetic resonance imaging-based thrombolysis in wake-up stroke (WAKE-UP). *International Journal of Stroke*, *9*(6), 829–836.

Thomalla, G., Rossbach, P., Rosenkranz, M., Siemonsen, S., Krützelmann, A., Fiehler, J., & Gerloff, C. (2009). Negative fluid-attenuated inversion recovery imaging identifies acute ischaemic stroke at 3 hours or less. *Annals of Neurology*, *65*(6), 724–732.

Thomalla, G., Simonsen, C. Z., Boutitie, F., Andersen, G., Berthezene, Y., Cheng, B., Cheripelli, B., Cho, T.-H., Fazekas, F., Fiehler, J., Ford, I., Galinovic, I., Gellissen, S., Golsari, A., Gregori, J., Günther, M., Guibernau, J., Häusler, K. G., Hennerici, M., ... Gerloff, C. (2018). MRI-guided thrombolysis for stroke with unknown time of onset. *New England Journal of Medicine*, *379*(7), 611–622.

Thulborn, K. R., Waterton, J. C., Matthews, P. M., & Radda, G. K. (1982). Oxygenation dependence of the transverse relaxation time of water protons in whole blood at high field. *Biochimica Et Biophysica Acta*, *714*(2), 265–270.

Tisserand, M., Malherbe, C., Turc, G., Legrand, L., Edjlali, M., Labeyrie, M.-A., Seners, P., Mas, J.-L., Méder, J. F., Baron, J. C., & Oppenheim, C. (2014). Is white matter more prone to diffusion lesion reversal after thrombolysis? *Stroke*, *45*(4), 1167–1169.

Tofts, P. (2005). *Quantitative MRI of the Brain: Measuring Changes Caused by Disease*. John Wiley & Sons.

Toole, J. F. (1999). *Cerebrovascular disorders ($5^{th}$ ed.)*. Lippincott Williams & Wilkins.

Varoquaux, G. (2018). Cross-validation failure: Small sample sizes lead to large error bars. *NeuroImage*, *180*, 68–77.

Wang Y., Hu W., Perez-Trepichio A. D., Ng T. C., Furlan A. J., Majors A. W., & Jones S. C. (2000). Brain tissue sodium is a ticking clock telling time after arterial occlusion in rat focal cerebral ischemia. *Stroke*, *31*(6), 1386–1392.

Wang, D., & Wang, Y. (2019). Tissue window, not the time window, will guide acute stroke treatment. *Stroke and Vascular Neurology*, *4*(1), 1–2.

Wansapura, J. P., Holland, S. K., Dunn, R. S., & Ball, W. S. (1999). NMR relaxation times in the human brain at 3.0 tesla. *Journal of Magnetic Resonance Imaging*, *9*(4), 531–538.

Warach, S., Boska, M., & Welch, K. M. (1997). Pitfalls and potential of clinical diffusion-weighted MR imaging in acute stroke. *Stroke*, *28*(3), 481–482.

Warach, S., Gaa, J., Siewert, B., Wielopolski, P., & Edelman, R. R. (1995). Acute human stroke studied by whole brain echo planar diffusion-weighted magnetic resonance imaging. *Annals of Neurology*, *37*(2), 231–241.

Wardlaw, J., Brazzelli, M., Miranda, H., Chappell, F., McNamee, P., Scotland, G., Quayyum, Z., Martin, D., Shuler, K., Sandercock, P., & Dennis, M. (2014). A survey of clinical and imaging services for stroke prevention after suspected transient ischaemic attack or minor stroke in the UK. *Health Technology Assesment, NIHR Journals Library*, *18* (27).

Wardlaw, J. M. (2005). What causes lacunar stroke? *Journal of Neurology, Neurosurgery & Psychiatry*, *76*(5), 617–619.

Wardlaw, J.M., Valdés Hernández, M. C., & Muñoz-Maniega, S. (2015). What are white matter hyperintensities Made of? *Journal of the American Heart Association: Cardiovascular and Cerebrovascular Disease*, *4*(6).

Wardlaw, J. M, Smith, E. E., Biessels, G. J., Cordonnier, C., Fazekas, F., Frayne, R., Lindley, R. I., O'Brien, J. T., Barkhof, F., Benavente, O. R., Black, S. E., Brayne, C., Breteler, M., Chabriat, H., DeCarli, C., de Leeuw, F.-E., Doubal, F., Duering, M., Fox, N. C., ... Dichgans, M. (2013). Neuroimaging standards for research into small vessel disease and its contribution to ageing and neurodegeneration. *The Lancet Neurology*, *12*(8), 822–838.

Wearn, A. R., Knight, M. J., McCann, B., McGarry, B. L., Norton, T. J., Jarutyte, L., & Kauppinen, R. A. (2017). JoVE article Matlab software. Website.

https://doi.org/10.5523/bris.1bjytiabmtwqx2kodgbzkwso0k

Westbrook, C., & Roth, C. K. (2011). *MRI in Practice*. John Wiley & Sons.

Williams, A., Qian, Y., & Chu, C. R. (2011). UTE-$T_2^*$ mapping of human articular cartilage in vivo: A repeatability assessment. *Osteoarthritis and Cartilage*, *19*(1), 84–88.

Wolbarst, A. B., Capasso, P., & Wyant,A. R. (2013). *Medical Imaging: Essentials for Physicians*. John Wiley & Sons.

Wouters, A., Cheng, B., Christensen, S., Dupont, P., Robben, D., Norrving, B., Laage, R., Thijs, V. N., Albers, G. W., Thomalla, G., & Lemmens, R. (2018). Automated DWI analysis can identify patients within the thrombolysis time window of 4.5 hours. *Neurology*, *90*(18), e1570–e1577.

Wouters, A., Dupont, P., Christensen, S., Norrving, B., Laage, R., Thomalla, G., Albers, G., Thijs, V., & Lemmens, R. (2016). Association between time from stroke onset and fluid-attenuated inversion recovery lesion intensity is modified by status of collateral circulation. *Stroke*, *47*(4), 1018–1022.

Wouters, A., Lemmens, R., Dupont, P., & Thijs, V. (2014). Wake-up stroke and stroke of unknown onset: A critical review. *Stroke*, *5*, 153.

Xu, X., Cheng, Q., Zu, Q., Lu, S., Yu, J., Sheng, Y., Shi, H., & Liu, S. (2014). Comparative study of the relative signal intensity on DWI, FLAIR, and $T_2$ images in identifying the onset time of stroke in an embolic canine model. *Neurological Sciences*, *35*(7), 1059–1065.

Yala, A., Lehman, C., Schuster, T., Portnoi, T., & Barzilay, R. (2019). A deep learning mammography-based model for improved breast cancer risk prediction. *Radiology*, *292*(1), 60–66.

Youden, W. J. (1950). Index for rating diagnostic tests. *Cancer*, *3*(1), 32–35.

Youl, B. D., Hawkins, C. P., Morris, J. K., DuBoulay, E. P., & Tofts, P. S. (1992). In vivo $T_1$ values from guinea pig brain depend on body temperature. *Magnetic Resonance in Medicine*, *24*(1), 170–173.

Yu, Z., Madelin, G., Sodickson, D. K., & Cloos, M. A. (2020). Simultaneous proton magnetic resonance fingerprinting and sodium MRI. *Magnetic Resonance in Medicine*, *83*(6), 2232–2242.

Zhang, K., & Sejnowski, T. J. (2000). A universal scaling law between gray matter and white matter of cerebral cortex. *Proceedings of the National Academy of Sciences of the United States of America*, *97*(10), 5621–5626.

Zhang, Y., Brady, M., & Smith, S. (2001). Segmentation of brain MR images through a hidden Markov random field model and the expectation-maximization algorithm. *IEEE Transactions on Medical Imaging*, *20*(1), 45–57.

Zihni, E., Madai, V. I., Livne, M., Galinovic, I., Khalil, A. A., Fiebach, J. B., & Frey, D. (2020). Opening the black box of artificial intelligence for clinical decision support: A study predicting stroke outcome. *PLOS ONE*, *15*(4), e0231166.

# Appendices

# Appendix A

# Chapter 7 supplementary information

## Contextualised descriptions and definitions of performance metrics used

Performance of MRI classifiers was assessed using measures that consider true positive (TP), false positive (FP), true negative (TN) and false negative (FN) rates, where TP and TN refer to the number of patients *correctly* identified as within or beyond the treatment window, respectively. FP and FN refer to the number of patients *incorrectly* identified as within or beyond the treatment window, respectively. The measures used, defined in the context of estimating stroke onset time of patients, are given below (Bekkar & Djemaa, 2013).

*Measures of accuracy*

- **Accuracy:** the overall ability of the classifier to differentiate between patients within and beyond the treatment window correctly (TP+TN/TP+TN+FP+FN).
- **Sensitivity/recall:** the ratio of patients correctly identified as within the treatment window to all the patients that were within the treatment window (TP/TP+FN). Represents the ability of the classifier to identify patients within the treatment window correctly.
- **Specificity:** the ratio of patients correctly identified as beyond the treatment window to all the patients that were beyond the treatment window (TN/TN+FP). Represents the ability of the classifier to identify patients beyond the treatment window correctly.

*Measures of correctness*

- **Precision / positive predictive value (PPV):** the ratio of patients correctly predicted to be within the treatment window to the total predicted to be within the treatment window (TP/TP+FP). Approximates the

probability that a patient with an image intensity ratio below the optimal cut-off (or above for ADC) is within the treatment window.

- **Negative predictive value (NPV):** the ratio of patients correctly predicted to be beyond the treatment window to the total predicted to be beyond the treatment window (TN/TN+FN). Approximates the probability that a patient with an image intensity ratio above the optimal cut-off (or below for ADC) is beyond the treatment window.

*Performance metrics*

– **Receiver operating characteristic (ROC) curves** demonstrate the trade-off between sensitivity and specificity for every possible image intensity ratio cut-off. Classifiers with high discriminative ability have lines closest to the top left-hand corner of the ROC plot, and classifiers with random performance are close to the 0.5-area reference line, which is a straight diagonal line from (0,0) to (1,1) (Zweig & Campbell, 1993).

– **The area under the ROC (AUC)** is a numerical indication of overall performance. An AUC of 0.5 indicates a classifier that performs no better than random guessing and an AUC of 1 indicates a perfect classifier (Hanley & McNeil, 1983). In the context of this study, the AUC is an estimate of the probability that a randomly selected scan before 4.5 hours will have an image intensity ratio lower (or higher for ADC) than the image intensity ratio of a randomly selected scan performed after 4.5 hours.

– **The Youden J Index** (max[sensitivity + specificity – 1]) identifies the cut-off that minimises misclassification by giving equal weight to sensitivity and specificity and corresponds to the point on the ROC curve with a vertical distance furthest from the 0.5 reference line, where the summation of sensitivity and specificity are maximum (Habibzadeh, Habibzadeh, & Yadollahie, 2016; Youden, 1950). The image intensity ratio with the highest

Youden J index will, therefore, be the one that can be used to distinguish the highest number of patients within and beyond the treatment window.

– **Logistic Regression** is used to describe and test hypotheses about the relationship between a categorical outcome variable, $Y$ (e.g., within or beyond the treatment window) and one or more independent predictor variables (e.g., image intensity ratios) (Peng, Lee, & Ingersoll, 2002). The logistic model predicts the natural logarithm, $Y$, of the ratio of the probability of an event happening (e.g., the patient is within the treatment window) to the probability of the event not happening (e.g., the patient is beyond the treatment window). The logistic model, therefore, takes the form of:

$$Y = \alpha + \beta_1\chi_1 + \beta_2\chi_2 + \beta_3\chi_3 + \beta_4\chi_4 \ldots.$$

In the context of this study, $Y$ is the predicted log-odds of the patient being within the treatment window ($Y = 1$ for onset time $< 270$ minutes, $Y = 0$ for onset time $> 270$ minutes) $\alpha$ is the estimated intercept, $\beta_1$ is the estimated regression coefficient and $\chi_{1\ldots n}$ are the predictor variables (e.g. image intensity ratio of ADC, DWI, $T_2$w, $T_2$). The probability of being within the treatment window ($P$) is therefore calculated as:

$$\frac{e^{(\alpha + \beta_1\chi_1 + \beta_2\chi_2 + \beta_3\chi_3 + \beta_4\chi_4 \ldots.)}}{1 + e^{(\alpha + \beta_1\chi_1 + \beta_2\chi_2 + \beta_3\chi_3 + \beta_4\chi_4 \ldots.)}}$$

– **Akaike information criteria (AIC)** (Akaike, 1973) is a measure of the quality of a model relative to other models in the same dataset and represents the amount of information lost by using the model (Symonds & Moussalli, 2011). The most accurate model has the lowest AIC (Akaike, 1973). The AIC is calculated using the number of fitted parameters, including the intercept in the model ($k$), and the maximum likelihood estimate for the model ($L$):

$$AIC = -2\ln(L) + 2k.$$

However, when $k$ and the sample size ($n$) is less than 40, AIC corrected for sample size ($AIC_c$) is recommended (Symonds & Moussalli, 2011) and was thus used in this study. Where:

$$AIC_c = AIC + \frac{2k(k+1)}{n-k-1}$$

The lowest AIC the generalized linear model produced by the logistic regression analysis with the lowest $AIC_c$ value represents the one that, in comparison to other models, best predicts whether a patient is within the thrombolysis treatment window.

- **Precision-recall-gain (PRG) methods** developed by Flach and Kull (2015) is a more interpretable variation of the traditional precision-recall analysis. Precision-gain and recall-gain are linearized versions of precision (or PPV) and recall (or sensitivity) values. PRG methods have been shown to be an appropriate alternative to ROC analysis in class imbalanced data sets and overcome problems associated with traditional precision-recall analysis (see Flach & Kull, 2015).

- **The precision-recall-gain (PRG) curve** provides a visual indication of overall performance by plotting precision-gain on the y-axis and recall-gain on the x-axis, ignoring negative gains. Lines closest to the top right of the graph indicate parameters with high overall ability to identify patients scanned before 4.5 hours.

- **The area under the PRG curve (AUPRG)** provides a numerical indication of overall performance. An AUPRG of zero indicates a trivial

classifier and positive and negative AUPRGs indicate more and less optimal classifiers, respectively (Flach & Kull, 2015). There is no predefined limit as to what constitutes a high overall performance, but a higher AUPRG would indicate a classifier that performs better at identifying patients within the treatment window.

- **The $F_1$ score** (Rijsbergen, 1979) is considered an appropriate measure for evaluation of a class-imbalanced data set, where the higher the $F_1$ score, the better the overall performance. (Bekkar & Djemaa, 2013). The $F_1$ score gives equal weighting to the importance of precision and recall and is defined as the harmonic mean of precision and recall:

$$F_1 = 2\left(\frac{precision \times recall}{precision + recall}\right)$$

## Power analyses referenced in the Discussion of Chapter 7

Apriori power analyses were conducted using G*Power (Faul et al., 2007).

**Power analysis for the FLAIR image intensity ratio:** based on Wouters et al.'s (2016) report of relationship of the FLAIR ratio with time from symptom onset in patients scanned within nine hours (r = 0.4).

**Analysis:** A priori: Compute required sample size

**Input:** Tail(s) = Two

Correlation ρ $H_1$ =0.4

α err prob =0.05

Power (1-β err prob=0.9

Correlation ρ $H_0$ =0

**Output:** Lower critical r =-0.2520938

Upper critical r =0.2520938

Total sample size =61

Actual power = 0.9020915

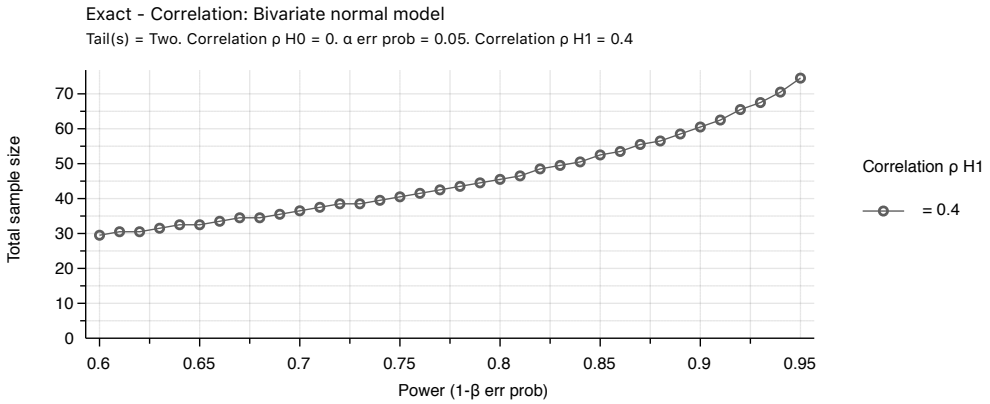

**Power analysis for the $T_2$ relaxation time:** based on Siemonsen et al.'s (2009) report of relationship of hemispheric differences in $T_2$ relaxation times with time from symptom onset in patients scanned within six hours of symptom onset (r = 0.5) and the relationship of the $T_2$ image intensity ratio with time from symptom onset in patients scanned within nine hours of symptom onset reported in McGarry et al. (2020) and Chapter 7 (r = 0.5).

**Analysis:** A priori: Compute required sample size

**Input:** Tail(s) =Two

Correlation ρ $H_1$ =0.5

α err prob =0.05

Power (1-β err prob) =0.9

Correlation ρ $H_0$ =0

**Output:** Lower critical =-0.3245729

Upper critical r =0.3245729

Total sample size =37

Actual power =0.9011434

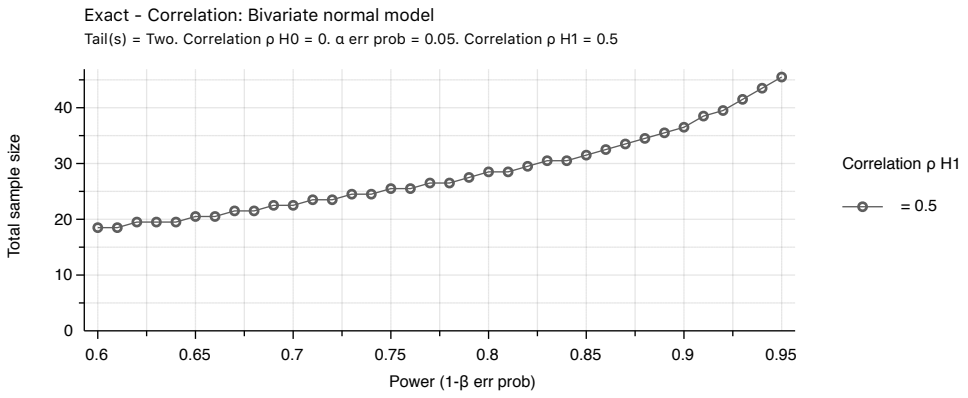

## Appendix A References

Akaike, H. (1973). Information theory and an extension of the maximum likelihood principle. In: Petrov, B. N., Csaki, F. eds., 2nd International Symposium on Information Theory. Budapest: Akademiai Kiado, pp. 267–281. (Reproduced in Breakthroughs in Statistics, Vol. 1, Kotz, S., Johnson, N. L. eds., New York: Springer Verlag, 1992.)

Bekkar, M., & Djemaa, D. H. K. (2013). Evaluation measures for models assessment over imbalanced data sets. *Journal of Information Engineering and Applications. 3*(10), 27-38.

Faul, F., Erdfelder, E., Lang, A.-G., & Buchner, A. (2007). G*Power 3: A flexible statistical power analysis program for the social, behavioral, and biomedical sciences. *Behavior Research Methods*, *39*, 175-191.

Flach, P., & Kull, M. (2015). Precision-Recall-Gain Curves: PR analysis done right. In C. Cortes, N. D. Lawrence, D. D. Lee, M. Sugiyama, & R. Garnett (Eds.), *Advances in Neural Information Processing Systems 28* (pp. 838– 846).

Habibzadeh, F., Habibzadeh, P., & Yadollahie, M. (2016). On determining the most appropriate test cut-off value: The case of tests with continuous results. *Biochemia Medica*, 297–307.

Hanley, J. A., & McNeil, B. J. (1983). A method of comparing the areas under receiver operating characteristic curves derived from the same cases. *Radiology*, *148*(3), 839–843.

McGarry, B. L., Damion, R. A., Chew, I., Knight. M. J., Harston, G. J., Carone, D. Jezzard, P., Sitaram, A, Muir, W. K. Clatworthy, P. L., & Kauppinen, R. A. (2020). A comparison of $T_2$ relaxation-based MRI stroke timing methods in hyperacute ischaemic stroke patients: A pilot study. Journal of Central Nervous System and Disease, recommended for publication subject to minor revisions, 26th May 2020.

Peng, C.Y. J., Lee, K. L., & Ingersoll, G. M. (2002). An introduction to logistic regression analysis and reporting. *The Journal of Educational Research*, *96*(1), 3–14.

Rijsbergen, C. J. V. (1979). *Information Retrieval* (2nd ed.). Butterworth-Heinemann.

Siemonsen, S., Mouridsen, K., Holst, B., Ries, T., Finsterbusch, J., Thomalla, G., Ostergaard, L., & Fiehler, J. (2009). Quantitative $T_2$ values predict time from symptom onset in acute stroke patients. *Stroke; a Journal of Cerebral Circulation*, *40*(5), 1612–1616.

Symonds, M. R. E., & Moussalli, A. (2011). A brief guide to model selection, multimodel inference and model averaging in behavioural ecology using Akaike's information criterion. *Behavioral Ecology and Sociobiology*, *65*(1), 13–21.

Wouters, A., Dupont, P., Christensen, S., Norrving, B., Laage, R., Thomalla, G., Albers, G., Thijs, V., & Lemmens, R. (2016). Association between time from stroke onset and fluid-attenuated inversion recovery lesion intensity is modified by status of collateral circulation. *Stroke*, *47*(4), 1018–1022.

Youden, W. J. (1950). Index for rating diagnostic tests. *Cancer*, *3*(1), 32–35

Zweig, M. H., & Campbell, G. (1993). Receiver-operating characteristic (ROC) plots: A fundamental evaluation tool in clinical medicine. *Clinical Chemistry*, *39*(4), 561–577.

# Appendix B

# Chapter 7 additional tables

Table B1. Test statistics for Shapiro-Wilk and correlation analyses.

| Classifier | Shapiro-Wilk | | Correlation Coefficient | | | | | |
|---|---|---|---|---|---|---|---|---|
| | W | p | Pearson's r (r) | p | Spearman's rank ($r_s$) | p | Kendall's Tau ($r_t$) | p |
| **All 35 patients** | | | | | | | | |
| ADC | 0.99 | 0.998 | - 0.07 | 0.708 | - .09 | 0.620 | - 0.08 | 0.514 |
| DWI† | 0.90 | 0.005* | 0.25 | 0.153 | 0.15 | 0.395 | 0.11 | 0.370 |
| $T_2w$† | 0.86 | 0.001* | 0.36 | 0.032* | 0.22 | 0.201 | 0.17 | 0.168 |
| $T_2$ | 0.98 | 0.779 | 0.49 | 0.003* | 0.48 | 0.005* | 0.32 | 0.006* |
| **Sub-cohort with FLAIR** | | | | | | | | |
| ADC | 0.99 | 0.999 | - 0.17 | 0.511 | -.10 | 0.715 | - 0.09 | 0.621 |
| DWI | 0.90 | 0.065 | 0.39 | 0.119 | 0.27 | 0.305 | 0.18 | 0.323 |
| $T_2w$ | 0.91 | 0.090 | 0.36 | 0.152 | 0.28 | 0.286 | 0.22 | 0.217 |
| $T_2$ | 0.96 | 0.725 | 0.35 | 0.166 | 0.39 | 0.127 | 0.29 | 0.099 |
| FLAIR† | 0.89 | 0.044* | 0.56 | 0.831 | 0.25 | 0.342 | 0.21 | 0.266 |

*Note.* W = Shapiro-Wilk statistic, $p$ = significance level, * indicates significant relationship as $p < .05$, †indicates a parameter that was not normally distributed and therefore Spearman's Rank and Kendall's Tau results should be referred to. r = Pearson's r correlation coefficient for normally distributed data, $r_s$ = Spearman's rank correlation coefficient for non-normally distributed data, and $r_t$ is the Kendall's Tau correlation coefficient for non-normally distributed data.

Table B2. Statistics for comparisons of areas under the ROC curves.

| Parameters | Difference between AUCs (SE) | 95% CI | z-statistic | p |
|---|---|---|---|---|
| **ADC vs DWI** | 0.09 (0.09) | -0.08 – 0.26 | 1.06 | 0.288 |
| **ADC vs $T_2$w** | 0.12 (0.14) | -0.15 – 0.38 | 0.84 | 0.399 |
| **ADC vs $T_2$** | 0.22 (0.12) | 0.00 – 0.45 | 1.92 | 0.055 |
| **DWI vs $T_2$w** | 0.02 (0.09) | -0.15 – 0.20 | 0.26 | 0.794 |
| **DWI vs $T_2$** | 0.13 (0.11) | -0.08 – 0.34 | 1.24 | 0.215 |
| **$T_2$w vs $T_2$** | 0.11 (0.12) | -0.10 – 0.32 | 1.01 | 0.313 |

*Note.* AUC = area under the receiver operating characteristic (ROC) curve, SE = standard error, CI = confidence interval, $p$ = significance level.

# Appendix C

# Chapter 8 supplementary information

Table C1. Test statistics for Shapiro-Wilk and correlation analysis of distributional parameters and lesion size.

| Parameters | Shapiro-Wilk | | Correlation | |
|---|---|---|---|---|
| | *W* | *p* | *r or $r_s$* | *p* |
| Whole Lesion | | | | |
| SD | 0.93 | 0.095 | 0.34 | 0.117 |
| *GEV parameters* | | | | |
| μ (location) | 0.95 | 0.258 | 0.19 | 0.385 |
| σ (scale) | 0.86 | 0.005* | 0.38 | 0.077 |
| k (shape) | 0.94 | 0.185 | 0.11 | 0.617 |
| *Burr parameters* | | | | |
| α (scale) | 0.92 | 0.053 | 0.09 | 0.681 |
| c (shape) | 0.95 | 0.332 | 0.05 | 0.837 |
| k (shape) | 0.52 | < 0.000* | -0.15 | 0.488 |
| GM Lesion | | | | |
| SD | 0.92 | 0.276 | 0.139 | 0.650 |
| *GEV parameters* | | | | |
| μ (location) | 0.90 | 0.120 | 0.220 | 0.470 |
| σ (scale) | 0.88 | 0.068 | 0.156 | 0.611 |
| k (shape) | 0.93 | 0.319 | 0.319 | 0.289 |
| *Burr parameters* | | | | |
| α (scale) | 0.77 | 0.004* | -0.609 | 0.052 |
| c (shape) | 0.83 | 0.021* | 0.118 | 0.735 |
| k (shape) | 0.93 | 0.445 | 0.364 | 0.273 |
| WM Lesion | | | | |
| SD | 0.95 | 0.386 | 0.104 | 0.655 |
| *GEV parameters* | | | | |
| μ (location) | 0.90 | 0.037* | 0.225 | 0.326 |
| σ (scale) | 0.90 | 0.036* | 0.243 | 0.289 |
| k (shape) | 0.97 | 0.820 | 0.036 | 0.876 |
| *Log-logistic parameters* | | | | |
| μ (location) | 0.87 | 0.953 | 0.345 | 0.126 |
| σ (scale) | 0.011 | 0.390 | 0.065 | 0.780 |

*Note.* W = Shapiro-Wilk statistic, *p* = significance level, * indicates significant test, r = Pearson's correlation coefficient for normally distributed data, and $r_s$ = Spearman's correlation coefficient for non-normally distributed data, r values are $r_s$ for parameters where W is significant.

## Distributions tested

- Birnbaum Saunders
- Burr Type X11
- Extreme Value
- Exponential
- Gamma
- Generalised Extreme Value
- Generalised Pareto
- Inverse Gaussian
- Logistic
- Loglogistic
- Lognormal
- Nakagami
- Normal
- Rayleigh
- Rician
- T location scale
- Uniform
- Weibull

# Appendix D

# Figure permissions

**Chapter 2, Figure 2.2. Schematic diagram illustrating the types of oedema during ischaemia.**

ELSEVIER LICENSE
TERMS AND CONDITIONS
May 28, 2020

This Agreement between Dr. Bryony McGarry ("You") and Elsevier ("Elsevier") consists of your license details and the terms and conditions provided by Elsevier and Copyright Clearance Center.

| | |
|---|---|
| License Number | 4822071011678 |
| License date | May 04, 2020 |
| Licensed Content Publisher | Elsevier |
| Licensed Content Publication | The Lancet Neurology |
| Licensed Content Title | Brain oedema in focal ischaemia: molecular pathophysiology and theoretical implications |
| Licensed Content Author | J Marc Simard, Thomas A Kent,Mingkui Chen, Kirill V Tarasov, Volodymyr Gerzanich |
| Licensed Content Date | Mar 1, 2007 |
| Licensed Content Volume | 6 |
| Licensed Content Issue | 3 |
| Licensed Content Pages | 11 |
| Start Page | 258 |
| End Page | 268 |
| Type of Use | reuse in a thesis/dissertation |
| Portion | figures/tables/illustrations |
| Number of figures/tables/illustrations | 1 |
| Format | both print and electronic |
| Are you the author of this Elsevier article? | No |
| Will you be translating? | No |
| Title | A preclinical and clinical investigation into quantitative magnetic resonance imaging as a tool for estimating onset time in hyperacute ischaemic stroke |
| Institution name | University of Bristol |
| Expected presentation date | Jun 2020 |
| Portions | Figure 5 on page 261 |
| Requestor Location | Dr. Bryony McGarry<br>University of Bristol<br>School of Psychological Science |

| | |
|---|---|
| | Bristol, BS8 1TU<br>United Kingdom<br>Attn: Dr. Bryony McGarry |
| Publisher Tax ID | GB 494 6272 12 |
| Total | 0.00 GBP |

INTRODUCTION

1. The publisher for this copyrighted material is Elsevier. By clicking "accept" in connection with completing this licensing transaction, you agree that the following terms and conditions apply to this transaction (along with the Billing and Payment terms and conditions established by Copyright Clearance Center, Inc. ("CCC"), at the time that you opened your Rightslink account and that are available at any time at http://myaccount.copyright.com).

GENERAL TERMS

2. Elsevier hereby grants you permission to reproduce the aforementioned material subject to the terms and conditions indicated.

3. Acknowledgement: If any part of the material to be used (for example, figures) has appeared in our publication with credit or acknowledgement to another source, permission must also be sought from that source. If such permission is not obtained then that material may not be included in your publication/copies. Suitable acknowledgement to the source must be made, either as a footnote or in a reference list at the end of your publication, as follows:

"Reprinted from Publication title, Vol /edition number, Author(s), Title of article / title of chapter, Pages No., Copyright (Year), with permission from Elsevier [OR APPLICABLE SOCIETY COPYRIGHT OWNER]." Also Lancet special credit - "Reprinted from The Lancet, Vol. number, Author(s), Title of article, Pages No., Copyright (Year), with permission from Elsevier."

4. Reproduction of this material is confined to the purpose and/or media for which permission is hereby given.

5. Altering/Modifying Material: Not Permitted. However figures and illustrations may be altered/adapted minimally to serve your work. Any other abbreviations, additions, deletions and/or any other alterations shall be made only with prior written authorization of Elsevier Ltd. (Please contact Elsevier at permissions@elsevier.com). No modifications can be made to any Lancet figures/tables and they must be reproduced in full.

6. If the permission fee for the requested use of our material is waived in this instance, please be advised that your future requests for Elsevier materials may attract a fee.

7. Reservation of Rights: Publisher reserves all rights not specifically granted in the combination of (i) the license details provided by you and accepted in the course of this

licensing transaction, (ii) these terms and conditions and (iii) CCC's Billing and Payment terms and conditions.

8. License Contingent Upon Payment: While you may exercise the rights licensed immediately upon issuance of the license at the end of the licensing process for the transaction, provided that you have disclosed complete and accurate details of your proposed use, no license is finally effective unless and until full payment is received from you (either by publisher or by CCC) as provided in CCC's Billing and Payment terms and conditions. If full payment is not received on a timely basis, then any license preliminarily granted shall be deemed automatically revoked and shall be void as if never granted. Further, in the event that you breach any of these terms and conditions or any of CCC's Billing and Payment terms and conditions, the license is automatically revoked and shall be void as if never granted. Use of materials as described in a revoked license, as well as any use of the materials beyond the scope of an unrevoked license, may constitute copyright infringement and publisher reserves the right to take any and all action to protect its copyright in the materials.

9. Warranties: Publisher makes no representations or warranties with respect to the licensed material.

10. Indemnity: You hereby indemnify and agree to hold harmless publisher and CCC, and their respective officers, directors, employees and agents, from and against any and all claims arising out of your use of the licensed material other than as specifically authorized pursuant to this license.

11. No Transfer of License: This license is personal to you and may not be sublicensed, assigned, or transferred by you to any other person without publisher's written permission.

12. No Amendment Except in Writing: This license may not be amended except in a writing signed by both parties (or, in the case of publisher, by CCC on publisher's behalf).

13. Objection to Contrary Terms: Publisher hereby objects to any terms contained in any purchase order, acknowledgment, check endorsement or other writing prepared by you, which terms are inconsistent with these terms and conditions or CCC's Billing and Payment terms and conditions. These terms and conditions, together with CCC's Billing and Payment terms and conditions (which are incorporated herein), comprise the entire agreement between you and publisher (and CCC) concerning this licensing transaction. In the event of any conflict between your obligations established by these terms and conditions and those established by CCC's Billing and Payment terms and conditions, these terms and conditions shall control.

14. Revocation: Elsevier or Copyright Clearance Center may deny the permissions described in this License at their sole discretion, for any reason or no reason, with a full refund payable to you. Notice of such denial will be made using the contact information provided by you. Failure to receive such notice will not alter or invalidate the denial. In no event will Elsevier or Copyright Clearance Center be responsible or liable for any costs, expenses or damage incurred by you as a result of a denial of your permission request, other than a refund of the amount(s) paid by you to Elsevier and/or Copyright Clearance Center for denied permissions.

LIMITED LICENSE

The following terms and conditions apply only to specific license types:

15. Translation: This permission is granted for non-exclusive world English rights only unless your license was granted for translation rights. If you licensed translation rights you may only translate this content into the languages you requested. A professional translator must perform all translations and reproduce the content word for word preserving the integrity of the article.

16. Posting licensed content on any Website: The following terms and conditions apply as follows: Licensing material from an Elsevier journal: All content posted to the web site must maintain the copyright information line on the bottom of each image; A hyper-text must be included to the Homepage of the journal from which you are licensing at http://www.sciencedirect.com/science/journal/xxxxx or the Elsevier homepage for books at http://www.elsevier.com; Central Storage: This license does not include permission for a scanned version of the material to be stored in a central repository such as that provided by Heron/XanEdu.

Licensing material from an Elsevier book: A hyper-text link must be included to the Elsevier homepage at http://www.elsevier.com . All content posted to the web site must maintain the copyright information line on the bottom of each image.

Posting licensed content on Electronic reserve: In addition to the above the following clauses are applicable: The web site must be password-protected and made available only to bona fide students registered on a relevant course. This permission is granted for 1 year only. You may obtain a new license for future website posting.

17. For journal authors: the following clauses are applicable in addition to the above:

Preprints:

A preprint is an author's own write-up of research results and analysis, it has not been peer-reviewed, nor has it had any other value added to it by a publisher (such as formatting, copyright, technical enhancement etc.).

Authors can share their preprints anywhere at any time. Preprints should not be added to or enhanced in any way in order to appear more like, or to substitute for, the final versions of articles however authors can update their preprints on arXiv or RePEc with their Accepted Author Manuscript (see below).

If accepted for publication, we encourage authors to link from the preprint to their formal publication via its DOI. Millions of researchers have access to the formal publications on ScienceDirect, and so links will help users to find, access, cite and use the best available version. Please note that Cell Press, The Lancet and some society-owned have different preprint policies. Information on these policies is available on the journal homepage.

Accepted Author Manuscripts: An accepted author manuscript is the manuscript of an article that has been accepted for publication and which typically includes author-incorporated changes suggested during submission, peer review and editor-author communications.

Authors can share their accepted author manuscript:

- immediately
    - via their non-commercial person homepage or blog
    - by updating a preprint in arXiv or RePEc with the accepted manuscript
    - via their research institute or institutional repository for internal institutional uses or as part of an invitation-only research collaboration work-group
    - directly by providing copies to their students or to research collaborators for their personal use
    - for private scholarly sharing as part of an invitation-only work group on commercial sites with which Elsevier has an agreement
- After the embargo period
    - via non-commercial hosting platforms such as their institutional repository
    - via commercial sites with which Elsevier has an agreement

In all cases accepted manuscripts should:

- link to the formal publication via its DOI
- bear a CC-BY-NC-ND license - this is easy to do
- if aggregated with other manuscripts, for example in a repository or other site, be shared in alignment with our hosting policy not be added to or enhanced in any way to appear more like, or to substitute for, the published journal article.

Published journal article (JPA): A published journal article (PJA) is the definitive final record of published research that appears or will appear in the journal and embodies all value-adding publishing activities including peer review co-ordination, copy-editing, formatting, (if relevant) pagination and online enrichment.

Policies for sharing publishing journal articles differ for subscription and gold open access articles:

Subscription Articles: If you are an author, please share a link to your article rather than the full-text. Millions of researchers have access to the formal publications on ScienceDirect, and so links will help your users to find, access, cite, and use the best available version.

Theses and dissertations which contain embedded PJAs as part of the formal submission can be posted publicly by the awarding institution with DOI links back to the formal publications on ScienceDirect.

If you are affiliated with a library that subscribes to ScienceDirect you have additional private sharing rights for others' research accessed under that agreement. This includes use for classroom teaching and internal training at the institution (including use in course packs and courseware programs), and inclusion of the article for grant funding purposes.

Gold Open Access Articles: May be shared according to the author-selected end-user license and should contain a CrossMark logo, the end user license, and a DOI link to the formal publication on ScienceDirect.

Please refer to Elsevier's posting policy for further information.

18. For book authors the following clauses are applicable in addition to the above: Authors are permitted to place a brief summary of their work online only. You are not allowed to download and post the published electronic version of your chapter, nor may you scan the printed edition to create an electronic version. Posting to a repository: Authors are permitted to post a summary of their chapter only in their institution's repository.

19. Thesis/Dissertation: If your license is for use in a thesis/dissertation your thesis may be submitted to your institution in either print or electronic form. Should your thesis be published commercially, please reapply for permission. These requirements include permission for the Library and Archives of Canada to supply single copies, on demand, of the complete thesis and include permission for Proquest/UMI to supply single copies, on demand, of the complete thesis. Should your thesis be published commercially, please reapply for permission. Theses and dissertations which contain embedded PJAs as part of the formal submission can be posted publicly by the awarding institution with DOI links back to the formal publications on ScienceDirect

Elsevier Open Access Terms and Conditions

You can publish open access with Elsevier in hundreds of open access journals or in nearly 2000 established subscription journals that support open access publishing. Permitted third party re-use of these open access articles is defined by the author's choice of Creative Commons user license. See our open access license policy for more information.

Terms & Conditions applicable to all Open Access articles published with Elsevier:

Any reuse of the article must not represent the author as endorsing the adaptation of the article nor should the article be modified in such a way as to damage the author's honour or reputation. If any changes have been made, such changes must be clearly indicated.

The author(s) must be appropriately credited and we ask that you include the end user license and a DOI link to the formal publication on ScienceDirect.

If any part of the material to be used (for example, figures) has appeared in our publication with credit or acknowledgement to another source it is the responsibility of the user to ensure their reuse complies with the terms and conditions determined by the rights holder.

Additional Terms & Conditions applicable to each Creative Commons user license:

CC BY: The CC-BY license allows users to copy, to create extracts, abstracts and new works from the Article, to alter and revise the Article and to make commercial use of the Article (including reuse and/or resale of the Article by commercial entities), provided the user gives appropriate credit (with a link to the formal publication through the relevant DOI), provides a link to the license, indicates if changes were made and the licensor is not represented as endorsing the use made of the work. The full details of the license are available at http://creativecommons.org/licenses/by/4.0.

CC BY NC SA: The CC BY-NC-SA license allows users to copy, to create extracts, abstracts and new works from the Article, to alter and revise the Article, provided this is not done for commercial purposes, and that the user gives appropriate credit (with a link

to the formal publication through the relevant DOI), provides a link to the license, indicates if changes were made and the licensor is not represented as endorsing the use made of the work. Further, any new works must be made available on the same conditions. The full details of the license are available at http://creativecommons.org/licenses/by-nc-sa/4.0.

CC BY NC ND: The CC BY-NC-ND license allows users to copy and distribute the Article, provided this is not done for commercial purposes and further does not permit distribution of the Article if it is changed or edited in any way, and provided the user gives appropriate credit (with a link to the formal publication through the relevant DOI), provides a link to the license, and that the licensor is not represented as endorsing the use made of the work. The full details of the license are available at http://creativecommons.org/licenses/by-nc-nd/4.0. Any commercial reuse of Open Access articles published with a CC BY NC SA or CC BY NC ND license requires permission from Elsevier and will be subject to a fee.

Commercial reuse includes:

- Associating advertising with the full text of the Article
- Charging fees for document delivery or access
- Article aggregation
- Systematic distribution via e-mail lists or share buttons

Posting or linking by commercial companies for use by customers of those companies.

20. Other Conditions:

v1.9

Questions? customercare@copyright.com or +1-855-239-3415 (toll free in the US) or +1-978-646-2777.

**Chapter 3, Figure 3.6 Free Induction Decay**

BMJ PUBLISHING GROUP LTD. LICENSE
TERMS AND CONDITIONS

May 28, 2020

This Agreement between Dr. Bryony McGarry ("You") and BMJ Publishing Group Ltd. ("BMJ Publishing Group Ltd.") consists of your license details and the terms and conditions provided by BMJ Publishing Group Ltd. and Copyright Clearance Center.

| | |
|---|---|
| License Number | 4825380633735 |
| License date | May 10, 2020 |
| Licensed Content Publisher | BMJ Publishing Group Ltd. |

| | |
|---|---|
| Licensed Content Publication | Postgraduate Medical Journal |
| Licensed Content Title | Understanding MRI: basic MR physics for physicians |
| Licensed Content Author | Stuart Currie,Nigel Hoggard,Ian J Craven,Marios Hadjivassiliou,Iain D Wilkinson |
| Licensed Content Date | Apr 1, 2013 |
| Licensed Content Volume | 89 |
| Licensed Content Issue | 1050 |
| Type of Use | Dissertation/Thesis |
| Requestor type | Individual |
| Format | Print and electronic |
| Portion | Figure/table/extract |
| Number of figure/table/extracts | 1 |
| Descriptionof figure/table/extracts | Figure 8 on page 214 |
| Will you be translating? | No |
| Circulation/distribution | 1 |
| Title | A preclinical and clinical investigation into quantitative magnetic resonance imaging as a tool for estimating onset time in hyperacute ischaemic stroke |
| Institution name | University of Bristol |
| Expected presentation date | Jun 2020 |
| Portions | Figure 8 on page 214 |
| Requestor Location | Dr. Bryony McGarry<br>University of Bristol<br>School of Psychological Science<br><br>Bristol, BS8 1TU<br>United Kingdom<br>Attn: Dr. Bryony McGarry |
| Publisher Tax ID | GB674738491 |
| Total | 0.00 GBP |

**Chapter 3. Figure 3.7 $T_1$, $T_2$ and $T_2$* relaxation.**

BMJ PUBLISHING GROUP LTD. LICENSE
TERMS AND CONDITIONS

May 28, 2020

This Agreement between Dr. Bryony McGarry ("You") and BMJ Publishing Group

Ltd. ("BMJ Publishing Group Ltd.") consists of your license details and the terms and conditions provided by BMJ Publishing Group Ltd. and Copyright Clearance Center.

| | |
|---|---|
| License Number | 4823050612290 |
| License date | May 06, 2020 |
| Licensed Content Publisher | BMJ Publishing Group Ltd. |
| Licensed Content Publication | Postgraduate Medical Journal |
| Licensed Content Title | Understanding MRI: basic MR physics for physicians |
| Licensed Content Author | Stuart Currie, Nigel Hoggard ,Ian J Craven, Marios Hadjivassiliou, Iain D Wilkinson |
| Licensed Content Date | Apr 1, 2013 |
| Licensed Content Volume | 89 |
| Licensed Content Issue | 1050 |
| Type of Use | Dissertation/Thesis |
| Requestor type | Individual |
| Format | Print and electronic |
| Portion | Figure/table/extract |
| Number of figure/table/extracts | 1 |
| Description of figure/table/extracts | Figure 7 page 213 |
| Will you be translating? | No |
| Circulation/distribution | 1 |
| Order reference number | 2 |
| Title | A preclinical and clinical investigation into quantitative magnetic resonance imaging as a tool for estimating onset time in hyperacute ischaemic stroke |
| Institution name | University of Bristol |
| Expected presentation date | Jun 2020 |
| Order reference number | 2 |
| Portions | Figure 7 page 213 |
| Requestor Location | Dr. Bryony McGarry<br>University of Bristol<br>School of Psychological Science<br><br>Bristol, BS8 1TU<br>United Kingdom<br>Attn: Dr. Bryony McGarry |
| Publisher Tax ID | GB674738491 |
| Total | 0.00 GBP |
| Terms and Conditions | |

Terms and Conditions

BMJ Group Terms and Conditions for Permissions

When you submit your order you are subject to the terms and conditions set out below. You will also have agreed to the Copyright Clearance Center's ("CCC") terms and conditions regarding billing and payment https://s100.copyright.com/App/PaymentTermsAndConditions.jsp. CCC are acting as the BMJ Publishing Group Limited's ("BMJ Group's") agent.

Subject to the terms set out herein, the BMJ Group hereby grants to you (the Licensee) a non- exclusive, non-transferable licence to re-use material as detailed in your request for this/those purpose(s) only and in accordance with the following conditions:

1) Scope of Licence: Use of the Licensed Material(s) is restricted to the ways specified by you during the order process and any additional use(s) outside of those specified in that request, require a further grant of permission.

2) Acknowledgement: In all cases, due acknowledgement to the original publication with permission from the BMJ Group should be stated adjacent to the reproduced Licensed Material. The format of such acknowledgement should read as follows:

"Reproduced from [publication title, author(s), volume number, page numbers, copyright notice year] with permission from BMJ Publishing Group Ltd."

3) Third Party Material: BMJ Group acknowledges to the best of its knowledge, it has the rights to licence your reuse of the Licensed Material, subject always to the caveat that images/diagrams, tables and other illustrative material included within, which have a separate copyright notice, are presumed as excluded from the licence. Therefore, you should ensure that the Licensed Material you are requesting is original to BMJ Group and does not carry the copyright of another entity (as credited in the published version). If the credit line on any part of the material you have requested in any way indicates that it was reprinted or adapted by BMJ Group with permission from another source, then you should seek permission from that source directly to re-use the Licensed Material, as this is outside of the licence granted herein.

4) Altering/Modifying Material: The text of any material for which a licence is granted may not be altered in any way without the prior express permission of the BMJ Group. Subject to Clause 3 above however, single figure adaptations do not require BMJ Group's approval; however, the adaptation should be credited as follows:

"Adapted by permission from BMJ Publishing Group Limited. [publication title, author, volume number, page numbers, copyright notice year]

5) Reservation of Rights: The BMJ Group reserves all rights not specifically granted in the combination of (i) the licence details provided by you and accepted in the course of this licensing transaction, (ii) these terms and conditions and (iii) CCC's Billing and Payment Terms and Conditions.

6) Timing of Use: First use of the Licensed Material must take place within 12 months of the grant of permission.

7). Creation of Contract and Termination: Once you have submitted an order via Rightslink and this is received by CCC, and subject to you completing accurate details of your proposed use, this is when a binding contract is in effect and our acceptance occurs. As you are ordering rights from a periodical, to the fullest extent permitted by law, you will have no right to cancel the contract from this point other than for BMJ Group's material breach or fraudulent misrepresentation or as otherwise permitted under

a statutory right. Payment must be made in accordance with CCC's Billing and Payment Terms and conditions. In the event that you breach any material condition of these terms and condition or any of CCC's Billing and Payment Terms and Conditions, the license is automatically terminated upon written notice from the BMJ Group or CCC or as otherwise provided for in CCC's Billing and Payment Terms and Conditions, where these apply. Continued use of materials where a licence has been terminated, as well as any use of the Licensed Materials beyond the scope of an unrevoked licence, may constitute intellectual property rights infringement and BMJ Group reserves the right to take any and all action to protect its intellectual property rights in the Licensed Materials.

8. Warranties: BMJGroup makes no express or implied representations or warranties with respect tote Licensed Material and to the fullest extent permitted by law this is provided on an "as is" basis. For the avoidance of doubt BMJ Group does not warrant that the Licensed Material is accurate or fit for any particular purpose.

9. Limitation of Liability: To the fullest extent permitted by law, the BMJ Group disclaims all liability for any indirect, consequential or incidental damages (including without limitation, damages for loss of profits, information or interruption)arising out of the use or inability to use the Licensed Material or the inability to obtain additional rights to use the Licensed Material. To the fullest extent permitted by law, the maximum aggregate liability of the BMJ Group for any claims, costs, proceedings and demands for direct losses caused by BMJ Group's breaches of its obligations herein shall be limited to twice the amount paid by you to CCC for the licence granted herein.

10. Indemnity: You hereby indemnify and hold harmless the BMJ Group and their respective officers, directors, employees and agents, from and against any and all claims, costs, proceeding or demands arising out of your unauthorised use of the Licensed Material.

11. No Transfer of License: This licence is personal to you, and may not be assigned or transferred by you without prior written consent from the BMJ Group or its authorised agent(s). BMJ Group may assign or transfer any of its rights and obligations under this Agreement, upon written notice to you.

12. No Amendment Except in Writing: This licence may not be amended except in a writing signed by both parties (or, in the case of BMJ Group, by CCC on the BMJ Group's behalf).

13. Objection to Contrary terms: BMJ Group hereby objects to any terms contained in any purchase order, acknowledgment, check endorsement or other writing prepared by you, which terms are inconsistent with these terms and conditions or CCC's Billing and Payment Terms and Conditions. These terms and conditions, together with CCC's Billing and Payment Terms and Conditions (which to the extent they are consistent are incorporated herein), comprise the entire agreement between you and BMJ Group (and CCC) and the Licensee concerning this licensing transaction. In the event of any conflict between your obligations established by these terms and conditions and those established by CCC's Billing and Payment Terms and Conditions, these terms and conditions shall control.

14. Revocation: BMJ Group or CCC may, within 30 days of issuance of this licence, deny the permissions described in this licence at their sole discretion, for any reason or no reason, with a full refund payable to you should you have not been able to exercise your rights in full. Notice of such denial will be made using the contact information provided by you. Failure to receive such notice from BMJ Group or CCC will not, to the fullest extent permitted by law alter or invalidate the denial. For the fullest extent permitted

by law in no event will BMJ Group or CCC be responsible or liable for any costs, expenses or damage incurred by you as a result of a denial of your permission request, other than a refund of the amount(s) paid by you to BMJ Group and/or CCC for denied permissions.

15. Restrictions to the license:
15.1 Promotion: BMJ Group will not give permission to reproduce in full or in part any

Licensed Material for use in the promotion of the following:

a) non-medical products that are harmful or potentially harmful to health: alcohol, baby milks and/or, sunbeds

b) medical products that do not have a product license granted by the Medicines and Healthcare products Regulatory Agency (MHRA) or its international equivalents. Marketing of the product may start only after data sheets have been released to members of the medical profession and must conform to the marketing authorization contained in the product license.

16. Translation: This permission is granted for non-exclusive world English language rights only unless explicitly stated in your licence. If translation rights are granted, a professional translator should be employed and the content should be reproduced word for word preserving the integrity of the content.

17. General: Neither party shall be liable for failure, default or delay in performing its obligations under this Licence, caused by a Force Majeure event which shall include any act of God, war, or threatened war, act or threatened act of terrorism, riot, strike, lockout, individual action, fire, flood, drought, tempest or other event beyond the reasonable control of either party.

17.1 In the event that any provision of this Agreement is held to be invalid, the remainder of the provisions shall continue in full force and effect.

17.2 There shall be no right whatsoever for any third party to enforce the terms and conditions of this Agreement. The Parties hereby expressly wish to exclude the operation of the Contracts (Rights of Third Parties) Act 1999 and any other legislation which has this effect and is binding on this agreement.

17.3 Tote fullest extent permitted by law, this Licence will be governed by the laws of England and shall be governed and construed in accordance with the laws of England. Any action arising out of or relating to this agreement shall be brought in courts situated in England save where it is necessary for BMJ Group for enforcement to bring proceedings to bring an action in an alternative jurisdiction.

Questions? customercare@copyright.com or +1-855-239-3415 (toll free in the US) or +1-978-646-2777.